



Universidade do Estado do Rio de Janeiro
Centro de Tecnologia e Ciências
Instituto de Física Armando Dias Tavares

Mapse Barroso Ferreira Filho

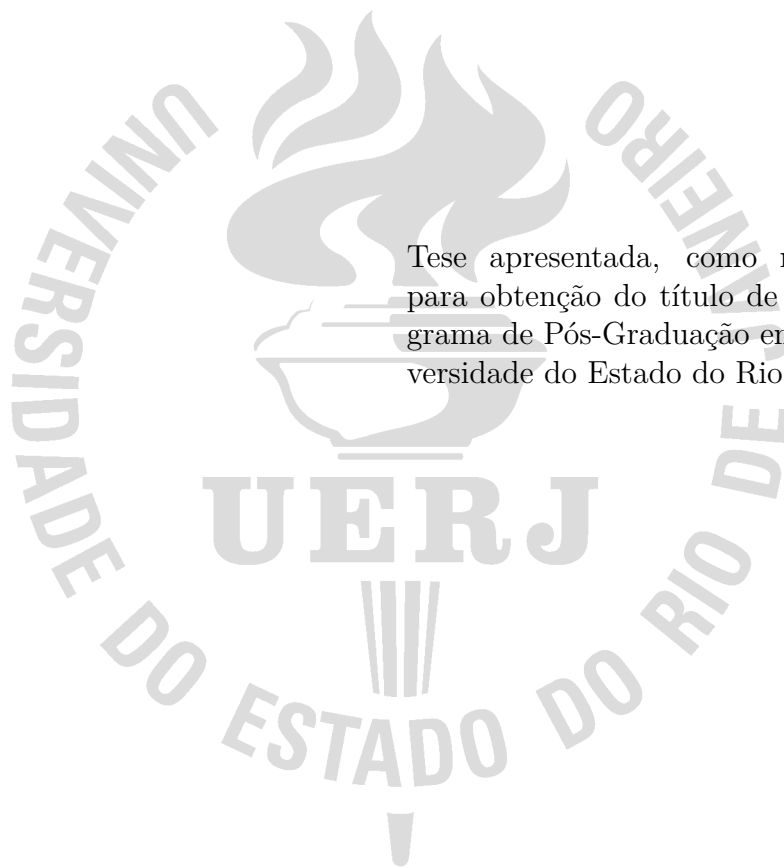
**Associated production of J/ψ and D^* in pp collisions at $\sqrt{s} = 13$
TeV with the full Run 2 data in CMS detector and CMS-RPC
upgrade project studies**

Rio de Janeiro

2023

Mapse Barroso Ferreira Filho

Associated production of J/ψ and D^* in pp collisions at $\sqrt{s} = 13$ TeV with the full Run 2 data in CMS detector and CMS-RPC upgrade project studies



Tese apresentada, como requisito parcial para obtenção do título de Doutor, ao Programa de Pós-Graduação em Física, da Universidade do Estado do Rio de Janeiro.

Orientador: Prof. Sandro Fonseca de Souza
Coorientador: Prof. Alberto Franco de Sá Santoro

Rio de Janeiro

2023

CATALOGAÇÃO NA FONTE
UERJ/ REDE SIRIUS / BIBLIOTECA CTC/D

F383a Ferreira Filho, Mapse Barroso.
Associated production of J/ψ and D^* in pp collisions at $\sqrt{s} = 13$ TeV with the full run 2 data in CMS detector and CMS-RPC upgrade project studies / Mapse Barroso Ferreira Filho. – 2023.
299 f. : il.

Orientador: Sandro Fonseca de Souza.
Coorientador: Alberto Franco de Sá Santoro.
Tese (doutorado) - Universidade do Estado do Rio de Janeiro,
Instituto de Física Armando Dias Tavares.

1. Colisões (Física nuclear) – Teses. 2. Solenóide de múon compacto – Teses. 3. Grande colisor de hádrons (França e Suíça) – Teses. 4. Partículas (Física nuclear) – Teses. I. Souza, Sandro Fonseca de (Orient.). II. Santoro, Alberto Franco de Sá (Coorient.). III. Universidade do Estado do Rio de Janeiro. Instituto de Física Armando Dias Tavares. IV. Título.

CDU 539.12-17

Bibliotecária: Teresa da Silva CRB7/5209

Autorizo, apenas para fins acadêmicos e científicos, a reprodução total ou parcial desta tese, desde que citada a fonte.

Assinatura

Data

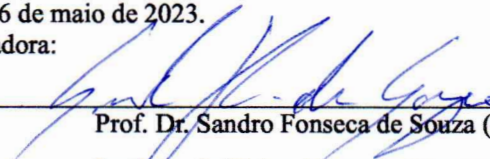
Mapse Barroso Ferreira Filho

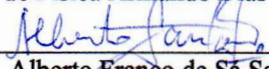
Associated production of J/ψ and D^* in pp collisions at $\sqrt{s} = 13$ TeV with the full Run 2 data in CMS detector and CMS-RPC upgrade project studies

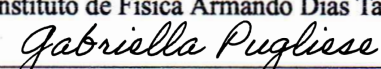
Tese apresentada, como requisito parcial para obtenção do título de Doutor, ao Programa de Pós Graduação em Física, da Universidade do Estado do Rio de Janeiro.

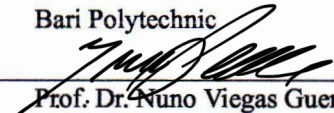
Aprovada em 26 de maio de 2023.

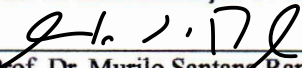
Banca Examinadora:



Prof. Dr. Sandro Fonseca de Souza (Orientador)
Instituto de Física Armando Dias Tavares – UERJ



Prof. Dr. Alberto Franco de Sá Santoro (Coorientador)
Instituto de Física Armando Dias Tavares – UERJ

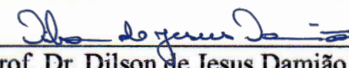

Profa. Dra. Gabriella Pugliese
Bari Polytechnic

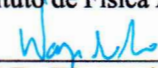

Prof. Dr. Nuno Viegas Guerreiro Leonardo
Lab. de Instrumentação e Física Experimental de Partículas - LIP


Prof. Dr. Murilo Santana Rangel
Universidade Federal do Rio de Janeiro - UFRJ


Profa. Dra. Eliza Melo da Costa
Instituto de Física Armando Dias Tavares – UERJ


Prof. Dr. Helio Nogima
Instituto de Física Armando Dias Tavares – UERJ


Prof. Dr. Dilson de Jesus Damião
Instituto de Física Armando Dias Tavares – UERJ


Prof. Dr. Wagner de Paula Carvalho
Instituto de Física Armando Dias Tavares – UERJ

Rio de Janeiro

2023

DEDICATION

This work is dedicated to my beloved wife Sinara Santos

ACKNOWLEDGEMENTS

First of all, I would like to thank all the forces in the universe that are accompanying me.

I have a very special thanks to my wife Sinara, who has been the biggest support and encouragement during all the challenges I faced during the development of this work. I really thank you for all the patience, support, care, and love during those four years of my life.

To my mother, who has been always present in my life, showing me how to be a good person. I'm really happy to finish this work and dedicate it to you.

To my grandfather/grandmother Camundo/Lucimar, who always trusted in my efforts, without you I would never have had the opportunity to develop this work.

To my sister, who was the first person to help me with my studies, really thank you, my dear sister.

To my supervisor, Sandro Fonseca de Souza, for the friendship, patience, valuable tips, and support during difficult times.

To my co-supervisor, Alberto Santoro, for the remarkable conversations, tips, and training.

To my main research partner, Kevin, who is with me since graduation, we did it, my friend!

To Wagner Carvalho, for the remarkable tips.

To all professors at UERJ, especially Dilson, and Helio.

To all my friends at UERJ, especially Felipe and Mauricio.

To my external advisor, Gabriella, thank you for the opportunity and teachings.

To my RPC colleagues, Mehar, Nicolas, Andres, Ece, Mariana, Dayron, Iuri, Irakli, Reham, Anton, Ian, Jan, Omar, and Maxime (Sorry if I forgot someone).

To ecogas colleagues, Luca and Livia.

To B-physics colleagues, Achim and Stefanos for the very nice discussions.

To Harvey Newman, for providing access to the Caltech T2 storage.

A special thanks to Caio and Bia, who provided me with a very good place to live during difficult times.

Finally, I would like to thank everyone who has been present during these four years of my life, they were, for sure, the best of all!

This work was carried out with the support of the Coordination for the Improvement of Higher Education Personnel - Brazil (CAPES) - Financing Code 001.

Whoever doesn't flare up at someone who's angry wins a battle hard to win.

Buddha

ABSTRACT

FERREIRA FILHO, M. B. *Associated Production of J/ψ and D^* in pp Collisions at $\sqrt{s} = 13$ TeV With the Full Run 2 Data in CMS Detector and CMS-RPC Upgrade Project Studies.* 2023. 299 f. Tese (Doutorado em Física) – Instituto de Física Armando Dias Tavares, Universidade do Estado do Rio de Janeiro, Rio de Janeiro, 2023.

In this work, two main subjects are addressed. The first topic concerns the Compact Muon Solenoid-Resistive Plate Chamber (CMS-RPC) upgrade project, where two main sub-topics are studied. In the first sub-topic, the performance of eco-friendly gas mixtures for the Resistive Plate Chambers (RPC) is analyzed. The performance of two gas mixtures (HFO (35%), CO₂ (60%), i-C₄H₁₀ (4%), SF₆ (1%) and HFO (25%), CO₂ (69%), i-C₄H₁₀ (5%), SF₆ (1%)) based on CO₂-tetrafluoropropene is compared with the performance of the standard gas mixture (C₂H₂F₄ (95.2%), i-C₄H₁₀ (4.5%), SF₆ (0.3%)) used in the RPCs of the Compact Muon Solenoid (CMS) experiment. The performance of both ecogas mixtures is slightly lower than the performance of the standard gas mixture. Still, they can be classified as good candidates and more tests must be performed to validate the long-term operation. In the second sub-topic, the study of the aging of an iRPC prototype is discussed. The data-taking is performed at the Gamma Irradiation Facility (GIF++), a place that combines a 14 TBq ¹³⁷Cs source with a high-energy particle beam. The performance results during the beam tests are satisfactory. However, during the long-term operation, the currents in one of the gaps started to increase after the accumulation of 50 mC/cm² of charge. The cause is still being studied. In the second topic, the associated production of J/ψ and D^* in pp collisions at $\sqrt{s} = 13$ TeV with the full Run 2 in CMS detector is analyzed. This is the first time that this measurement was performed. The cross-section has been measured in the fiducial region, $4 < p_T^{D^*} < 60$ GeV/c, $|y^{D^*}| < 2.1$, $25 < p_T^{J/\psi} < 100$ GeV/c, $|y^{J/\psi}| < 1.2$ as 585 ± 6 (stat) ± 52 (sys) pb, where the fraction due to the DPS contribution was estimated to be 97.5%. In this scenario, the effective cross-section was found to be $2.53_{-0.08}^{+0.09}$ (stat) $_{-0.29}^{+0.25}$ (sys) mb.

Keywords: Double parton scattering. Effective sigma. Ecogas. Resistive plate chamber.

RESUMO

FERREIRA FILHO, M. B. *Produção associada de J/ψ e D^* em colisões pp em $\sqrt{s} = 13$ TeV com a segunda tomada de dados do detector CMS e estudos de atualização do Projeto CMS-RPC.* 2023. 299 f. Tese (Doutorado em Física) – Instituto de Física Armando Dias Tavares, Universidade do Estado do Rio de Janeiro, Rio de Janeiro, 2023.

Nesse trabalho, dois tópicos principais são abordados. O primeiro tópico é relacionado ao projeto de atualização das câmaras de placas resistivas (RPC, do inglês Resistive Plate Chamber) do experimento solenóide de múon compacto (CMS, do inglês Compact Muon Solenoid), em que dois subtópicos principais são estudados. No primeiro subtópico, o desempenho de misturas gasosas ambientalmente amigáveis para as RPCs. O desempenho de duas misturas (HFO (35%), CO₂ (60%), i-C₄H₁₀ (4%), SF₆ (1%) and HFO (25%), CO₂ (69%), i-C₄H₁₀ (5%), SF₆ (1%)) que são baseadas em CO₂-tetrafluoropropeno é comparado com o desempenho da mistura padrão (C₂H₂F₄ (95.2%), i-C₄H₁₀ (4.5%), SF₆ (0.3%)) usada nas RPCs do CMS. O desempenho das duas misturas alternativas é um pouco mais baixo do que o desempenho da mistura padrão. Mesmo assim, elas podem ser classificadas como boas candidatas e mais testes devem ser realizados para validar a operação a longo prazo. No segundo subtópico, o estudo do envelhecimento de um protótipo de iRPC é discutido. As tomadas de dados são realizadas na instalação de radiação gama (GIF++, do inglês Gamma Irradiation Facility), um local que combina uma fonte de 14 TBq ¹³⁷Cs com um feixe de partículas de alta energia. Os resultados de desempenho durante os testes com o feixe de partícula são satisfatórios. No entanto, durante a operação de longo termo a corrente de um dos volumes de gás (gas gap) começou a aumentar após um acúmulo de carga integrada de 50 mC/cm². A causa do aumento ainda está sendo estudada. No segundo tópico, a produção associada de J/ψ e D^* em colisões pp em $\sqrt{s} = 13$ TeV com a segunda tomada de dados do detector CMS é analisada. Essa é a primeira vez que essa medida foi realizada. A seção de choque foi medida na região fiducial $4 < p_T^{D^*} < 60$ GeV/c, $|y^{D^*}| < 2.1$, $25 < p_T^{J/\psi} < 100$ GeV/c, $|y^{J/\psi}| < 1.2$ em 585 ± 6 (stat) ± 52 (sys) pb, em que a fração devida à contribuição de duplo espalhamento partônico foi estimada em 97.5%. Nesse cenário, a seção de choque efetiva resultante é $2.53^{+0.09}_{-0.08}$ (stat) $^{+0.25}_{-0.29}$ (sys) mb.

Palavras-chave: Espalhamento partônico duplo. Seção de choque efetiva. Ecogas.
Câmaras de placas resistivas.

LIST OF FIGURES

Figure 1	- Pillars of the Standard Model.	27
Figure 2	- Higgs peak in the diphoton invariant mass distribution.	29
Figure 3	- Fermion and gluon loop contributions.	31
Figure 4	- Charmonium Spectroscopy.	34
Figure 5	- Bottomonium Spectroscopy.	35
Figure 6	- The CLEO detector	41
Figure 7	- The Belle II detector	42
Figure 8	- Feynman diagram for D^* decaying into D^0 and π_{slow}	43
Figure 9	- SPS representation.	46
Figure 10	- DPS representation.	47
Figure 11	- σ_{eff} measured by several experiments.	49
Figure 12	- CERN accelerator complex	52
Figure 13	- The Compact Muon Solenoid	53
Figure 14	- CMS tracking system	55
Figure 15	- CMS tracking system efficiency	56
Figure 16	- The Electromagnetic Calorimeter.	57
Figure 17	- The ECAL performance.	57
Figure 18	- The Hadronic Calorimeter.	58
Figure 19	- Performance comparison between HPDs and SiPMs.	59
Figure 20	- The CMS solenoid magnet.	60
Figure 21	- A R-z cross-section of a quadrant of the CMS detector.	61
Figure 22	- The CSC detector and its signal formation	62
Figure 23	- Schematic view of a drift tube.	63
Figure 24	- DT single hit efficiency	64
Figure 25	- RPC single hit efficiency	65
Figure 26	- DT segment efficiency	65
Figure 27	- CSC segment efficiency	66
Figure 28	- Schematic view of the L1 trigger	67
Figure 29	- L1 trigger performance	68
Figure 30	- Trigger efficiencies of isolated single muon.	69
Figure 31	- Higgs boson statistics improvement in the HL-LHC phase.	70
Figure 32	- Precision improvement - HL-LHC.	71
Figure 33	- The CMS Phase-II upgrade changes	72
Figure 34	- Electric field in a wire gaseous detector.	74
Figure 35	- RPC schematic.	75
Figure 36	- The streamer signal.	77

Figure 37 - The avalanche signal.	77
Figure 38 - Schematic of the CMS RPC System	79
Figure 39 - Double Gap RPC	80
Figure 40 - GHG emission in Run 2 for the big LHC experiments.	82
Figure 41 - GHG emission in Run 2 for the sub-detectors.	83
Figure 42 - Reduction of F-gases in LHC Runs.	83
Figure 43 - Gain in the efficiency after gas leaky repairs.	84
Figure 44 - Schematics of the C ₂ H ₂ F ₄ (R134a) recuperation system.	85
Figure 45 - CMS-RPC gas recuperation system.	86
Figure 46 - Various refrigerant candidates.	87
Figure 47 - Comparison of different gas mixtures in an RPC.	88
Figure 48 - GIF++ facility	90
Figure 49 - Ecogas gas rack.	91
Figure 50 - Ecogas detectors position in GIF++ bunker	92
Figure 51 - GIF++ setup	92
Figure 52 - RE/1/001 chamber	93
Figure 53 - Data Acquisition system at GIF++	94
Figure 54 - Connection diagram	95
Figure 55 - RE1/1 gaps distribution	96
Figure 56 - RE1/1 partitions.	97
Figure 57 - RE1/1 installed in the bunker.	98
Figure 58 - Gamma source and its filters	98
Figure 59 - Photon flux in the bunker	100
Figure 60 - Trigger Logic.	101
Figure 61 - Photomultipliers disposition.	101
Figure 62 - Hits distribution.	102
Figure 63 - Standard gas: Current Density x HV _{eff}	106
Figure 64 - Standard gas: Muon Cluster Size x HV _{eff}	107
Figure 65 - Standard gas: Efficiency x HV _{eff}	107
Figure 66 - Standard gas: Efficiency x HV _{gas}	108
Figure 67 - Ecomix-2: Current Density x HV _{eff}	109
Figure 68 - Ecomix-2: Muon Cluster Size x HV _{eff}	110
Figure 69 - Ecomix-2: Efficiency x HV _{eff}	110
Figure 70 - Ecomix-2: Efficiency x HV _{gas}	111
Figure 71 - Ecomix-3: Current Density x HV _{eff}	112
Figure 72 - Ecomix-3: Muon Cluster Size x HV _{eff}	112
Figure 73 - Ecomix-3: Efficiency x HV _{eff}	113
Figure 74 - Ecomix-3: Efficiency x HV _{gas}	113
Figure 75 - Current Density comparison	114

Figure 76 - Efficiency at source OFF comparison	115
Figure 77 - Efficiency at absorption factor 4.6 comparison	116
Figure 78 - Current density versus cluster rate at WP	117
Figure 79 - Efficiency versus gamma rate	117
Figure 80 - Working point as a function of the gamma rate at WP	118
Figure 81 - A CMS quadrant.	120
Figure 82 - iRPC demonstrator installation	121
Figure 83 - Density current as a function of high voltage for various rates	123
Figure 84 - Muon efficiency in function of the high voltage for various rates	123
Figure 85 - Muon efficiency at the working point as a function of the gamma rate at the working point	124
Figure 86 - Density current as a function of the cluster rate	125
Figure 87 - Working point as a function of the gamma rate	125
Figure 88 - Current density in the top gap as a function of the effective voltage	126
Figure 89 - Current density in the bottom gap as a function of the effective voltage	127
Figure 90 - Efficiency comparison between threshold 45 fC and 75 fC without gamma rate	128
Figure 91 - Efficiency comparison between threshold 45 fC and 75 fC with gamma rate	129
Figure 92 - Ohmic current as a function of the integrated charge in the top gap	130
Figure 93 - Ohmic current as a function of the integrated charge in the bottom gap	131
Figure 94 - Physics current as a function of the integrated charge in the top gap	132
Figure 95 - Physics current as a function of the integrated charge in the bottom gap	132
Figure 96 - Comparison between CMS and LHCb	134
Figure 97 - The DPS and SPS contributions to the cross-section.	135
Figure 98 - Transverse momentum distribution of generated and reconstructed dimuons using DPS MC.	140
Figure 99 - Pseudorapidity distribution of generated and reconstructed dimuons using DPS MC.	141
Figure 100 - Phi distribution of generated and reconstructed dimuons using DPS MC.	142
Figure 101 - Transverse momentum distribution of generated and reconstructed D* using DPS MC.	143
Figure 102 - Pseudorapidity distribution of generated and reconstructed D* using DPS MC.	144
Figure 103 - Phi distribution of generated and reconstructed D* using DPS MC.	145
Figure 104 - Transverse momentum distribution of generated and reconstructed dimuons using SPS MC.	146
Figure 105 - Pseudorapidity distribution of generated and reconstructed dimuons using SPS MC.	147

Figure 106 - Phi distribution of generated and reconstructed dimuons using SPS MC.	148
Figure 107 - Transverse momentum distribution of generated and reconstructed D^* using SPS MC.	149
Figure 108 - Pseudorapidity distribution of generated and reconstructed D^* using SPS MC.	150
Figure 109 - Phi distribution of generated and reconstructed D^* using SPS MC. . .	151
Figure 110 - Association of J/ψ and D^*	156
Figure 111 - Muon acceptance with particle gun sample.	158
Figure 112 - J/ψ acceptance with particle gun sample.	160
Figure 113 - D^* acceptance with particle gun sample.	161
Figure 114 - Pseudo-significance versus applied cut.	163
Figure 115 - J/ψ control plots 1 - 2017 data.	165
Figure 116 - J/ψ control plots 2 - 2017 data.	165
Figure 117 - D^* control plots 1 - 2017 data.	166
Figure 118 - D^* control plots 2 - 2017 data.	166
Figure 119 - $J/\psi D^*$ control plots 1 - 2017 data.	167
Figure 120 - Phase space as a function of p_T	168
Figure 121 - The $\mu^+ \mu^-$ invariant mass distribution	172
Figure 122 - J/ψ decay length	173
Figure 123 - $D^* - D^0$ mass difference distribution	174
Figure 124 - J/ψ acceptance in bins of rapidity and p_T - 2017 data.	197
Figure 125 - D^* acceptance in bins of rapidity and p_T - 2017 data.	198
Figure 126 - D^* cuts efficiency in bins of rapidity and p_T - 2017 data.	199
Figure 127 - J/ψ cuts efficiency in bins of rapidity and p_T - 2017 data.	200
Figure 128 - HLT efficiency in bins of rapidity and p_T - 2017 data.	201
Figure 129 - Association efficiency in bins of $D^* p_T$ and $J/\psi p_T$ - 2017 data.	202
Figure 130 - Feynman diagram for the SPS production.	213
Figure 131 - Effective sigma measurements	216
Figure 132 - Pile-up correction in Monte Carlo.	247
Figure 133 - J/ψ control plots 1 - 2016-pre-VFP data.	248
Figure 134 - J/ψ control plots 2 - 2016-pre-VFP data.	249
Figure 135 - D^* control plots 1 - 2016-pre-VFP data.	249
Figure 136 - D^* control plots 2 - 2016-pre-VFP data.	250
Figure 137 - $J/\psi D^*$ control plots 1 - 2016-pre-VFP data.	250
Figure 138 - J/ψ control plots 1 - 2016-pos-VFP data.	251
Figure 139 - J/ψ control plots 2 - 2016-pos-VFP data.	251
Figure 140 - D^* control plots 1 - 2016-pos-VFP data.	252
Figure 141 - D^* control plots 2 - 2016-pos-VFP data.	252
Figure 142 - $J/\psi D^*$ control plots 1 - 2016-pos-VFP data.	253

Figure 143 - J/ψ control plots 1 - 2018 data.	254
Figure 144 - J/ψ control plots 2 - 2018 data.	254
Figure 145 - D^* control plots 1 - 2018 data.	255
Figure 146 - D^* control plots 2 - 2018 data.	255
Figure 147 - $J/\psi D^*$ control plots 1 - 2016-pre-VFP data.	256
Figure 148 - The $\mu^+ \mu^-$ invariant mass distribution - 2016-pre-VFP data	259
Figure 149 - J/ψ decay length - 2016-pre-VFP data	260
Figure 150 - $D^* - D^0$ mass difference distribution - 2016-pre-VFP data	261
Figure 151 - The $\mu^+ \mu^-$ invariant mass distribution - 2016-pos-VFP data	262
Figure 152 - J/ψ decay length - 2016-pos-VFP data	263
Figure 153 - $D^* - D^0$ mass difference distribution - 2016-pos-VFP data	264
Figure 154 - The $\mu^+ \mu^-$ invariant mass distribution - 2018 data	265
Figure 155 - J/ψ decay length - 2018 data	266
Figure 156 - $D^* - D^0$ mass difference distribution - 2018 data	267
Figure 157 - J/ψ acceptance in bins of rapidity and p_T - 2016-pre-VFP data.	269
Figure 158 - D^* acceptance in bins of rapidity and p_T - 2016-pre-VFP data.	270
Figure 159 - D^* cuts efficiency in bins of rapidity and p_T - 2016-pre-VFP data.	271
Figure 160 - J/ψ cuts efficiency in bins of rapidity and p_T - 2016-pre-VFP data.	272
Figure 161 - HLT efficiency in bins of rapidity and p_T - 2016-pre-VFP data.	273
Figure 162 - Association efficiency in bins of $D^* p_T$ and $J/\psi p_T$ - 2016-pre-VFP data.	274
Figure 163 - J/ψ acceptance in bins of rapidity and p_T - 2016-pos-VFP data.	275
Figure 164 - D^* acceptance in bins of rapidity and p_T - 2016-pos-VFP data.	276
Figure 165 - D^* cuts efficiency in bins of rapidity and p_T - 2016-pos-VFP data.	277
Figure 166 - J/ψ cuts efficiency in bins of rapidity and p_T - 2016-pos-VFP data.	278
Figure 167 - HLT efficiency in bins of rapidity and p_T - 2016-pos-VFP data.	279
Figure 168 - Association efficiency in bins of $D^* p_T$ and $J/\psi p_T$ - 2016-pos-VFP data.	280
Figure 169 - J/ψ acceptance in bins of rapidity and p_T - 2018 data.	281
Figure 170 - D^* acceptance in bins of rapidity and p_T - 2018 data.	282
Figure 171 - D^* cuts efficiency in bins of rapidity and p_T - 2018 data.	283
Figure 172 - J/ψ cuts efficiency in bins of rapidity and p_T - 2018 data.	284
Figure 173 - HLT efficiency in bins of rapidity and p_T - 2018 data.	285
Figure 174 - Association efficiency in bins of $D^* p_T$ and $J/\psi p_T$ - 2018 data.	286
Figure 175 - 2016-pre-VFP data: case 2.	287
Figure 176 - 2016-pre-VFP data: case 3.	288
Figure 177 - 2016-pre-VFP data: case 4.	288
Figure 178 - 2016-pre-VFP data: case 5.	289
Figure 179 - 2016-pre-VFP data: case 6.	289
Figure 180 - 2016-pos-VFP data: case 2.	290
Figure 181 - 2016-pos-VFP data: case 3.	290

Figure 182 - 2016-pos-VFP data: case 4.	291
Figure 183 - 2016-pos-VFP data: case 5.	291
Figure 184 - 2016-pos-VFP data: case 6.	292
Figure 185 - 2017 data: case 2.	292
Figure 186 - 2017 data: case 3.	293
Figure 187 - 2017 data: case 4.	293
Figure 188 - 2017 data: case 5.	294
Figure 189 - 2017 data: case 6.	294
Figure 190 - 2018 data: case 2.	295
Figure 191 - 2018 data: case 3.	295
Figure 192 - 2018 data: case 4.	296
Figure 193 - 2018 data: case 5.	296
Figure 194 - 2018 data: case 6.	297

LIST OF TABLES

Table 1	- Particles generations	28
Table 2	- Summary of the spectroscopic notation for quarkonia particles.	33
Table 3	- Color evaporation mode parameters.	37
Table 4	- Average values for c quark fragmentation function at LEP from e^+e^- collisions.	44
Table 5	- Average values for c quark fragmentation functions at LHC from pp collisions.	45
Table 6	- α factor as a function of the interaction particles	48
Table 7	- Ecogas mixtures used in RE1/1 at GIF++	95
Table 8	- All possible gamma source attenuation factors	99
Table 9	- Absorption factors used during data taking	105
Table 10	- Resistance for each plate	108
Table 11	- Run-2 datasets and corresponding JSON files.	137
Table 12	- Muons and J/ψ selection cuts.	154
Table 13	- D^* selection cuts	154
Table 14	- D^* tracks selection cuts.	155
Table 15	- Selection criteria applied in π_{slow}	155
Table 16	- Selection criteria applied in D^0	156
Table 17	- Vertex probability cut applied to the $\mu^+ \mu^- \pi_{slow}$ common vertex.	157
Table 18	- Cuts to be optimized.	162
Table 19	- Optimized cuts - final values.	164
Table 20	- 2016-pre-VFP yields	175
Table 21	- 2016-pos-VFP yields	175
Table 22	- 2017 Yields.	176
Table 23	- 2018 yields	176
Table 24	- Muon and J/ψ cuts considered in the acceptance calculation.	177
Table 25	- J/ψ acceptance - entire phase space considered in the study.	178
Table 26	- J/ψ acceptance in bins of p_T in 2016-pre-VFP. The rapidity is $ y < 2.4$	179
Table 27	- J/ψ acceptance in bins of p_T in 2016-pos-VFP. The rapidity is $ y < 2.4$	179
Table 28	- J/ψ acceptance in bins of p_T in 2017. The rapidity is $ y < 2.4$	180
Table 29	- J/ψ acceptance in bins of p_T in 2018. The rapidity is $ y < 2.4$	180
Table 30	- D^* kinematic cuts considered in the acceptance calculation.	181
Table 31	- D^* acceptance - entire phase space considered in the study.	181
Table 32	- D^* acceptance in bins of p_T in 2016-pre-VFP. The rapidity is $ y < 2.4$	182
Table 33	- D^* acceptance in bins of p_T in 2016-pos-VFP. The rapidity is $ y < 2.4$	182
Table 34	- D^* acceptance in bins of p_T in 2017. The rapidity is $ y < 2.4$	183

Table 35	- D* acceptance in bins of p_T in 2018. The rapidity is $ y < 2.4$	183
Table 36	- D* cuts efficiency - entire phase space considered in the study.	184
Table 37	- D* cuts efficiency in bins of p_T in 2016-pre-VFP. The rapidity is $ y < 2.4$	184
Table 38	- D* cuts efficiency in bins of p_T in 2016-pos-VFP. The rapidity is $ y < 2.4$	185
Table 39	- D* cuts efficiency in bins of p_T in 2017. The rapidity is $ y < 2.4$	185
Table 40	- D* cuts efficiency in bins of p_T in 2018. The rapidity is $ y < 2.4$	185
Table 41	- J/ ψ cuts efficiency - entire phase space considered in the study.	186
Table 42	- J/ ψ cuts efficiency in bins of p_T in 2016-pre-VFP. The rapidity is $ y < 2.4$	186
Table 43	- J/ ψ cuts efficiency in bins of p_T in 2016-pos-VFP. The rapidity is $ y < 2.4$	187
Table 44	- J/ ψ cuts efficiency in bins of p_T in 2017. The rapidity is $ y < 2.4$	187
Table 45	- J/ ψ cuts efficiency in bins of p_T in 2018. The rapidity is $ y < 2.4$	188
Table 46	- High level trigger efficiency - entire phase space considered in the study.	188
Table 47	- <i>HLT_Dimuon16_Jpsi</i> efficiency in bins of p_T in 2016-pre-VFP. The rapidity is $ y < 2.4$	189
Table 48	- <i>HLT_Dimuon16_Jpsi</i> efficiency in bins of p_T in 2016-pos-VFP. The rapidity is $ y < 2.4$	190
Table 49	- <i>HLT_Dimuon25_Jpsi</i> efficiency in bins of p_T in 2017. The rapidity for J/ ψ is $ y < 2.4$	190
Table 50	- <i>HLT_Dimuon25_Jpsi</i> efficiency in bins of p_T in 2018. The rapidity is $ y < 2.4$	191
Table 51	- Association efficiency - entire phase space considered in this study.	191
Table 52	- Association efficiency in bins of J/ ψ p_T in 2016-pre-VFP. The rapidity is $ y < 2.4$	192
Table 53	- Association efficiency in bins of J/ ψ p_T in 2016-pos-VFP. The rapidity is $ y < 2.4$	192
Table 54	- Association efficiency in bins of J/ ψ p_T in 2017. The rapidity is $ y < 2.4$	193
Table 55	- Association efficiency in bins of J/ ψ p_T in 2018. The rapidity is $ y < 2.4$	193
Table 56	- Association efficiency in bins of D* p_T in 2016-pre-VFP. The rapidity is $ y < 2.4$	194
Table 57	- Association efficiency in bins of D* p_T in 2016-pos-VFP. The rapidity is $ y < 2.4$	194
Table 58	- Association efficiency in bins of D* p_T in 2017. The rapidity is $ y < 2.4$.	195
Table 59	- Association efficiency in bins of D* p_T in 2018. The rapidity is $ y < 2.4$.	195

Table 60	- Integrated luminosity - systematic uncertainty.	204
Table 61	- Branching fraction - systematic uncertainty.	204
Table 62	- Signal yields - systematic uncertainty.	205
Table 63	- Tracking - systematic uncertainty.	206
Table 64	- Acceptance and efficiency - systematic uncertainty.	207
Table 65	- Total cross-section - 2016-pre-VFP.	208
Table 66	- Total cross-section - 2016-pos-VFP.	209
Table 67	- Total cross-section - 2017.	209
Table 68	- Total cross-section - 2018.	210
Table 69	- Total cross-section - all years	211
Table 70	- Measurement of prompt inclusive J/ψ and D^*	212
Table 71	- Total cross-section for the σ_{eff} calculation.	212
Table 72	- $J/\psi + D^*$ DPS cross-sections.	214
Table 73	- Effective sigma.	214
Table 74	- DPS Samples: 2016-pre-VFP.	242
Table 75	- DPS Samples: 2016-pos-VFP.	243
Table 76	- DPS Samples: 2017	243
Table 77	- DPS Samples: 2018	244
Table 78	- SPS Samples: 2016-pre-VFP.	245
Table 79	- SPS Samples: 2016-pos-VFP.	245
Table 80	- SPS Samples: 2017	246
Table 81	- SPS Samples: 2018	246
Table 82	- Tracking - details of the systematic uncertainty.	297
Table 83	- Muon ID - details of the systematic uncertainty.	298
Table 84	- Pointing angle - details of the systematic uncertainty.	298
Table 85	- Association - details of the systematic uncertainty.	298

ACRONYMS AND ABBREVIATIONS LIST

SM	Standard Model
BSM	Beyond Standard Model
MPI	Multiple Parton Interaction
TPS	Triple Parton Scattering
QFT	Quantum Field Theory
TGR	Theory of General Relativity
QCD	Quantum Chromodynamics
QED	Quantum Electrodynamics
pQCD	Perturbative Quantum Chromodynamics
TMD	Transverse-Momentum-Dependent
CEM	Color-Evaporation Model
CSM	Color-Singlet Model
NRQCD	Nonrelativistic Quantum Chromodynamics
NLO	Next-to-Leading Order
NNLO	Next-to-Next-Leading Order
LDME	Long-Distance Matrix Elements
CDF	Collider Detector at Fermilab
LHCb	Large Hadron Collider beauty
LHC	Large Hadron Collider
CESR	Cornell Electron Storage Ring
PDF	Parton Distribution Function or Probability Density Function
FF	Fragmentation Functions
LEP	Large Electron Positron Collider
ALEPH	Apparatus for LEP Physics
DELPHI	DEtector With Lepton, Photon and Hadron Identification
OPAL	Omni-Purpose Apparatus at LEP
ALICE	A Large Ion Collider Experiment
SPS	Single Parton Scattering or Super Proton Synchrotron
DPS	Double Parton Scattering
ATLAS	A Toroidal LHC Apparatus
CMS	Compact Muon Solenoid
BPix	Barrel Pixel
EPix	Endcap Disks
DAQ	Data Acquisition System
ECAL	Electro Magnetic Calorimeter
HCAL	Hadronic Calorimeter

WLS	Wavelength-shifting
HPD	Hybrid Photodiode
CSC	Cathode Strip Chambers
DR	Drift Tubes
RPC	Resistive Plate Chambers
MB	Muon Barrel
ME	Muon Endcap
HL-LHC	High-Luminosity LHC
iRPC	Improved Resistive Plate Chambers
GEM	Gas Electron Multiplier
HLT	High Level Trigger
EMTF	Endcap Muon Track-Finder
MBTF	Muon Barrel Track-Finder
OMTF	Overlap Muon Track-Finder
GMT	Global Muon Trigger
RTC	Regional Trigger
GCT	Global Trigger
TTC	Timing and Control
EVM	Event Filter Farm
DQM	Data Quality Monitoring
GIF	Gamma Irradiation Facility
HF	Hydrofluoric Acid
GWP	Global Warming Potential
ODP	Ozone Depletion Layer
GHG	Greenhouse Gases
LS2	Long Shutdown 2
EPDT	Experimental Physics and Detector Technologies
sMDT	Monitored Drift Tube
MFC	Mass Flow Controller
DIP	Data Interchange Protocol
TDC	Time-to-Digital Converter
USB	Universal Serial Bus
PMT	Photo-Multiplier
LVDS	Low-Voltage-Differential-Signal
CS	Cluster Size
CLR	Cluster Rate
WP	Working Point
GR	Gamma Rate
MPS	Multiple Parton Scattering

LHE	Les Houches Event Files
UL	Ultra Legacy
JSON	JavaScript Object Notation
AOD	Analysis Object Data
EDM	Event Data Model
APV	Analogue Pipeline Voltage
CB	Crystall Ball
TF	Threshold Function
POG	Physics Object Group

SYMBOL LIST

$SU(3)$	Special Unitary Group of Degree 3
$SU(2)$	Special Unitary Group of Degree 2
$U(2)$	Unitary Group of Degree 2
$U(1)$	Unitary Group of Degree 1
W^\pm	W boson
Z	Z boson
$\Lambda^{(a)}$	Delta baryon
α_s	Strong Coupling Parameter
Λ_{QCD}	Quantum Chromodynamics Scale
$\psi(2S)$	$\psi(2S)$ Meson
J/ψ	J/ψ Meson
D^0	D^0 Meson
D^*	D^* Meson
σ_{eff}	Effective Sigma
$d\sigma_{C_1C_2}^{DPS}$	Double Parton Scattering cross section of Sub-Process C_1 and C_2
HV_{eff}	Effective High Voltage
HV_{WP}	High Voltage at Working Point

CONTENTS

	INTRODUCTION	24
1	THEORETICAL MOTIVATIONS	27
1.1	Standard Model	27
1.2	Higgs Boson Discovery	28
1.3	Quantum Chromodynamics	29
1.4	Renormalization and asymptotic freedom	31
1.5	Quark masses	32
1.6	Quarkonium Spectroscopy	32
1.7	Quarkonium Production	36
1.7.1	<u>The color-Evaporation Model (CEM)</u>	36
1.7.2	<u>The color Singlet Model (CSM)</u>	38
1.7.3	<u>The color Octet Mechanism and the NRQCD factorisation</u>	38
1.8	Open Charm Production	40
1.8.1	<u>D mesons</u>	42
1.8.1.1	Fragmentation functions	43
1.9	Parton Scattering	45
1.9.1	<u>Single Parton Scattering</u>	45
1.9.2	<u>Double Parton Scattering</u>	46
1.10	Recent results in the associated production of quarkonia and open-charms	50
2	EXPERIMENTAL SETUP	51
2.1	The Compact Muon Solenoid detector	53
2.1.1	<u>CMS Sub-detectors</u>	54
2.1.1.1	The Tracking System	54
2.1.1.2	Calorimeters	55
2.1.1.3	The Solenoid Magnet	60
2.1.1.4	The Muon System	60
2.1.1.5	Performance of CMS Muon Detector in Run 2	63
2.1.1.6	Trigger and data acquisition	64
2.1.2	<u>CMS Phase-2 Upgrades</u>	69
2.1.2.1	Phase II Upgrades of CMS Muon Detector	71
3	ACTIVITIES AND CONTRIBUTIONS TO THE CMS-RPC PHASE-II PROJECT	73
3.1	The Resistive Plate Chamber	74
3.1.1	<u>The Principle of Operation</u>	75
3.1.1.1	Streamer mode	76

3.1.1.2	Avalanche mode	76
3.1.2	<u>The RPC gain factor</u>	76
3.1.3	<u>The CMS RPC System</u>	78
3.2	Eco-friendly gas mixtures for Resistive Plate Chambers	80
3.2.1	<u>Choice of gas mixtures</u>	80
3.2.2	<u>Greenhouse Gases Emissions at CERN</u>	81
3.2.2.1	European Union gas regulation	82
3.2.3	<u>RPC Leak Repairs in Long Shutdown 2</u>	84
3.2.4	<u>CO2-tetrafluoropropene based gas mixtures</u>	86
3.2.5	<u>The Ecogas Collaboration</u>	88
3.2.6	<u>The Gamma Irradiation Facility</u>	89
3.2.7	<u>Ecogas Collaboration Setup at GIF++</u>	89
3.2.7.1	Gas System	89
3.2.7.2	Monitoring and controlling	90
3.2.7.3	Detectors	91
3.3	Ecogas results at GIF++	91
3.3.1	<u>Chamber Description and Experimental Schematic</u>	93
3.3.2	<u>Software and Data Acquisition</u>	93
3.3.3	<u>Experimental Conditions</u>	94
3.3.3.1	Trigger Logic	100
3.3.3.2	Signal Readout	102
3.3.4	<u>Data Analysis</u>	102
3.3.4.1	Important detector parameters	103
3.3.5	<u>Standard gas results</u>	105
3.3.6	<u>Ecomix-2 gas results</u>	109
3.3.7	<u>Ecomix-3 gas results</u>	111
3.3.8	<u>Comparison between the mixtures</u>	114
3.4	iRPC Aging Studies	118
3.4.1	<u>The Improved Resistive Plate Chambers</u>	120
3.5	Experimental setup	122
3.5.1	<u>Results</u>	122
4	ASSOCIATED PRODUCTION OF J/ψ AND D^* WITH THE CMS DETECTOR	133
4.1	Introduction of Analysis	133
4.1.1	<u>Motivations</u>	133
4.2	Datasets and Monte Carlo Samples	134
4.2.1	<u>Dataset samples</u>	136
4.2.2	<u>Monte Carlo Samples</u>	136
4.2.3	<u>Monte Carlo Weighting</u>	138

4.2.4	<u>Monte Carlo Matching</u>	138
4.3	Selection Strategy	152
4.3.1	<u>Preselection Cuts</u>	152
4.3.2	<u>High Level Trigger</u>	153
4.3.3	<u>Selection Cuts</u>	153
4.3.4	<u>Acceptance studies to optimize Monte Carlo production</u>	157
4.3.5	<u>Optimization of Selection Cuts</u>	162
4.3.6	<u>Control Plots</u>	164
4.4	Signal Extraction	168
4.5	Acceptance	171
4.5.1	<u>J/ψ Acceptance</u>	177
4.5.2	<u>D* Acceptance</u>	178
4.6	Efficiencies	182
4.6.1	<u>D* cuts Efficiency</u>	182
4.6.2	<u>J/ψ Cuts Efficiency</u>	184
4.6.3	<u>Trigger Efficiency</u>	188
4.6.4	<u>Association Efficiency</u>	189
4.7	Systematic Uncertainties	203
4.7.1	<u>Luminosity</u>	203
4.7.2	<u>Branching Fraction</u>	204
4.7.3	<u>Signal yields</u>	204
4.7.4	<u>Tracking</u>	205
4.7.5	<u>Cuts Efficiency</u>	206
4.8	Cross-Section	207
4.8.1	<u>Effective Cross-Section Extraction</u>	210
4.9	Discussion of Results and Conclusions	215
	CONCLUSION	218
	REFERENCES	220
	APPENDIX A – Presentations and Awards	236
	APPENDIX B – Particle Gun Monte Carlo	237
	APPENDIX C – Single Parton Scattering Monte Carlo	239
	APPENDIX D – Monte Carlo Samples	242
	APPENDIX E – Pile-up reweighting	247
	APPENDIX F – Control Plots	248
	APPENDIX G – Fitting Strategy	257
	APPENDIX H – Acceptance and Efficiency - Plots	268
	APPENDIX I – Systematic Uncertainties: strategies	287

INTRODUCTION

In November of 1974, a new particle with a mass peak at 3095 MeV was discovered simultaneously at Brookhaven National Lab and at SLAC. This discovery was very significant to the high-energy physics community and today this event is known as the November revolution (1). The narrowness of the peak, the fact that the lifetime was around 1000 times higher than that of other particles of similar mass and that the two laboratories that discovered it used different types of detectors were of great importance. Two years later, Samuel Ting and Burton Richter, who led the groups, were awarded the Nobel Prize in physics. In the 1970s, the three-quark model for elementary particles was the most accepted theory, because it successfully explained the spectroscopy of known hadrons (2, 3).

The main impact of this measurement was the discovery of the charm quark, in fact, the particle discovered was J/ψ meson, which is composed of a c and \bar{c} quarks. Soon after the J/ψ discovery, other bound states of $c\bar{c}$ were discovered as well. Besides that, it was natural to imagine the existence of charmed mesons, *i.e.* mesons with another quark (u, d, s) and a c or \bar{c} quark. Indeed, the study of the e^+e^- annihilation led to the discovery of the so-called charmed mesons. The D mesons, which are the lightest particles composed of a charm quark, were discovered in 1976, giving more evidence for the validity of the charm theory. The first discovery of D mesons were D^0 and D^+ . They were observed at SLAC-LBL Mark I collaboration at SPEAR in e^+e^- annihilation at \sqrt{s} ranging from 3.9 to 4.6 GeV (4). The importance of this discovery was the possibility to study the weak hadronic decay because both particles do not experience strong and electromagnetic interactions (5).

Nearly 50 years after the discovery of the J/ψ and other quarkonium states (including bottomonium states) the theory that describes this framework is still not fully understood. Furthermore, in the study of the D mesons, there is a great possibility for a better comprehension of the interaction of the charm quark with other quarks. This is an interesting part of the Quantum Chromodynamics (QCD) and the understanding of the production of such particles provides a way to test the QCD models. Thus, studying the hadronic production of these states is very important.

In addition, Multiple Parton Interaction (MPI) (6) is raising a lot of attention in the past years. The interest in the MPI is due to the possibility to study the contribution of the Double Parton Scattering (DPS) in the associated production of pairs of quarkonia (7, 8, 9, 10), pairs of quarkonia and charmed mesons (11, 12), pairs of W^\pm (13), etc. Besides that, in November of 2021 the Compact Muon Solenoid (CMS) published an analysis of the measurement of the associated production of triple J/ψ (14). This measurement identified what is called Triple Parton Scattering (TPS), which brings more astonishing

possibilities of new particle channels. Therefore, in this framework, several experiments conducted measurements of the so-called effective sigma. This quantity, in principle, should not vary from particle channel to particle channel, but surprisingly the values found in different channels vary significantly (6).

Furthermore, the experimental apparatus used in this kind of measurement have become more complex in the past years. As the energy of the collision and the luminosity increased significantly, the accelerators and detectors needed many improvements to cope with the changes. Since the discovery of the Higgs boson, in 2012 at the LHC, the physics community work hard looking forward to new discoveries. The upgrade of the LHC accelerator complex, as well as the main detectors, A Large Ion Collider Experiment (ALICE) (15), A Toroidal LHC Apparatus (ATLAS) (16), Compact Muon Solenoid (CMS) (17), and LHC beauty (LHCb) (18) started after the end of the first data taking period, the so-called Run 1 (2008 - 2013). From 2013 to 2022 many upgrades (LHC Phase-I Program (19)) have been implemented during the accelerator shutdown. Thenceforth, many upgrades are foreseen for the upcoming years, where the main upgrade is towards the High Luminosity LHC (HL-LHC) (20), which is called upgrade Phase-II. The upgrade project at the CMS involves many important activities of which two are discussed in this work: the development of the improved Resistive Plate Chambers (iRPC) (21) and the search for ecological gas mixtures (22) for the existing and improved versions of the RPCs.

The iRPCs will be installed in the forward region of the CMS, on the 3rd and 4th endcap disk at a pseudorapidity (η) range from 1.8 to 2.1. The new experimental conditions, with higher particle background, can introduce non-recoverable aging effects in the detectors. To cope with these changes it is crucial to validate the detectors in experimental tests with similar conditions that will be found in HL-LHC. It is worth mentioning that two iRPC demonstrator chambers were installed in December 2022. Dedicated commissioning is ongoing and the plan is to install all 72 chambers by the end of 2028. Besides that, with environmental concerns as well as the current F-gas regulation, eco-friendly gas mixtures, with lower Global Warm Potential (GWP) are under study.

In this thesis, the main topics studied are the measurement of the associated production of J/ψ and D^* using the full Run 2 data in CMS, the characterization of eco-friendly gas mixtures in a high background environment, and the aging study of an iRPC prototype. The rest of the thesis is organized as follows.

Chapter 2 describes the theoretical motivations. The Standard Model (SM) of particles and the Quantum Chromodynamics (QCD) are described. Then, the quarkonium and open charms production mechanisms are discussed. Finally, Multiple Parton Scattering (MPS) is described. Chapter 3 describes the experimental setup used in the analysis. The LHC accelerator complex is briefly described. Then, the CMS detector is described in detail. Chapter 4 describes the activities and contributions of the CMS-RPC Phase-II project. The eco-friendly gas studies are covered and the characterization of an

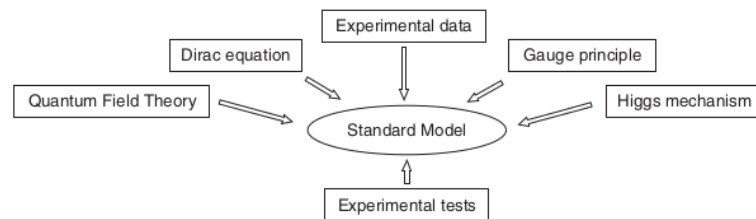
RPC detector using the standard gas and two eco-friendly gas is studied. Besides that, the aging of the CMS-RPC detector is studied and the aging of an iRPC prototype is studied in detail. Chapter 5 describes in detail the measurement of the associated production of J/ψ and D^* using the full Run 2 data in CMS. The last chapter is dedicated to the conclusion and future perspectives.

1 THEORETICAL MOTIVATIONS

1.1 Standard Model

The standard model of particle physics is a set of models that best describe existing particles and their interactions, explaining well three out of four nature interactions, or in other words, it is said that all matter is made of three kinds of elementary particles: quarks, leptons, and mediators. It consists of three fields: gauge field, Higgs field, and fermions (23). In group theory language it is said that the SM is based on the gauge symmetry group $SU(3)_C \otimes SU(2)_L \otimes U(1)_Y$, where C represents the color charge, L represents the left-handed coupling of the weak isospin and Y represents the weak charge (24). Although the SM is the best modern approach to describe particle physics, it is known that it is a low-energy approach to a fundamental theory (25). To describe the SM it is necessary to bring together theoretical and experimental ideas as can be seen in Figure (1). The Quantum Field Theory (QFT) provides tools to describe particles and their interactions; the Dirac Equation (26) describes quantum and relativistically the dynamics of fermions; the experimental results are ways of testing the hypothesis and theoretical arguments; the gauge principle¹ determines the exact nature of these interactions; the Higgs mechanism that comes from the electroweak symmetry breaking explains the existence of the mass of some particles (26).

Figure 1 - Pillars of the Standard Model.



Legend: The main pillars of the Standard Model: Theoretical and experimental.

Source: THOMSON, 2013, p. 500.

¹ The gauge principle is a fundamental symmetry where a physical theory can be expressed with different equations that describe the same physical system. In this case, it is said that the theory is described by "redundant" degrees of freedom. This principle is, for instance, applied in electrodynamics and in linearized gravity, where two or more equations can describe the same physical situation, but one equation is much easier to be solved. Therefore, a mathematical transformation can be applied (gauge transformation) in a complex equation, providing a much more easier equation that can be solved with known methods.

The SM has three generations of particles in which each generation is divided into two categories of particles: quarks and leptons, as Table (2) shows.

Table 1 - Particles generations

Generation	I	II	III
Leptons	$e^- \nu_e$	$\mu^- \nu_\mu$	$\tau^- \nu_\tau$
Quarks	u, d	s, c	b, t

Legend: The three particle generations in the SM.

Source: The author, 2023.

Leptons and quarks are both fermions (spin $\frac{1}{2}$ particles) and interact mediated by the exchange of gauge bosons. Each fundamental interaction has a gauge vector boson associated with it; the electromagnetic interaction is mediated by photons, the strong interaction is mediated by eight different types of gluons, and the weak interaction is mediated by W^\pm and Z bosons. It is worth mentioning that thus far, the SM does not describe the gravitational interaction, which is well characterized by the Theory of General Relativity (TGR) (27). This last interaction plays a significant role at very high energy scales and one of the major problems in modern physics is to incorporate gravity in the SM (28).

Finally, the weak force particles of the SM acquire mass through spontaneous symmetry breaking, in which a Yukawa coupling² exists. This mechanism is known by the Brout, Englert, and Higgs mechanism (30, 31). This symmetry breaking does not violate the gauge invariance, it only reduces the gauge structure to $SU(3)_C \otimes SU(2)_L \otimes U(1)_Q$, where the Hypercharge Y is changed by the electrical charge Q .

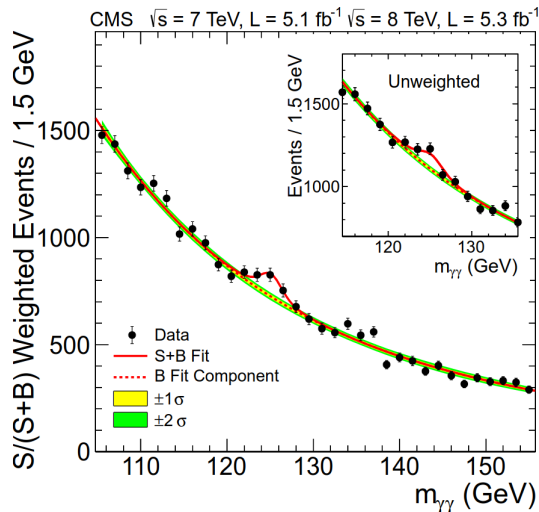
1.2 Higgs Boson Discovery

In the electroweak theory, the acquisition of the mass of the W^+ , W^- , and Z^0 bosons is understood with the use of the Higgs mechanism (32). Such a mechanism occurs when a spontaneous symmetry breaking involving a gauge field and a local symmetry invariance (U1) are present. This framework was developed by Brout-Englert-Higgs-Hagen-Guralnik-Kibble in 1964 (30, 31, 33, 34, 35). On 4 July 2012, 48 years after its theoretical formulation, the Higgs boson was jointly discovered by the Compact Muon Solenoid and A Toroidal LHC Apparatus collaborations. Both experiments observed a new particle in the mass region of around 125 GeV, a value consistent with the mass of the Higgs boson (36). Figure (2) shows the Higgs boson peak at 125 GeV in the diphoton

² In Weinberg-Salam theory, the Yukawa term couples matter fields to the Higgs field (29)

invariant mass distribution with the Compact Muon Solenoid data.

Figure 2 - Higgs peak in the diphoton invariant mass distribution.



Legend: The peak around 125 GeV is seen by combining the Compact Muon Solenoid data in two different data-taking periods. Each event in the diphoton invariant mass distribution is weighted by the $S/(S+B)$ value. The lines represent the fitted data, the yellow band represents the ± 1 standard deviation uncertainty, and the green band represents the ± 2 standard deviation uncertainty.

Source: CHATRCHYAN, 2012, p. 11.

With the Higgs boson discovery, many new branches in particle physics were opened. The properties of this particle, such as rare decays, Beyond Standard Model (BSM) decays, total mass width, differential, and fiducial cross-sections are examples of new branches that were opened just after the Higgs boson discovery (37).

1.3 Quantum Chromodynamics

The first ideas that are known today by Quantum Chromodynamics (QCD) were postulated by Gell-Mann and Zweig in 1963 (38). They hypothesized that hadrons, such as protons, neutrons, and pions were not fundamental particles but composed of other particles, known today as *quarks*. In principle, all hadrons at that time could be classified with the use of three spin $1/2$ particles, namely up (u), down (d), and strange (s) quarks. Today it is well known that there are three more species: charm (c), bottom (b), and top (t). These six types of quarks are called *flavors*. Also, to handle baryons these quarks were supposed to have fractional charges, $+2/3e$ for up, charm, and top quarks and $-1/3e$ for down, strange, and bottom quarks, where e is the elementary electrical charge. However, this model could not handle the existence of baryons composed of three quarks with the same flavor having total angular momentum $3/2$, (*e.g.* Δ^{++}) (26). As

quarks were thought to be spin 1/2 particles, thus obeying Fermi-Dirac statistics it was expected that the baryon wavefunction would be anti-symmetric under the exchange of a pair of quarks. Besides that, as Δ^{++} is composed of three up quarks it does not respect the Pauli exclusion principle. Therefore, it was necessary to introduce a new quantum number, known as *color* (39). Then, requiring the wavefunction to be anti-symmetric by the exchange of this new quantum number and symmetric under the exchange of flavor and spin, would be consistent with what is expected (29).

QCD is a local gauge theory that describes the strong interaction of colored quarks and gluons. It is based on the SU(3) gauge group, having a structure similar to that of Quantum Electrodynamics (QED) (based on the U(1) group) (39). The mediator boson for QED is the photon, while for QCD it is eight different gluons. In QED the gauge group is Abelian, while in QCD it is non-Abelian then consequently gluons are self-interacting. Besides that, it is well known that quarks and gluons have a property called confinement, implying that they can not be found isolated, and consequently cannot be observed as free particles by the experiments. The Lagrangian density of QCD is given by Equation (1)

$$L_{QCD} = -\frac{1}{4}G_{\mu\nu}^{(a)}G^{(a)\mu\nu} + \sum_j \bar{\Psi}_j(i\gamma^\mu D_\mu - m_j)\Psi_j, \quad (1)$$

where $G_{\mu\nu}^{(a)}$ is the QCD field strength given by,

$$G_{\mu\nu}^{(a)} = \partial_\mu A_\nu^{(a)} - \partial_\nu A_\mu^{(a)} - g_s f^{(abc)} A_\mu^{(b)} A_\nu^{(c)}. \quad (2)$$

Then, if the Lagrangian density given by (1) is decomposed it is possible to see all important terms that represent the type of interactions that are present in QCD

$$\begin{aligned} L_{QCD} = & -\frac{1}{4}(\partial_\mu A_\nu^{(a)} - \partial_\nu A_\mu^{(a)})(\partial_\mu A^\nu{}^{(a)} - \partial^\nu A^{\mu(a)}) \\ & + \sum_j \bar{\Psi}_j(i\gamma_\mu \partial^\mu - m_j)\Psi_j - g_s A_\mu^{(a)} \sum_j \bar{\Psi}_j^l \gamma_\mu \left(\frac{\lambda^{(a)}}{2}\right)_{lm} \Psi_j^m \\ & + \frac{g_s}{2} f^{(abc)}(\partial_\mu A_\nu^{(a)} - \partial_\nu A_\mu^{(a)})A^{\mu(b)}A^{\nu(c)} - \frac{g_s^2}{4} f^{abc} f^{ade} A_\mu^{(b)} A_\nu^{(c)} A^{\mu(d)} A^{\nu(e)}, \end{aligned} \quad (3)$$

where A_μ is the gluon field; Ψ_j is the Dirac spinor component, representing a quark with mass m_j ; γ^μ are the Dirac matrices; g_s is the coupling constant, being similar to the electric charge q ; $\lambda^{(a)}$ are the 3×3 Gell-Mann color matrices, satisfying $[\lambda^{(a)}, \lambda^{(b)}] = i2f_{abc}\lambda^{(a)}$; f^{abc} are the structure constants of the SU(3) group; a , b , and c are color indices running over the 8 gluon colors.

The first term in Equation (3) is the kinetic term for gluons, the second is the kinetic and mass term for quarks, the third gives the quark-gluon interaction, the fourth gives the interaction among three gluons and the fifth gives the interaction among four

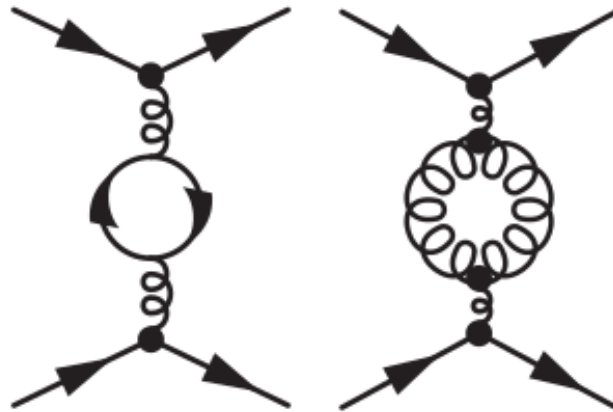
gluons (40). Then, after some long calculations it is possible to assure that this Lagrangian density is invariant under gauge transformations, allowing the theory to be renormalizable (41), *i.e.* at high energies quarks behave such as free particles.

1.4 Renormalization and asymptotic freedom

It is well known that in the QED the coupling constant depends on the energy when the distance between the particles is too small ($d < 10^{-10}$ m) (42). Similarly, the strong coupling parameter (α_s) also depends on the energy. For the QCD case the greater the energy, the lower the parameter, while for QED the opposite occurs. This means that for very high energy quarks can be seen as free particles. In this regime, it is possible to perform perturbative calculations for quarks and gluons using the Feynman rules. This characteristic is known as asymptotic freedom (39).

Both in QED and QCD there is a fermion loop process associated with the vacuum polarization. However, only in QCD exists a gluon loop process that also contributes to the variation of the coupling parameter. This last process does not occur in QED because photons do not have a charge. Figure (3) shows the two diagrams.

Figure 3 - Fermion and gluon loop contributions.



Legend: The left diagram represents a fermion loop that contributes to both QED and QCD. The right diagram represents a gluon loop that contributes to QCD only. Note that only gluons have self-interactions.

Source: THOMSON, 2013, p. 258. Adapted by the author.

QED is one of the most successful theories in physics, it provides tools so that fundamental constants and nuclear properties of the particles can be measured. In the last years, many tests have been conducted in QED: anomalous magnetic dipole moment (43), vacuum polarization (29), and that the photon does not have mass, for example. In QCD: photon production, jet production, and weak boson plus jet production, for example, (44).

1.5 Quark masses

Quark masses are fundamental parameters of the SM, however, they are confined inside hadrons so they are not observed as free particles, thus their masses can be only determined indirectly. It is worth mentioning when discussing the meaning of the quark masses, one must take into account which model is being used to define it. This means that it is important to know which theoretical framework is used to estimate it. Therefore the quark masses values tabulated are scheme dependent (45). When talking about quark masses the light quarks (u, d, s) must be treated differently from the heavy quarks (c, b, t), because in the former their masses are much lower than the QCD scale³ ($m_Q \ll \Lambda_{QCD}$), while in the later their masses are much greater than the QCD scale ($m_Q \gg \Lambda_{QCD}$). While the case of the heavy quarks can be treated with the perturbative QCD, the light case can not as it is within the non-perturbative Λ_{QCD} region. For instance, the contribution to the hadron mass that may contain light quarks is mainly due to the energy from non-perturbative gluons (46).

One successful way to define and compute the quark masses is based on the modified minimal subtraction scheme (\overline{MS} scheme). This is a renormalization scheme that simply removes the poles that contribute with divergent quantities (29). By using a certain renormalization scale and the chiral perturbation theory (47) one can perform calculations to determine the current-quark masses.

1.6 Quarkonium Spectroscopy

Within the non-relativistic chromodynamics, a quarkonium state is well characterized by the total angular momentum

$$\mathbf{J} = \mathbf{L} + \mathbf{S}, \tag{4}$$

³ The QCD scale Λ_{QCD} is a parameter in QCD which gives the characteristic of the confinement and other processes in QCD.

where \mathbf{L} is the orbital angular momentum between the $Q\bar{Q}$ pair, \mathbf{S} is the total spin of the $Q\bar{Q}$ pair, and \mathbf{J} is the total angular momentum. It is worth mentioning that charge conjugation $C = (-1)^{L+S}$ and parity $P = (-1)^{L+1}$ are conserved quantities in this framework. Normally a quarkonia state is labeled using the notation J^{PC} and, sometimes, one can add the information of isospin I and G-parity (defined as $G = Ce^{i\pi I_2}$, where I_2 is the second component of the isospin and it is represented by a rotation by π in isospin space), represented by I^G . The spectroscopic notation is given by $n^{2S+1}L_J$ where n is the principal quantum number. For instance, for J/ψ meson the values are $n = 1$, $S = 1$, $L = 0$ (S-wave), $J = L + S = 1$, $P = (-1)^{L+1} = -1$, $C = (-1)^{L+S} = -1$, $G = C \cdot e^{i\pi I_2} = -1$, consequently the representation is: $n^{2S+1}L_J = 1^3S_1$ (S_1 is used to represent the S-wave), $I^G = 0^-$, $J^{PC} = 1^{--}$. The representation for the other mesons can be seen in Table (2).

Table 2 - Summary of the spectroscopic notation for quarkonia particles.

Meson name	$n^{2S+1}L_J$	$I^G(J^{PC})$	Mass (MeV)
η_c	1^1S_0	$0^+(0^{-+})$	2980.4 ± 1.2
J/ψ	1^3S_1	$0^-(1^{--})$	3096.916 ± 0.011
$\chi_{c0}(1P)$	1^3P_0	$0^+(0^{++})$	3414.76 ± 0.35
$\chi_{c1}(2P)$	1^3P_1	$0^+(1^{++})$	3510.66 ± 0.07
$\chi_{c2}(2P)$	1^3P_2	$0^+(2^{++})$	3556.20 ± 0.09
$\Psi(2S)$	2^3S_1	$0^-(1^{--})$	3686.093 ± 0.034
η_b	1^1S_0	$0^+(0^{-+})$	$9388.9_{-2.3}^{+3.1} \pm 2.7$
$\Upsilon(1S)$	1^3S_1	$0^-(1^{--})$	9460.30 ± 0.26
$\chi_{b0}(1P)$	1^3P_0	$0^+(0^{++})$	$9859.44 \pm 0.42 \pm 0.31$
$\chi_{b1}(1P)$	1^3P_1	$0^+(1^{++})$	$9892.78 \pm 0.26 \pm 0.31$
$\chi_{b2}(1P)$	1^3P_2	$0^+(2^{++})$	$9912.21 \pm 0.26 \pm 0.31$
$\Upsilon(2S)$	2^3S_1	$0^-(1^{--})$	10023.26 ± 0.31
$\chi_{b0}(2P)$	2^3P_0	$0^+(0^{++})$	$10232.5 \pm 0.4 \pm 0.5$
$\chi_{b1}(2P)$	2^3P_1	$0^+(1^{++})$	$10255.46 \pm 0.22 \pm 0.50$
$\chi_{b2}(2P)$	2^3P_2	$0^+(2^{++})$	$10268.65 \pm 0.22 \pm 0.50$
$\Upsilon(3S)$	3^3S_1	$0^-(1^{--})$	10355.2 ± 0.5

Legend: Standard notation for the quarkonia particles. The first column shows the name of the particle, the second shows the standard spectroscopic notation, the third shows the notation concerning the isospin and total angular momentum, and the last shows the mass estimate.

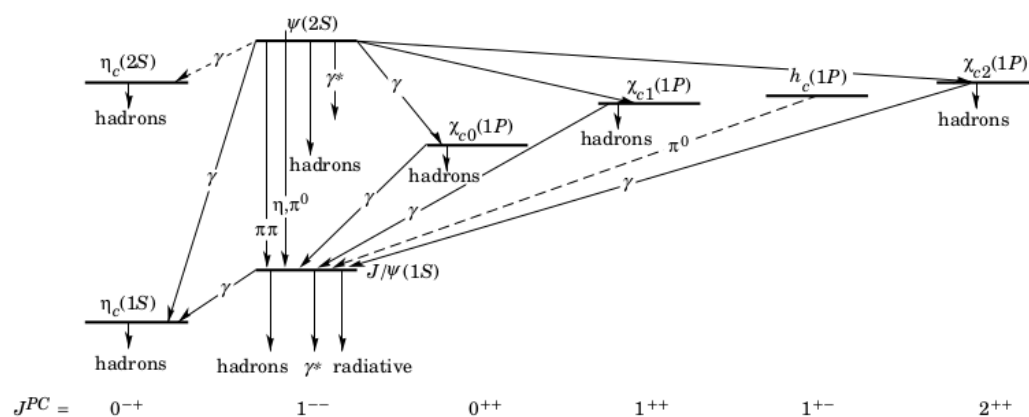
Source: PRICE, 2008, p. 20. Adapted by the author.

In the case of J/ψ and $\Psi(2S)$, both S_1 states are well known. It is possible to see in Table (2) that they have better mass precision. This result comes from the

KEDR experiment⁴, which relies on a special technique called depolarisation to reduce the systematic error of the measurement.

Finally, to understand the spectrum of charmonia and bottomonia, it is well understood that it is possible to compare the heavy quark-antiquark pair with the hydrogen atom and with positronium. Again, it is worth mentioning that this is possible because the systems $c\bar{c}$ and $b\bar{b}$ are essentially non-relativistic while the other quarks are not. A very good explanation of this approach is given in (42). Figures (4) and (5) show the diagrams for the charmonia case and bottomonia case respectively.

Figure 4 - Charmonium Spectroscopy.

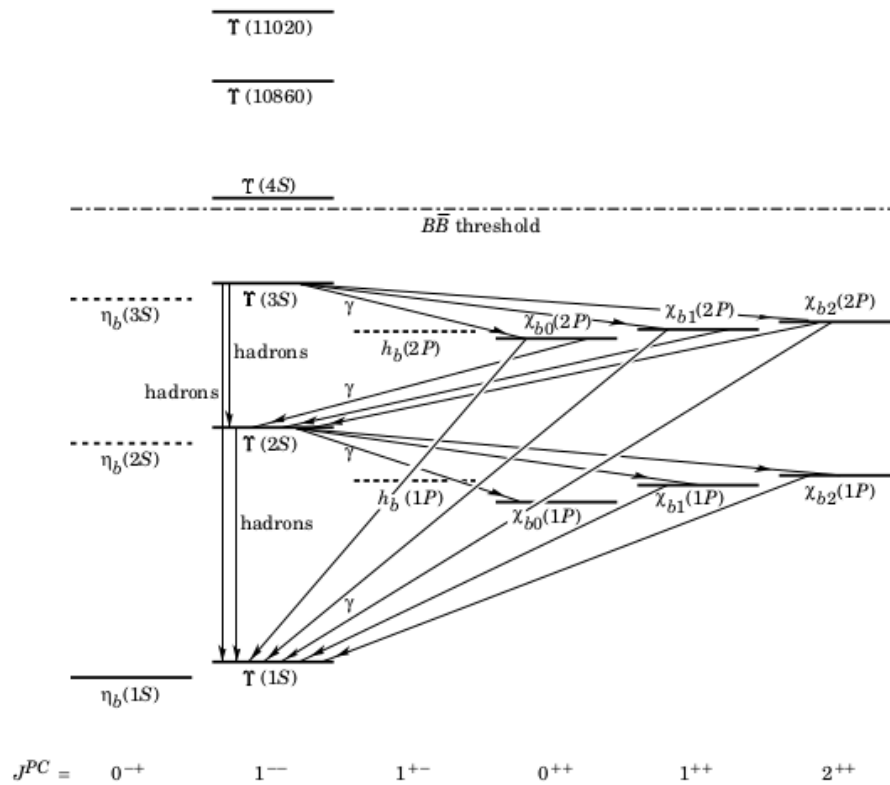


Legend: Diagram of the charmonium spectroscopy. The charmonia resonances are shown as well as their decay channels, including the radiate decays (γ + something). Note that each stage is categorized by the J^{PC} notation. The figure is divided by energy level, where the S-waves with n=2 are on the top, the P-waves with n=1 are on the middle, and the S-waves with n=1 are on the bottom. It is possible to see the charmonia transition via the emission of another particle (photon, for instance).

Source: PRICE, 2008, p. 21.

⁴ The KEDR detector is a magnetic detector installed at the VEPP-4M e^+e^- collider at the Budker Institute of Nuclear Physics (BINP) in Novosibirsk. It is designed for studying c and b quarks. It is also used for studying physics involving two photons.

Figure 5 - Bottomonium Spectroscopy.



Legend: Diagram of the bottomonium spectroscopy. The bottomonia resonances are shown as well as their decay channels, including the radiate decays ($\gamma + \text{something}$). Note that each stage is categorized by the J^{PC} notation. The figure is divided by energy level. In this case, it is possible to see states with $n = 1, 3, 3, 4$. Besides that, two upsilon states are shown as well, $\Upsilon(11020)$ and $\Upsilon(10860)$.

Source: PRICE, 2008, p. 22.

1.7 Quarkonium Production

The name quarkonium refers to a subatomic system composed of a heavy quark Q and a heavy anti-quark \bar{Q} , *i.e.* a quark anti-quark pair. It is divided into two distinct systems, one containing bottom quarks $b\bar{b}$ called bottomonium and the other containing charm quarks $c\bar{c}$ called charmonium. It is worth mentioning that thus far the state with top quark $t\bar{t}$ has not been observed experimentally. The reason is that this quark has a lifetime (around $5 \cdot 10^{-25}$ s) lower than the time scale of the strong interaction, then decaying before forming a bound state (48).

The first time quarks were seen as real particles was when J/ψ meson was discovered. That identified the fourth quark, the charm quark, and the belief that quarks were only mathematical entities invented by M. Gell-Mann started to be abandoned (49). After that, many mesons with c quarks were discovered, for instance, $\Psi(2S)$ that is the first excitation of the J/ψ was discovered at SLAC, indicating that at short distances strong interaction was indeed weak. Besides that, theorists used quarkonia to test the asymptotic freedom of QCD (50). Later, charmonium P waves, χ_c , and a pseudoscalar ground state called η_c were discovered. Besides that, not only charmonium mesons but also bottomonium mesons were found thereafter. However, after four decades after these discoveries, the quarkonium production mechanism is still not completely understood. In this sense, the LHC experiments have performed several measurements (51, 52, 48) in these states in recent years. Such results are very important to help in the development of the quarkonia theory.

Quarkonium production can be treated in two different approaches: the heavy-quark pair production, which could be tractable with perturbative methods such as perturbative QCD (pQCD), Feynman graphs, and heavy-quark binding, that is non-perturbative and sensitive to the confinement properties of the strong interaction. Despite having several different theoretical approaches the majority are based on the collinear factorization (53). Some of them use k_T factorization (54) to treat specific effects in the high-energy realm whereas a number of recent studies use the Transverse-Momentum-Dependent (TMD) factorization (55), to cope with spin-dependent objects. Three methods are discussed: the color-evaporation model (CEM), the color-singlet model (CSM), and the color-octet mechanism within nonrelativistic QCD (NRQCD).

1.7.1 The color-Evaporation Model (CEM)

The CEM was proposed a few years after the discovery of J/ψ and its major success was the description of quarkonium production in hadronic collisions. In this approach, the cross-section of quarkonia is directly connected to that of a $Q\bar{Q}$ pair mass if one

considers that the hadronization takes place inside the range $2m_Q < k_{threshold} < 2m_H$, where $k_{threshold}$ is the kinematical threshold, $2m_H$ is the lightest open-heavy-flavor hadron pair and $2m_Q$ is the quark pair mass (56). This will happen regardless of quark spin and color configuration, *i.e.*, the quark pair goes to an arranged state of quarkonium with the same quantum numbers. This is possible due to soft gluon interactions.

However, if m_Q is below the threshold, the probability of the quark pair evolving into a quarkonium state Q is given by the phenomenological factor F_Q , which is extracted from data and assumed independent of the process. This constant does not depend on the quantum numbers of the quark pair, on the kinematic variables, and on the quark pair production mechanism. Table (3) shows different F_Q values for different processes. The leading order cross section for the inclusive quarkonia production is given by Equation (5).

Table 3 - Color evaporation mode parameters.

Charmonium state Q	$F_Q^{dir.}/F_{J/\psi}^{inc.}$	Bottomonium state Q	$F_Q^{dir.}/F_{\Upsilon}^{inc.}$
J/ψ	0.62	$\Upsilon(1S)$	0.52
$\Psi(2S)$	0.14	$\Upsilon(2S)$	0.33
χ_{c1}	0.60	$\Upsilon(3S)$	0.20
χ_{c2}	0.99	$\chi_b(1P)$	1.08
—	—	$\chi_b(2P)$	0.84

Legend: $F_Q^{dir.}$ for the direct production of charmonium and bottomonium states with respect to the inclusive parameters ($F_{J/\psi}^{inc.}$ or $F_{\Upsilon}^{inc.}$) for J/ψ and $\Upsilon(1S)$ respectively.

Source: CHISHOLM, 2015, p. 19.

$$\sigma_{CEM}(pp \rightarrow Q + X) = F_Q \sum_{i,j} \int_{4m_Q^2}^{4M_Q^2} d\hat{s} \int dx_1 dx_2 f_i(x_1, \mu) f_j(x_2, \mu) \sigma_{ij}^{Q\bar{Q}}(s) \delta(\hat{s} - x_1 x_2 s), \quad (5)$$

where the indices i, j run over all partons, m_Q is the mass of the heavy quark, M_Q is the mass of the lightest meson that is composed of the quark Q (57), $\sigma_{ij}^{Q\bar{Q}}(s)$ is the partonic cross section for the process $ij \rightarrow Q\bar{Q}$ that is calculated in pQCD and $\sqrt{\hat{s}}$ is the center of mass energy.

Despite explaining with success some process (58) the CEM showed some contrast with experimental observations. As an example, the cross-section for χ_c production with respect to J/ψ is considered to be constant. However, the data and this expectation are not in agreement (59). Due to the soft gluons interactions, the cross-section of the final quarkonia state is directly connected to the quark pair, this implies that for quarkonium states with the same orbital angular momentum quantum number L , the production is given by simple counting of the allowed spin states, $P_Q = 1/9 \cdot (2J_Q + 1) / \sum_i (2J_i + 1)$ (60),

where the sum over i runs over all the charmonium states below the open heavy-flavor threshold (60). This result suggests that the χ_c producing should satisfy specific ratios, which does not occur experimentally, as more χ_{c1} is observed relative to χ_{c2} (11).

1.7.2 The color Singlet Model (CSM)

This model is based on the idea that the produced quark pair $Q\bar{Q}$ and its evolved quarkonia state have the same quantum number (61). As it is expected, any hadronic state is in a color singlet, so the quark pair must be directly produced in a color singlet state with the same spin and angular momentum as the quarkonium state. In order to evaluate the probability for a quark pair to evolve into a quarkonium state one needs to use the color singlet $Q\bar{Q}$ wavefunction evaluated at the origin. To compute the parameters of the wavefunction it is necessary to use potential models of $Q\bar{Q}$. Also, these parameters are constrained with experimental data and the CSM contains no free parameters. The cross section for the production of a quarkonium state \mathcal{Q} is given by

$$\hat{\sigma}_{CSM}(ij \rightarrow \mathcal{Q}^{[2S+1]L_J} + X) = \left| \frac{d^L \Psi_{nl}(0)}{dr^l} \right|^2 \hat{\sigma}(ij \rightarrow Q\hat{Q}^{[2S+1]L_J}), \quad (6)$$

Ψ_{nl} is the quark pair wavefunction and $\hat{\sigma}$ is the cross-section for the quark pair production from the interaction of the partons i and j .

Despite the success of describing quarkonia production, studies from the Tevatron (62) concluded that the prompt charmonium production had been underestimated with the use of the CSM model. Also, the model fails when describing the production and decay of $L = 1$ χ states, which are states with non-zero orbital angular momentum. Finally, it is well known that the CSM leads to infrared divergences in the case of P -wave decay at next-to-leading (NLO), which needs the inclusion of non-relativistic QCD (NRQCD) (63). To cope with these bad modeling new approaches have been developed: new calculations include NLO and next-to-next-to-leading (NNLO) order in α_s , implying in good agreement with data (62). To conclude it is well known that such corrections are found to be large and sometimes the perturbative series may not be convergent. Therefore, because of such divergences and due to the lack of experimental support, CSM is not considered a robust model for describing quarkonium production.

1.7.3 The color Octet Mechanism and the NRQCD factorisation

In NRQCD (64) framework, the hadronisation of a heavy-quark pair into a quarkonium is known through the long-distance matrix elements (LDMEs). The NRQCD fac-

torisation is one of the best ways to describe quarkonium production, giving theoretical completeness as well as good matching with experimental results (65). Depending on the energy scale one should have problems using the NRQCD, for example, the heavy quark mass and parton hard-scattering momentum scales are significantly larger than Λ_{QCD} (59). In this regime, the QCD constant is small enough that perturbative methods can be used. On the other side, the evolution of a quark pair into a quarkonium involves small energy, not allowing the use of the perturbative calculation.

In the case of quarkonium production, one should consider three energy-momentum scales, m_Q : mass of the heavy quark; $m_Q v$ (v is the velocity of the heavy quark in the center of mass (CM) frame): the momentum of the heavy quark in the CM frame of a $Q\bar{Q}$ bound state and $m_Q v^2$: the binding energy of the quark pair (59). In the case of charmonium and bottomonium, the non-relativistic approximation can be used as their speed are around $v_c^2 \approx 0.3$ and $v_b^2 \approx 0.1$, respectively (considering $c = 1$). Also, more accurate predictions are obtained for the $b\bar{b}$ system, as it can be treated in the non-relativistic regime with a good approximation. The other momentum scale relevant to this process is the hard scattering scale, Q^2 , which is given by the p_T of the produced quarkonia.

The factorization approach consists of separating the high p_T contributions (short-distance effects) from the short p_T contributions (long-distance effects). The former can be treated with perturbative methods while the latter cannot (57). To accomplish that one needs to use the effective field theory⁵ NRQCD that takes into account momentum scales at the order of m_Q and below. To compute the inclusive cross-section for the production of quarkonium in a proton-proton collision one needs to take into account the contribution of the short distance coefficients $\sigma_n[pp \rightarrow Q\bar{Q}[n]]$, which can be calculated with perturbative QCD and the contribution of the long term elements, given by the LDMEs, $Q\mathcal{O}_nQ = \mathcal{O}_n^{\mathcal{Q}}(\Lambda)$, which can not be calculated with perturbative QCD. This cross-section is given by Equation (7)

$$\sigma(pp \rightarrow \mathcal{Q} + X') = \sum_n \sigma_n[pp \rightarrow Q\bar{Q}[n]](\Lambda) \cdot \mathcal{O}_n^{\mathcal{Q}}(\Lambda), \quad (7)$$

where \mathcal{Q} is the quarkonium state, \mathcal{O} are the four-fermion NRQCD operators, and Λ is the energy scale limit of the effective theory. An interesting fact here is that the quark pair and the resulting quarkonium are not necessarily in the same state, *i.e.*, they can have different spin, color, and angular momentum, allowing the quark pair to be produced either in a color octet or in a color singlet configuration (59). The non-perturbative part of the process is encoded by the LDMEs, which are the vacuum expectation values of the

⁵ An effective field theory is an approximation of a fundamental theory. In other words, an effective field theory treats processes up to a certain energy scale.

operators \mathcal{O} (66). Besides that, the LDMEs are process independent (57) and thus far they can be found only phenomenologically, *i.e.* until now there is no theoretical way to extract them.

Another way to express Equation (7) is performing the expansion in powers of α_S and the velocity v . Then, it is possible to consider higher-Fock states in v where the quark pair is in an octet state with different angular momentum and spin states. It is worth mentioning that the consideration of the leading Fock state only is a way to derive the CSM (49). As commented in the previous section the CSM predictions showed some discrepancies when compared with the data. This was seen in the first direct measurements of J/ψ and $\Psi(2S)$ at $\sqrt{s} = 1.8$ TeV done by the Collider Detector at Fermilab (CDF) collaboration (64). Then, by introducing the COM with the NRQCD it was possible to match the data observed with the theory. Finally, recent results at the LHC showed that the measurements of the production of J/ψ and $\psi(2S)$ are in agreement with the theory (48, 67) and the polarization of the χ_{c1} and χ_{c2} states in CMS at $\sqrt{s} = 8$ TeV are in good agreement with NRQCD prediction (52).

1.8 Open Charm Production

Open charm can be defined as a meson or baryon composed of a charm quark plus a light quark (*e.g.* D^0 contains c and \bar{u}). The characteristic of the process depends on the type of collision. In e^+e^- colliders the level of interaction vertices is low and consequently, the level of background is low. In hadron colliders, one can reach much higher energies, and higher cross-sections, but the level of interaction vertices is much higher, providing more background events. In the end, this distinction can be understood as a trade-off between quality and quantity.

Concerning the production of D mesons, they are the lightest particles containing c quark. There are two different experimental set-ups to be considered in e^+e^- colliders: "D-factories" and "B-factories".

a) D-factories

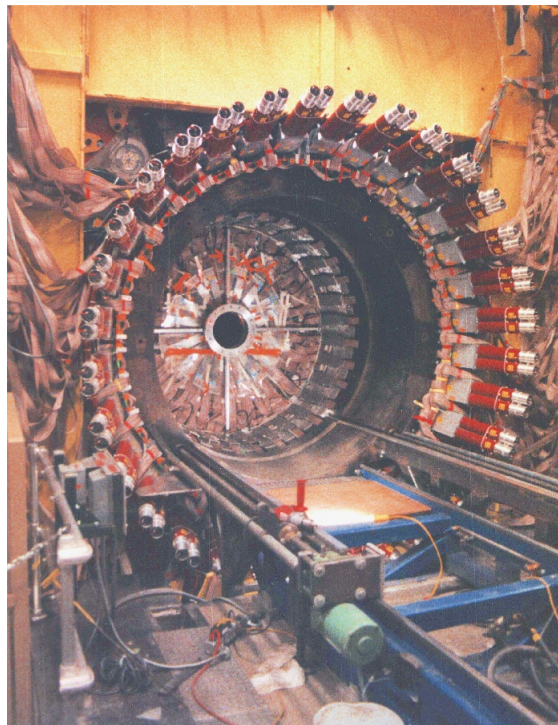
This kind of configuration is used in experiments BESIII, CLEO-c, and MARK III. The energy of interaction is set around 3770 MeV, which is the mass of $\Psi(3770)$. This charmonium state decays 93% of the time in D meson states, being 52% in $D^0\bar{D}^0$ and 41% in D^-D^+ . The cross-section production of D mesons in this process is about 8 nb. Figure (6) shows the CLEO detector.

b) B-factories

This configuration is used by Belle and BaBar experiments at asymmetric colliders

(the colliding beams have different energies) (68). The center-of-mass energy of this configuration is 10.6 GeV, which allows the production of $\Upsilon(4S)$. This bottomonium state decays 48.6% of the time in $B^0\bar{B}^0$ (decays to charm, where the cross-section to produce at least one D^0 is ≈ 1.45 nb) and 51.4% in B^+B^- . In B-factories one has a smaller cross-section and a higher instantaneous luminosity. As an example, BaBar and Belle, both b-factories, collected about 500 fb^{-1} and 1000 fb^{-1} respectively, while CLEO-c and BESIII, both D-factories, accumulated only 0.5 fb^{-1} and 3 fb^{-1} respectively. Figure (7) shows the CLEO detector.

Figure 6 - The CLEO detector



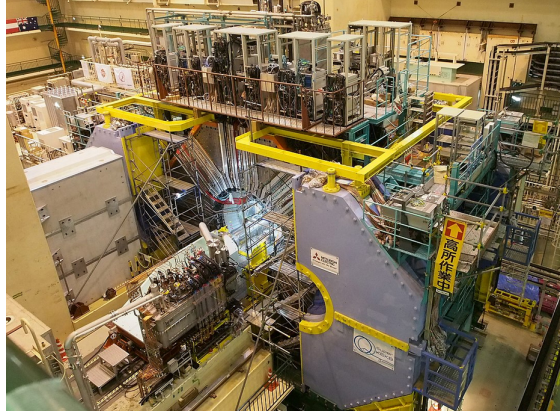
Legend: Frontal view of CLEO detector at the Cornell Electron Storage Ring (CESR) (69).

Source: CLEO detector, 2022.

c) Hadron colliders

In this case, the production cross section is many times bigger than that found in e^+e^- experiments. The CDF experiment installed at the Tevatron accelerator collides proton-antiproton at $\sqrt{s} = 2$ TeV. In this scenario, D^0 meson production cross-section has been found to be $13\ \mu\text{b}$ (71), considering the detector acceptance, with an integrated luminosity of 10 fb^{-1} . In turn at the LHCb (Large Hadron Collider beauty), one of the detectors installed at the LHC accelerator, the production cross section is even higher: 1.4 mb at $\sqrt{s} = 7$ TeV with 1.1 fb^{-1} , 1.6 mb at $\sqrt{s} = 8$ TeV with 2.1 fb^{-1} and 2.7 mb at $\sqrt{s} = 13$ TeV with 5.9 fb^{-1} .

Figure 7 - The Belle II detector



Legend: View of Belle II detector at the Super KEKB accelerator complex (70).

Source: BELLE II detector, 2022.

1.8.1 D mesons

The so-called D mesons are a group of particles formed by either a charm quark or an anti-charm quark and a light quark. The D mesons studied here are D^0 and $D^{*\pm}$. The D^0 decay that is studied is $D^{*\pm} \rightarrow D^0 \pi_{slow}^{\pm}$ (Branching ratio (BR): $(67.7 \pm 0.5)\%$), where $D^0 \rightarrow K^- \pi^+$ (BR: $(3.946 \pm 0.03)\%$). The D^* and D^0 decays are shown sequentially in Figure (8).

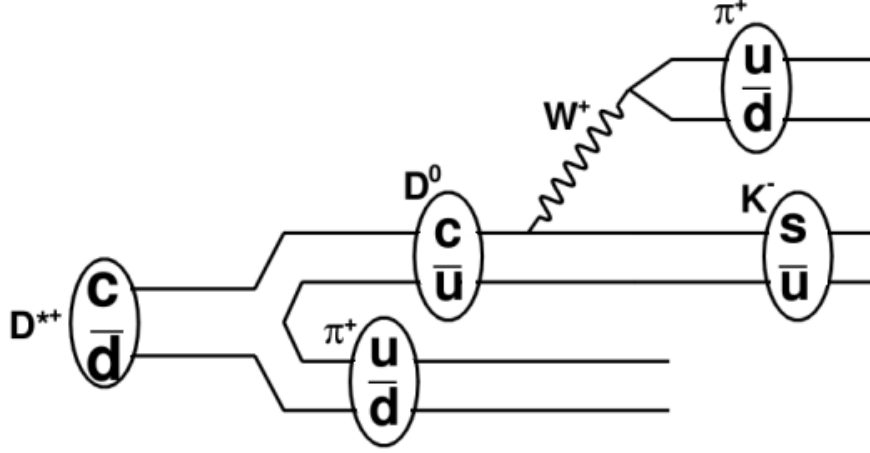
The D^* meson is composed of a charm quark and an antiquark \bar{d} , while the meson D^0 is composed of a quark c and an antiquark \bar{u} . Both of them have a c quark, therefore their flavor quantum number C is $+1$. By analyzing the quark content of the products one can study how this reaction occurs. The flavor change from c quark to s quark occurs by the weak interaction, where it is possible to see it by the existence of a boson W , which decays into a u quark and a \bar{d} quark.

The differential cross-section for D mesons in proton-proton collisions is given by the Equation (8)

$$\frac{d\sigma^{pp \rightarrow D+X}}{dp_T}(m_c, \mu_F^2, \mu_R^2) = \sum_{i,j=q,\bar{q},g} f_i(x_1, \mu_F^2) \cdot f_j(x_2, \mu_F^2) \times \frac{d\hat{\sigma}^{ij \rightarrow c+X}}{dp_T}[\alpha(\mu_R^2), \mu_F^2, \mu_R^2] \cdot \mathcal{D}_c^D(x, \mu_F^2), \quad (8)$$

where,

- p_T is the transverse momentum of the D meson;
- m_c is the c quark mass;
- μ_F^2 is the factorization scale;

Figure 8 - Feynman diagram for D^{*+} decaying into D^0 and π_{slow} .

Legend: The D^{*+} is composed of a charm quark and an anti-down quark.
 Through electroweak interaction, it decays into D^0 and π_{slow} . After that, D^0 , composed of a charm quark and an anti-up quark, decays into kaon and pion through a W boson emission (72).

Source: COELHO, 2019, p. 25. Adapted by the author.

- μ_R^2 is the renormalization scale;
- x_1 : is the fraction of momentum carried by the parton i ;
- $f_i(x_1, \mu_F^2)$: is the parton distribution function (PDF) of the parton i ;
- $\frac{d\hat{\sigma}^{ij \rightarrow c+x}}{d\hat{p}_T}$: is the partonic cross section. In the case that it is a high- Q^2 interaction it can be calculated with perturbative QCD;
- $\mathcal{D}_c^D(x, \mu_F^2)$: is the fragmentation function for a quark c to turn into a D meson with a momentum fraction $x = p_D/p_c$.

1.8.1.1 Fragmentation functions

Fragmentation functions (FF) are used to describe final state particle energy distributions in the hard scattering process, as in the proton-proton collisions (73). As commented in Equation (8) it represents the probability that a specific quark hadronizes into a specific hadron. In general, the FF can be represented by $\mathcal{D}_i^h(x, \mu_F^2)$ ($i = q, \bar{q}, g$), where i represents the flavor. They obey the momentum sum rule constraint

$$\sum_h \int_0^1 dx x \mathcal{D}_i^h(x, \mu_F^2) = 1, \quad (9)$$

where the sum involves all possible produced hadrons h .

In the case of the heavy quark fragmentation, it is well understood that a heavily flavored meson should have a large fraction of the momentum of the hadronized heavy quark (74). The non-perturbative FF for D^0 and D^* was measured for the first time at (NNLO) in the \overline{MS} factorization scheme (75). This was done considering the QCD fit to the OPAL experimental data in electron-positron single-inclusive annihilation (76).

It is worth mentioning that the hadronization of charm quark into mesons and baryons was found to be non-universal, *i.e.* recent studies have shown that the measurements in pp collisions can differ significantly from the measurements in e^+e^- and ep collisions. Table (4) shows the measurements of c quark hadronization, given by $f(c \rightarrow H_c)\%$, into charmed hadrons and Λ_c^+ baryon performed at LEP (Large Electron-Positron Collider) combining all experiments, ALEPH (Apparatus for LEP Physics), DELPHI (Detector with Lepton, Photon, and Hadron Identification) and OPAL (Omni-Purpose Apparatus at LEP),

Table 4 - Average values for c quark fragmentation function at LEP from e^+e^- collisions.

H_c	$f(c \rightarrow H_c)[\%]$
D^0	$54.2 \pm 2.4 \pm 0.7$
D^{*+}	$23.6 \pm 0.6 \pm 0.3$
D^+	$22.5 \pm 1.0 \pm 0.5$
D_s^+	$9.2 \pm 0.8 \pm 0.5$
Λ_c^+	$5.7 \pm 0.6 \pm 0.3$

Legend: Average values for c quark fragmentation function to charmed mesons and Λ_c^+ baryon. These values are the combined measurements from the LEP experiments, where the first error is statistical and the second error is systematic. It is worth mentioning that the sum of the fragmentation functions should add up to unity, not considering the values for D^{*+} , which decays into the D^0 and D^+ mesons (77).

Source: GLADILIN, 2015, p. 2.

Note that the value of the fragmentation function for Λ_c^+ is the lowest one. However, on a recent measurement performed at LHC with the ALICE (A Large Ion Collider Experiment), this conclusion is not the same. Table (5) shows the same measurements, with the addition of Ξ_c^0 baryon, performed for the first time,

What is well visible is that the main difference with respect to LEP measurement are the values for D^0 and Λ_c^+ . Therefore this measurement indicates that the hadronization of charm quark into charm hadrons is not universal as it is possible to see large differences between the measurements performed at LEP from e^+e^- collisions and the measurements performed at LHC from pp collisions.

Table 5 - Average values for c quark fragmentation functions at LHC from pp collisions.

H_c	$f(c \rightarrow H_c)[\%]$
D^0	$39.1 \pm 1.7(\text{stat})_{-3.7}^{+2.5}$ (syst)
D^{*+}	$15.5 \pm 1.2(\text{stat})_{-1.9}^{+4.1}$ (syst)
D^+	$17.3 \pm 1.8(\text{stat})_{-2.1}^{+1.7}$ (syst)
D_s^+	$7.3 \pm 1.0(\text{stat})_{-1.1}^{+1.9}$ (syst)
Λ_c^+	$20.4 \pm 1.3(\text{stat})_{-2.2}^{+1.6}$ (syst)
Ξ_c^0	$8.0 \pm 1.2(\text{stat})_{-2.4}^{+2.5}$ (syst)

Legend: Average values for c quark fragmentation function to charmed mesons and Λ_c^+ baryon. Note that to obtain the complete fragmentation of a c quark, one should add also a contribution for Ξ_c^+ , which feeds Λ_c^+ . Also here the sum of the fragmentation functions should add up to unity, not considering the values for D^{*+} , which decays into the D^0 and D^+ mesons (78).

Source: ALICE COLLABORATION et, 2012, p. 5.

1.9 Parton Scattering

In a scattering process, it is possible to classify two different types of scattering. In a hard scattering process, heavy particles are produced at high energies and this scenario is well described within the pQCD framework. On the other hand, the soft scattering is not well explained by the pQCD, requiring the use of lattice QCD.

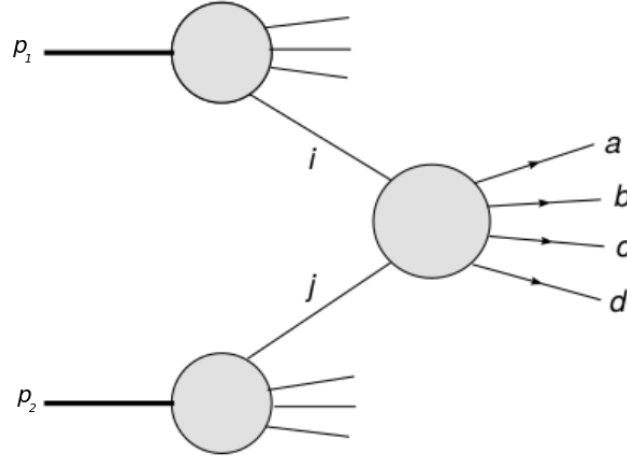
Depending on the case it is possible to have more than one parton collision, in fact, some analyses have shown that pp collisions in high energies frequently generate multiple hard parton collisions.

1.9.1 Single Parton Scattering

The SPS (Single Parton Scattering) is one of the most familiar hard processes, it occurs when only one parton of each colliding hadron interacts with each other. Figure (9) represents the SPS mechanism for the process $ij \rightarrow abcd$, where i and j are the interaction partons, $abcd$ is the final state ($c\bar{c}c\bar{c}$, for instance), and the two incoming hadrons are protons.

To compute the cross-section for the SPS process one needs to take into account the integral of the PDFs convoluted with the partonic cross-section and sum over all possible

Figure 9 - SPS representation.



Legend: SPS representation, where i and j are the interacting partons (79).

Source: BERGER, 2011, p. 2.

scatterings, as shown in Equation (10),

$$d\sigma^{SPS} = \sum_{i,j} \int dx_1 dx_2 \cdot f_1^i(x_1, \mu_F) \cdot f_2^j(x_2, \mu_F) \cdot d\hat{\sigma}_{ij}(x_1, x_2, \mu_F) \quad (10)$$

1.9.2 Double Parton Scattering

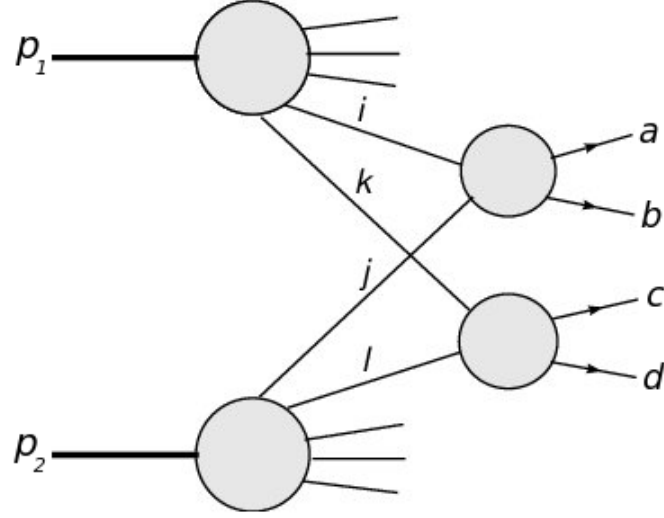
In the DPS (Double Parton Scattering) process two partons of each incoming proton can interact, which means that this process is characterized by two hard interactions. Figure (10) represents the DPS mechanism for the process $ij \rightarrow ab$ and $kl \rightarrow cd$, where i and k are partons from the first proton and j and l are partons from the second proton.

The DPS cross-section can be estimated from the expression (10) by considering that the two hard interactions are uncorrelated. This means that one can consider the cross-section of each interaction separately

$$\begin{aligned} d\sigma^A &= \sum_{i,j} \int dx_1 dx'_1 \cdot f_1^i(x_1, \mu_F^A) \cdot f_2^j(x'_1, \mu_F^A) \cdot d\hat{\sigma}_{(ij \rightarrow ab)}(x_1, x'_1, \mu_F^A), \\ d\sigma^B &= \sum_{k,l} \int dx_2 dx'_2 \cdot f_1^k(x_2, \mu_F^B) \cdot f_2^l(x'_2, \mu_F^B) \cdot d\hat{\sigma}_{(kl \rightarrow cd)}(x_2, x'_2, \mu_F^B), \end{aligned} \quad (11)$$

which can be combined, provided that the fractional momenta of the partons is small

Figure 10 - DPS representation.



Legend: DPS representation, where i, j, k and, l are the interacting partons.

Source: BERGER, 2011, p. 2.

(80), to estimate the DPS cross-section,

$$d\sigma^{DPS} = \frac{m}{2\sigma_{eff}} \sum_{i,j,k,l} \int dx_1 dx_2 dx'_1 dx'_2 \cdot f_1^i(x_1, \mu_F^A) \cdot f_2^j(x'_1, \mu_F^A) \cdot f_1^k(x_2, \mu_F^B) \cdot f_2^l(x'_2, \mu_F^B) \times d\hat{\sigma}_{(ij \rightarrow ab)}(x_1, x'_1, \mu_F^A) d\hat{\sigma}_{(kl \rightarrow cd)}(x_2, x'_2, \mu_F^B), \quad (12)$$

where,

- m is a factor related to the symmetry of the problem. This will be explained better later;
- σ_{eff} is the effective cross-section, which will be explained later as well;
- A refers to the process $ij \rightarrow ab$ and B refers to the process $kl \rightarrow cd$;
- x_1/x'_1 is the fraction of momentum carried by parton i/j ;
- x_2/x'_2 : is the fraction of momentum carried by parton k/l ;
- $f_p^q(x_r, \mu_F^S)$ is the PDF for parton q ($q \in \{i, j, k, l\}$), carrying a fraction of momentum x_r ($x_r \in \{x_1, x'_1, x_2, x'_2\}$) from the proton p ($p \in \{1, 2\}$), associated to the process S ($S \in \{A, B\}$).

Therefore, the DPS differential cross-section becomes

$$d\sigma_{AB}^{DPS} = \alpha \frac{d\sigma^A \cdot d\sigma^B}{\sigma_{eff}}, \quad (13)$$

where $\alpha = m/2$ depends on A and B process, as shown in Table (6)

Table 6 - α factor as a function of the interaction particles

α	A and B	<i>e.g</i>
1/4	Identical and non-self-conjugate	$D^0 D^0$
1	Different and either B or C is self-conjugate	$J/\psi D^0$
1/2	Otherwise	-

Legend: The values depend on the distinguishability of the states

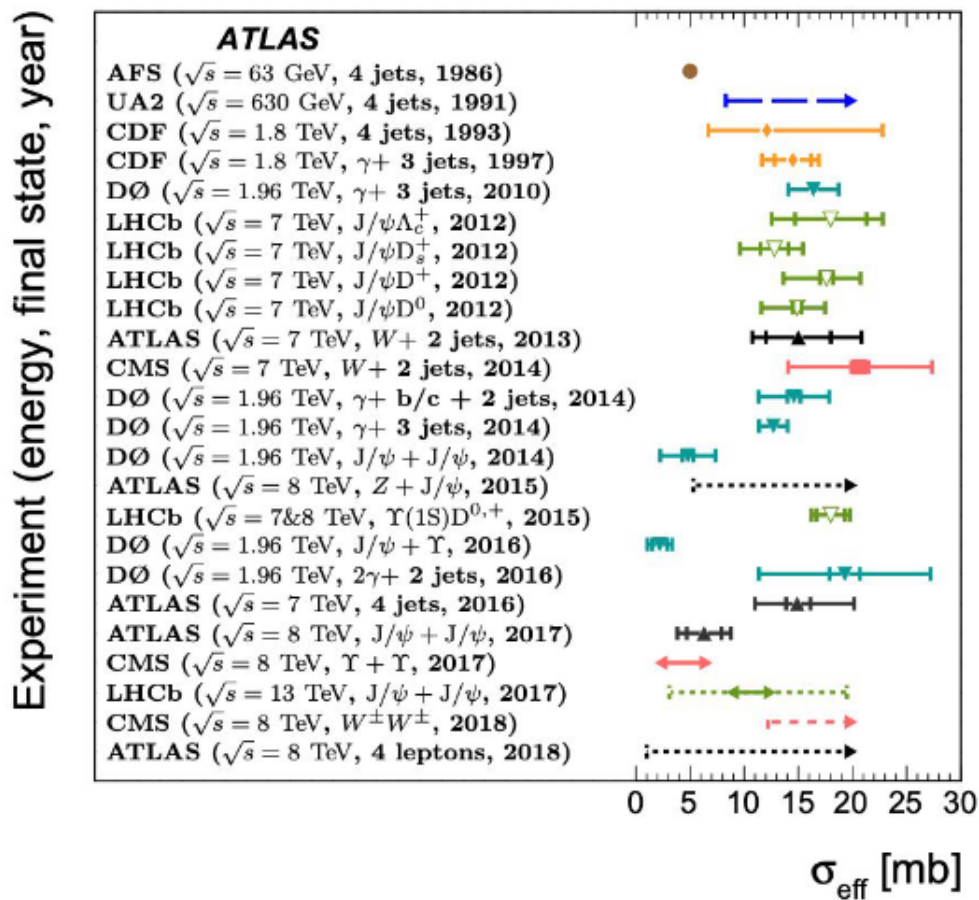
Source: The author, 2023.

As Equation (12) shows, the DPS cross-section depends only on longitudinal momentum fraction and its factorization scale. However, it is well known that for describing pp scattering correctly, the transversal distance b (impact parameter) between the two partons must be considered (81, 82, 80).

In fact, σ_{eff} is a parameter that encodes the information about the impact parameter b of the interaction, that is the distance of separation of the interacting partons

$$\sigma_{eff} = \frac{1}{\int d^2b G^2(\mathbf{b})}, \quad (14)$$

where $G^2(\mathbf{b})$ is the transversal component of the PDF. Figure (11) shows a summary of measurements of the effective cross-section in different experiments. It is worth mentioning that for many measurements σ_{eff} fluctuates around 15 mb. Besides that, for associated quarkonia measurements, σ_{eff} is lower compared with the other values. This means that for certain channels this value can change, which might indicate the non-universality of this parameter. More details on this are given in Section (4.9).

Figure 11 - σ_{eff} measured by several experiments.

Legend: σ_{eff} measurements in different experiments. It is worth mentioning that even for the same channels different values are observed. This indicates that this variable can depend on other variables, such as parton content of the interaction particles, for example (83).

Source: AABOUD, et al., 2017, p. 12.

1.10 Recent results in the associated production of quarkonia and open-charms

The results obtained at the LHC on the associated production of quarkonia and open charms were measured by the LHCb collaboration. The associated production of J/ψ with (D^0 , D^+ , D_s^+ , and Λ_c^+) (84) and the associated production of $\Upsilon(1S)$ and $\Upsilon(2S)$ with (D^0 , D^+ , D_s^+) (12), both at $\sqrt{s} = 7$ TeV (Also $\sqrt{s} = 8$ TeV in Υ analysis) were measured in the frontal region, $2 < y^{J/\psi C} < 4$; $2 < y^{\Upsilon C} < 4.5$, where C denotes charm particle. The results obtained in the associated production of J/ψ with open charms at the LHCb are compared with the results of this work in Section (11).

2 EXPERIMENTAL SETUP

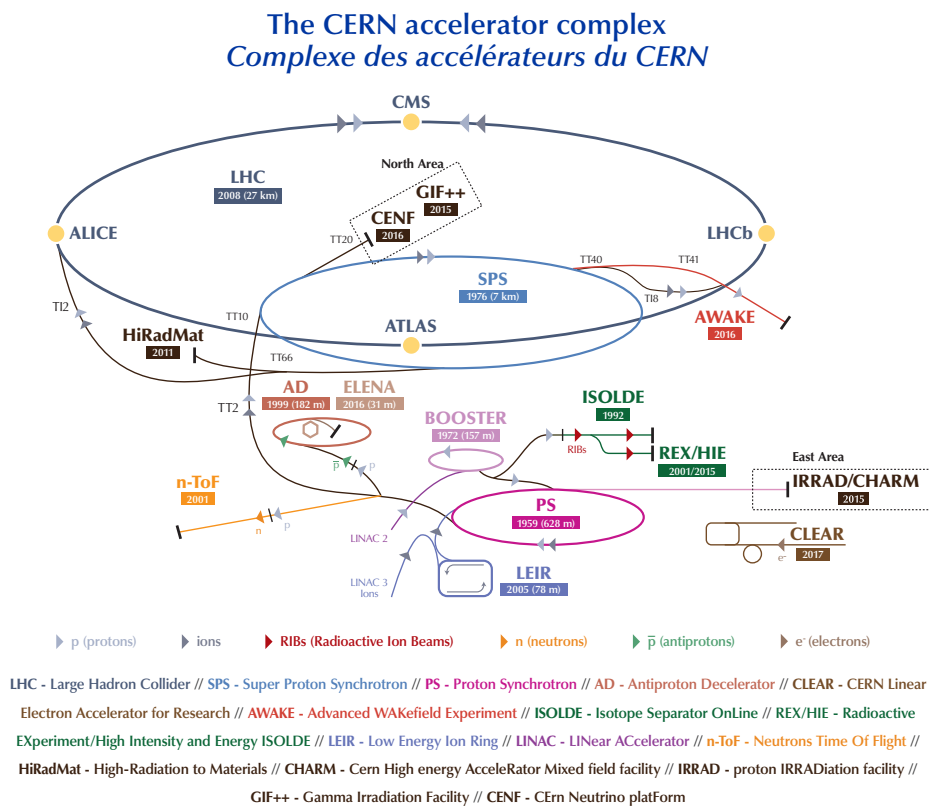
In this chapter, the experimental apparatus is discussed. The Large Hadron Collider (LHC) and its main detectors are discussed. The data used to study the associated production of J/ψ and D^* are from 2016, 2017, and 2018. Thus, the characteristics of each experimental setup are referred to the end of 2018, when the second period of data taking of the LHC was finished. It is worth mentioning that throughout the years the experiments have been subjected to upgrades, which are discussed in the sub-detector sections.

The LHC is a proton-proton synchrotron collider and the largest and most powerful in the world (85). The particles travel inside an ultrahigh vacuum circuit of approximately 27 km close to the speed of light before the collision. The strong magnetic field which steers the particles in the tube is maintained by superconducting electromagnets that are built from coils of niobium electric cables, operating in a superconducting state. This configuration provides a high conducting electricity efficiency without any loss of energy. To assure this, liquid helium-4 is used to cool the magnets at $-271.3\text{ }^\circ\text{C}$ - a temperature colder than outer space. The LHC uses thousands of different magnets, among which the most used are dipole magnets (1232 units), used to bend the particle beam, quadrupole magnets (392 units), used to focus the particle beam and just prior entering the detector for collision there are insertion magnets, in which makes the particles squeeze close together to increase the probability of collisions. The designed energy of the LHC proton-proton collisions at the center-of-mass is $\sqrt{s} = 13\text{ TeV}$, in which each beam of protons, one traveling in clockwise and the other traveling anti-clockwise, carries $\sqrt{s} = 6.5\text{ TeV}$. Besides that, at the LHC is possible to produce beams of lead (pb), being capable to produce collisions of both proton-lead and lead-lead (86).

The LHC has four large experiments, ALICE (A Large Ion Collider Experiment), ATLAS (A Toroidal LHC Apparatus), CMS (Compact Muon Solenoid), and LHCb (LHC beauty). ATLAS and CMS are general-purpose detectors, *i.e.* they are designed to investigate several physics phenomena, including the search for the Higgs boson and physics beyond the SM. On the other hand, LHCb and ALICE are dedicated experiments, where the first one is designed to study b-physics and the second one heavy ion collisions. Fig. (12) shows the entire CERN accelerator complex, including the LHC and the four large experiments commented on above.

The CMS experiment aims to investigate a wide range of physics, including the search for the Higgs boson, extra dimensions, and particles that could make up dark matter.

Figure 12 - CERN accelerator complex



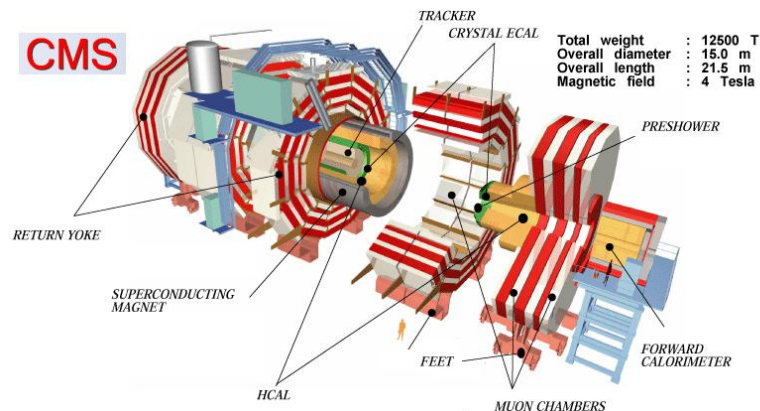
Legend: The CERN accelerator complex: There are many accelerator stages before the particle reaches the LHC (87).

Source: CERN, 2019.

2.1 The Compact Muon Solenoid detector

The CMS (88) is designed to measure with high precision the particles produced in collisions at the LHC accelerator. It has a cylindrical shape with 21 m in length and 15 m in diameter containing several layers of different sub-detectors. It is divided into two regions: the central region (barrel) and the forward region (endcap). One of the key elements of the detector is the superconducting solenoid capable of producing a 3.8 T magnetic field. The purpose of this field is to measure the momentum of the charged particles with the help of the Lorentz force as it is well known that when a charged particle travels through a magnetic field it suffers a curvature that can be related to its momentum. To produce such a field CMS uses a large superconducting solenoid of 12.5 m long with an inner diameter of 5.9 m, being the world's largest superconducting solenoid magnet ever built. The tracker system and the calorimeters are placed inside the solenoid while an iron yoke is placed outside, which is used to return the magnetic field and provide mechanical support for the detector. Besides that, the magnetic field of 1.8 T inside the yoke is used to determine the momentum of the muon with a good resolution. The barrel region is divided into five wheels, while the endcap region is divided into eight regions. The central wheel of the barrel is used to accommodate the solenoid with the cryostat and the sub-detectors (89).

Figure 13 - The Compact Muon Solenoid



Legend: The Compact Muon Solenoid and its subsystems: Tracker, calorimeters, muon chambers.

Source: BUNKOWSKI, 2009, p. 8.

2.1.1 CMS Sub-detectors

The CMS detector is composed of several sub-detectors that together allow the study of several physical phenomena. Each sub-detector is designed to measure different types of particles. This section is dedicated to describing these sub-detectors.

2.1.1.1 The Tracking System

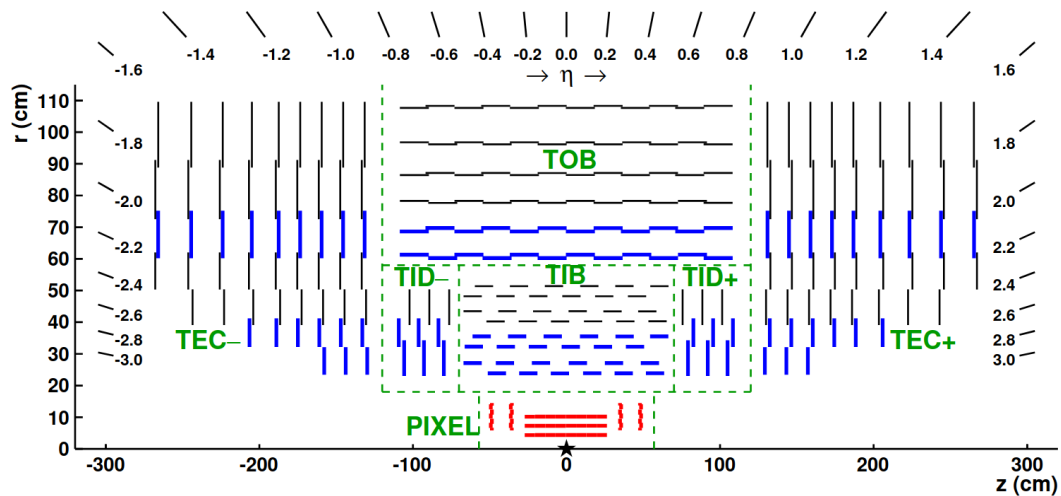
The tracking system is used to measure with high resolution the charge and the momentum of particles. It records and reconstructs the path of high-energy muons, electrons, and hadrons as well as other charged particles such as tracks coming from the decay of b quarks. This sub-detector is very important to reconstruct the trajectory of the particles, allowing the identification of primary and secondary vertices. It takes position measurements with an accuracy of $10\ \mu\text{m}$. The system is divided into a silicon pixel sub-detector and a silicon strip sub-detector (90).

The silicon pixel is installed at the inner radius being the sub-detector closest to the interaction point, which is submitted to a high particle rate, thus it must be resistant to radiation. It is composed of a four-barrel pixel (BPix) that is installed next to the beam pipe and three endcap disks (EPix), present in each endcap region. To detect the charged particles is necessary that the electrons present in the silicon be excited from the valence to the conduction band, allowing the creation of small currents. Then, to have data on the data acquisition system (DAQ) these currents should be amplified with the use of electronics and should fire a trigger. Figure (14) shows a schematic view of the tracking system.

Their 65 million pixels allow them to track the paths of particles with very high accuracy. Also, it has cylindrical layers at 4 cm, 7 cm, and 11 cm and disks at either end, being very important for the track reconstruction of short-lived particles. The particle rate received at a distance of 8 cm from the beamline is around 10 million particles per square per second. The silicon sensor has dimensions of $100\ \mu\text{m}$ and $150\ \mu\text{m}$. When a particle passes through it, electrons are ejected from the silicon atoms, creating the so-called electron-hole pair. Then, this charge is collected on the surface as a small electric signal.

One of the uses of the pixel detector is to distinguish the secondary vertex from the primary vertex, which is important for several analyzes such as in b-physics, in which some particles have a large lifetime, allowing them to travel several millimeters (92). As this detector is installed very close to the beampipe it suffers from high radiation, causing inefficiencies in the readout chip. For this reason, it had an upgrade called *Phase-1 Pixel Upgrade*, realized during the technical stop at the end of 2016 (93). This upgrade kept the

Figure 14 - CMS tracking system



Legend: Schematic of the CMS tracker system in the r - z plane. There is a symmetry with respect to $r = 0$, *i.e.*, only the top half is shown. The star at the origin represents the collision point. The system is divided into Tracker Inner Barrel (TIB), Tracker Inner Disk (TID), Tracker Outer Barrel (TOB), Tracker Endcap (TEC), and pixel (91).

Source: CHATRCHYAN, 2014, p. 3.

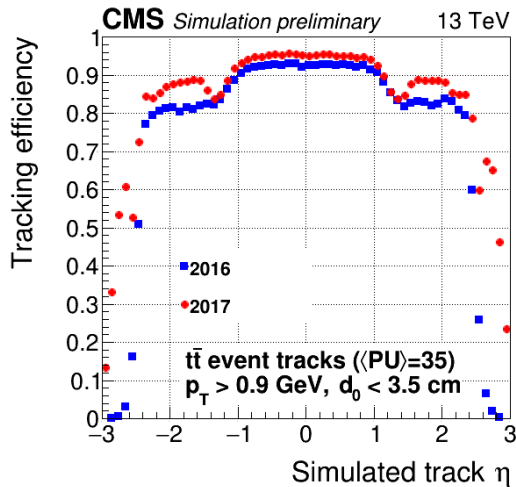
main features of the original detector, improving the performance at higher rates, with better radiation tolerance. This was achieved by adding one additional tracking point, reducing the radius of the innermost pixel layer, and reducing the material budget (94). The pixel detector is expected to operate at high quality until the end of LHC Run 3 when the whole CMS tracker detector will be improved towards the HL-LHC. Figure (15) shows the comparison of the tracking efficiencies between 2016 and 2017 data.

The microstrip system is at the outer part of the tracker system and it is composed of 10 cylinder layers in the barrel ($|\eta| < 1.6$) and 24 disks in the endcap ($|\eta| < 2.5$). It is divided into four layers on Tracker Inner Barrel (TIB) and six layers on Tracker Outer Barrel (TOB). The endcap is divided into 12 disks on the Tracker Endcap (TEC) and 12 layers on the Tracker Inner Disk (TID). For tracks with momentum between 1 GeV and 100 GeV the resolution is between 0.7% and 1.5%.

2.1.1.2 Calorimeters

The calorimeter system is used to measure the deposited energy of neutral and charged particles. Taking into account the depth of penetration of a particle, it can measure the energy lost by it as well as the profile of the energy lost, being capable to

Figure 15 - CMS tracking system efficiency



Legend: It is possible to see that for all values of η the 2017 detector shows better performance than 2016 detector (95).

Source: CMS Tracking POG Performance Plots, 2017.

identify the incident particle. There are three calorimeters installed in the CMS detector: the electromagnetic calorimeter (ECAL) (96), the hadronic calorimeter (HCAL) (97), and the forward calorimeter. They are described one by one below.

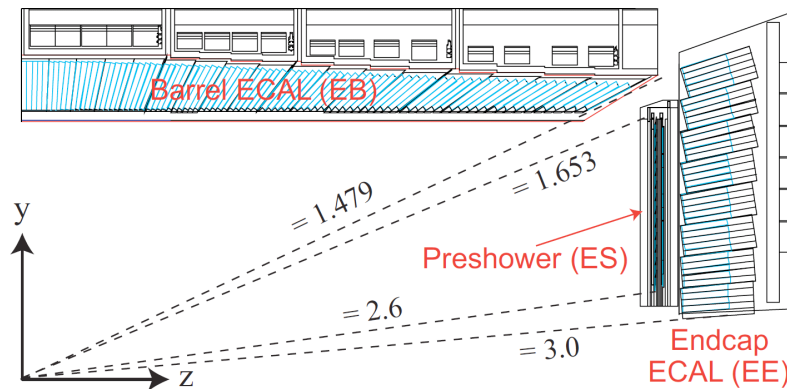
a. Electromagnetic Calorimeter

The CMS ECAL is a homogeneous, hermetic, and high-granularity system composed of inorganic scintillating crystals. It is used to measure the energy of photons, electrons, and positrons. It uses lead tungstate ($PbWO_4$) scintillating crystals to detect the particles. As these crystals have a high density (8.28 g/cm^3) and short radiation length (0.89 cm), they are capable of absorbing electrons and photon showers using a small area. Besides that, they have the characteristic of performing an electromagnetic shower separation. When an electron or photon collides with the nuclei of the crystal it generates an electromagnetic shower of electrons, positrons, and photons. These secondary electrons and positrons can ionize the atoms of the crystals, which can emit scintillation photons with blue scintillating light. The energy deposited in the crystal can be inferred from this generated light that is measured by attached photo-detectors. Also, if the particle stops completely inside the crystal, its total energy can be known.

The ECAL is present in both the barrel and the endcap. There are 61200 crystals in the barrel covering a pseudorapidity region of $|\eta| < 1.479$. They have a cross-section area of approximately $22 \times 22 \text{ cm}^2$ and a length of 230 mm, while in the endcap there are 7324 crystals covering the region $1.479 < |\eta| < 3$ with a cross-section area of approximately $28.6 \times 28.6 \text{ mm}^2$ and length of 220 mm. Besides that, in the endcap, the ECAL system is completed by preshower (ES) detectors. This part of the system is used to measure the position of photons with higher granularity, allowing the distinguishment between single

photon emission and double photon emission (*e.g.* $\pi \rightarrow \gamma\gamma$). The ES is composed of two lead radiators with about 2 and 1 thick radiation lengths respectively. Each of these lead parts is followed by a layer of silicon strip. The longitudinal view of the ECAL endcap, barrel, and preshower is shown in Figure (16).

Figure 16 - The Electromagnetic Calorimeter.

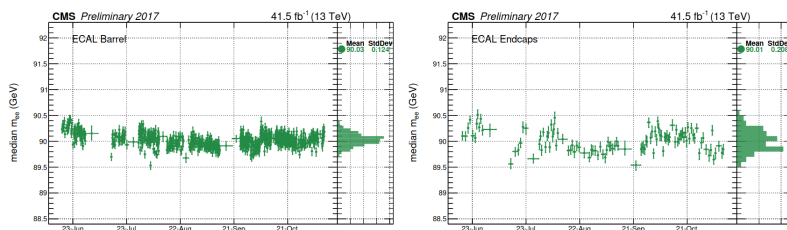


Legend: Longitudinal view of ECAL endcap, barrel, and preshower (92).

Source: ALY, 2021, p. 38.

The performance of the ECAL during Run 2 is considered stable. If the energy scale in Run 2 is compared with that in Run 1, *i.e.*, it is stable within 0.1 GeV and 0.2 GeV uncertainty in the barrel and in the endcaps, respectively. Figure (17) shows the di-electron invariant mass stability during 2017.

Figure 17 - The ECAL performance.



Legend: Left plot shows ECAL barrel and the right plot shows ECAL endcaps. Note that the di-electron invariant mass is reconstructed with $Z \rightarrow ee$ events (98).

Source: BARTOSIK, 2019, p. 12.

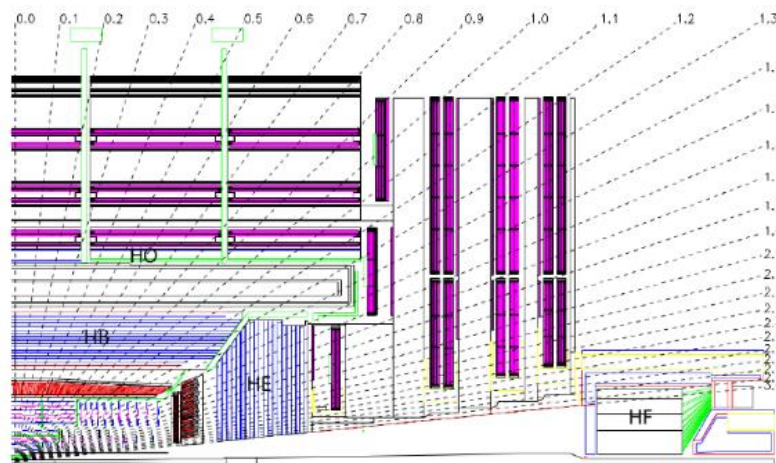
b. Hadronic Calorimeter

The CMS HCAL measures precisely the energy and position of strongly interacting particles, such as hadrons (protons, neutrons, pions, and kaons) and hadronic jets. In

a similar way to ECAL, this calorimeter is composed of a material with high density and short interaction length, capable of measuring precisely the energy of these particles. It also provides information about non-interacting particles in terms of missing energy E_T^{miss} . It is composed of dense brass plates, 5 cm in endcap and 8 cm in the barrel as an absorber, and plastic fluorescent scintillator tiles 3.7 mm thick as active material. When a particle hits the brass it initiates a cascade process that produces several secondary particles which can produce a shower of particles when they interact with the layers of the brass. Therefore, these created particles pass through the scintillator material causing them to emit blue-violet light. This light is read by wavelength-shifting (WLS) fibers that are based on multi-channel hybrid photodiodes (HPDs).

The HCAL is surrounded by the ECAL and its main part is placed inside the solenoid. It is made of 70,000 tiles in total, being divided into barrel region with $|\eta| \approx 1.3$ and endcap, $1.3 < |\eta| < 3$. The longitudinal view of HCAL is shown in Figure (18).

Figure 18 - The Hadronic Calorimeter.

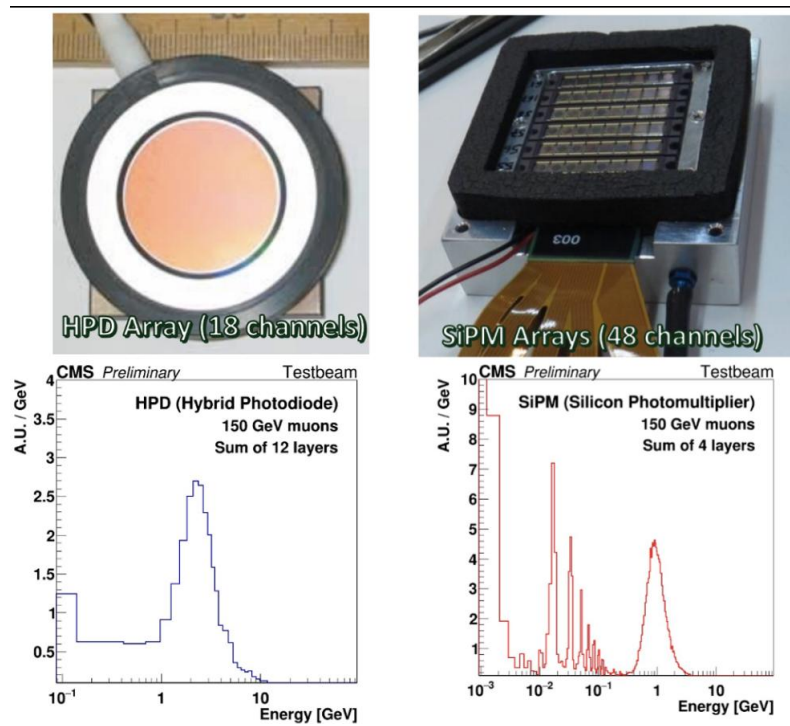


Legend: Longitudinal view of HCAL. HO refers to hadronic outer,
 HB refers to HCAL barrel, HE refers to HCAL endcap and
 HF refers to forward HCAL (99).

Source: GUL, 2016, p. 2.

The phase I upgrade of the CMS HCAL took place in 2016-17, during the extended technical stop. The main motivation was to improve the performance during LHC Run 3 and during HL-LHC. The upgrade was conducted in the HE, which used Hybrid Photodiode transducers (HPDs). They were replaced with Silicon Photomultiplier Devices (SiPMs), guaranteeing better photon detection efficiency and higher gain. Figure (19) shows the performance comparison between HPDs and SiPMs.

Figure 19 - Performance comparison between HPDs and SiPMs.



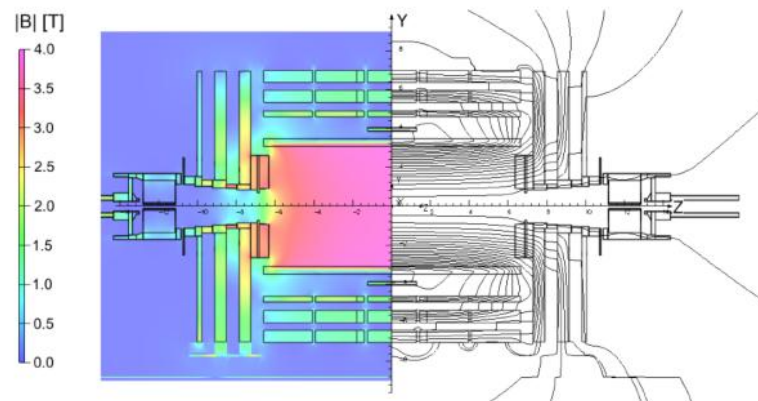
Legend: It is possible to see the improvement in the energy resolution in SiPM (bottom-right). The HPD array has 18 channels (top-left) and the SiPM array has 48 channels (top-right) (100).

Source: COOPER, 2016, p. 2.

2.1.1.3 The Solenoid Magnet

The core of the CMS detector is a solenoid magnet (101) that is used to bend charged particles as they fly away from the collision point. This bending allows for precise measurement of the momentum of the particles and helps in identifying their charge. The solenoid magnet has an internal diameter of 6 m and a length of 12.5 m and is formed of a cylindrical coil of superconducting fibers. When the current circulates through it, it can create a magnetic field of about 4 T, which is 100,000 times stronger than the Earth's electromagnetic field, having 19.5 kA of current, and storing energy of 2.3 GJ. Due to the high current, it is necessary a cooling system composed of helium at temperature 4 K. A longitudinal view of the CMS magnet is shown in Figure (20).

Figure 20 - The CMS solenoid magnet.



Legend: Longitudinal view of the CMS magnet. The right side shows the field lines while the left side shows the amplitude of the field (99).

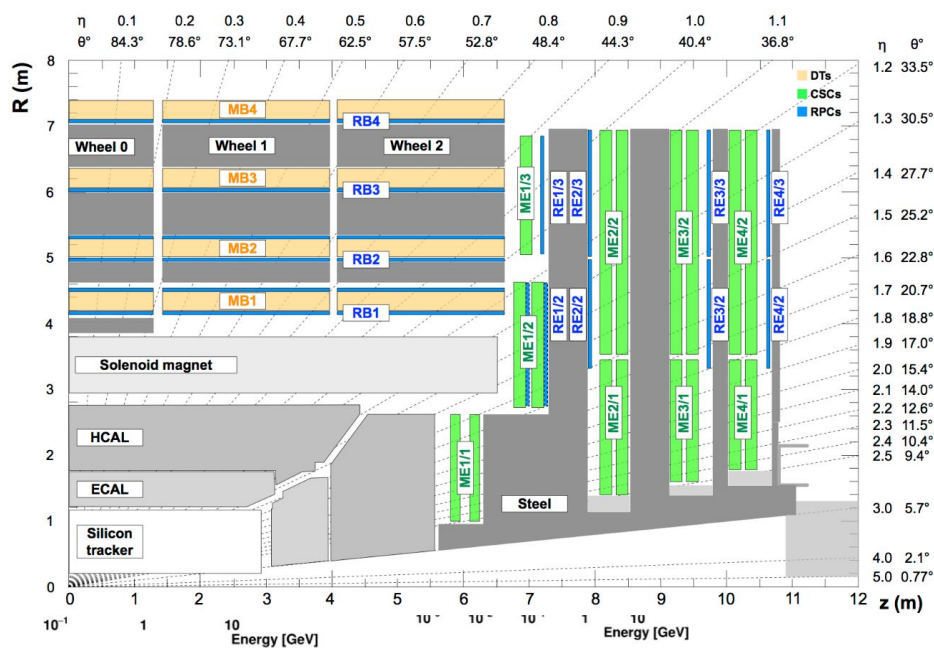
Source: GUL, 2016, p. 2.

2.1.1.4 The Muon System

The CMS muon system (102) occupies the outermost layers of the CMS detector since the muons are not stopped by the calorimeters or by the iron yoke. The system is embedded in the return yoke of the solenoid and uses three different types of detectors technologies (103): Cathode Strip Chambers (CSC) in the endcap region, Drift Tubes (DT) in the barrel region, and Resistive Plate Chambers (RPC) in both regions. The CSCs and the RPCs in the endcap cover the region $0.9 < |\eta| < 2.4$, while the DTs and RPCs in the barrel cover the region $|\eta| < 1.2$.

The CMS muon system has been specially designed to provide precise measurement of muon momentum and charge. Muons are not stopped by the CMS calorimeters, they produce showers and achieve the outermost part of the detector. As most of the hadrons "die" inside the calorimeters the occupancy in the muon detectors is normally low, implying good muon detection and reconstruction. Besides that, the magnetic field produced by the solenoid bends the muon trajectory, allowing the calculation of the transverse momentum p_T , that is, the momentum component lying in a perpendicular plane with respect to the beam line. A cross-section of a quadrant of the CMS detector is shown in Figure (21). The point $(R, z) = (0, 0)$ is the interaction point where the beams coming in opposite directions collide. The region starting near $R = 4$ m is the barrel, where is possible to see the stations containing alternating layers of DTs, Muon Barrel (MB) in yellow, and RPCs, in blue, while the region starting near $z = 6$ m is the endcap, containing alternating layers of CSCs, Muon Endcap (ME) in green and RPCs in blue.

Figure 21 - A R-z cross-section of a quadrant of the CMS detector.



Legend: On this cross-sectional view of CMS is possible to see the muon stations and the yoke (dark gray) where the magnetic flux returns. The CSC detectors are labeled muon endcap station (ME), while the DT detectors are labeled muon barrel (MB). As RPCs are present in both barrel and endcap they are labeled RE and RB (104).

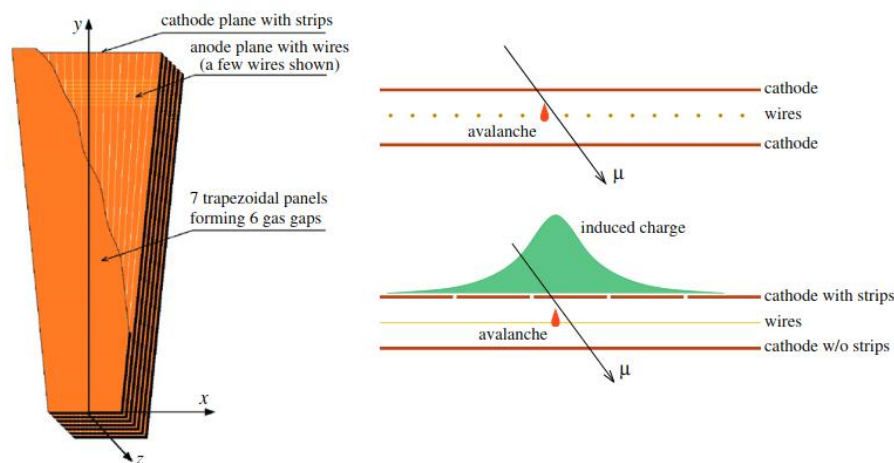
Source: SIRUNYAN, et al. P, 2020, p. 3.

a. The Cathode Strip Chambers

The CSCs (105) are multi-wire proportional counters in a trapezoidal form con-

sisting of cathode strip planes and anode wires. They are installed in the endcap region ($0.9 < |\eta| < 2.4$), where there is a high muon flux and an inhomogeneous magnetic field and it is composed of four stations namely ME1, ME2, ME3, ME4. Because of that, the CSCs are designed to be radiation-resistant, fast, and robust. The gas particles inside the chamber are ionized by muons, resulting in the formation of electrons and positive ions. The electrons come toward anode wires, forming an avalanche, while the positive ions come toward the copper cathode, inducing a charge in the strips. The CSCs use a gas mixture of *Ar* (40%), *CO₂* (50%) and *CF₄* (10%) (to reduce the polymerization of the wires) having a spatial resolution of $80 \mu\text{m}$. They have good spatial and time resolution and are more radiation-resistant than the DTs.

Figure 22 - The CSC detector and its signal formation



Legend: Left: a schematic view of a typical CMS-CSC. Note that the first strip plane is cut out to show the anode wires running across the strips (there are more wires, but for illustration, few of them are shown.)

Right: signal formation in the CSC. When a muon passes through the chamber the gas is ionized, and then the electron avalanche drifts toward the anode wires which induces a charge on cathode strips (106).

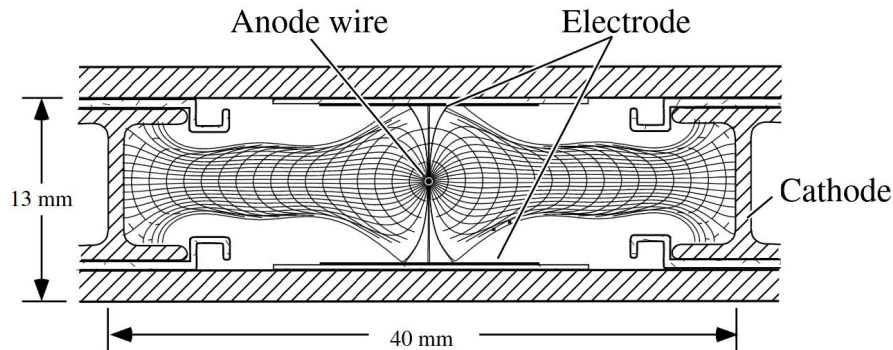
Source: ACOSTA, et al., 2005, p. 2.

b. The Drift Tubes

The DTs (105) use a drift cell as a basic constituent. They are installed in barrel regions where in general the magnetic field is constant and the muon rate is low, being ideal for the use of DTs. They are installed in four barrel stations covering a region $|\eta| < 1.2$, interleaved among the plates of the CMS yoke. The drift cell is a tube filled with a gas having a rectangular cross-section of $42 \times 13 \text{ mm}^2$. Around this cell, there are two parallel aluminum planes and I-shaped aluminum beams that are the cathodes, as shown

in Figure (23). The drift tube has one wire localized in the center which is the anode. A particle passing through the DT ionizes the gas and then the electrons drift to the wire and induce a signal. The gas mixture of this detector is Ar (85%) and CO_2 (15%) providing a good quenching. Normally a single cell has a resolution of $180 \mu m$ and an efficiency of around 99.8%.

Figure 23 - Schematic view of a drift tube.



Legend: Transverse view of the drift tube cell. Drift lines are shown (103).
Source: CMS COLLABORATION, 1997d, p. 52.

The RPC detector will have a dedicated chapter devoted to it.

2.1.1.5 Performance of CMS Muon Detector in Run 2

During the LHC Run 2, the performance of the CMS muon system was evaluated in terms of the resolution and efficiency of muon hits and muon track segments. Muon hits are defined from muon tracks, where the reconstructed crossing position of the muon track of a single detector layer defines it (107). Muon hits are one-dimensional in DT and RPC chambers, while in CSC they are two-dimensional. The efficiency measurement is made using a well-known data-driven method called tag-and-probe⁶ using opposite-sign muon pairs from $Z \rightarrow \mu^+ \mu^-$ or Drell-Yan⁷ events.

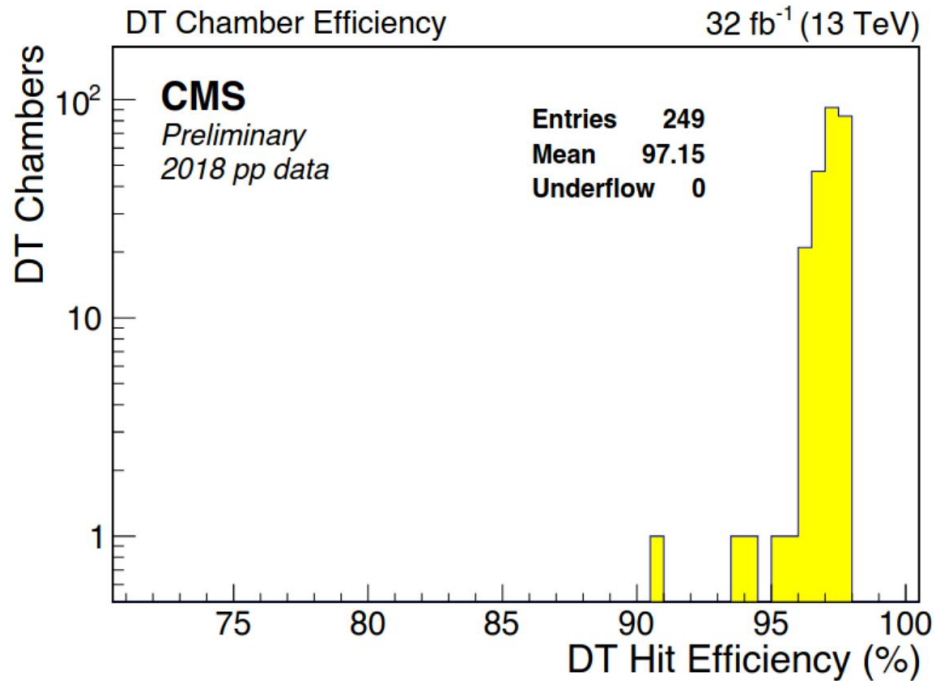
The DT and RPC hit efficiencies are stable during the whole Run 2. Some inefficiencies can be seen in the 2017 data in DT segment efficiency because of readout failures.

⁶ The tag-and-probe method is a data-driven method, often used to measure the identification, reconstruction, and trigger efficiency. Events with opposite-sign muons from known decays ($Z \rightarrow \mu^+ \mu^-$ and $J/\psi \rightarrow \mu^+ \mu^-$, for instance) and from another decay product are used. The decay product is reconstructed with tight selection and its muons are called tag muon and probe muon (108)

⁷ Drell-Yan process happens when a quark-anti-quark pair from distinct hadrons annihilate, creating either a virtual photon or a Z boson which decays to an opposite-pair of leptons (109)

This was recovered in 2018 with the use of an improved front end. In the case of CSCs, the segment efficiency was larger than 90%. Figures (24), (25), (26), and (27) show the DT single hit efficiency, RPC single hit efficiency, DT segment reconstruction efficiency, and CSC segment reconstruction in efficiency.

Figure 24 - DT single hit efficiency



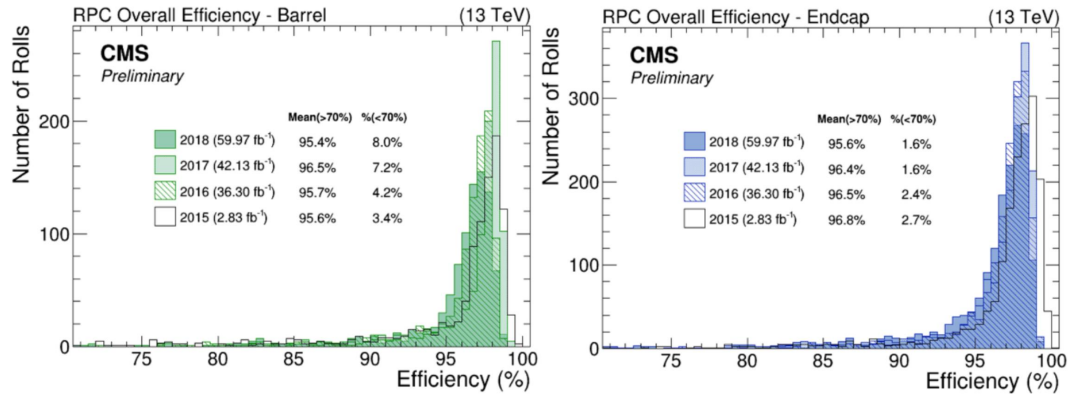
Legend: The mean of the single hit efficiency is 97.15%. The data was collected in 2018 (110).

Source: BATTILANA, 2019, p. 2.

2.1.1.6 Trigger and data acquisition

Considering the design instantaneous luminosity of $10^{34} \text{ cm}^{-2} \text{ s}^{-1}$ the beam of protons in the LHC collides 40 million times per second or every 25 ns. This means that the size of the data is very high, corresponding to 40 TB/s or about 1 MB for each bunch crossing (event), even after considering the zero suppression strategy, when only the channels with activated channels are read out. Alternatively, this corresponds on average to 20 proton-proton collisions per bunch crossing. This amount of data is impossible to be processed by the existing detector technology and impossible to be stored so it is necessary to use a trigger system and data acquisition to filter and store the interesting events. The CMS system implements a two-level trigger system called Level-1 (L1) trigger and High-Level Trigger (HLT), which reduces the number of events from $40 \cdot 10^6 \text{ Hz}$ to 100

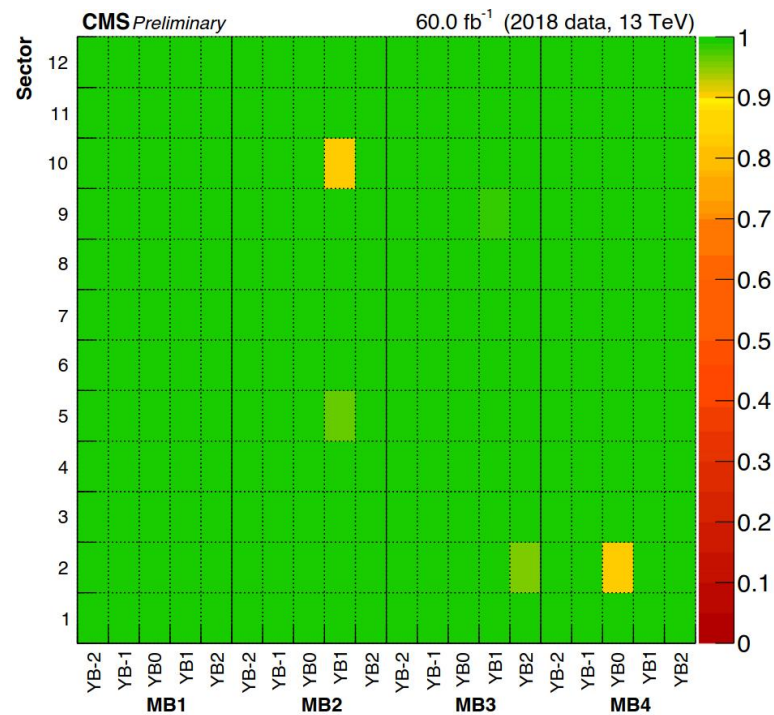
Figure 25 - RPC single hit efficiency



Legend: Left shows the efficiency in the barrel chambers and the right shows the efficiency in the endcap chambers. The comparison of 2015, 2016, 2017, and 2018 data shows that the efficiency remains stable (110).

Source: BATTILANA, 2019, p. 2.

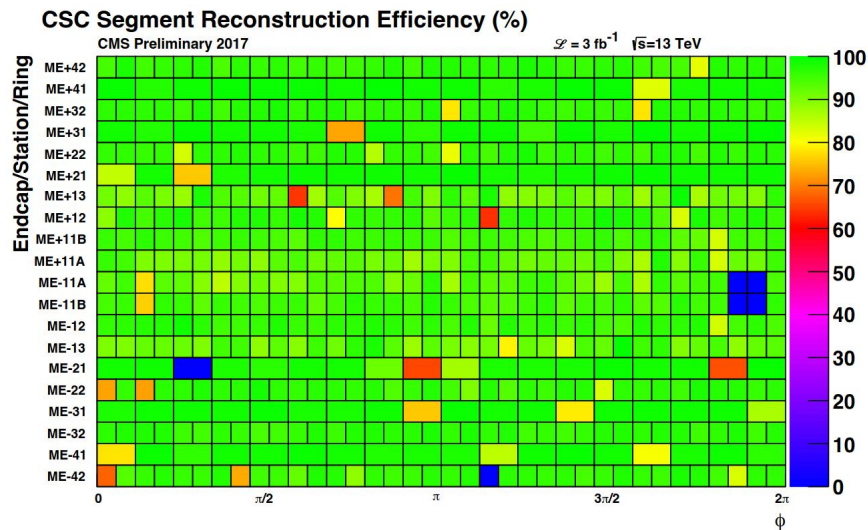
Figure 26 - DT segment efficiency



Legend: The local muon track segment in DTs is, in general, above 90%. The data was collected in 2018 (110).

Source: BATTILANA, 2019, p. 2.

Figure 27 - CSC segment efficiency



Legend: The CSC segment efficiency is high in both endcaps. The values are larger than 90%, with few chambers with lower values, due to hardware problems.

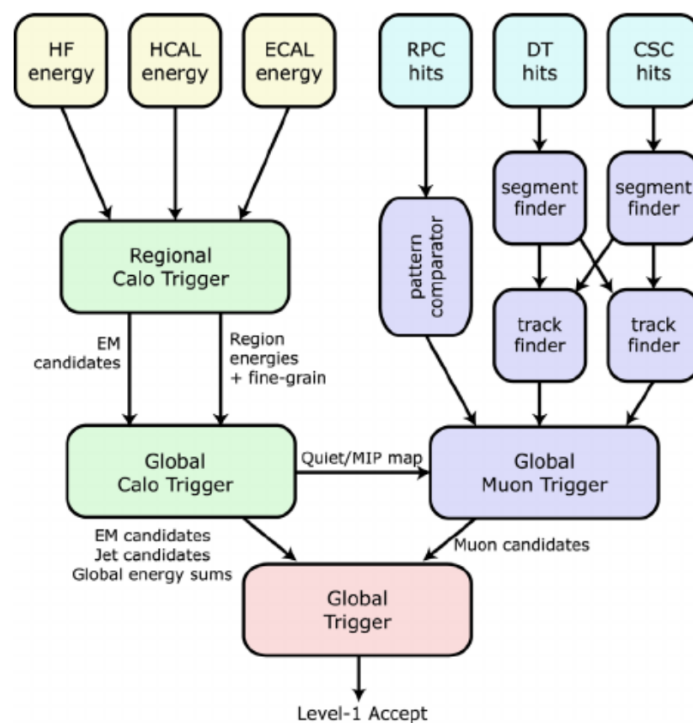
Source: BATTILANA, 2019, p. 2.

Hz.

a. Level-1 Trigger

The main goal of the L1 trigger is to reduce the event rate from 40 MHz to 100 kHz. This is done with the use of a hardware system with a fixed latency. The system takes the information from the calorimeter and muon detectors to decide if the event should be accepted or rejected. This decision is performed within $4 \mu\text{s}$ of a collision. It is worth mentioning that the tracking system does not participate because its reconstruction time exceeds the time limits of L1 decision (111). The L1 trigger structure is shown in Figure (28). Hits from the RPCs, CSC, and DTs are processed with the help of either a system of segment and track-finders or via a pattern comparator. The track-finder system is divided in the following way: endcap muon track-finder (EMTF) in the endcap, barrel muon track-finder (BMTF) in the barrel, and overlap muon track-finder (OMTF) that takes hits from both barrel and endcap. The combination of both pattern comparator and track-finder is sent onwards to a global muon trigger (GMT). In turn, the data from the HF, HCAL, and ECAL is processed in a regional trigger (RTC) and then in a global trigger (GCT). Then, the information of both GMT and GCT is combined in a global trigger which makes the final decision. After that, the final decision is then sent to the ECAL, HCAL, muon systems, and tracker via the trigger, timing, and control (TTC) system. Also, the DAQ system reads this data from the subsystems for offline storage.

Figure 28 - Schematic view of the L1 trigger

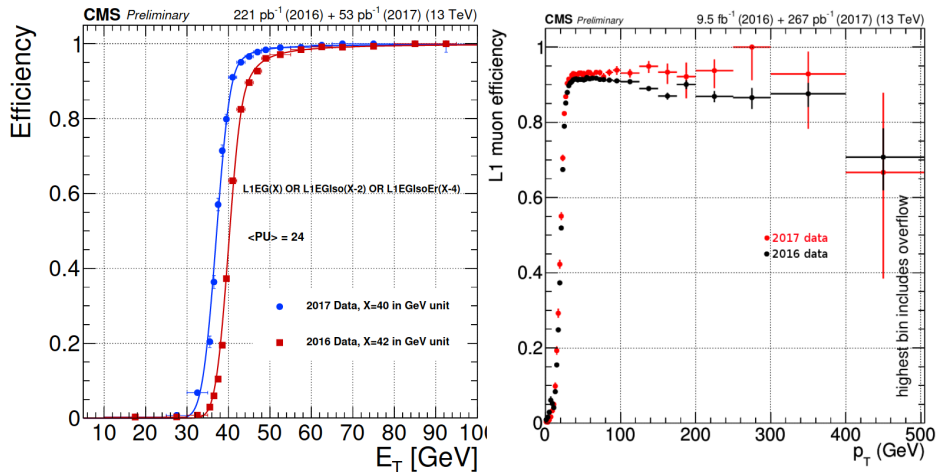


Legend: The structure of the L1 trigger is shown. Note the main components of the structure: HF, HCAL, and ECAL energy and RPC, CSC, and DT hits.

Source: ALY, 2021, p. 46.

The performance of the L1 trigger system in Run 2 was analyzed with the efficiency measurement for the single e/γ and for the single muon triggers. The efficiency was measured using the tag-and-probe technique with $Z \rightarrow \mu^+\mu^-$ events. Figure (29) shows the efficiency measurement for both cases.

Figure 29 - L1 trigger performance



Legend: Left figure shows the trigger efficiency of the e/γ objects with 2016 and 2017 data. The right figure shows the trigger efficiency for the μ objects with 2016 and 2017 data.

Source: TOSI, 2017, p. 3.

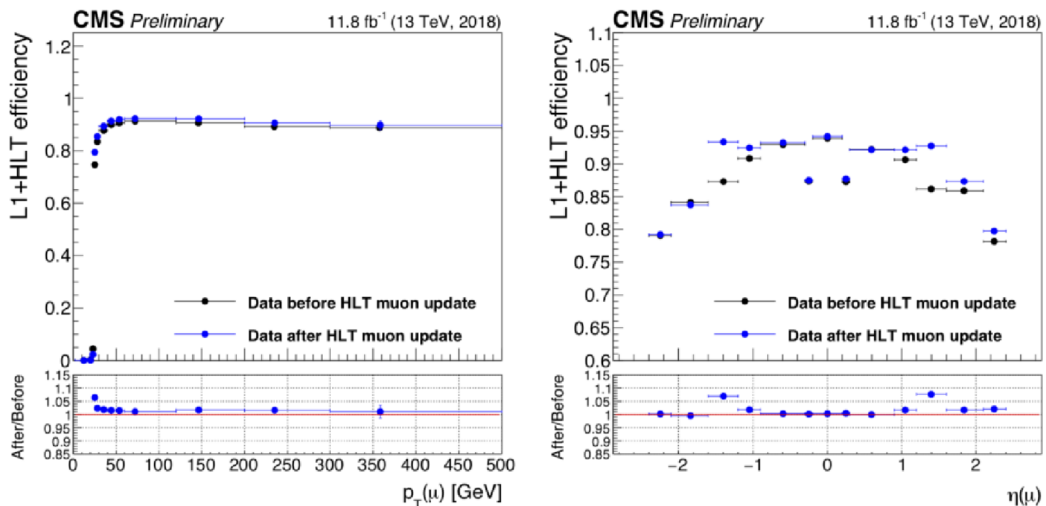
b. High-Level Trigger

The High-Level Trigger (HLT) (111) is software-based and consists of a single processor farm composed of computer systems based on open standards. It uses the event filter farm (EVM), which runs Scientific Linux. The HLT is responsible for reducing the event rate from 100 kHz to around 1 kHz to be written on the tape with a processing time of about 100 ms. The event selection is done with the application of identification criteria for objects such as electrons, jets, and muons. This event reconstruction and selection is similar to the one used in the offline analysis. To pass the HLT the event needs to satisfy the criteria of the HLT menu, that is a list of dedicated triggers (*e.g.* muon trigger) in a similar way as in the L1 trigger. Then the DAQ system records permanently on the disk the events that passed the HLT criteria To provide the data for further analysis and transfer it to the CERN Tier0 (T0) storage system. Finally, data quality monitoring (DQM) qualifies the data and gives a label if the data is good or bad. In the end, a list of certified datasets is produced.

The performance of the HLT trigger can be analyzed by measuring the trigger efficiency of many physics objects, such as trackings, electrons, muons, tau leptons, and

jets. For example, the muon reconstruction is performed in two steps. In the first step, only information from muon detectors is used. In the second step, full detector information is used. It is worth mentioning that in 2016 there were two different reconstruction algorithms used to reconstruct the muons trigger paths. In 2017, these two algorithms were combined. Whereas in 2018 high purity with a lower rate was required (112). Figure (30) shows the isolated single muon efficiency.

Figure 30 - Trigger efficiencies of isolated single muon.



Legend: The minimum p_T is 24 GeV. The left figure shows the isolated single muon efficiency as a function of p_T and the right figure shows the same efficiency as a function of η

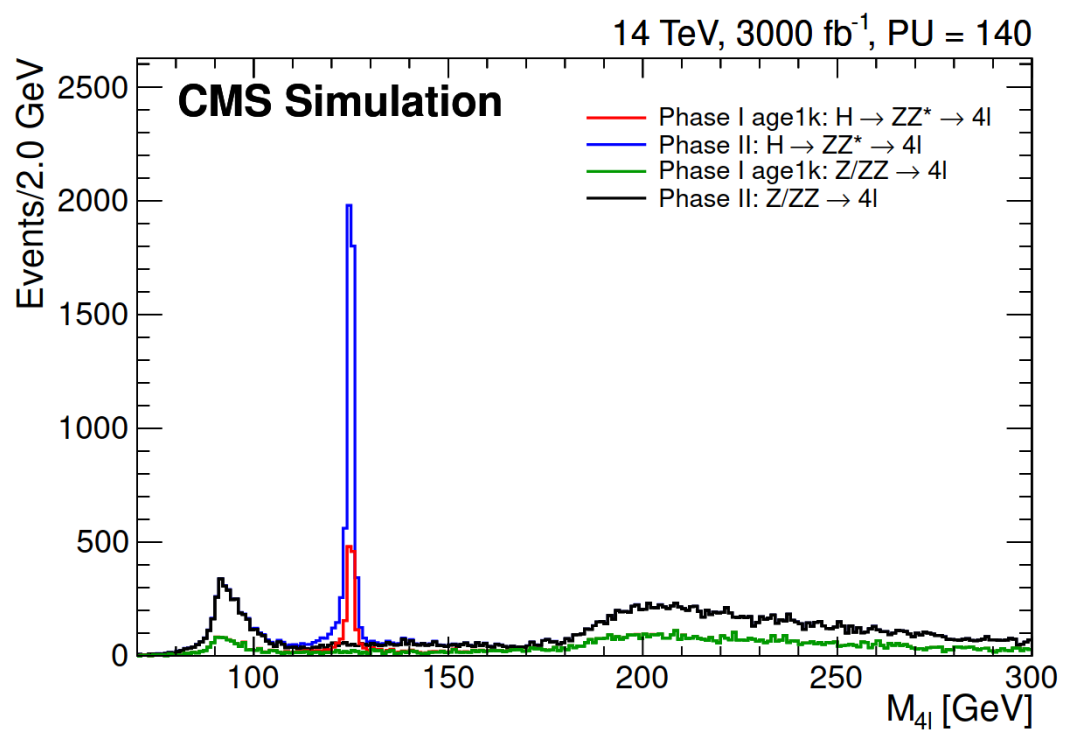
Source: TOSI, 2017, p. 5.

2.1.2 CMS Phase-2 Upgrades

The CMS Phase-2 upgrades are a set of developments and improvements that are being implemented in the CMS detectors toward the HL-LHC. This project is fundamental so that the CMS sub-detectors are able to operate with good performance in the new instantaneous luminosity levels (the value will increase from $5 \cdot 10^{34} \text{ cm}^{-2} \text{ s}^{-1}$ to $2 \cdot 10^{35} \text{ cm}^{-2} \text{ s}^{-1}$ and in the impressive 3 ab^{-1} of integrated luminosity (20).

The main physics program of the CMS will still be the Higgs boson. More complete and detailed measurements will be possible. Higgs boson couplings and the search for rare decays either in SM or BSM will be studied. The amount of pp-collision data to be collected in the HL-LHC will give a considerable increase in the number of detectable Higgs bosons. Figure (31) shows that the difference in the number of events containing the Higgs boson will increase from the LHC Phase I age to the LHC Phase II age.

Figure 31 - Higgs boson statistics improvement in the HL-LHC phase.

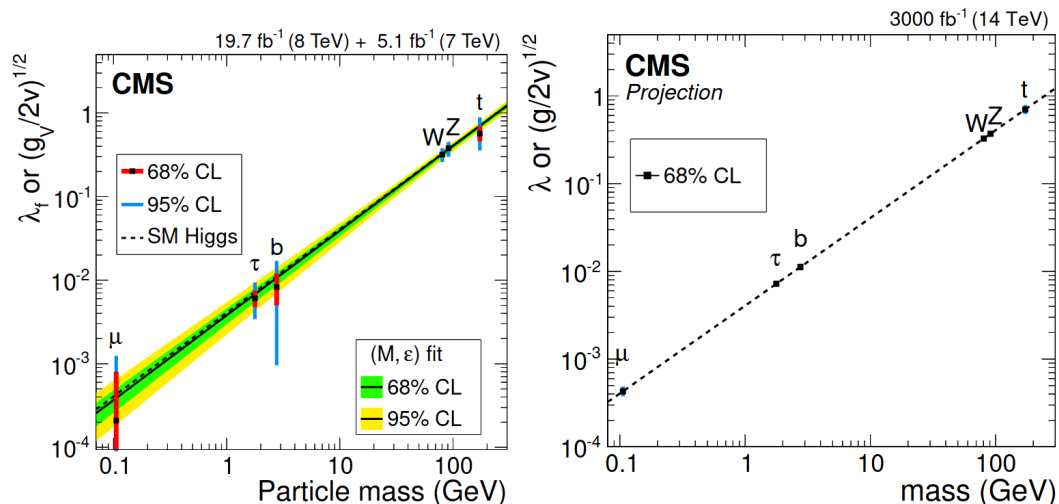


Legend: The simulation considers the full Phase II luminosity of 3 ab⁻¹. The Higgs boson is reconstructed through $H \rightarrow ZZ \rightarrow 4l$, and the irreducible $ZZ \rightarrow 4l$ background.

Source: CMS COLLABORATION, 2016, p. 9.

The measurement of the couplings of the Higgs boson will also have a good improvement. The projection for the measurement of Higgs boson couplings in the full phase II luminosity (3 ab^{-1}) and at the center-of-mass energy of 14 TeV is compared with the observed values measured during LHC Run 1 (integrated luminosity of 13.7 fb^{-1} at center-of-mass energy 8 TeV plus 5.1 fb^{-1} at center-of-mass energy 7 TeV⁻¹). It is noted that the precision at percent-level (today it is 20 %) is achieved. Figure (32)

Figure 32 - Precision improvement - HL-LHC.



Legend: The left figure shows the observed results and the right figure shows the projection for the HL-LHC. Note the improvement in the precision.

Source: CMS COLLABORATION, 2016, p. 8.

Therefore, each CMS detector needs to be optimized to cope with the HL-LHC radiation conditions. The technical proposal for the CMS Phase-II upgrade contains the main details of the upgrades of each CMS sub-detector (113). In the next sub-section, the upgrades of the muon system are briefly described. Figure (33) shows the CMS sub-detectors highlighting the main upgrades for each part of the CMS detector.

2.1.2.1 Phase II Upgrades of CMS Muon Detector

With the HL-LHC the whole CMS muon system will need an upgrade to assure good performance of muon tracking and triggering (115). Each of the detectors is going to be submitted to a different upgrade. As during the HL-LHC the L1 trigger latency and the rate will increase (116) the CSCs localized at regions closer to the beam will need a refurbishment in their front-end boards to cope with this change. In the case of DTs, they will need an improvement in their electronics to increase the trigger rate capability. Also, they will need an improvement to tolerate the radiation to not lose performance.

Figure 33 - The CMS Phase-II upgrade changes

Trigger/HLT/DAQ

- Track information in hardware event selection
- 750 kHz hardware event selection
- 7.5 kHz events registered

Barrel EM calorimeter

- New electronics
- Low operating temperature $\approx 10^\circ$

Muon systems

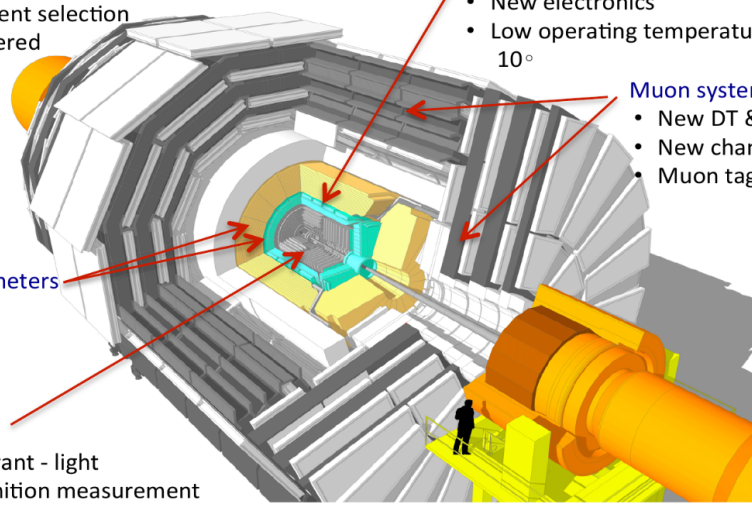
- New DT & CSC electronics
- New chambers $1.6 < \eta < 2.4$
- Muon tagging $2.4 < \eta < 3$

New Endcap Calorimeters

- Rad. Tolerant
- 5D measurement

New Tracker

- Rad. Tolerant - light
- High Definition measurement
- 40 MHz selective readout for hardware trigger
- Extended Pixel coverage to $\eta = 3.8$

Beam radiation and luminosity**Common systems and infrastructure**

Legend: Each part of the CMS detector will have a specific project to cope with the HL-LHC radiation conditions (114).

Source: CMS COLLABORATION, 2016, p. 8.

In the case of the RPCs, new detectors called improved RPCs (iRPCs) will be installed in the endcap stations three and four, in disk one, the innermost part, *i.e.* the region with high- η regions. The new RPCs will cover the region $1.5 < |\eta| < 2.4$. In the present system, only CSCs are installed, then with this upgrade, the muon system will be capable of providing a better momentum resolution as well as a good L1 muon trigger acceptance. Besides that, a new detector technology will be installed in endcap stations one and two, also covering high eta regions. The Triple Gas Electron Multiplier (GEM) (117) are gaseous detectors that have efficiencies higher than 98% for a high rate, in the order of MHz/cm² with good time resolution (the order depends on the gas mixture), high spatial resolution (order of 100 μ , operating with a gas mixture of Ar (70%) and CO₂ (30%) (time resolution around 8 ns) and 45% Ar, 15% CO₂ and 40% CF₄ (time resolution around 5 ns).

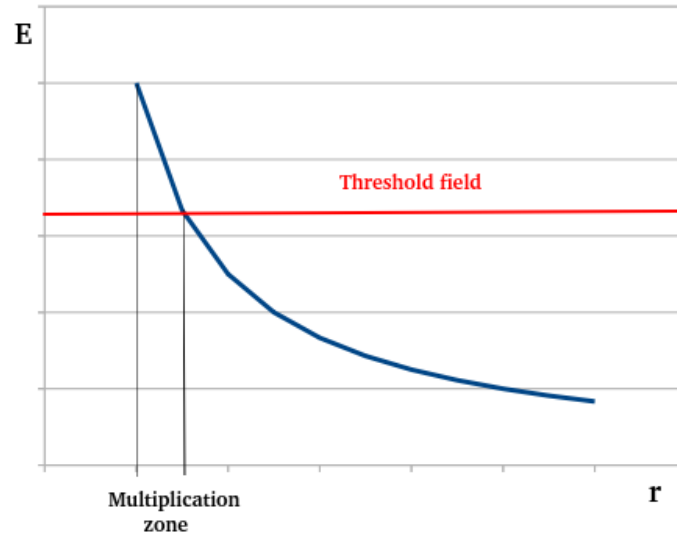
3 ACTIVITIES AND CONTRIBUTIONS TO THE CMS-RPC PHASE-II PROJECT

The first gaseous detector used at the beginning of the last century was the ionization chamber (118) that depending on the experimental configuration, can have different geometries: planar, cylindrical, spherical, etc. In a simple way, the planar configuration of this detector consists of two parallel metal plates, called electrodes (anode and cathode) with a certain voltage applied between them filled with a gas mixture with pressure around 1 atm. Since then, several different types of gaseous detectors have been tested from single-wire counters to multi-proportional chambers (119). The gas detector technologies have evolved through time and despite that evolution, they have the same working principle: they rely on the ionization of the gas molecules due to the passage of an ionizing particle.

The first gaseous detectors were based on the cylindrical geometry, where the primary electrons, which are resulting electrons from the primary ionization are collected at a central wire. This type of device dates back to the beginning of 1900 and is still largely used in big experiments (118). In turn, detectors with planar geometry were developed later in the 1940s. The main difference between central wire and planar detectors is that in the former the electrical field is inversely proportional with respect to the distance from the wire ($|E| \approx 1/r$) and later it is constant between the plates. This difference implies that in detectors with the central wire design, the multiplication phenomena depend on the distance from the central wire because the ionization is more likely to occur next to the central region as shown in Figure (34).

In the case of the detectors with planar geometry, the electric field inside the gas volume is constant, meaning that the whole region can be used for the multiplication process. This means that, in principle, any primary electron can give a start to an avalanche immediately after its generation. In other words, in a detector of this kind, any region of the gas volume can be used for the amplification (of course, the electric field must be strong enough). As there is no separation between drift and multiplication regions, this characteristic reduces the timing fluctuation. Besides that, it is worth mentioning that this conclusion is gas dependent, *i.e.* depending on the gas mixture used it could vary. The drawback, however, is that in gaseous planar detectors, there are no simple quenching mechanisms, and once a discharge is initiated it needs some mechanism to stop it.

Figure 34 - Electric field in a wire gaseous detector.



Legend: The figure illustrates the drop in the electric field as a function of the distance. Note that for the high electric field (a few kilovolts per centimeter) there is a multiplication zone inside the detector, where the avalanche process may occur. The red line is called the threshold field, showing the minimum electrical field where the avalanche process may occur.

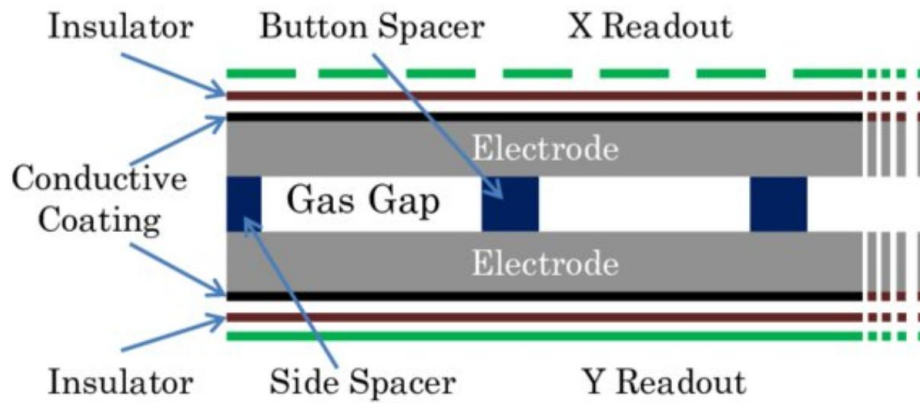
Source: The author, 2023.

3.1 The Resistive Plate Chamber

The first modern Resistive Plate Chamber (RPC) was developed in the early 1980s (120). The main idea behind this was the use of the phenolic laminate compressed (bakelite) at high pressure as an electrode operated at atmospheric pressure. The main ingredients used were: the use of planar geometry, taking advantage of the good time resolution, and the use of bakelite for building the resistive electrodes. Besides that, this idea was in some sense easily executable. The modern RPCs are planar gaseous detectors with good intrinsic time resolution ($O(1 \text{ ns})$ for a 2 mm gap) and spatial resolution (tens of micrometers), thus providing a very fast muon measurement system. Its design consists of two bakelite (could be another material, like glass) parallel plates with high resistivity ($10^{10} - 10^{11} \Omega \text{ cm}$), which are separated by a gas gap of a few millimeters. One bakelite electrode is connected to the ground and the other is connected to the high voltage. Both electrodes are covered with an insulator and coated on the outer surface with conductive graphite. The outermost layer is the readout strips, where the signal is read by the electronics. This description is shown in Figure (35).

The outer bakelite surface is coated with a conductive graphite paint, where the HV and ground cables are connected, while the inner bakelite surface is coated with

Figure 35 - RPC schematic.



Legend: The RPC detector consists of two resistive material plates that enclose a gas gap. Both insulators have a conductive coating in the outermost part. The side spacer is a high-resistivity material used to create the gap between the two electrodes (121).

Source: RPC design, 2022.

linseed oil diluted in pentane (C_5H_{12}). This is necessary because any small rough point in the electrode surface can provoke an intense local field. With this solution the surface becomes smooth, suppressing this effect.

3.1.1 The Principle of Operation

The RPC has the same principle of operation as any gas detector: it relies on gas ionization when an ionizing particle passes through it. The RPCs can be operated in two different modes, streamer mode, and avalanche mode. When operating in streamer mode, the RPC efficiency decreases when the rate is high ($>200\text{Hz}/\text{cm}^2$), because the electric field is too intense and the electrode plates need tens of microseconds to get charged again (122).

A way to overcome this problem is to operate RPCs in avalanche mode. The idea is to use lower electric fields to reduce the size and charge of the avalanches that occur in the gas gap and the corresponding electrode discharged area. In this way, a consistent improvement in the rate capability can be achieved. Satisfactory results up to a rate of about $1\text{ kHz}/\text{cm}^2$ have been reported (123). For this reason, RPCs operating in avalanche mode have been proposed as the dedicated detector for the generation of the first-level muon trigger, both in CMS and ATLAS at the LHC. Both modes of operation are commented in more detail in the next sub-sections.

3.1.1.1 Streamer mode

Historically this mode of operation was the first to be used in the RPCs. In the streamer mode, the electric field inside the gas gap is intense enough so that discharges are generated inside it. Depending on the voltage at the electrodes it is possible to see two output signals: one signal that comes from the primary avalanche and a signal that comes after some time. It is well known that the higher the voltage at the electrodes the lower the time difference between these two signals, so there is a voltage at which will be not possible to distinguish between the two signals commented above. In that case, one says that the RPC is operating in streamer mode. A better way to define when the streamer mode is achieved is the following: the transition from avalanche to streamer arises when the avalanche size overcomes the Raether limit⁹ (124). A particle accelerator such as LHC that has a collision rate of 40 MHz (one collision every 25 ns) requires detectors with a good timing characteristic. This is still more relevant in the case of the HL-LHC, as the total number of collisions will increase by a factor of 10 (20). However, the rate capability obtained in streamer mode is around 100 Hz/cm² which is not adequate for the LHC. This means that the RPCs designed for this application must not operate in streamer mode. Figure (36) shows an example of a streamer signal.

3.1.1.2 Avalanche mode

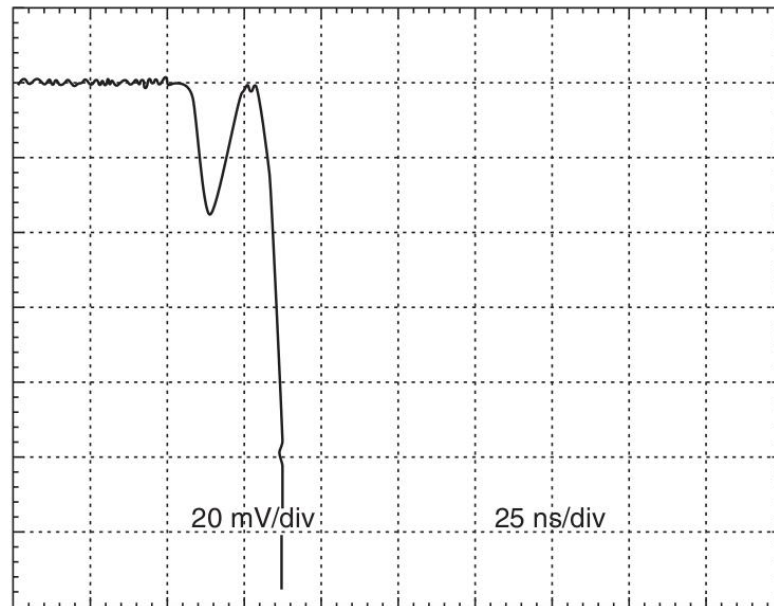
In the avalanche mode, the electric field across the gap can be considered reduced so that the RPC has a reduced charge traveling inside the gas gap, which provides a fast signal with a smaller amplitude component. This implies a higher rate capability but due to the smaller signal amplitude, it needs a robust signal amplification that is introduced at the front-end electronics. This mode of operation is adopted by the LHC experiments because it has a rate capability that copes with the LHC bunch crossing time. A typical avalanche signal is shown in Figure (37).

3.1.2 The RPC gain factor

When ionization occurs inside the RPC gas gap, an electron-ion pair is created. Due to the applied electric field inside the gap, the electron drifts toward the anode. In this way, the electron can have enough energy to produce further ionization, creating

⁹ The Raether limit says that sparks appear when the total charge in the avalanche is equal or greater than 10⁸ electrons (118)

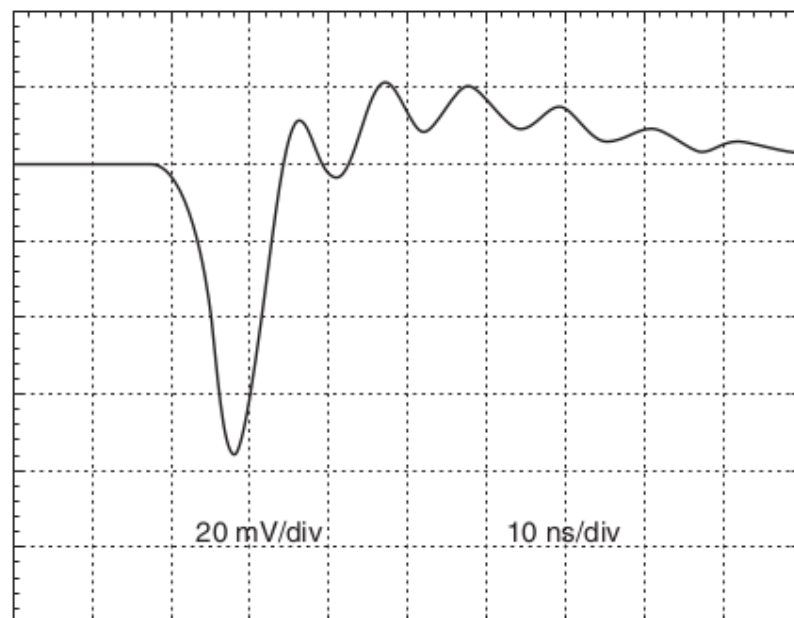
Figure 36 - The streamer signal.



Legend: An avalanche signal followed by a streamer signal.

Source: ABBRESCIA; PESKOV; FONTE, 2018, p. 64.

Figure 37 - The avalanche signal.



Legend: A typical avalanche signal for an RPC operated with argon and isobutane.

Source: ANDERSON; KWAN; PESKOV, 1994, p. 326. Adapted by the author.

more pairs. This is the process that leads to the avalanche of particles as described in the previous section. This is known as multiplication.

It is possible to categorize the multiplication process by the first Townsend coefficient (it depends on the electric field, pressure, and the nature of the gas), α , which represents the number of ionizations per unit length, and by the attachment coefficient, β , which represents the number of electrons captured by the gas per unit length. With these two coefficients defined, the number of electrons on the anode is given by

$$n = n_0 e^{\alpha - \beta x}, \quad (15)$$

where n_0 is the number of primary electrons and x is the distance between the anode and the spot where the cluster of the electrons was formed. Therefore the working mode of the RPC detector can be defined with the help of the gain factor variable

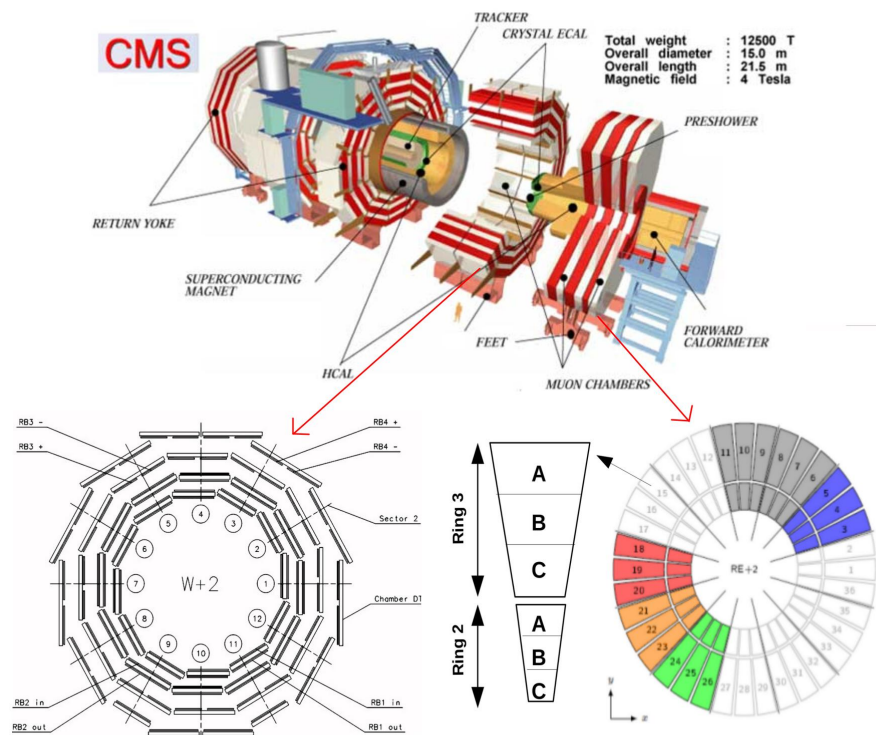
$$M = \frac{n}{n_0}. \quad (16)$$

If the value of M is lower than 10^6 , it is said that the RPC is operating in the avalanche mode, otherwise, if it is equal to or higher than the order of 10^8 , it is said that the RPC is operating in the streamer mode, that has a higher induced signal in the readout strips. Despite having higher signal amplitude the streamer mode operates with low rate capability, being suitable for low-rate experiments. In the case of the CMS RPCs, they need to operate in the avalanche mode, which has a high rate capability, allowing the RPCs to cope with the high rate of events from the LHC.

3.1.3 The CMS RPC System

The CMS RPC system contributes to the identification, reconstruction, and triggering of muons. The endcap region is divided into 8 regions, called RE \pm 4, RE \pm 3, RE \pm 2, RE \pm 1, while the barrel region is divided into 5 wheels, called W \pm 2, W \pm 1, W0. The endcap is divided into 36 sectors while a wheel consists of 4 muon stations (*RB1*, *RB2*, *RB3*, *RB4*) at the increasing radius and is divided into 12 sectors in ϕ , this description is illustrated in Figure (38). There are 1056 RPC chambers in total, covering an area of more than 3000 m². They work in double-gap mode, where each gap is 2 mm width and each copper strip readout is a plane located between the gas gaps, this is shown in Figure (39). The gas mixture used is composed of tetrafluoroethane (*C₂H₂F₄* - 95.2%), isobutane (*iC₄H₁₀* - 4.5%) and sulfur hexafluoride (*SF₆* - 0.3%) with a relative humidity of 40 – 50% (125).

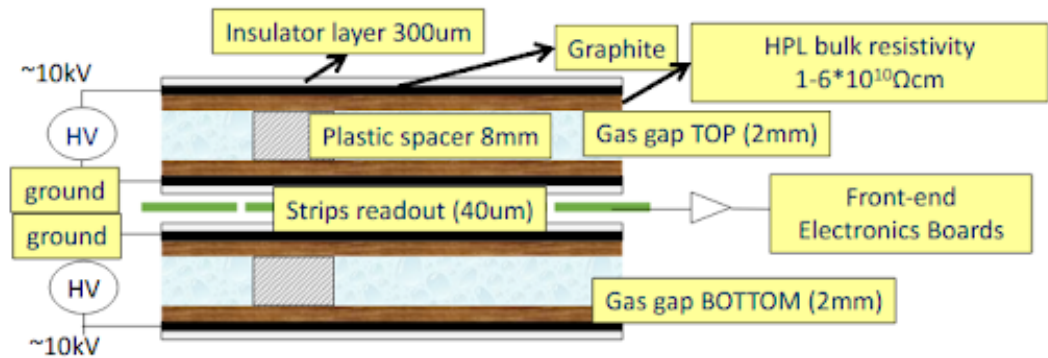
Figure 38 - Schematic of the CMS RPC System



Legend: The CMS system: (top) the entire system, showing the tracker, electromagnetic calorimeter (ECAL), hadronic calorimeter (HCAL), muon (CSC, DT, and RPC) subsystems and the 3.8 T solenoid; (bottom-left) a typical CMS-RPC wheel with its respective stations, and (bottom-right) a typical endcap station, showing ring 2 and ring 3 of RPC.

Source: FERREIRA, 2021, p. 2.

Figure 39 - Double Gap RPC



Legend: A usual CMS RPC. It is composed of two 2 mm gaps, called the bottom gap and the top gap. Depending on the location where the chamber is installed (barrel, endcap) the gaps are called by another name (see for example the RE1/1 chamber in section (3.3.3) (126).

Source: CABRERA, 2016, p. 1. Adapted by the author.

3.2 Eco-friendly gas mixtures for Resistive Plate Chambers

In this section, the difficult task of selecting the gas mixture for the RPC detector will be discussed. The main characteristics that the gaseous mixture used will be commented on. Then, an introduction to the eco-friendly gas mixtures for the RPC will be given followed by the results obtained in 2021 at the GIF++ facility.

3.2.1 Choice of gas mixtures

The choice of the gas mixture for an RPC detector is one of the most delicate issues. It is very important to find the right mixture in the sense that the detector must operate with high efficiency and with certain well-defined properties. These properties are listed in the topics below.

- It should provide a high density of primary ion-electron clusters. This property assures high detection efficiency that depends on the particle energy deposition calculated by the Bethe-Bloch equation, the average atomic number, the gas mixture density, and the potential ionization of the gas mixture used (118).
- It should have high electronegativity. This is necessary to improve the charge localization, as the gas will capture more electrons and prevent a high multiplication process (127).
- It should have low photon emission and/or transmission. In other words, it should

be a quenching mixture, allowing the reduction of the photon feedback phenomena.

- It should be not dangerous for human health.
- The chemical reactions that occur inside the gaps should produce a limited amount of aggressive components. One of the known elements is Hydrofluoric Acid (HF) which may attack the chamber and its components.
- This point is very important for the RPC operation because the aging of its components can bring many problems during the RPC operation. This will be discussed in the section (3.4).
- The gas mixture should not be aggressive to the environment, *i.e.*, it should have low global warm potential (GWP) and a negligible ozone depletion power (ODP). GWP refers to the amount of energy the emission of 1 tonne of a gas will absorb given a period of time, with respect to the emissions of 1 tonne of carbon dioxide. This means that CO₂ has GWP 1 and the other gases are compared with this reference. Therefore the larger this measure, the more the gas has the capacity to warm the earth compared to the CO₂. ODP is a measure of the reduction of the ozone layer in the atmosphere. The reduction of this layer increases the radiation on the earth's surface, which can contribute to climate changes (128).

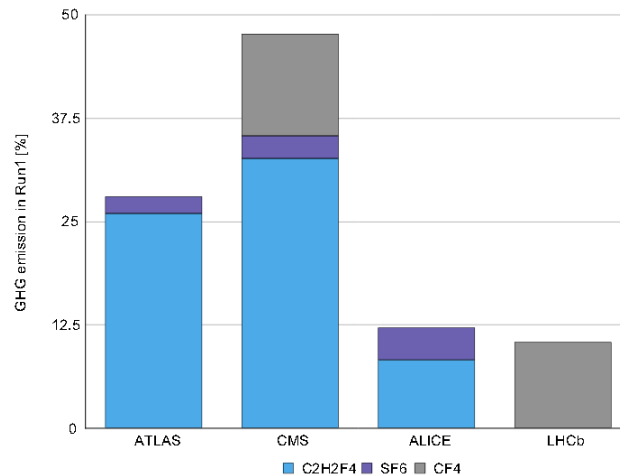
The current gas mixture of the RPC is ozone friendly, *i.e.*, it does not represent risks to the ozone layer. On the contrary, the main gas component, tetrafluoroethane (C₂H₂F₄) has a GWP of around 1,430. Besides that, it is worth mentioning that the sulfur hexafluoride (SF₆), despite its low concentration in the RPC gas mixture, has a GWP of around 22,800. In view of this, the European Community applied some regulations to ban some applications of the use of gas mixtures with GWP greater than 150. Despite the scientific communities being out of this regulation, some of them are pushing the experiments that work with these mixtures to reduce their use.

3.2.2 Greenhouse Gases Emissions at CERN

Greenhouse gas (GHG) emissions at CERN come from different experiments and facilities. In 2018 there were 192,000 tonnes of CO_{2e}, where the LHC experiments contributed to 92% of this emission. The main GHG used at the LHC experiments for particle detection is 1,1,1,2 - tetrafluoroethane (C₂H₂F₄) (78%), commercially known as R134a with GWP of 1430. This gas is largely used in the RPC system of the main experiments, ALICE, ATLAS, and CMS. This is followed by CF₄ (15%) with GWP 7390 and SF₆ (8%) with GWP 22800. Followed by the LHC experiments - particle detection, the rest

of the contribution to the GHG emissions are LHC experiments - detector cooling, other experiments, heating (gas and fuel), and electrical power consumption. Figures (40) and (41) show the GHG emissions in the large LHC experiments and in the subdetectors of these experiments during Run 2 respectively.

Figure 40 - GHG emission in Run 2 for the big LHC experiments.



Legend: As explained before C₂H₂F₄ is the main contribution. Also, it is worth mentioning that CMS is the main responsible for the GHG emission (129).

Source: CAPEANS; GUIDA; MANDELLI, 2017, p. 2.

3.2.2.1 European Union gas regulation

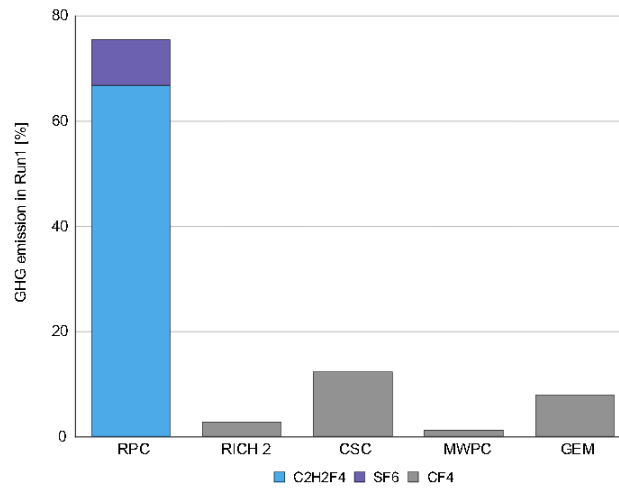
It is worth mentioning that the European Union is with a campaign to regulate the emission of Fluorinated gases (F-gases). This regulation comprises three points:

- The total amount of F-gases that can be sold in Europe should be reduced: In 2030 it should be one-fifth of what it was in 2014.
- The activities where the use of alternative gases are available can not use F-gases, *i.e.* the use of F-gases in such applications is banned.
- Equipment that still uses F-gases must have adequate maintenance to prevent the emissions of F-gases.

In principle, scientific collaborations are not directly affected by such regulations. However, these regulations imposed by the European Union can increase the prices and put in doubt the availability of the F-gases, which means that the reduction of the use of C₂H₂F₄ is fundamental for future applications as well as for the next LHC runs. In fact, Figure (42) shows this impact on the LHC runs.

To conclude this section, it is worth mentioning that the CERN collaborations are working in two scenarios: a short-term one, in view of the reduction of the emission

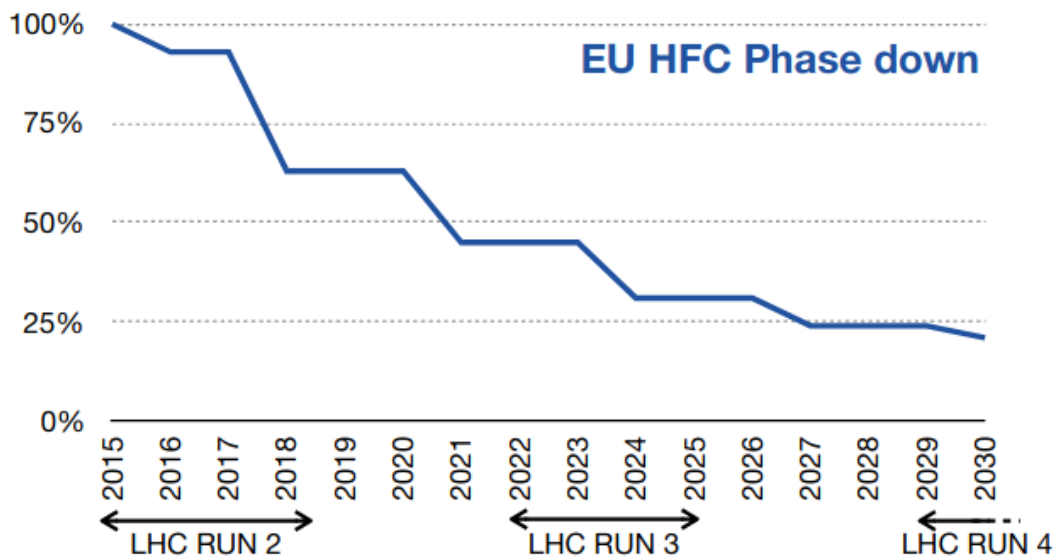
Figure 41 - GHG emission in Run 2 for the sub-detectors.



Legend: Note again that C₂H₂F₄ contribution is much higher than the other gases.

Source: CAPEANS; GUIDA; MANDELLI, 2017, p. 2.

Figure 42 - Reduction of F-gases in LHC Runs.



Legend: Since the beginning of Run 2 the availability of F-gases is going down. Around 2030, during LHC Run 4, the total amount should be around 25% of the total (130).

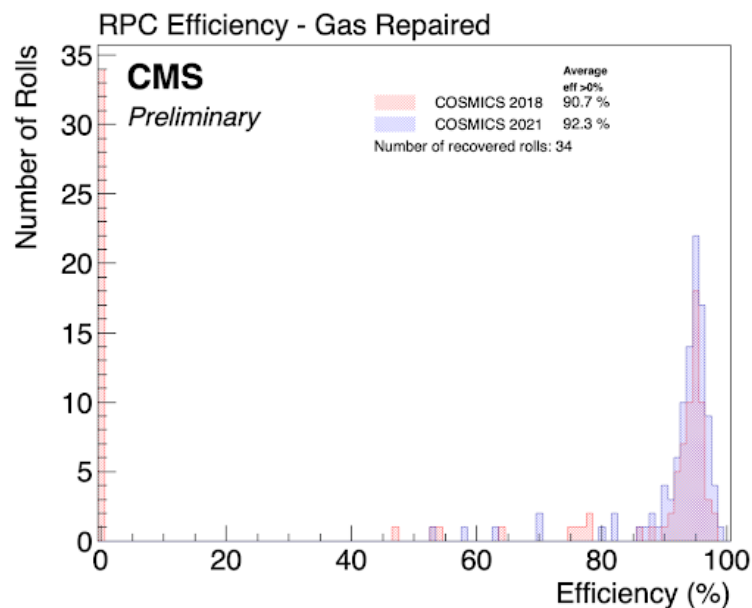
Source: EU HFC Phase Down, 2022.

of such gases, and in a middle/long-term one, the complete replacement of such gases, mainly $C_2H_2F_4$. In the next section, the strategy of reduction of $C_2H_2F_4$ adopted by the CMS-RPC collaboration is explained.

3.2.3 RPC Leak Repairs in Long Shutdown 2

During the LHC Long Shutdown¹⁰ 2 (LS2) the activity with the highest priority was the RPC gas system consolidation. Two main activities were done: Fixing of leaks and installation of a recuperation system for freon. In the barrel region, 49 out of 99 gas leaky RPCs were repaired. There, where possible, the gas connection was modified to the leaky chambers, where the leak rate was around 900 l/h. The impact of this maintenance can be seen in the increase in efficiency. During COSMICS¹¹ 2018, the average efficiency (considering values greater than 0%) was 90.7%, while after the maintenance in LS2, it was found to be 92.3%. Figure (43) shows the scenario commented.

Figure 43 - Gain in the efficiency after gas leaky repairs.



Legend: Comparison of the efficiency between COSMICS 2018 and COSMICS 2021 for the barrel chambers that were repaired during LS2. The total number of rolls recovered is 34 meaning 1.6% in efficiency gain (132).

Source: FERREIRA, 2021, p. 3.

¹⁰ Long Shutdown is a period in which the operation in the LHC accelerator complex stops for maintenance and consolidation of all equipment and upgrade (131)

¹¹ Cosmics runs in the CMS detector

Besides that, some actions have been taken to reduce the amount of gas delivered to the atmosphere. The expected conditions during Run 3 include turning off all leaking chambers, as well as, no leaking chambers that are connected to leaking chambers (this corresponds to 6% of the system), reducing the leak rate to 200 l/h, and restoring some amount to the exhaust (around 1000 l/h). Finally, a recuperation system for $C_2H_2F_4$ with an efficiency of 80% is now installed to receive 1000 l/h. This system works in three phases as described in items *a*, *b*, and *c* and as highlighted in Figure (44).

a. Phase 1: Removal of N_2 and SF_6

In the first phase, the gas mixture cools down at $\approx -35\text{ }^\circ\text{C}$. Here R134a and iC_4H_{10} go to liquid phase together, while N_2 , SF_6 , iC_4H_{10} losses, and R134a losses remain vapour. In the end, N_2 and SF_6 are removed by simple distillation.

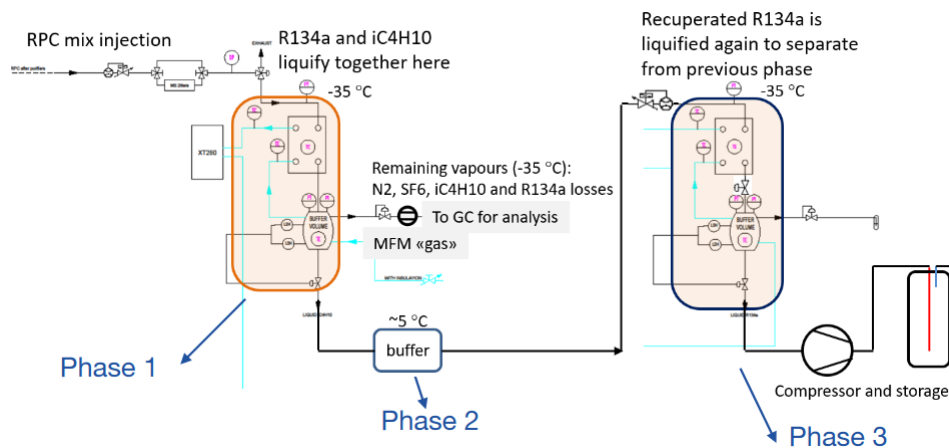
b. Phase 2: Detachment of R134a from iC_4H_{10}

In this phase, the remaining mixture is submitted in a buffer at $\approx 5\text{ }^\circ\text{C}$. With the increase of the temperature iC_4H_{10} becomes vapor again, returning to buffer 1 while R134a goes to buffer 2.

c. Phase 3: Compression and storage of R134a

In this phase, the remaining R134a is cooled down at $\approx -35\text{ }^\circ\text{C}$ again to separate from the previous phase. Finally, it is performed a compression of R134a to the storage place. The whole process has an efficiency of $\approx 80\%$.

Figure 44 - Schematics of the $C_2H_2F_4$ (R134a) recuperation system.

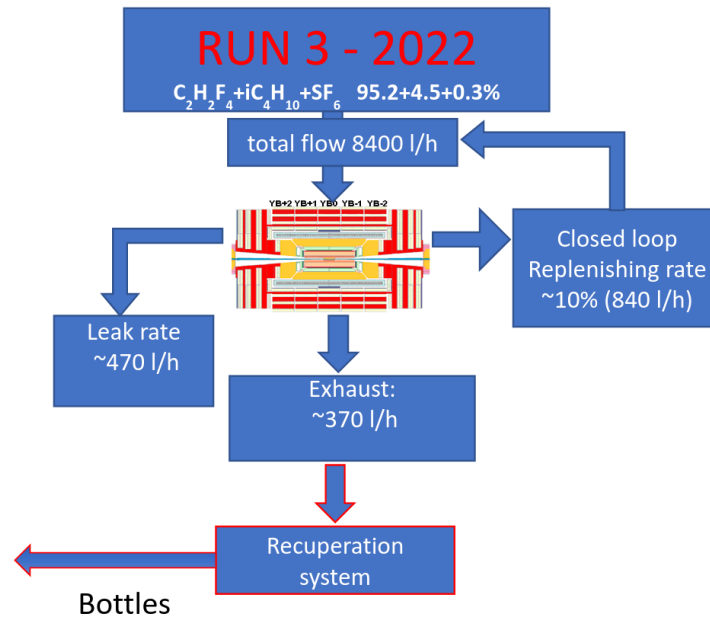


Legend: Schematic of the $C_2H_2F_4$ (R134a) recuperation plant. The three phases are highlighted, phase 1: Removal of N_2 and SF_6 ; phase 2: Detachment of R134a from iC_4H_{10} ; phase 3: Compression and storage of R134a (133).

Source: CORBETTA, 2021, p. 112.

The total flow for all systems is 8400 l/h, corresponding to an increase of 10% with respect to Run 2, because of the increase in luminosity. Figure (45) shows the strategy for Run 3.

Figure 45 - CMS-RPC gas recuperation system.



Legend: Gas recuperation system. Now instead of throwing all the gas into the environment a percentage of it is recovered.

Source: FERREIRA, 2021, p. 4.

3.2.4 CO₂-tetrafluoropropene based gas mixtures

The search for an eco-friendly gas replacement started in the last decade when the review of possible gas present on the market was investigated (134). This study analyzed various gas parameters such as stopping power, radiation length, and ion pair production.

The stopping power can be defined as the average energy loss per unity length. In turn, the radiation length (X_0) of a material can be defined as the distance at which the electron energy is reduced by a factor $1/e$ due to radiation loss only. Figures (46) show a summary of refrigerant candidates.

The idea of finding a candidate for $C_2H_2F_4$ replacement is to find a molecule as similar as possible to it with an acceptable GWP. Some studies in the laboratory started, where the main candidate to replace $C_2H_2F_4$ belongs to the family of the HydroFluoroOlefin (HFO). In particular, the molecule $C_3H_2F_4$ (Tetrafluoropropene) differs from it by only one carbon. It has two allotropic forms, HFO-1234yf and HFO-1234ze with GWP of 4 and 6 respectively. The former was found to be flammable while the second was not and therefore chosen to be a candidate. As it is not too electronegative it can not replace SF_6 . Several tests have been performed at CERN to understand if HFO could replace R134a. At first, it was noted that the total replacement of R134a with HFO in the gas mixture brought the working point of the detector up, consequently, the detector was operating at lower efficiency. The solution found was to use CO_2 together with HFO to

Figure 46 - Various refrigerant candidates.

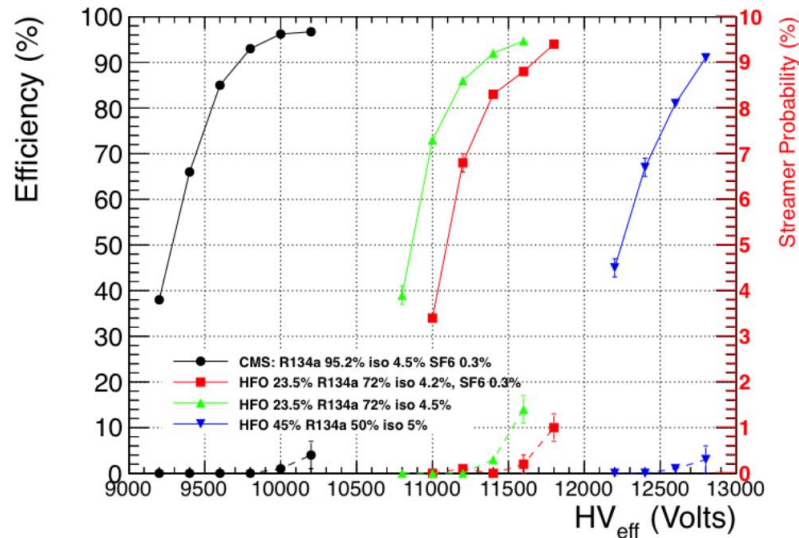
Molecular name	Chemical formula	CAS	Refrigerant identifier	GWP	ODP
Chloropentafluoroethane	C_2ClF_5	76-15-3	R115	7370	0.44
Hexafluoroethane	C_2F_6	76-16-4	R116	-	-
2,2-Dicloro-1,1,1-trifluoroethane	$C_2HCl_2F_3$	306-83-2	R123	120	0
1-Chloro-3,3,3-Trifluoropropene	$C_3H_2ClF_3$	2730-43-0	R1233zd	4.7-7	0
2,3,3,3-Tetrafluoropropene	$C_3H_2F_4$	754-12-1	R1234yf	4	0
1,3,3,3 Tetrafluoropropene	$C_3H_2F_4$	29118-24-9	R1234ze	6	0
Trifluoroiodomethane	CF_3I	2314-97-8	R131I	0.4	0.01-0.02
1,1,1,2-Tetrafluoroethane	CH_2FCF_3	811-97-2	R134a	1430	0
Tetrafluoromethane	CF_4	75-73-0	R14	7390	0
1,1,1-trifluoroethane	CH_3CF_3	420-46-2	R143a	4300	-
1,1-Difluoroethane	$C_2H_4F_2$	75-37-6	R152a	124	0
Octafluoropropane	C_3F_8	76-19-7	R218	-	-
Propane	C_3H_8	74-98-6	R290	3	0
Difluoromethane	CH_2F_2	75-10-5	R32	650	0
Isobutane	C_4H_{10}	75-28-5	R600a	3	0
Sulfur Hexafluoride	SF_6	2551-62-4	R7146	23000	0.04
Carbon Dioxide	CO_2	124-38-9	R744	1	0
Octafluorocyclobutane	C_4F_8	115-25-3	R318	-	-
Pentafluoroethane	HF_2CF_3	354-33-6	R125	3400	0
Trifluoromethane	CHF_3	75-46-7	R23	0	0
R409:	$CHClF_2$	75-45-6 2837-89-0 75-68-3	R22 (60%), R142b (25%), R124 (15%)	1700-620	0.5/0.065/0.02
R407c:	CH_2F_2 , CF_3CHF_2 , CH_2FCF_3	75-10-5, 354-33-6, 811-97-2	R32 (21-25%), R125 (23-27%), R134a (50-54%)	650 3400 1430	0 0 0

Legend: The acronym CAS refers to Chemical Abstracts Service, which is a division of the American Chemical Society, which can be understood as a registry number. The refrigerant identifier is the commercial name of the gas. The main information concerning the impact of the gas on the environment is given by the GWP and ODP.

Source: SAVIANO, et al., 2018, p. 3. Adapted by the author.

reduce the gas density, requiring lower voltage to operate with safety (135). Figure (47) shows four different scenarios, one with the standard gas mixture used, one with CO_2 , and two with both CO_2 and HFO. Note that the more the CO_2 with respect to HFO, the lower the Working Point (WP) of the detector.

Figure 47 - Comparison of different gas mixtures in an RPC.



Legend: Efficiencies (solid line) and streamer probability (dashed line) versus effective voltage for CO_2 based mixtures. Note that the increase of CO_2 percentage with respect to HFO brings the efficiency curve to the left.

Source: ABBRESCIA, et al. 2016, p. 4.

Therefore, this study indicated that the CO_2 -tetrafluoropropene-based gas mixtures would be a good candidate for future operation.

3.2.5 The Ecogas Collaboration

In view of finding a good candidate for the current RPC gas mixture a joint collaboration was set up in 2019. The main detectors collaborations at LHC, ALICE, ATLAS, CMS, and LHCb as well as the CERN gas group from the Experimental Physics and Detector Technologies (EPDT) started a collaboration, with the goal of studying the RPC performance with eco-friendly mixtures under irradiation at the Gamma Irradiation Facility (GIF++) (136).

3.2.6 The Gamma Irradiation Facility

The Gamma Irradiation Facility (GIF++) (137) is a unique facility that combines a 14 TBq ^{137}Cs source with a high energy particle beam from the secondary Super Proton Synchrotron (SPS) beamline H4¹² in CERN Prévessin site.¹³ The secondary beam line H4 is produced from the collision of the primary beam from SPS onto the T2¹⁴ target. It can be a pion or muon beam, where the particle beam momentum is between 10 GeV/c and 450 GeV/c, selected using six dipole magnets. The beam energy is not fixed as it depends on the settings defined in the primary beam line. The GIF++ irradiation bunker is divided into two regions, called upstream (30 m²) and downstream (70 m²), where each region can receive a specific radiation dose regardless of the dose of the other region.

Many detectors from different LHC experiments are tested at the facility: CMS Cathode Strip Chambers (CSC), CMS Drift Tubes (DT), CMS Gas Electron Multiplier (GEM), ATLAS Micro-Megas, ATLAS small-diameter Monitored Drift Tube (sMDT), and RPCs from ATLAS, CMS and Ecogas collaborations, and so forth. The area outside the bunker is called *preparation area* and is used to prepare and test the detectors before installing them in the bunker. Besides that, GIF++ has a two-floor area for hosting electronic and gas services. Figure (48) shows the GIF++ facility.

3.2.7 Ecogas Collaboration Setup at GIF++

The ecogas setup at GIF++ is composed of chambers from ALICE, ATLAS, EPDT, CMS, and LHCb/SHiP. Each detector has its own technology, that is each RPC has its own bakelite material, gap width, electronics, etc. The gas system has its own rack that feeds the gas for all detectors, while the electronics will depend on the detector.

3.2.7.1 Gas System

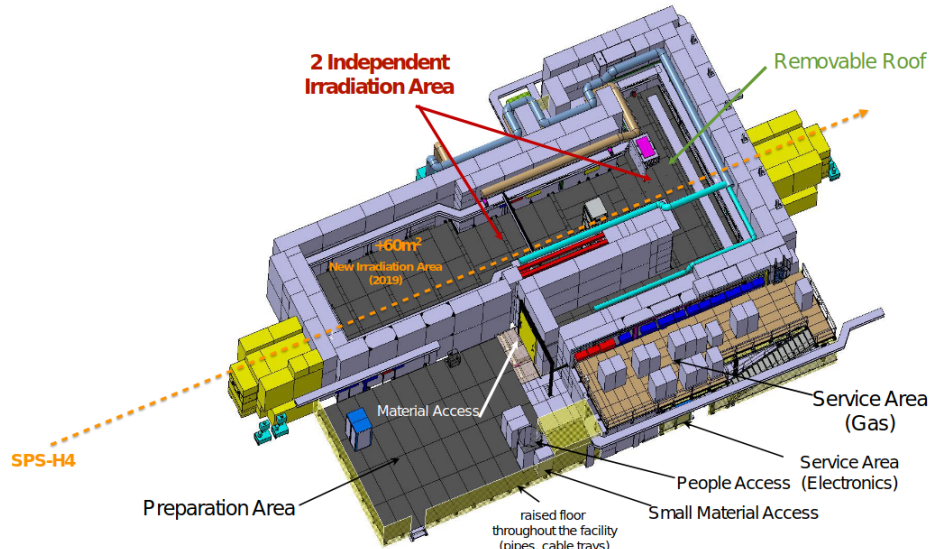
The gas system is installed at the GIF++ service zone on the second floor. The system has a mixer that creates the gas mixture and a humidifier that is responsible for sending a humidified mixture to the detectors. Two racks are used for the gas system, where the main components of the setup are the Mass Flow Controllers (MFC), which are responsible for sending the right gas mixture and controlling the mass flow of the mixture.

¹² This beamline was designed to provide beams of hadrons, electrons, muons, and ions

¹³ Nowadays, due to the radioactivity activity this value resides around 12 TBq

¹⁴ T2 is a target used to produce the secondary beams to GIF++ facility

Figure 48 - GIF++ facility



Legend: 3D view of GIF++ facility. There are two independent irradiation areas with around 105 m², a preparation area, and two service areas: gas and electronics. The orange dashed line represents the muon beamline (138).

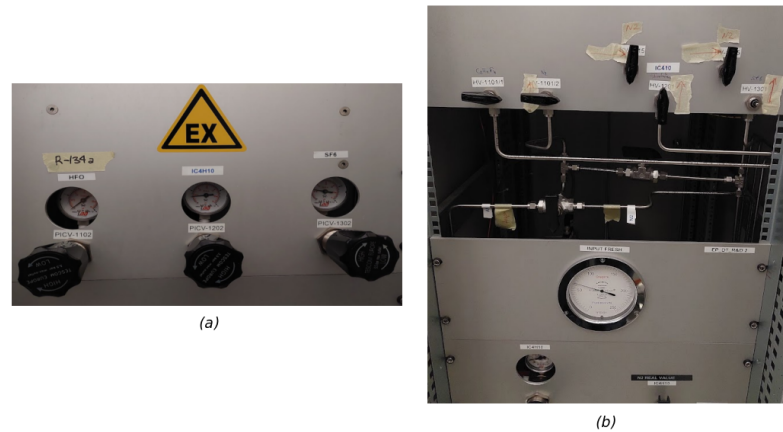
Source: GKOTSE, et al., 2021, p. 20.

Four different MFCs are used, one for each gas, CO₂, HFO, iC₄H₁₀, and SF₆. Besides that, there are two other MFCs that are installed just after the mixer to control the humidity. They are split into two gas lines, where one of the additional MFCs is used to send the dry gas mixture, while another one is used for injection of the gas into a water reservoir, where just after is installed a bubbler, that indicates if there is gas or not. The two lines are later merged together and the humidity of the gas is measured with a Dew point analyzer. This analyzer sends a current signal that is read by a device that is connected to a computer. Finally, all MFCs are controlled by a dedicated software installed on this computer, called FlowDEE. There, it is possible to set the proper gas mixtures that go to the detectors, controlling their volume, percentage, flow, and humidity. In the bunker, there is a common input line that is split to the detectors by using dedicated flow rotameters. The ecogas gas rack is shown in Figure (49).

3.2.7.2 Monitoring and controlling

The monitoring is done with grafana (139), which is open-source software designed for the monitoring and visualization of data. The grafana dashboard is designed for quick monitoring of the system, as well as to spot potential issues on the gas, as the system reads the environmental parameters through data interchange protocol (DIP). The control of

Figure 49 - Ecogas gas rack.



Legend: (a): From left to right, main rotameters for HFO, iC_4H_{10} and SF_6 . (b): From left to right, control valves for $C_2H_2F_4/HFO$, N_2 for purging the gas line, iC_4H_{10} and SF_6 .

Source: The author, 2023.

the detectors is made either manually by connecting to the CAEN mainframe with telnet protocol or with the WebDCS software (140). WebDCS is a software developed by the CMS-RPC group to control and perform data taking with the detectors. By using it is possible to access the CAEN library to perform any type of data taking with the detectors.

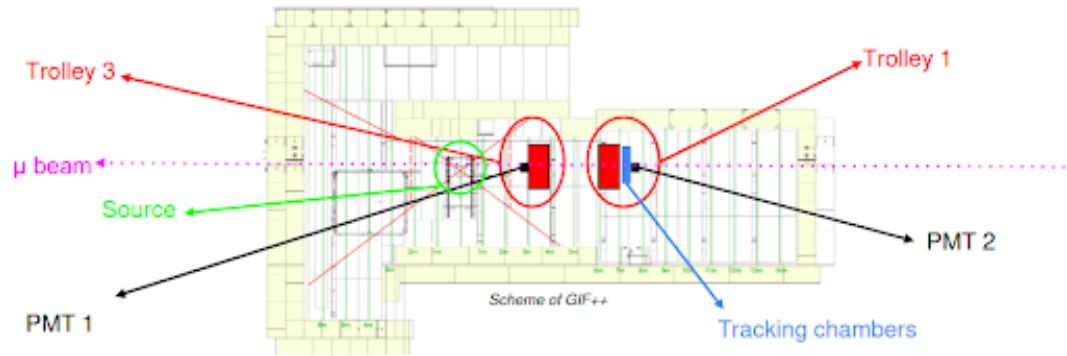
3.2.7.3 Detectors

The detectors are housed in two trolleys named Trolley 1 and Trolley 3. They are located about 6 m and 3 m from the source respectively. Figure (50) shows a schematic of the position of the trolleys in the bunker and Figure (51) shows a picture of the GIF++ facility highlighting the position of the gamma source, trolleys, and beamline.

3.3 Ecogas results at GIF++

This section is dedicated to the discussion of the results obtained by the Ecogas collaboration at GIF++ in 2021. The author of this thesis actively participated in all steps of these results, including the planning of the activities, operation, shifts, coordination, analysis, and discussions. As the author is a CMS collaborator only CMS chamber results are presented.

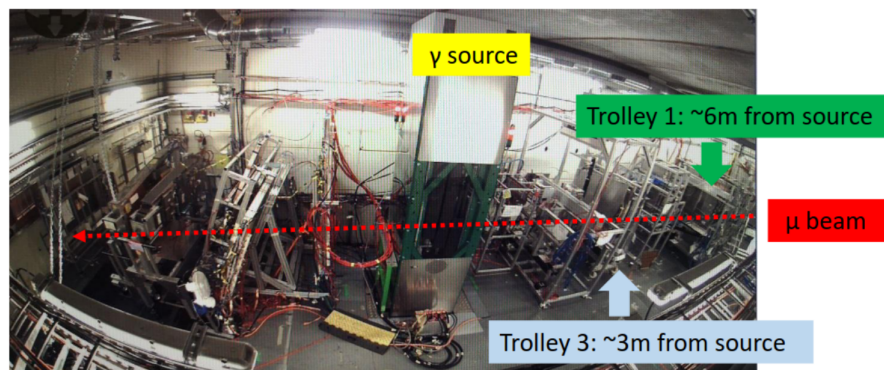
Figure 50 - Ecogas detectors position in GIF++ bunker



Legend: Two different trolleys are used to house the chambers, where the trolley closer to the source is trolley 3.

Source: The author, 2023.

Figure 51 - GIF++ setup



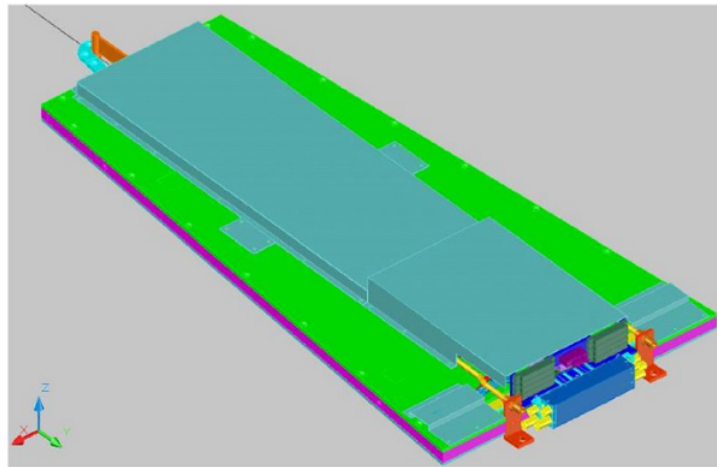
Legend: The picture shows the GIF++ facility and highlights the position of both trolleys, the gamma source, as well as the beamline.

Source: The author, 2023.

3.3.1 Chamber Description and Experimental Schematic

The CMS chamber used in the data taking is a prototype endcap chamber of the type RE1/1, named RE1/1/001. Before being used by ecogas collaboration this chamber has been tested at CMS forward region ($1.6 < \eta < 2.1$) with rates beyond 1 kHz/cm^2 (141). It is a typical trapezoidal CMS endcap chamber with the usual CMS RPC technology. The chamber is housed in Trolley 3. Figure (52) shows the model of the chamber.

Figure 52 - RE/1/001 chamber



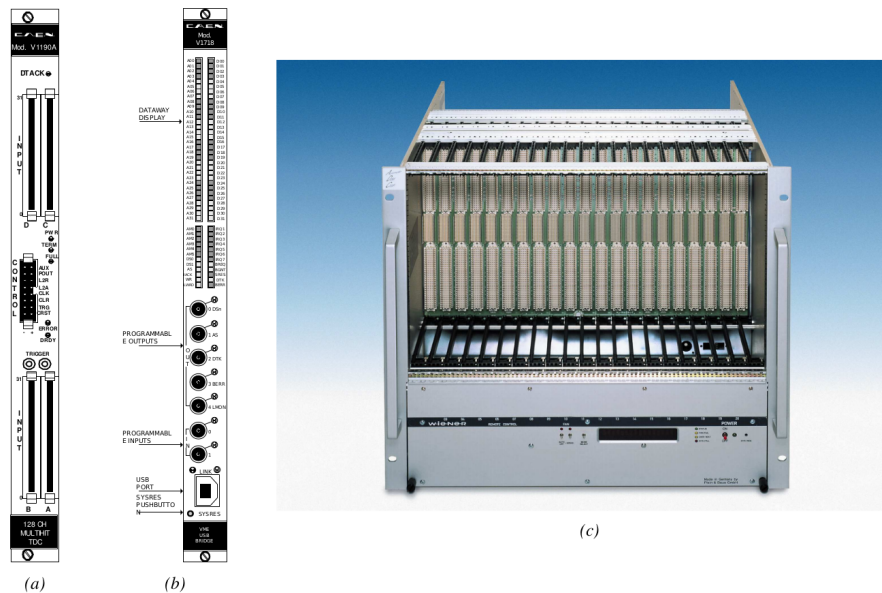
Legend: The RE/1/001 chamber with trapezoidal shape.

Source: PARK, et al., 2009, p. 2.

3.3.2 Software and Data Acquisition

As mentioned in section (3.2.7.2) the software used for the detector control is WebDCS. The data acquisition is performed using a CAEN Time-to-Digital Converter (TDC) module of type V1190A (142). This TDC is a 1-unit wide VME 6U module with 128 Multi-Hit/Multi-Event independent time to digital conversion channels. This module houses four 100 ps TDC chips developed by CERN/ECP-MIC Division (140). The detector signal output is connected to its channel and a V1718 VME master module is responsible for the communication between the computer, which is running the WebDCS, and the TDC, where the communication is done with a Universal Serial Bus (USB). To host the VME and the TDC a 6U VME 6021 crate is used. Figure (53) shows the three components and Figure (54) shows the connection diagram of the data acquisition system and of the power system in the chamber.

Figure 53 - Data Acquisition system at GIF++



Legend: (a) Front of CAEN TDV V1190A module. (b). Front of V1718 Bridge module. (c) Front of 6U 6021 VME crate responsible.

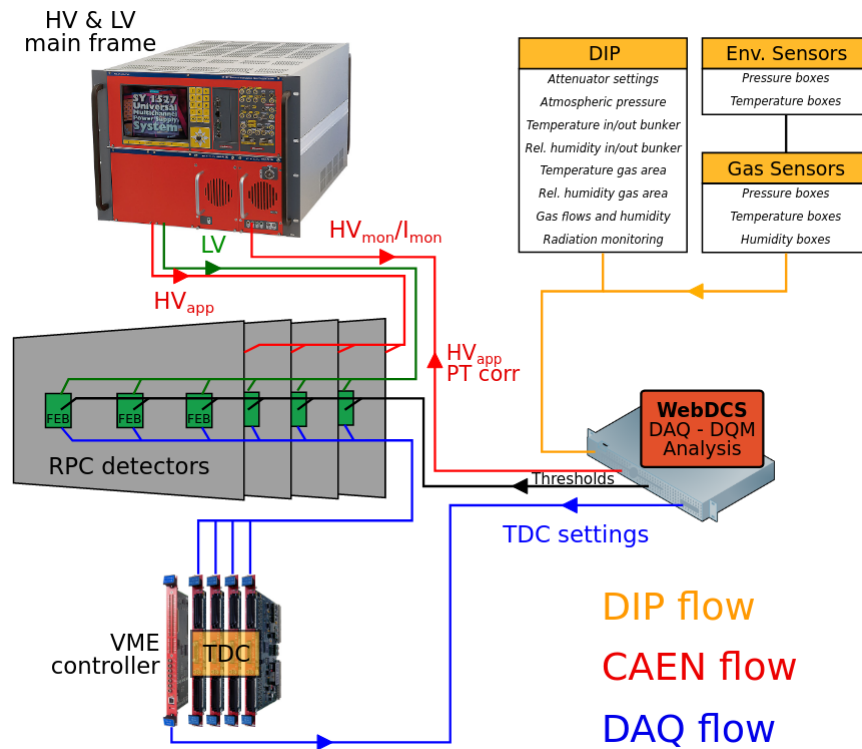
Source: CFAGOT, 2020, p. 221.

3.3.3 Experimental Conditions

During 2021 four time slots were dedicated to data taking with the gamma source and muon beam at GIF ++, which are called test beams. The RE1/1 chamber was used in three slots: September, October, and November. Besides the standard gas mixture, two ecogas mixtures have been used, they are called Ecomix-2 (tested in September and October) and Ecomix-3 (tested in October). Both mixtures are composed of the same components but with different concentrations. Table (8) shows both ecogas mixtures used as well as the CMS standard gas mixture.

The chamber is installed at Trolley 3 (see Figure (50)) at a distance of approximately 3 meters from the source. The chamber is composed of two 2 mm Pampla Bakelite gaps. The two gaps are divided into three layers. The first layer is composed of the larger gap, called the bottom gap (BOT). The second and third layers are divisions of the top gap (TOP), which are called Top-Narrow (TN) and Top-Wide (TW). Three high-voltage channels are used to provide the electric field inside the gaps, one for each gap. This configuration is good in the sense that if one gap has high voltage problems it does not affect the other two. Two gas lines are used to circulate the gas inside the chamber. There is one line for TW and TN and one for BOT). Around 1.2 liters of chamber volume is circulated inside each gap to provide good gas circulation. The chamber is composed of 128 readout strips, which are divided into four sectors of 32 strips. One CMS-RPC front-end electronics is dedicated to reading the signal of each sector *i.e.*, each set of 32

Figure 54 - Connection diagram



Legend: The data acquisition system is installed in a computer that runs the WebDCS software. Note that the DIP parameters and the environmental parameters are read by this system as well. The power system is provided by the HV & LV main frame.

Source: CFAGOT, 2020, p. 127.

Table 7 - Ecogas mixtures used in RE1/1 at GIF++

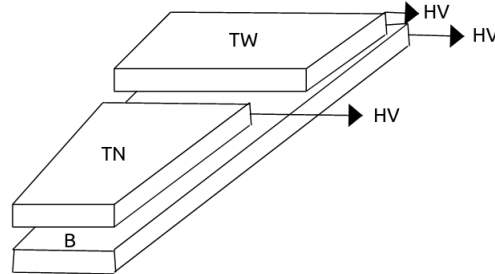
Mixture	Component 1	Component 2	Component 3	Component 4	GWP
Standard gas	C ₂ H ₂ F ₄ (95.2%)	i-C ₄ H ₁₀ (4.5%)	SF ₆ (0.3%)	Not present	≈ 1230
Ecomix-2	HFO (35%)	CO ₂ (60%)	i-C ₄ H ₁₀ (4 %)	SF ₆ (1%)	≈ 230
Ecomix-3	HFO (25%)	CO ₂ (69%)	i-C ₄ H ₁₀ (5%)	SF ₆ (1%)	≈ 230

Legend: Mixtures tested during the test beams. Note that ecomix-2 and ecomix-3 have approximately a GWP of 230, around 5 times lower than the one for the standard gas mixture. Another difference between the ecogas mixtures and the standard gas mixture is the number of gas mixtures used, which is three for the standard gas mixture and four for the ecological mixtures. Besides that, the main difference between the ecological mixtures is the difference between HFO and CO₂. There is also a 1% difference in i-C₄H₁₀ mixture, which can provide better quenching properties for ecomix-3.

Source: The author, 2023.

strips provides the signal for dedicated front-end electronics. Figures (55) and (56) show the gaps distribution and the distribution of the partitions respectively.

Figure 55 - RE1/1 gaps distribution



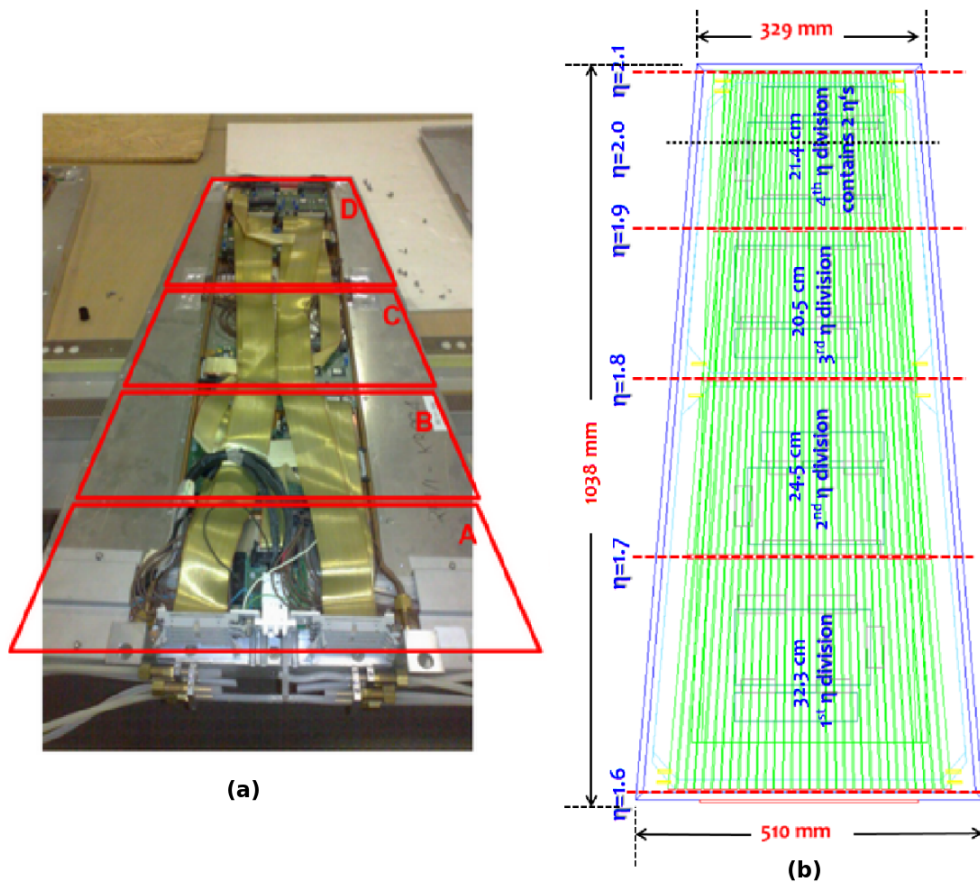
Legend: The RE1/1 chamber has three gap partitions: Bottom (BOT), Top-Narrow (TN), and Top-Wide (TW) (143).

Source: LEE, et al., 2016, p. 2.

During all beam tests, the chamber position was not changed in order to get the same beam conditions. Unfortunately, concerning the gamma source radiation, the conditions can not be the same for all measurements. Even with the chamber at the sample place, other experiments with setups inside the GIF++ bunker are constantly changing the spacial configuration, moving/installing their detectors. As the gammas interact with the matter more than muons, these changes inside the bunker can slightly modify the results with respect to the gamma rate. However, it is worth mentioning that during the different periods of data taking, no big modification has been carried out inside the bunker. Figure (57) shows the chamber installed in the GIF++ bunker.

The gamma source has two identical attenuation systems, which control the flux of radiation of each region (upstream and downstream). This means that the flux of radiation can be different at the same time in the two regions. One of the attenuation systems consists of one angular correction filter (Fe), which provides a constant distribution of photons over large detectors and six absorption filters. There are 24 possible attenuation factors (or Absorption Factor (ABS)), which are obtained with the combination of each filter: A, B, and C (For each region). Figure (58) shows the source, as well as the absorption factor combinations, and Table (8), shows the possible attenuation factors that can be obtained with the combination of each filter.

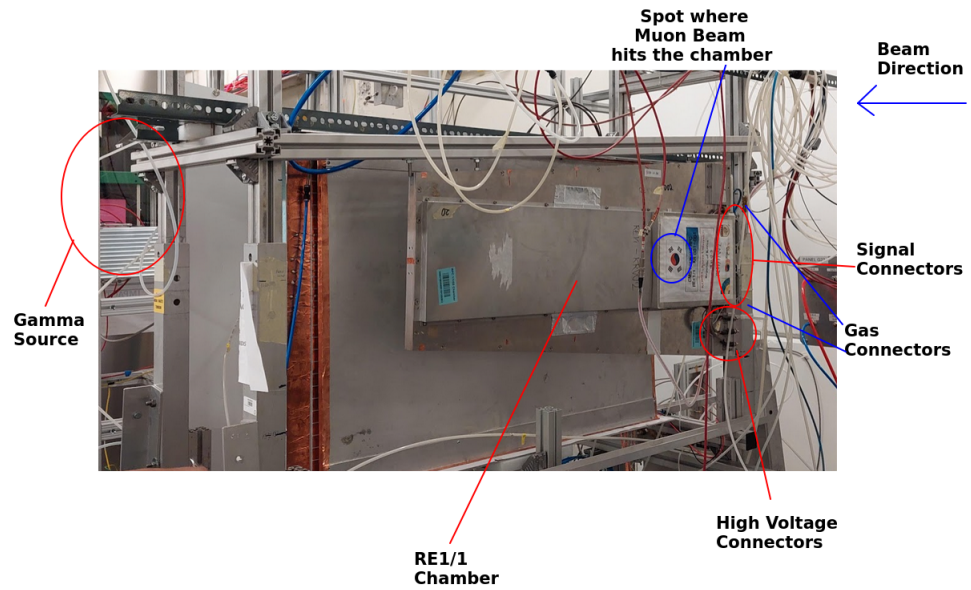
Figure 56 - RE1/1 partitions.



Legend: (a) During the data taking at GIF ++ the partitions are called A, B, C, and D.
 (b) Chamber with its dimensions. Note that each partition has been designed to fulfill η requirements in CMS. Each partition provides the signal for a dedicated CMS RPC Front-End electronics.

Source: LEE, et al., 2016, p. 2. Adapted by the author.

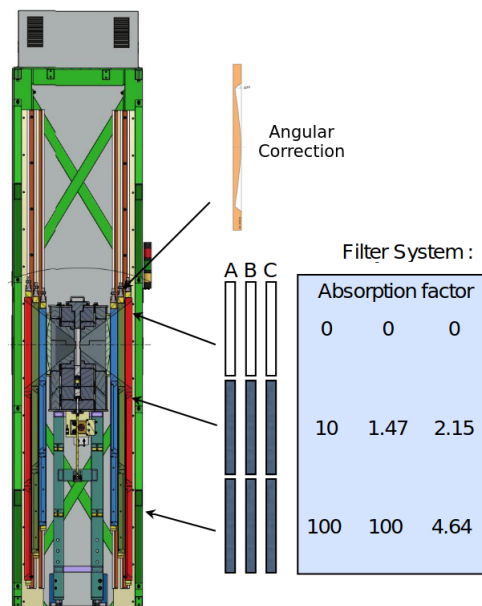
Figure 57 - RE1/1 installed in the bunker.



Legend: The chamber is installed in trolley three. Note that the center of the beam hits partition C. The gamma source is on the left while the muon beam comes from the right.

Source: The author, 2023.

Figure 58 - Gamma source and its filters



Legend: Each absorption filter is composed of three different numbers.

To get the final attenuation factor it is necessary to multiply the values of each filter as illustrated in Table (8)

Source: GKOTSE, et al., 2021, p. 21. Adapted by the author.

Table 8 - All possible gamma source attenuation factors

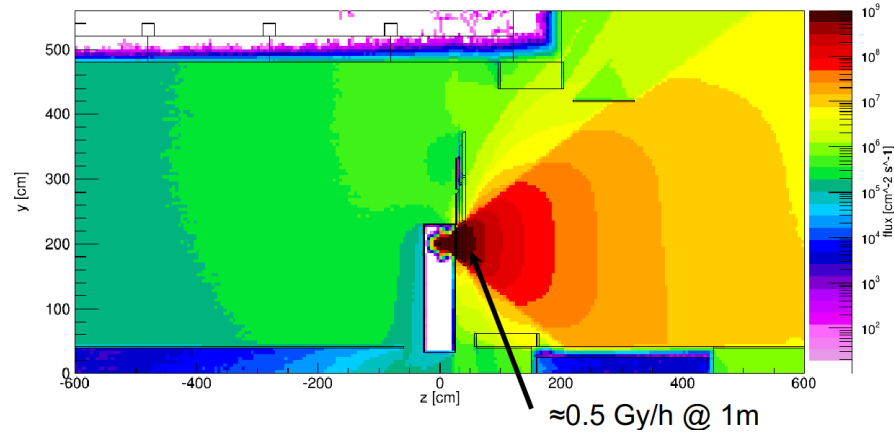
1	21.54	464.2
1.47	31.62	681.3
2.15	46.42	1000
3.16	68.12	2154
4.64	100	4642
6.81	146.8	10000
10	215.4	21544
14.68	316.2	46415

Legend: The 24 possible attenuation factors, where the lowest value provides the highest photon flux and the greatest value provides the lowest photon flux. Each number in this table is obtained by a different combination of filters A, B, and C. The final attenuation value is given by the multiplication of the value of each filter (Comment: If a filter is 0, then it is considered as 1 in the multiplication)
 Examples: to get 1 A, B, and C are 0, 0, 0; to get 6.81, A is 0, B is 1.47 and C is 4.64.

Source: The author, 2023.

As mentioned before the detector is installed about 3 meters from the source, therefore the photon flux without filters is between $10^8 \text{cm}^{-2}\text{s}^{-1}$ and $10^7 \text{cm}^{-2}\text{s}^{-1}$ as shown in Figure (59).

Figure 59 - Photon flux in the bunker



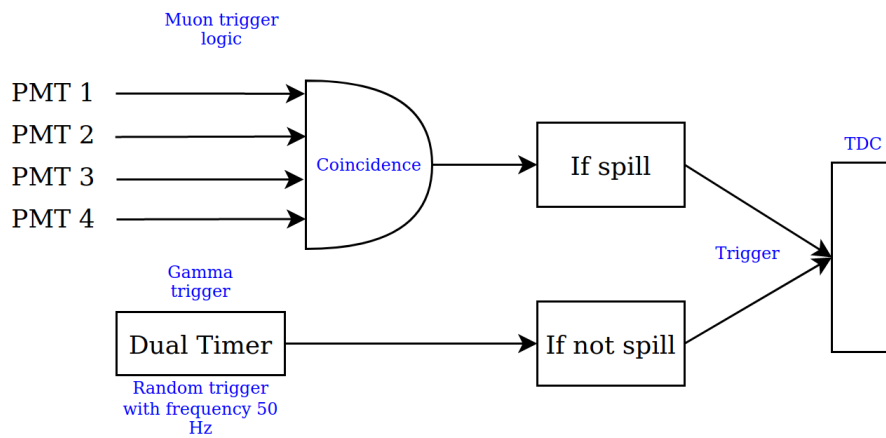
Legend: The photon flux distribution in the bunker. Note that the figure shows only one side of the source. At 1 meter the radiation dose is about 0.5 Gy/h. As the detector is installed at about 3 meters the photon flux with no filters is between $10^8 \text{ cm}^{-2} \text{ s}^{-1}$ and $10^7 \text{ cm}^{-2} \text{ s}^{-1}$.

Source: GKOTSE, et al., 2021, p. 22.

3.3.3.1 Trigger Logic

The measurement strategy consists of two main steps. The muon beam is characterized by the spill and non-spill cycle. The former is when the muon beam is passing through the bunker and the latter is when the muon beam is not passing through the bunker. In the first, the trigger logic is composed of the use of four scintillators. Two of them are installed inside the bunker, one is installed in trolley 1 and the other is installed in trolley 3. These two are called internal scintillators and they measure the signal of both muon beam and gammas from the source. The other two are big scintillators installed outside the bunker, which are responsible for detecting only muon signals. Therefore, the muon trigger is given by the AND combination of the four scintillators, where their signal is of the type Nuclear Instrumentation Module (NIM) and it is provided to a set of modules in the electronic area that are used to create the logic. The trigger output is then provided to the TDC V1190. The TDC acquisition window is set to 600 ns in this configuration. On the other side, the non-spill cycles are used to trigger the gamma events. When the beam is on the non-spill configuration, a random trigger is created by a dual-timer, model N93B. Its frequency is set around 50 Hz/cm² and it is provided to the TDC to trigger the gamma events. The TDC acquisition window is set to 10 μs in this configuration. Figure (60) shows the trigger schematic and Figure (62) shows the scintillator/photo-multiplier (PMT) distribution in the bunker.

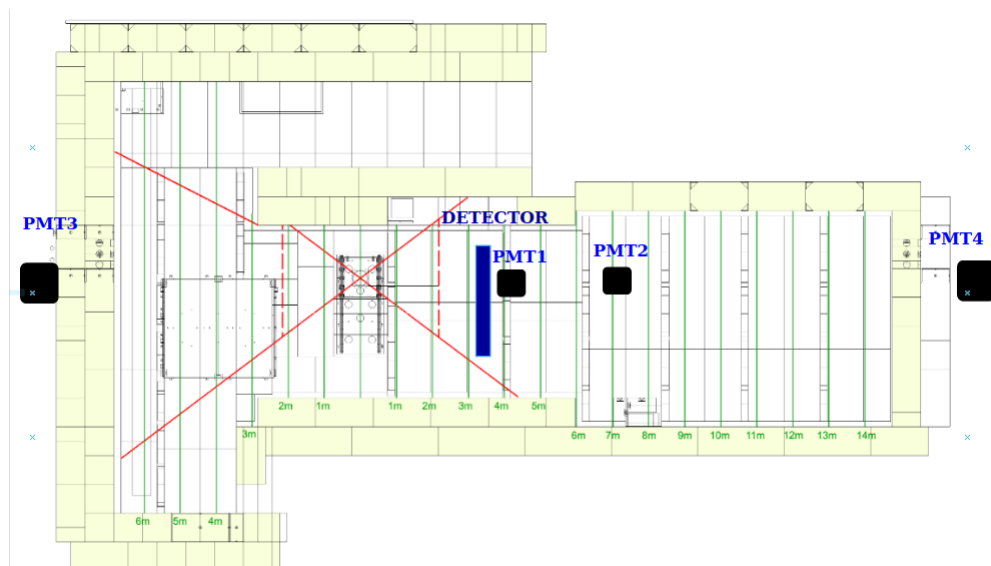
Figure 60 - Trigger Logic.



Legend: The trigger logic of the setup is composed of two different solutions: the muon trigger logic is performed by the coincidence of four scintillators, two are installed inside the bunker and two are installed outside the bunker.

Source: The author, 2023.

Figure 61 - Photomultipliers disposition.



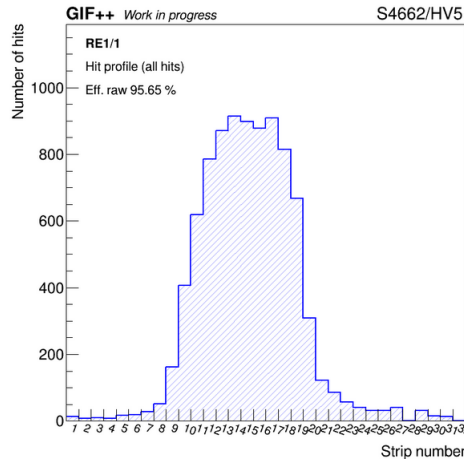
Legend: The PMTs 1 and 2 are installed at trolleys 3 and 1 respectively. They are responsible for triggering the gamma events. PMTs 3 and 4 are installed outside the bunker. They are responsible for triggering the muon events.

Source: The author, 2023.

3.3.3.2 Signal Readout

The signal from the strips is submitted to the following treatment in the FEB: Preamplification, gain stage, zero-crossing discriminator, monostable, and driver. The FEB signal output is LVDS (Low-Voltage-Differential-Signal) type, which is read by a flat cable that goes to the TDC channels. There is one FEB for each chamber partition. Each partition has 32 strips that are split into 2 flat cables. The chamber has been installed in a position where the center of the muon beam hits partition B. However it is worth mentioning that the beam halo (it extends a few centimeters from the beam center) also hits small parts of partitions A and C. Concerning the gamma signal, the whole chamber receives gammas. Finally, the data collected by the TDC is treated with the DAQ software with the use of the CAEN Library. Dedicated histograms with the hit distribution, efficiency, cluster size, and gamma rates can be produced by the WebDCS just after the data taking finishes. Figure (62) shows the control plot for the distribution of the hits over the strips that are read by partition B.

Figure 62 - Hits distribution.



Legend: This run shown here has been performed with gamma source off and muon beam on during the September data taking, in 2021. Note that the beam hits are concentrated among strips 9 to 20. The other hits out of this window can be considered cosmic muons or another type of noise. The name S4662/HV5 refers to the run number (4662) and the HV point 5 (9700 V).

Source: The author, 2023.

3.3.4 Data Analysis

This section is dedicated to discussing the data analysis for the data taken during the test beams. First, important parameters used and measured during the data taking

are discussed. In the sequence, the results for the standard gas as well as the eco-friendly mixtures are discussed. Finally, the performance comparison among the three gases is discussed.

3.3.4.1 Important detector parameters

This section is dedicated to explaining all the relevant parameters that are used and/or measured during the data taking and are important to characterize the detector performance.

a. High Voltage

The HV applied on the detector electrodes is provided by a CAEN HV power supply, model A1526 N (144), which is powered with the help of a universal power supply mainframe, model SY 1527 (145). For each data taking the order of magnitude of the applied voltage can vary from 1000 V to 12000 V depending on the gas mixture used. It is worth mentioning that the voltage applied by the supply is not the same voltage within the gaps, because of the effects of temperature and pressure. Significant experimental data has been collected in the past showing that they might affect the RPC operation (118). In fact, the increase in the temperature implies the reduction of the plate's resistivity. Besides that, both the temperature and pressure of the gas can impact drift and multiplication parameters because these parameters depend on the ratio of energy and gas density. In turn, the gas density is related to pressure and temperature. It is well known that an increase in temperature increases both current and counting rate (146). In turn, the increase in the pressure causes the opposite effect. Therefore, when comparing data with different pressures and temperatures it is needed to use the effective voltage (HVe_{eff}), defined as,

$$\Delta V_{eff} = \Delta V_{app} \frac{T}{T_0} \frac{P_0}{P}, \quad (17)$$

P_0 and T_0 are reference values for pressure and temperature and P and T , are the measured values at the moment of the data taking (147). The CMS-RPC uses 990 mb and 273.15 K for P_0 and T_0 respectively. It is worth mentioning that the CMS WebDCS uses another equation to perform the correction

$$\Delta V_{eff} = \Delta V_{app} \cdot \left[(1 - \alpha) + \alpha \frac{T_0}{T} \frac{P}{P_0} \right], \quad (18)$$

where α is 0.8. The Equation (18) has been obtained empirically to remove any environmental influence (148).

b. Currents

One key parameter is the current measured across the electrodes of the RPC. They are obtained by the CAEN High voltage supply, module A1526 N. The dark current is defined as the current provided by the detector in the presence of natural radioactivity, *i.e.*, in the absence of non-natural radiation, as the GIF++ gamma source and muon beam. Therefore this current is taken with the gamma source OFF and no muon beam. It is important to measure it before irradiating the chamber to spot any abnormal condition in the detector. This current in the RE1/1 chamber is expected to be a few microamperes. The behavior of the current as a function of the HV_{eff} is normally linear up to a certain voltage, which may depend on the detector, gas, mode of operation, and so forth. This is due to the resistive characteristic of the detector. In this region the multiplication process in the gas is negligible. After this voltage, the gas starts to ionize, and the behavior of the curve changes to exponential. This part of the curve is due to the gas multiplication process.

c. Cluster Size

Cluster size (CS) is the number of contiguous fired strips when a particle passes through the detector (149). It is desired to have low values of CS because it provides good particle determination. CS Values lower than 2 are required (150), providing good momentum resolution and reducing the number of fake hits.

d. Cluster Rate

Cluster rate (CLR) is calculated as the hit rate divided by the cluster size. This quantity represents the rate seen by the cluster, *i.e.* it considers the rate of the set of fired strips.

e. Efficiency

The efficiency is calculated as the ratio between the number of muon tracks detected in the chamber and the number of muon tracks detected in the trigger system

$$\epsilon = \frac{N_{chamber}}{N_{trigger}}. \quad (19)$$

The curve of the efficiency versus HV_{eff} can be modeled with a sigmoid curve

$$\epsilon(HV_{eff}) = \frac{\epsilon_{max}}{1 + e^{-\lambda(HV_{eff} - HV_{50})}}, \quad (20)$$

where ϵ_{max} is the maximum efficiency of the detector. λ is related to the slope at half of the curve, and HV_{50} is the voltage when the efficiency is 50% (151). Besides that, the working point of the detector is defined as $HV_{knee} + 150$ V, where HV_{knee} is the voltage where the efficiency is 95%.

3.3.5 Standard gas results

The results for the CMS-RPC operating with standard gas are presented first. These results are used as a reference when studying the performance of the detector with eco-friendly gas mixtures. In order to have similar values for rates in the detector, the same gamma source absorption values have been used during the data taking for the three mixtures. Table (9) shows the values of absorption value used during the data taking.

Table 9 - Absorption factors used during data taking

4.6
10
46
100
220
Source OFF

Legend: Six different conditions were used during the data taking. Note that the lower the absorption factor, the higher the gamma flux

Source: The author, 2023.

Instead of studying the gaps current as a function of HV_{eff} it is better to consider the total current density

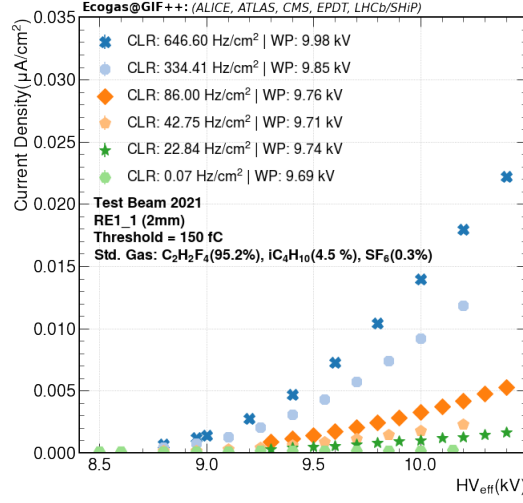
$$K_{total} = \frac{K_{BOT} \cdot S_{BOT} + K_{TN} \cdot S_{TN} + K_{TW} \cdot S_{TW}}{S_{BOT} + S_{TN} + S_{TW}}, \quad (21)$$

where K_i and S_i are the current density and surface area for the gap i and $i = (BOT, TN, TW)$. The surfaces are $S_{BOT} = 3150 \text{ cm}^2$, $S_{TN} = 990 \text{ cm}^2$, $S_{TW} = 1840 \text{ cm}^2$. Figure (63) shows the current density curves for each factor as a function of HV_{eff} for the chamber operating with the standard gas mixture.

It is worth mentioning that the HV points are different because it was needed to achieve the plateau in the efficiency curves for different rates. It is possible to see the linear behavior of the curve up to 9000 V. Then, after that the gas amplification takes place and the curve has exponential behavior. This is easily seen in the curves with a higher rate, as the gas amplification is higher.

In principle, it is desired to achieve a rate of 2000 Hz/cm², in order to validate the gas mixture performance in the HL-LHC. However, the data collected at a high rate was not validated. Therefore, the results up to the rate of 646.6 Hz/cm² are useful to compare the performance of the mixtures.

Figure (64) shows the Muon Cluster Size (MCS) versus HV_{eff} . The first behavior to be pointed out is that in the gas amplification region (after 9.2 kV) for the same curve, the MCS increases with the increase of the HV_{eff} . This occurs because when the HV_{eff} increases, the electric field applied on the gap increases, which increases the induced

Figure 63 - Standard gas: Current Density x HV_{eff} 

Legend: Six different curves are shown. The legend represents the cluster rate at the working point. The rate 0.07 Hz/cm^2 represents the noise and the rate 646.6 Hz/cm^2 is obtained with an absorption factor 4.6.

Source: The author, 2023.

signal.

Another important feature is that for a given HV_{eff} the MCS decreases with the increase in rate. This can be explained due to the higher voltage drop in the bakelite for the case with a higher rate. As the drop is higher the voltage in the gas is lower, causing a drop in the efficiency.

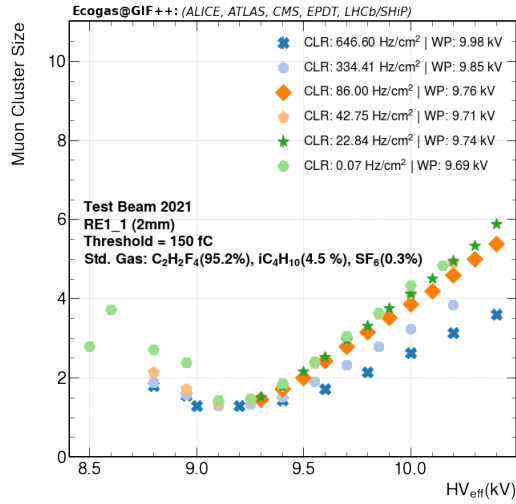
The efficiency of the detector as a function of HV_{eff} is shown in Figure (65). It is possible to see that at the same voltage the higher the background rate, the lower the efficiency. Such drop is in part explained by the drop of voltage in the plates. As commented in Figure (63) the level of currents increases with the increase of the background rate, which causes a high voltage drop across the plates. Consequently, the HV in the gas is lower implying lower gas amplification.

To study the behavior of the efficiency with respect to the HV in the gas, a resistivity measurement has been performed to estimate the resistance of the plates for each gap. Table (10) shows the measured values.

Therefore, to calculate the equivalent resistance seen by the HV supply it is necessary to consider the three gaps in parallel. Thus, the equivalent resistance R_{eq} is

$$R_{eq} = \frac{R_{BOT} \cdot R_{TN} \cdot R_{TW}}{R_{TN} \cdot R_{TW} + R_{BOT} \cdot R_{TW} + R_{BOT} \cdot R_{TN}}, \quad (22)$$

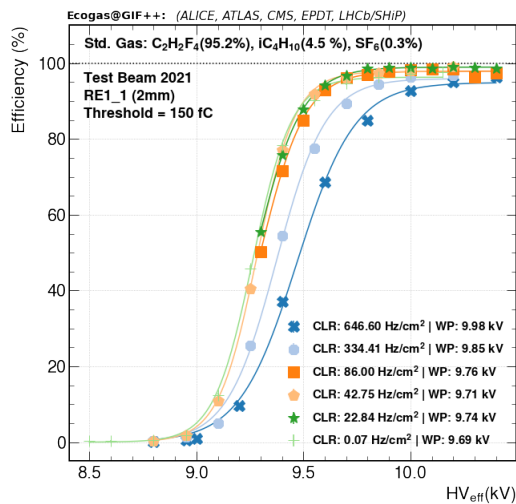
Figure 64 - Standard gas: Muon Cluster Size x HV_{eff}



Legend: The muon cluster size increases with the HV from around 9000 V for all cases. Besides that, for a given HV the higher the rate, the lower the muon cluster size. Also, it is possible to see that for all curves, the value of the muon cluster size at the WP is lower than 3.

Source: The author, 2023.

Figure 65 - Standard gas: Efficiency x HV_{eff}



Legend: The detector working point tends to move to a higher value as the rate increases. This can be inferred from the shift of the efficiency curve to the right.

Source: The author, 2023.

Table 10 - Resistance for each plate

Plate	Resistance (Ω)
Bottom	$9.98 \cdot 10^6$
Top narrow	$2.70 \cdot 10^7$
Top Wide	$4.02 \cdot 10^7$

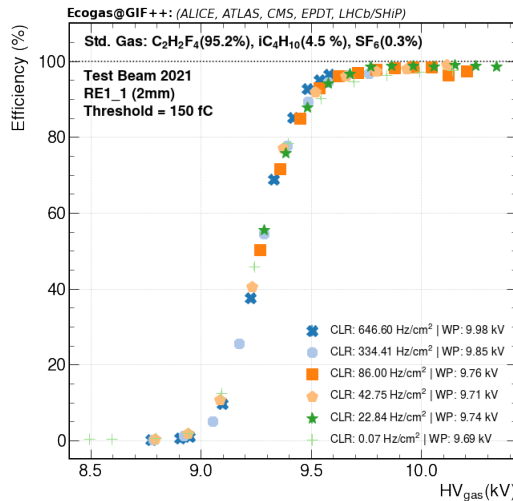
Legend: These results were obtained by flushing the chamber with argon. As this gas is characterized by a high Townsend coefficient with considerably low voltages (around 2 kV) a plasma is created inside the gas, removing any resistance between the electrodes. Therefore, by plotting the current versus HV, it is possible to obtain the plate resistance with Ohm's Law.

Source: The author, 2023.

which gives $R_{eq} = 6.17 \cdot 10^6 \Omega$. The HV across the gas is calculated as

$$HV_{gas} = HV_{eff} - R_{eq} \cdot I_{tot}, \quad (23)$$

where $I_{tot} = I_{BOT} + I_{TN} + I_{TW}$. Figure (66) shows the efficiency versus the HV_{gas} . It is possible to see that the HV shift between the curves is no longer present. Therefore, even with different background radiation levels the efficiency of detection in the gas is more or less constant.

Figure 66 - Standard gas: Efficiency x HV_{gas} 

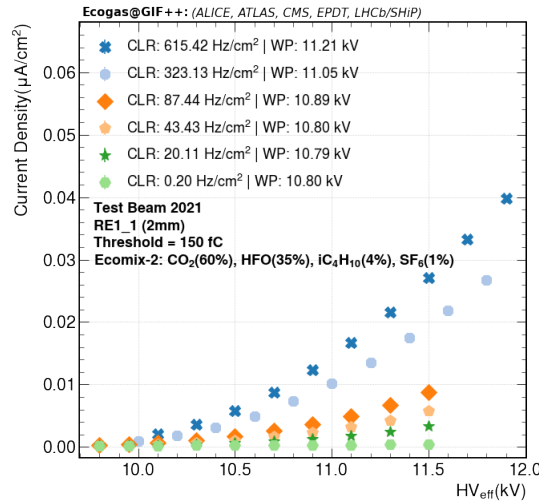
Legend: Removing the voltage drop in the bakelite it is possible to show that the efficiency of detection in the gas does not vary from the noise level to 646.6 Hz/cm²

Source: The author, 2023.

3.3.6 Ecomix-2 gas results

In this section, the results of the ecomix-2 are discussed. To get similar rates as in the standard gas the same absorption factors have been used: 4.6, 10, 4.6, 100, 220, and source off. Figure (67) shows the current density as a function of HV_{eff} . Also here, the HV points are not the same.

Figure 67 - Ecomix-2: Current Density x HV_{eff}



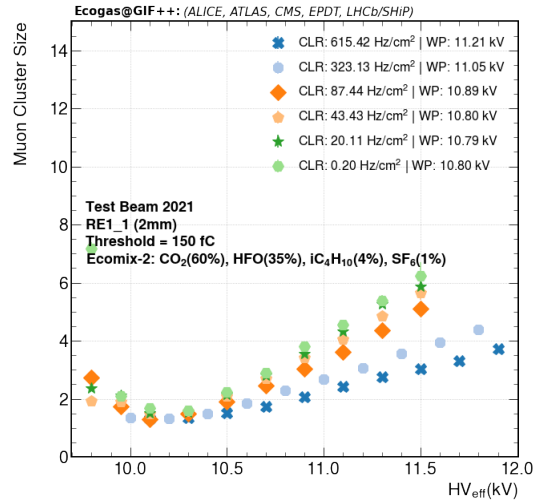
Legend: Six different curves are shown. The legend represents the cluster rate at the working point. The rate 0.2 Hz/cm^2 represents the noise and the rate 615.42 Hz/cm^2 is obtained with absorption factor 46.

Source: The author, 2023.

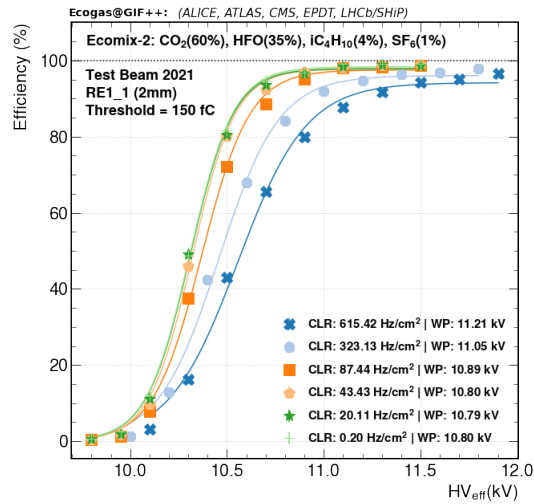
At the lowest absorption factor of 4.6, the cluster rate at the WP is 615.42 Hz/cm^2 , around 30 Hz/cm^2 lower than the one found for the standard gas mixture. Besides that, for the same rate level, the current is around 2 times the current found for the standard gas mixture. There will be a dedicated section to compare the results for the different gases. Figure (68) shows the MCS as a function of HV_{eff} for the ecomix-2. The results obtained are very similar to the ones obtained for the standard gas mixture. The main difference is the shift in the HV points.

Figure (69) shows the efficiency in function of HV_{eff} for ecomix-2. It is possible to note that the shift in the curves with respect to the HV is also found here. Besides that, the working point found is around 1 kV greater than the one found for the standard gas mixture. As commented in Section (3.2.4) the addition of HFO brings the WP to higher values.

As before, to see the effect of the HV drop in the plates on the efficiency, it is possible to calculate the gas voltage and plot the efficiency in function of it. Figure (70)

Figure 68 - Ecomix-2: Muon Cluster Size x HV_{eff} 

Legend: The muon cluster size increases with the HV from around 10 kV for all cases.
 Besides that, for a given HV the higher the rate, the lower the gamma cluster size.
 The muon cluster size at the WP is always lower than 2.5.
 Source: The author, 2023.

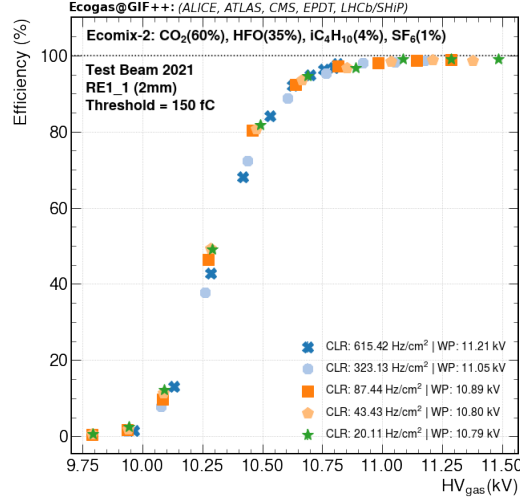
Figure 69 - Ecomix-2: Efficiency x HV_{eff} 

Legend: The detector working point tends to move to a higher value as the rate increases.
 This can be inferred from the shift of the efficiency curve to the right. Besides
 that, it is noted that the WP for the ecomix-2 is higher for all curves when
 compared with standard gas.

Source: The author, 2023.

shows this relationship.

Figure 70 - Ecomix-2: Efficiency x HV_{gas}



Legend: Removing the voltage drop in the bakelite it is possible to show that the efficiency of detection in the gas does not vary from the noise level to 615.42 Hz/cm²

Source: The author, 2023.

3.3.7 Ecomix-3 gas results

In this section, the same results for the ecomix-3 are discussed. Figure (71) shows the current density as a function of HV_{eff} . Again, the HV points are different for the same reason explained before.

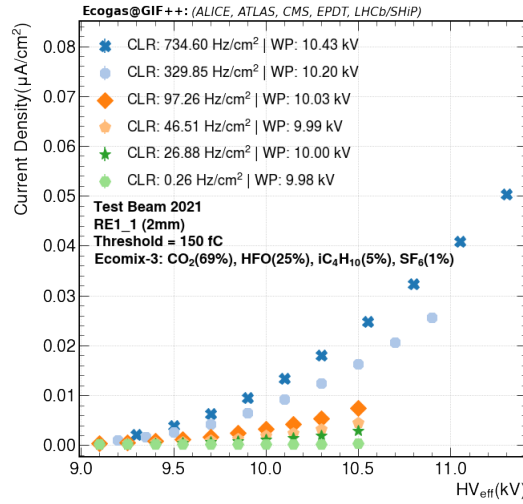
It is important to highlight that the cluster rate at absorption factor 4.6 is around 90 Hz/cm² greater than the one found for standard gas. Figure (72) shows the MCS as a function of HV_{eff} for the ecomix-3.

It is clear that for the curves with the lowest rates, the MCS is lower than the one found for the standard gas mixture. On the contrary, for the curves with the highest rate, the values of MCS are higher. Still, the values are well controlled under all the HV and rate ranges. Figure (73) shows the efficiency in function of the HV_{eff} . Again, it is possible to note the shift in the HV points as the rate increases.

If the WP is compared with the standard gas and ecomix-2, it is possible to see that they are higher than the ones for the standard gas and lower than the ones found for ecomix-2. This is discussed in more detail in the next section.

Finally, Figure (74) shows the efficiency in function of the HV_{gas} .

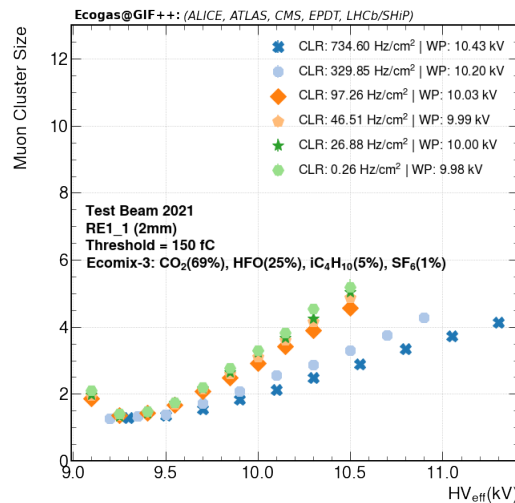
Figure 71 - Ecomix-3: Current Density x HV_{eff}



Legend: Six different curves are shown. The legend represents the cluster rate at the working point. The rate 0.07 Hz/cm² represents the noise and the rate 734.6 Hz/cm² is obtained with absorption factor 46.

Source: The author, 2023.

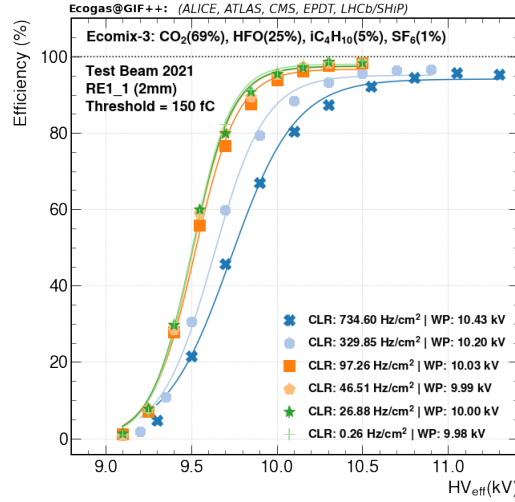
Figure 72 - Ecomix-3: Muon Cluster Size x HV_{eff}



Legend: The muon cluster size increases with the HV from around 9000 V for all cases, as in the standard gas case. Besides that, for a given HV the higher the rate, the lower the muon cluster size.

Source: The author, 2023.

Figure 73 - Ecomix-3: Efficiency x HV_{eff}

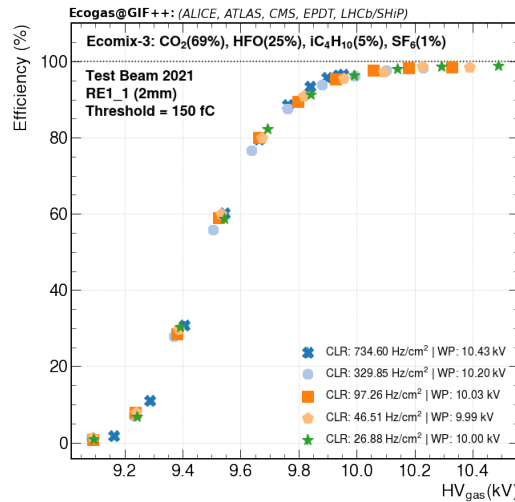


Legend: The detector working point tends to move to a higher value as the rate increases.

This can be inferred from the shift of the efficiency curve to the right.

Source: The author, 2023.

Figure 74 - Ecomix-3: Efficiency x HV_{gas}



Legend: Removing the voltage drop in the bakelite it is possible to show that the efficiency of detection in the gas does not vary from the noise level to 734.6 Hz/cm²

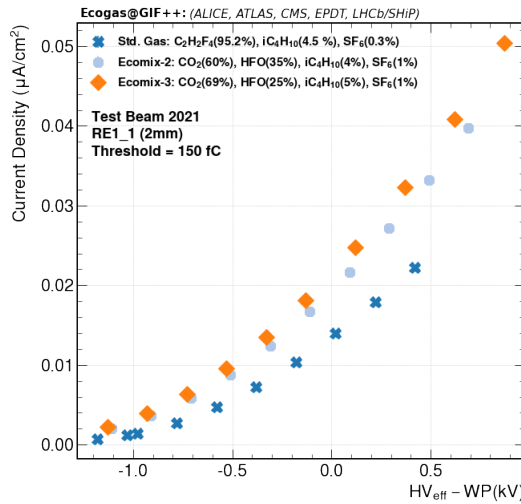
Source: The author, 2023.

3.3.8 Comparison between the mixtures

This section is dedicated to comparing the performance of the gas mixtures. The main parameters are compared and discussed. It is mentioned again that the maximum rates achieved by the detector in the tests are around 700 Hz/cm^2 and that the desirable values would be around 2000 Hz/cm^2 . However, even with this rate level, it is possible to compare the performance of the main detector parameters. This can give a good indication of what can be changed/improved in the future, *i.e.* this will give a hint if the tested gases can be used for further tests in the future or if they are not suitable and new mixtures should be studied.

The first comparison is the current density at absorption factor 4.6. This is the lowest absorption factor, consequently, it provides the greatest rate for each mixture, 646.6 Hz/cm^2 for standard gas, 615.42 Hz/cm^2 for ecomix-2, and 734.6 Hz/cm^2 for ecomix-3. To avoid confusion about the HV points, the current density is plotted in function of HV_{eff} - $HV_{W.P}$, where $HV_{W.P} = 9983.60 \text{ V}$ (standard gas), $HV_{W.P} = 11213.20 \text{ V}$ (ecomix-2), and $HV_{W.P} = 10430.60 \text{ V}$ (ecomix-3).

Figure 75 - Current Density comparison



Legend: The mixture with highest current is ecomix-3 followed by ecomix-2

Source: The author, 2023.

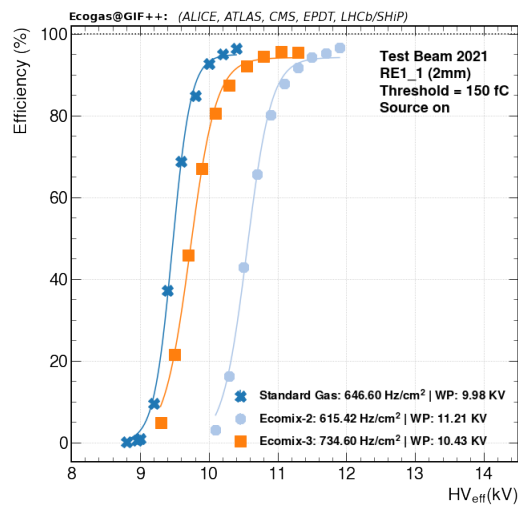
Therefore, the mixture with the highest current is ecomix-3 followed by ecomix-2. When compared for each (HV_{eff} - $HV_{W.P}$) point the percentage difference between standard gas and ecomix-2 ranges between 79% and 315.90%, while the percentage difference between standard gas and ecomix-3 ranges between 126.81% and 354.63%. The average difference in the first case is 158.70%, while in the second case is 190.32%.

When comparing ecomix-2 and ecomix-3, the percentage difference for each (HV_{eff} -

$HV_{W.P}$) point ranges between 7.09% and 26.57% with average of 13.52 %. It is worth mentioning that the percentage difference in the current density between standard gas and both eco gas mixtures does not depend on the $(HV_{eff}-HV_{W.P})$ point, while the difference between ecomix-2 and ecomix-3 increases with the increase of $(HV_{eff}-HV_{W.P})$.

Figure (76) shows the efficiency comparison among the three mixtures with source off, *i.e.* with no gamma flux. The noise rate for the three mixtures is negligible.

Figure 76 - Efficiency at source OFF comparison



Legend: The main characteristic is the shift in the working point between the mixtures.

The shift is more pronounced at ecomix-2 case

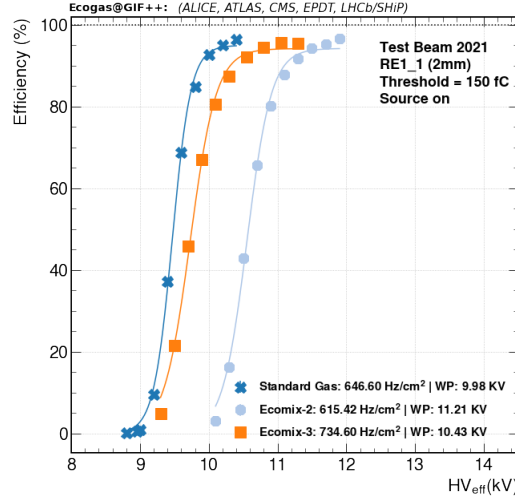
Source: The author, 2023.

The difference between the efficiencies at the WP in the case without radiation is around 1% less when comparing standard gas with ecomix-2 and ecomix-3. However, the main difference resides in the WP at the efficiency knee. The difference between the mixtures is seen in the shift between the curves. The difference between standard gas and ecomix-2 is around 1.1 kV and the difference between standard gas and ecomix-3 is around 0.3 kV. Therefore, the difference in the WP between ecomix-2 and ecomix-3 is around 0.8 kV. This means that the decrease in the HFO percentage from 35% in ecomix-2 to 25% in ecomix-3 reduces the WP in 7.53% at the efficiency knee in the case without radiation.

Figure (77) shows the efficiency comparison between the three mixtures with source on at absorption factor 4.6, *i.e.* with cluster rates around 700 Hz/cm².

The difference between the efficiencies at the WP in the radiation case is around 1% more when comparing standard gas and ecomix-2 and around 1.2% more when comparing standard gas and ecomix-3. However, the main difference resides in the WP at the efficiency knee. The difference between the mixtures is seen in the shift between the curves. The difference between standard gas and ecomix-2 is around 1.2 kV and the

Figure 77 - Efficiency at absorption factor 4.6 comparison



Legend: Also, the main feature is the shift in the working point between the mixtures. The shift is more pronounced at ecomix-2 case

Source: The author, 2023.

difference between standard gas and ecomix-3 is around 0.4 kV. Therefore, the difference in the WP between ecomix-2 and ecomix-3 is around 0.8 kV. This means that the decrease in the HFO percentage from 35% in ecomix-2 to 25% in ecomix-3 reduces the WP in 6.97% at the efficiency knee when the rate is around 700 Hz/cm².

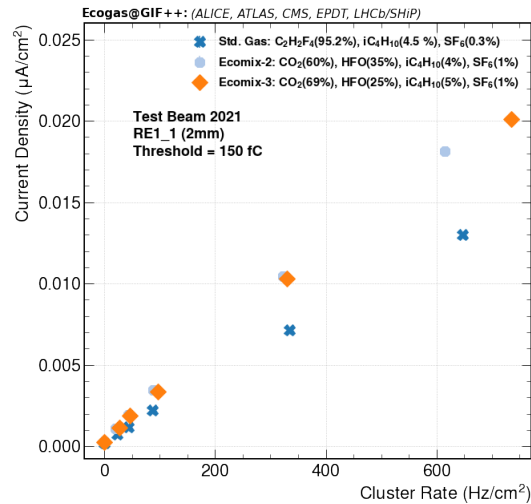
Figure (78) shows the current density as a function of the cluster rate. All values are at the WP. It is important to emphasize that the current values are taken only at partition B since the rates are processed by the DAQ considering only this partition. The current at partition B is provided by the BOT gap and TW gap as can be seen in Figures (55) and (56). Therefore, the current density in partition B is calculated as

$$K_{total} = \frac{K_{BOT} \cdot S_{BOT} + K_{TW} \cdot S_{TW}}{S_{BOT} + S_{TW}}. \quad (24)$$

It is possible to note a linear behavior for all mixtures, which is expected. Besides that, in all points, ecomix-2 and ecomix-3 need more current to get the same rate when compared to standard gas. The difference between the eco mixtures and the standard gas seems to be lower for rates less than 200 Hz/cm². The difference is clearly higher for rates greater than 300 Hz/cm². This is very important and should be studied carefully in the future, as the high current can contribute to the aging process faster.

Figure (79) shows the efficiency in function of gamma rate for all gases at WP. The gamma rate is calculated by dividing the cluster rate by the efficiency, *i.e.* it is the real gamma cluster rate seen by the detector.

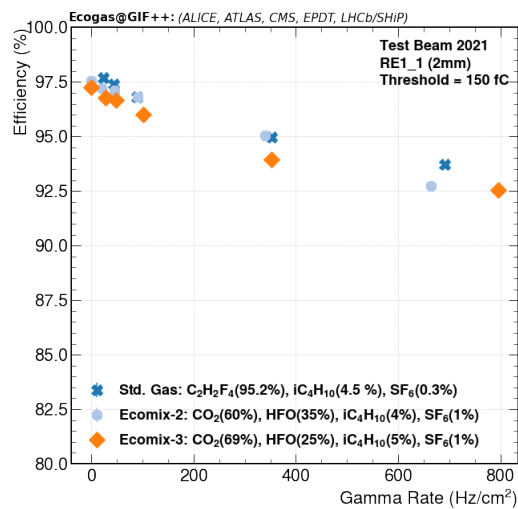
Figure 78 - Current density versus cluster rate at WP



Legend: Only currents at partition B are considered, which are provided by BOT and TW gaps. In low rates, the behavior is similar for all mixtures, while in high rates ecomix-2 and ecomix-3 have more current.

Source: The author, 2023.

Figure 79 - Efficiency versus gamma rate



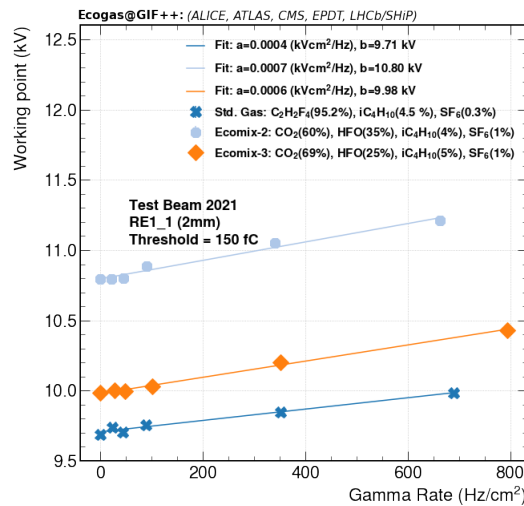
Legend: It is observed that for rates lower than 400 Hz/cm² the lowest efficiency is obtained for ecomix-3. For rates greater than 600 Hz/cm², is observed a better efficiency for the standard gas. Still, the values obtained for the eco mixtures are acceptable

Source: The author, 2023.

For low rates the drop in efficiency seems to be higher for ecomix-3, followed by ecomix-2 and standard gas. It is worth mentioning that the first point for standard gas does not follow the pattern, which means that probably it can be improved with other data taking. Around 400 Hz/cm² the values for ecomix-2 and standard gas are similar, while ecomix-3 is slightly lower. Finally, after 600 Hz/cm² it is clear that ecomix-2 has lower efficiency when compared with the standard gas. The value for ecomix-3 is also lower, but the rate is also higher compared with the standard gas.

Figure (80) shows the detector WP as a function of the gamma rate at WP for all mixtures. A linear function is used ($WP = a \cdot GR + b$) to fit the data points.

Figure 80 - Working point as a function of the gamma rate at WP



Legend: The slope indicates the faster increase of the WP as a function of the gamma rate for the eco mixtures.

Source: The author, 2023.

From the parameters obtained in the fitting is possible to see that ecomix-2 has the greatest slope, followed by ecomix-3. This shows that the working point for the eco mixtures increases faster as a function of the rate when compared with the standard gas mixture.

3.4 iRPC Aging Studies

The aging effects in the RPCs can be understood as the degradation of their performance due to long-term exposure to radiation (118). Such degradation is caused by the production of polymers by chemical reactions which attach to the electrode surfaces (152). There are several chemical processes occurring simultaneously inside the RPCs

that depend on many factors. These factors can be the type of material used in the electrodes and the composition of the gas, for example. Usually, the aging effects are manifested in the degradation of the efficiency, in the increase of the dark current, and in the increase of the noise pulses in the detector, which may cause sparks inside the gas gap during the operation (118).

Depending on the type of operation (streamer or avalanche) the aging effects can vary. The experiments L3¹⁵ (153) and Belle (154) operated RPCs in streamer mode and did not present any sign of degradation due to aging process during its operation.

However, the aging process affected the RPCs operated at the BaBar experiment. This experience helped the RPC community in the sense that many lessons were learned from the BaBar experience. As the RPCs installed in the modern experiments, the BaBar RPCs were made of bakelite coated with a layer of linseed oil (155). After some time of operation, an increase in the currents and a decrease in the efficiency were observed (156). After a detailed investigation, the presence of linseed oil droplets on the surfaces was found. Due to the bad coating of the linseed oil, the droplets were not polymerized, forming a thick layer on the bakelite, impacting the resistivity of the plate. In the BaBar RPCs, water vapor was not added to the gas mixture causing an increase in the bakelite resistivity after some time. It was observed that the efficiency close to the gas inlets was worse than the other parts of the detector, as in this part the bakelite was much drier. Another problem found was a discontinuity in the graphite paint film. Therefore, after detailed studies all problems were solved: water vapor was added to the gas mixture, the linseed oil coating was properly polymerized, and the graphite coating was improved.

The experience achieved in the LHC experiments helped in the understanding of the aging effects in RPCs operating in avalanche mode. Before the start of the LHC operation, many aging studies were performed to ensure that the RPCs could operate in good performance during the LHC operation. The ATLAS collaboration performed their measurements at GIF (157). The RPCs chambers were irradiated with gamma rays at a frequency of 600 Hz/cm² and the total accumulated charge corresponded to 7 ATLAS years¹⁶ (with a safety factor of 5). The tests showed that the chambers were robust to cope with the conditions of the LHC. In the case of the CMS, a test with gamma rays with an accumulated charge of 23 mC/cm² (158) found no degradation of the RPC performance due to the deterioration of the surface quality. In the case of ALICE the performance of an RPC prototype was studied with gamma rays as well. Up to 34 mC/cm² of accumulated charge, no problems were found (159). Finally, in the case of the LHCb, tests were performed up to 45 mC/cm² (160). A large increase in the resistivity of the bakelite and an increase in the dark current were observed. Despite this, the prototype

¹⁵ L3 was one of the main experiments at the Large Electron-Positron Collider (LEP)

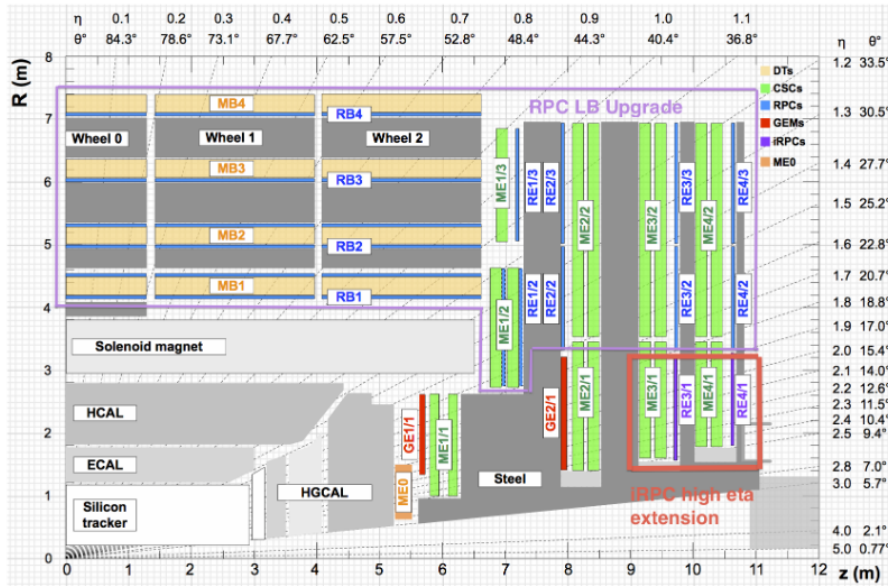
¹⁶ This is equivalent to the amount of accumulated charge during 1 year of operation in ATLAS detector.

remained operating with high efficiency at the expected maximum rate.

3.4.1 The Improved Resistive Plate Chambers

The CMS-RPC performance during the LHC Run 1 and Run 2, where the instantaneous luminosity was $10^{-34} \text{cm}^{-2} \text{s}^{-1}$, was very satisfactory. In the HL-LHC the luminosity will increase five times. Therefore, the detectors will be subject to a high level of particles which has many implications. This new condition can affect the detector properties, introducing non-recoverable aging effects. Besides that, the increase in the pileup will result in higher trigger rates, worsening the muon detection and reconstruction. To cope with these changes the CMS detector is under upgrade, as commented in Section (2.1.2). The existing system is being submitted to a longevity study with the radiation levels that will be found in HL-LHC (161). Besides that, an improved version of the RPCs known as improved RPCs (iRPC) will be installed in the high pseudorapidity region on the 3rd and 4th endcap disks. Figure (81) shows the CMS quadrant, where the iRPCs are highlighted by the orange square.

Figure 81 - A CMS quadrant.



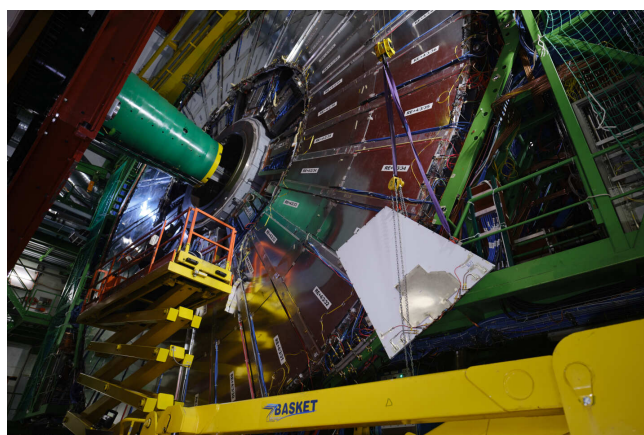
Legend: The iRPCs (orange) are installed at the high pseudorapidity region.

Source: ESTRADA, 2022, p. 3.

As the figure indicates, they will cover the pseudorapidity region up to 2.5. One of the motivations for installing the iRPCs in this region is that they will complement the existing Cathode Strip Chambers (CSCs) measurements. Their presence will add one more track hit that will enhance the local muon measurement and improve the background

hit rejection. In addition, the intrinsic time resolution will be improved by a factor of 2 when both measurements are combined (20). This will enhance the measurement of heavy-stable-charged particles. The new detector will be able to measure the time difference between the signals that arrive at both ends of the strip readout. This will provide a better spacial resolution along the strips, achieving the order of a few centimeters. Therefore, because of the better spacial and time resolution, it will be possible to resolve the low p_T tracks that are wrongly identified as high p_T tracks. Besides that, the inclusion of the iRPC hits in the trigger primitives will increase the trigger efficiency for the hits in the high pseudorapidity region, where the CSCs can not measure. Therefore, as in the present RPC system, it is very important to study the possible aging effects in the iRPC chambers in the radiation levels that will be found in HL-LHC as well. In the next section, the characterization of an iRPC-prototype detector with custom electronics is presented. The detector performance is studied in an environment with gamma radiation and muon beam, and the behavior of the currents of the same is analyzed for different accumulated charges. It is worth mentioning that The author, 2023 of this thesis actively participated in all steps of these results, including the planning of the activities, operation, shifts, coordination, analysis, and discussions. In December 2021, the installation of two iRPC prototypes was completed. Both prototypes are being submitted to the real conditions of the CMS detector and the acquired experience will help in the future installation of the final version of the iRPC detector. Figure (82) shows the installation of one iRPC demonstrator.

Figure 82 - iRPC demonstrator installation



Legend: The iRPC demonstrator was installed in the outer stations of the CMS muon endcap (162).

Source: iRPC installation, 2023.

3.5 Experimental setup

The system is set up at GIF++. The tracking system is installed in trolley 1 and the iRPC prototype under study is installed in trolley 3 (It is installed just after RE1/1 - see Figure (57)). The trigger system is the same one used by the RE1/1 chamber. The tracking system (163) is composed of two small RPCs arranged perpendicularly. The combined use of trigger and tracking systems was found to be a very good solution for the gamma background rejection. The iRPC prototype is a 1.4 mm double-gap (top and bottom gaps) chamber equipped with a custom-made 32-channel front-end-electronics (FEE) board operated in a voltage-sensitive mode. The digitization threshold on the FEE board is set to 0.5 mV with a 20 Ω input resistance. The threshold of 0.5 mV in the present FEE is approximately equivalent to 75 fC in typical charge-sensitive-mode FEEs. The detector was irradiated between January 2021 and April 2022 accumulating around 50 mC/cm² of charge. The data used for the characterization studies were collected during the beam tests in 2021. The aim of using this prototype is to understand the effects of the accumulated charge on its performance.

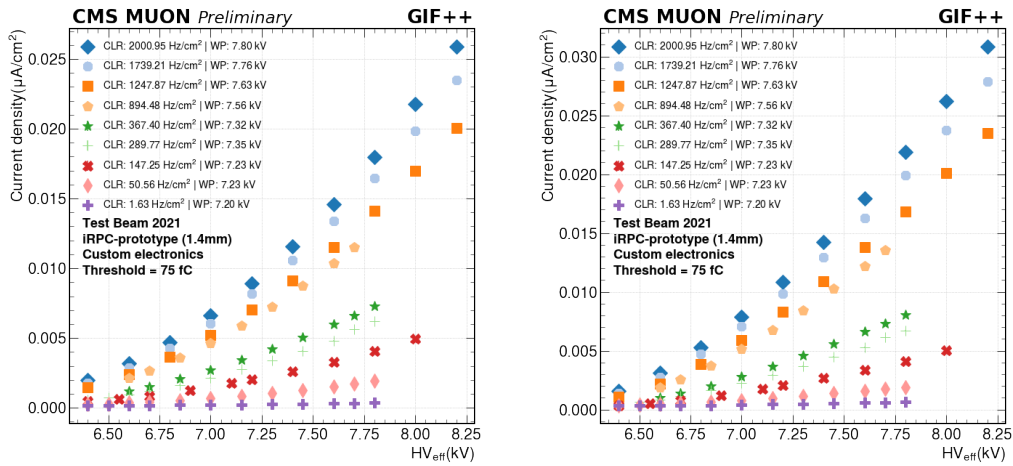
3.5.1 Results

Figure (83) shows the current density drawn in both gaps. The left figure shows the density current in the top gap and the right figure shows the current in the bottom gap. In the legend, CLR represents the cluster rate at the working point for each measurement as well as the WP itself. In general, the current in the bottom gap is around 1.2 times the current in the top gap. The point with cluster rate at 1.63 Hz/cm² refers to the situation without gamma background while the other points represent the situation with gamma background. Some scans have more points than others because it was needed to reach the plateau in the efficiency curves. The error bars are small and are behind the data points.

Figure (84) shows the muon efficiency versus HV_{eff} . The efficiency is obtained after subtracting the gamma background and using the tracking system. The detector's WP moves to higher values as the rate increases, which is visible in the shift in the efficiency curve with respect to the rate. In other words, as the rate increases, the curve moves to the right. The WP value increases from 7.2 kV to 7.8 kV, where the first value is obtained with the source off, *i.e.*, no gamma background, and the second value is obtained with cluster rate 2 kHz/cm².

Figure (85) shows the muon efficiency in function of the gamma rate at the WP. The efficiency drops with the increase in the rate. The efficiency is 99.46% without gamma background and 93.89% at a gamma rate 2.2 kHz/cm². Figure (86) shows current density versus cluster rate. The current is calculated for both gaps, bottom, and top. The linear

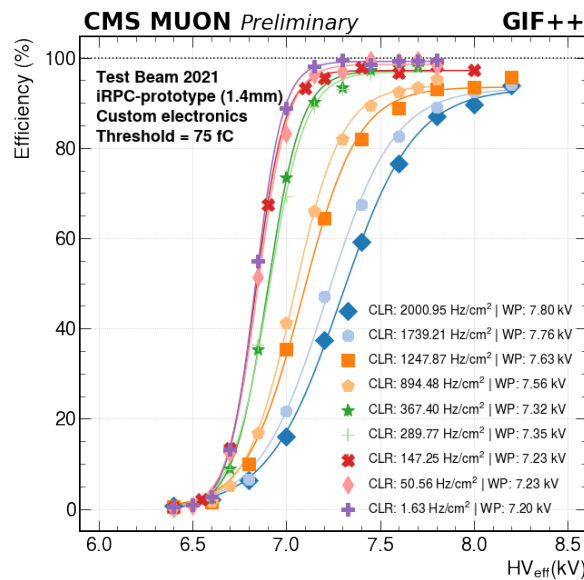
Figure 83 - Density current as a function of high voltage for various rates



Legend: The current is higher in the bottom gap. It is noted the increase in the WP as the rate increases.

Source: The author, 2023.

Figure 84 - Muon efficiency in function of the high voltage for various rates

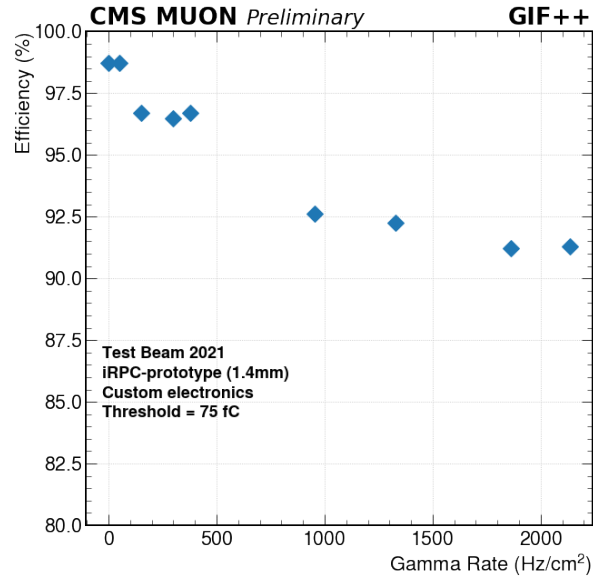


Legend: The increase in the working point is evidenced by the shift of the curve to the right with respect to the rate

Source: The author, 2023.

behavior is obtained as expected. Figure (87) shows WP versus gamma rate. As observed in the efficiencies sigmoid curves it is possible to see a shift of 650 V in the WP from source off condition to rate 2 kHz/cm².

Figure 85 - Muon efficiency at the working point as a function of the gamma rate at the working point



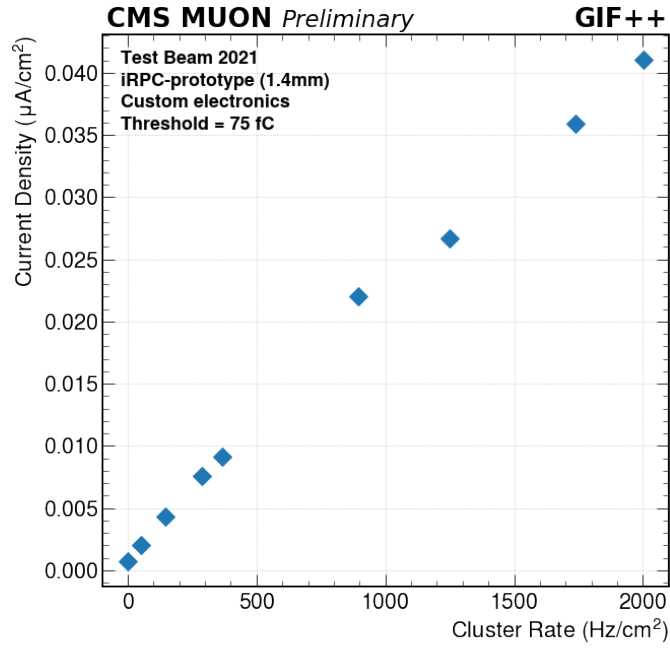
Legend: The drop in the efficiency with the increase of the rate is observed. However, the chamber efficiency is still higher than 90 %.

Source: The author, 2023.

Figure (88) shows the current density drawn in the top gap and Figure (89) shows the current density drawn in the bottom gap, respectively, as a function of HV_{eff} with a lower threshold (45 fC, 0.3 mV). The legend represents the cluster rate at the WP for each measurement as well as the WP itself. Compared to the 75 fC threshold results, currents are similar while the rates at the WP are lower.

Figure (90) shows the efficiency comparison between the two thresholds without gamma background and Figure (91) shows the measurement with the highest rate achieved with the chamber during the beam test in 2021. The tracking system was not used in both plots because it was not available during the 45 fC measurements. With source off without gamma background, the WP is similar in both cases (≈ 7.2 kV), while in the highest rate situation, it is 7.83 kV with 75 fC configuration and 7.59 kV with 45 fC configuration. This means that the WP is around 0.39 kV less than with the lower threshold configuration. This is evidenced by the shift between the two curves.

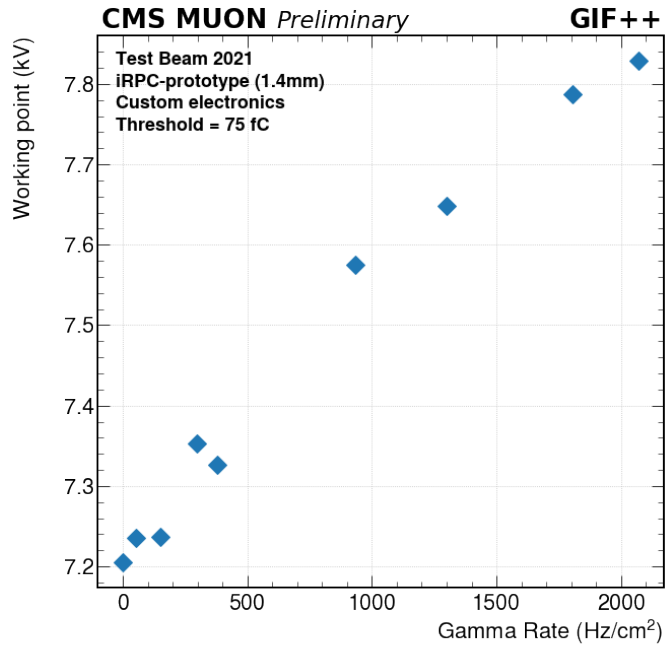
Figure 86 - Density current as a function of the cluster rate



Legend: As expected, the linear behavior is observed.

Source: The author, 2023.

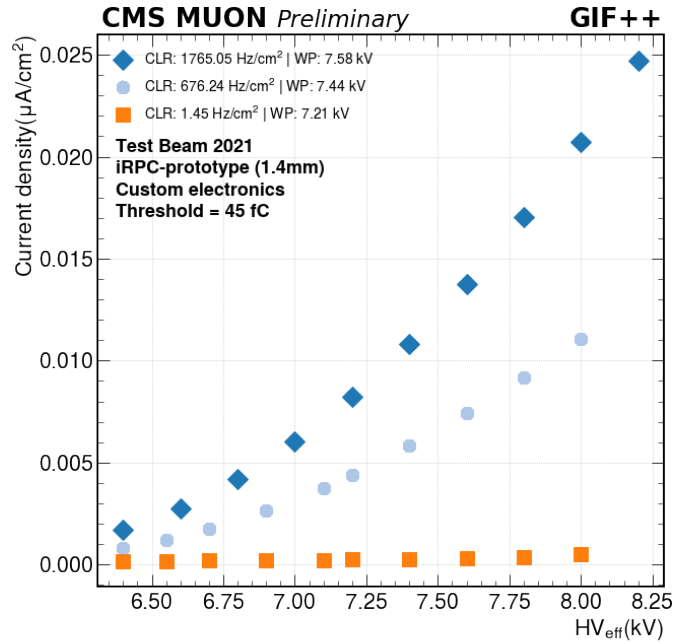
Figure 87 - Working point as a function of the gamma rate



Legend: The higher the rate, the higher the WP. The increase at the WP is around 600 V

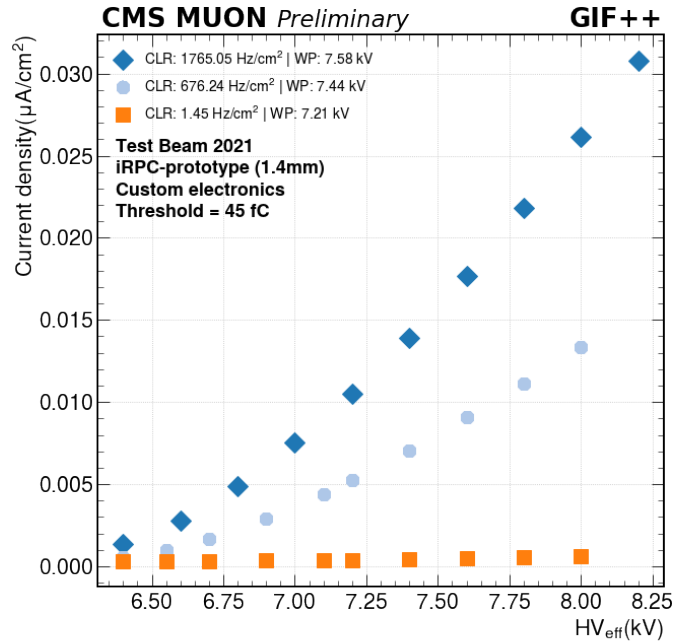
Source: The author, 2023.

Figure 88 - Current density in the top gap as a function of the effective voltage



Legend: The value of the currents are similar as in the case of 75 fC.
 Source: The author, 2023.

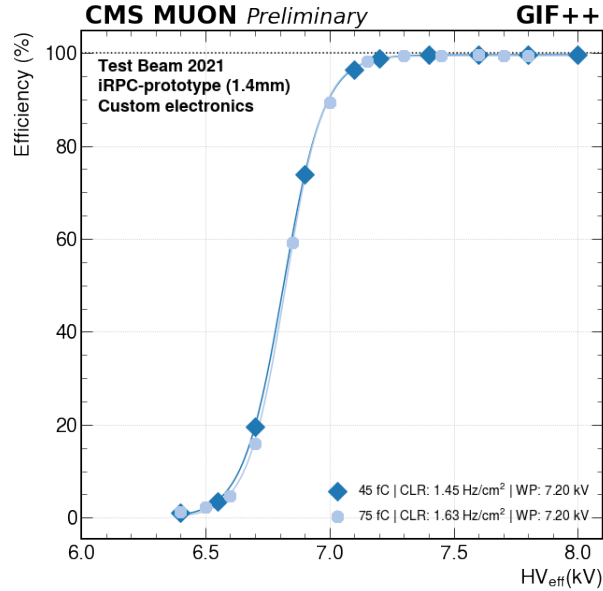
Figure 89 - Current density in the bottom gap as a function of the effective voltage



Legend: The value of the currents are similar as in the case of 75 fC as well.

Source: The author, 2023.

Figure 90 - Efficiency comparison between threshold 45 fC and 75 fC without gamma rate



Legend: As there is no gamma rate background the curves are practically the same.

Source: The author, 2023.

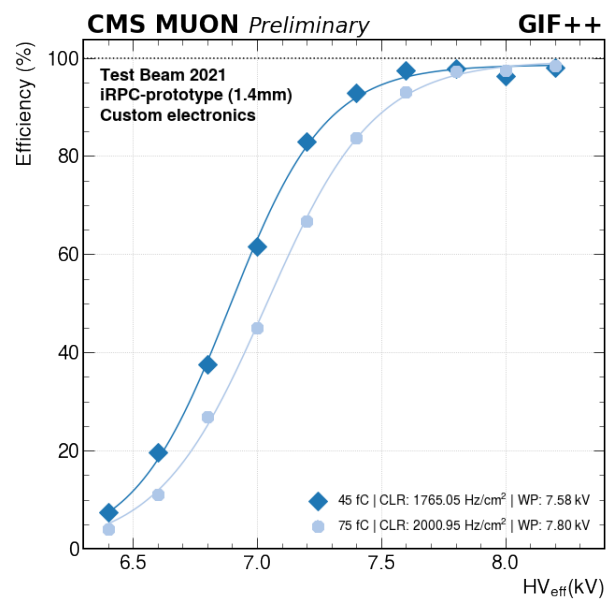
Figure (92) shows the ohmic current¹⁷ versus integrated charge in the top gap and Figure (93) shows the ohmic current versus integrated charge in the bottom gap, respectively. Each point is taken weekly without a gamma background at 5 kV for a given integrated charge. After each measurement, the chamber is irradiated again accumulating more charge, then one week later another experimental point is taken. There are 7 points at integrated charge 4 mC/cm². After the highest value of current at this point was obtained (around 0.3 μ A for both gaps) the chamber was turned off between the weekly measurements, therefore the current went down, reducing the currents in both gaps. The current in the top gap increases between 20 mC/cm² and 46 mC/cm² and drops again around 50 mC/cm². However, The current in the bottom gap is increasing until the last point and the cause is under study.

Figure (94) shows the physics current¹⁸ versus integrated charge in the top gap and Figure (95) shows the physics current versus integrated charge in the bottom gap,

¹⁷ In this detector, the ohmic current is defined as the current at 5 kV. Normally, the ohmic current in an RPC is the current measured in a voltage where the RPC current is not affected by the gas amplification effects.

¹⁸ Physics current is the operating current minus the extrapolation of the ohmic current at the same voltage.

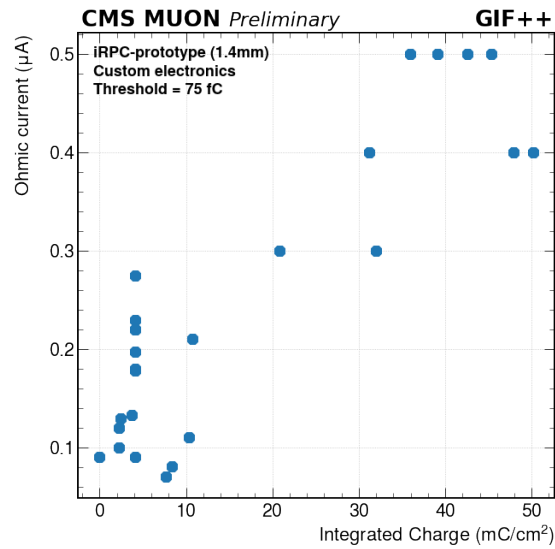
Figure 91 - Efficiency comparison between threshold 45 fC and 75 fC with gamma rate



Legend: It is possible to see that the WP is lower in the 45 fC configuration. This means that by lowering the electronics threshold the detector operates with a lower voltage.

Source: The author, 2023.

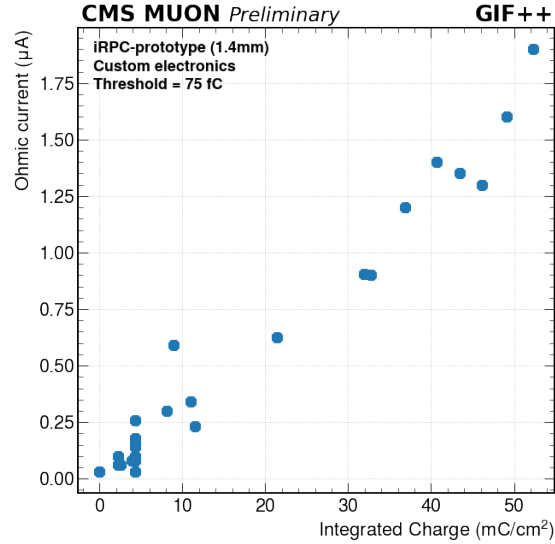
Figure 92 - Ohmic current as a function of the integrated charge in the top gap



Legend: In principle, at 50 mC/c^2 the current value is acceptable. The points at integrated charge 4 mC/cm^2 show that the current can reduce if the irradiation stops, that is, the current was around $0.28 \mu\text{A}$, and after stopping the irradiation, the current went down to around $0.1 \mu\text{A}$.

Source: The author, 2023.

Figure 93 - Ohmic current as a function of the integrated charge in the bottom gap

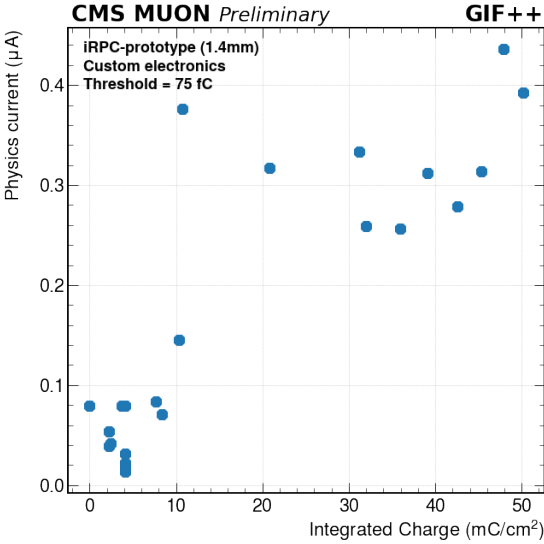


Legend: In the bottom gap, the current is constantly increasing. More studies will be done to understand what might be causing this.

Source: The author, 2023.

respectively. Each point is taken with the source off at 7.2 kV for a given integrated charge. The same measurement strategy used in the ohmic current measurement is considered here. It is desirable currents lower than $0.5 \mu\text{A}$, which is seen in the top gap in all points. On the other side, the bottom gap has values greater than $0.5 \mu\text{A}$ between $20 \text{ mC}/\text{cm}^2$ and $30 \text{ mC}/\text{cm}^2$, while the last value is around $0.5 \mu\text{A}$.

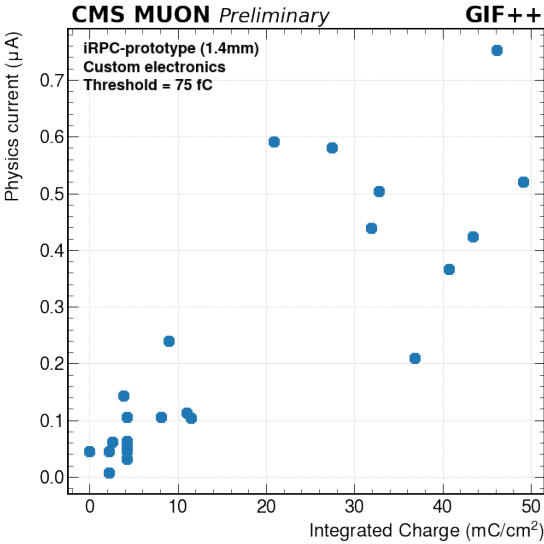
Figure 94 - Physics current as a function of the integrated charge in the top gap



Legend: The physics current in the top gap is well controlled as it is lower than 0.5 μA .

Source: The author, 2023.

Figure 95 - Physics current as a function of the integrated charge in the bottom gap



Legend: The physics current in the bottom gap, the current is higher than 0.5 μA in some points. Still, in the last point, it is close to μA . More studies will be done to understand this issue.

Source: The author, 2023.

4 ASSOCIATED PRODUCTION OF J/ψ AND D^* WITH THE CMS DETECTOR

In this chapter, the measurement of the associated production of J/ψ and D^* in the CMS detector is discussed. The data used are from the LHC Run 2 and were collected from proton-proton collisions at the center-of-mass energy of $\sqrt{s} = 13$ TeV in 2016, 2017, and 2018. The motivations are covered in Section (4.1.1). The datasets and Monte Carlo samples are discussed in Section (4.2). The selection strategy is covered in Section (4.3), where selection cuts, cuts optimization, and triggers are described. Still in this section, acceptance studies to optimize Monte Carlo production is detailed. The signal extraction is detailed in Section (4.4), where the probability density functions and the fitting strategy are discussed. Sections (4.5) and (4.6) are dedicated to the acceptance and efficiencies calculations, respectively. The systematic uncertainties are calculated in Section (4.7). Section (4.8) is dedicated to the calculation of the total cross-section and the contributions due to SPS and DPS. Furthermore, the sigma effective is extracted and the value is compared with other measurements. Finally, the results and conclusions are discussed in Section (4.9).

4.1 Introduction of Analysis

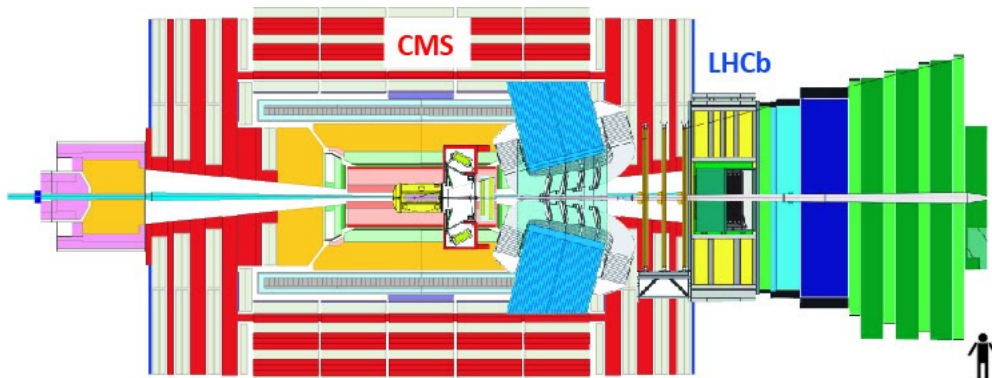
Due to the high energy and luminosity at the LHC, charm production studies can be done with great precision. Furthermore, the cross-section of open charm (164) and charmonium (165) production is large. Moreover, the production of double charmonium and charmonium associated with open charm helps in understanding the quarkonium production mechanism (166). Besides that, it also helps in understanding Multiple Parton Scattering and non-relativistic QCD.

4.1.1 Motivations

The LHCb experiment measured the J/ψ meson associated with open charms (D^0 , D^+ , D_s^+ , Λ_c^+) in the forward region (167) with Run 1 data. In addition to the fact that the CMS experiment never performed this measurement, this study covers a kinematic region complementary to that studied in the LHCb. Recent studies (168) have shown this fact. The LHCb study covered the region $2 < |y| < 4.5$ and $3 < p_T < 12$ GeV/c for D^* and $2 < |y| < 4$ and $p_T < 12$ GeV/c for J/ψ while this thesis covers the region $|y| < 2.4$ and $4 < p_T < 60$ GeV/c for D^* and $|y| < 2.4$ and 16 GeV/c $< p_T < 100$ GeV/c for J/ψ .

Figure (96) shows the difference between CMS and LHCb detectors (169).

Figure 96 - Comparison between CMS and LHCb



Legend: Note that the LHCb is a frontal detector well-designed for high pseudorapidity measurements ($2 < y < 5$) (170), while the CMS detector covers the central region ($|y| < 2.5$) (171).

Source: CMS LHCb, 2022.

In addition, Figure (97) indicates that for energies from approximately 1 TeV the DPS contribution to the total cross-section starts to become important. The leading-order collinear factorization approach is used in this estimation (172) for $pp \rightarrow c\bar{c} X$ and $pp \rightarrow c\bar{c}c\bar{c} X$ processes. For center-of-mass energies around 13 TeV, *i.e.* the LHC energy in LHC Run 2, the DPS contribution (right figure) to the total cross-section in $pp \rightarrow c\bar{c}c\bar{c} X$ is expected to be much higher than the SPS contribution (left figure).

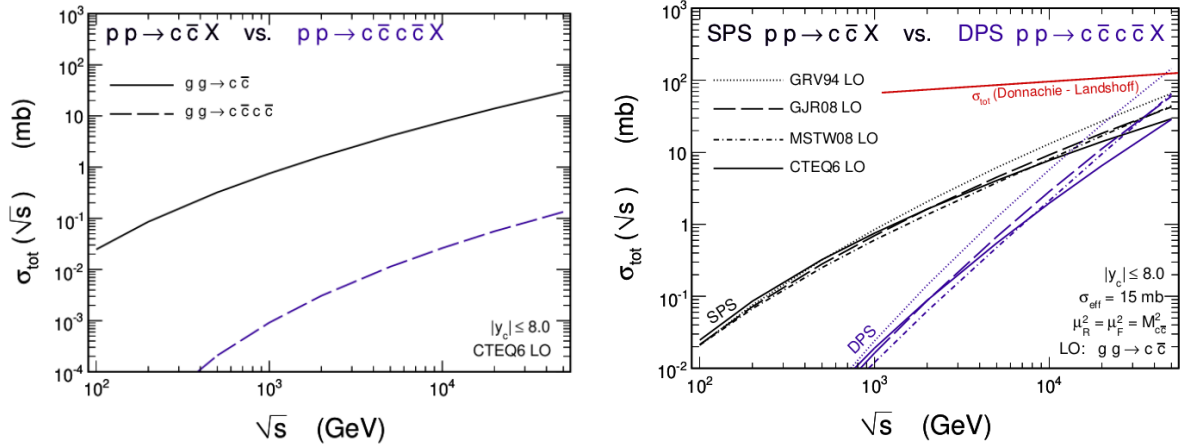
Finally, one of the biggest motivations is the calculation of the σ_{eff} and its comparison with other experiments.

4.2 Datasets and Monte Carlo Samples

The primary datasets are collision data that are composed of fragmented data from the sub-detectors. They provide collision data containing information of physics objects, *i.e.*, electrons, muons, jets, tracks, vertices, etc (173). The type of the dataset is defined according to the type of the physics objects, the data format, and whether it should be used for performance studies, calibration and alignment, and physics analysis (174). This kind of data can be obtained in secondary datasets/dedicated skims, which are special datasets for dedicated analysis.

In the context of physics analysis, the type of primary dataset is defined as a function of the particle candidates that are reconstructed by the HLT. The format of the collision data is known as Analysis Object Data (AOD), while the simulated events are known as AODSIM. With the start of Run 2, a new format super-seeded from the AOD

Figure 97 - The DPS and SPS contributions to the cross-section.



Legend: The figure in the left shows the expected SPS cross-section for both $pp \rightarrow c\bar{c} X$ and $pp \rightarrow c\bar{c}c\bar{c} X$ processes. The Figure on the right compares the SPS contribution to the $pp \rightarrow c\bar{c} X$ process with the DPS contribution to the $pp \rightarrow c\bar{c}c\bar{c} X$ process. When considering the double production of $c\bar{c}$ the expected SPS contribution (left) to the total cross-section (where the total is the sum of SPS and DPS process) is around 1% at a center-of-mass energy of $\sqrt{s} = 13$ TeV.

Source: SZCZUREK, 2015, p. 10; SCHÄFER ; SZCZUREK, 2012, p. 9-10.

format appeared, MiniAOD. This dataset is a reduced version of AOD, one-tenth of its size. This analysis uses another dataset format that is covered in Section (4.3).

Different types of Monte Carlo generators are used. Simulation of the proton-proton collisions and quark hadronization is performed by the Pythia 8.1 package (175). This package is well-suited for the generation of high-energy collisions. It contains multiple models and, for the purpose of this analysis, it includes multiple parton-parton interactions, which are necessary to generate a double parton scattering sample. To produce the decays of interest the Evtgen package is used (176). This is an event generator well suited for b-physics, where it provides models for semileptonic decays and Charge-Parity-violation (CP-violation) decays. It also includes angular distributions in sequential decays. To simulate the Single Parton Scattering Helac-Onia package is used before Pythia to produce Les Houches Events (LHE) Files¹⁹. It generates the matrix elements for the calculation of the heavy quarkonium helicity amplitudes with the use of nonrelativistic QCD factorized (178).

¹⁹ This is a generic format used by the Monte Carlo generators which organize the matrix elements, showering, and hadronization data in a common way (177)

4.2.1 Dataset samples

This study is performed using all Run 2 (2016, 2017, and 2018) Ultra Legacy (UL) data, containing around 137.85 fb^{-1} of integrated luminosity. The UL data is a reprocessing of all Run 2 data with improved reconstruction and calibration algorithms. The primary dataset used is Charmonium AOD. The list with all datasets as well as the JSON²⁰ files used in this analysis are shown in Table (11).

After selecting the datasets a dedicated code (179) is used to convert the AOD format to a format called NanoAODPlus. This is described in Section 4.3.

4.2.2 Monte Carlo Samples

The Monte Carlo samples used are J/ψ particle gun, D^* particle gun, Double Parton Scattering MC, and Single Parton Scattering MC. The description of each sample is given in the bullets below.

- **J/ψ particle gun:** This sample is produced with Pythia8ptGun. The events are generated with flat p_T and η distributions. It is used to study muon and J/ψ acceptance.
- **D^* particle gun:** This sample is also produced with Pythia8ptGun and with flat p_T and η distributions. It is used to study D^* acceptance.
- **Double Parton Scattering Monte Carlo:** This sample generates $J/\psi D^*$ events in double parton scattering mode. The events are produced in Pythia8 using CP5²¹ tune. EvtGen is used to force the decay of the D^0 meson, while filters are used to guarantee $J/\psi \rightarrow \mu^+ \mu^-$ and $D^* \rightarrow D^0 \pi_s$.
- **Single Parton Scattering Monte Carlo:** This sample uses Helac-Onia to generate LHE files with J/ψ and c quarks for producing D mesons. Pythia 8 is responsible for the hadronization. As in the DPS sample, Pythia is used for hadronization, and Evtgen is used to force the decay.

The particle gun sample has been privately produced and the instructions for producing it are highlighted in Appendix B. The DPS samples are divided into three different productions. Each sample is produced for a given dimuon p_T range. That was

²⁰ The JSON file contains a list with good quality runs that can be used to analyze the data.

²¹ CP stands for "CMS Pythia8" and CP5 is its fifth version. This is a tune that uses NNLO to describe well the observed data.

Table 11 - Run-2 datasets and corresponding JSON files.

Charmonium AOD 2016
JSON: Cert_271036-284044_13TeV_Legacy2016_Collisions16_JSON /Charmonium/Run2016B-21Feb2020_ver1_UL2016_HIPM-v1/AOD /Charmonium/Run2016B-21Feb2020_ver2_UL2016_HIPM-v1/AOD /Charmonium/Run2016C-21Feb2020_UL2016_HIPM-v1/AOD /Charmonium/Run2016D-21Feb2020_UL2016_HIPM-v1/AOD /Charmonium/Run2016E-21Feb2020_UL2016_HIPM-v1/AOD /Charmonium/Run2016F-21Feb2020_UL2016-v1/AOD /Charmonium/Run2016F-21Feb2020_UL2016_HIPM-v1/AOD /Charmonium/Run2016G-21Feb2020_UL2016-v1/AOD /Charmonium/Run2016H-21Feb2020_UL2016-v1/AOD
Charmonium AOD 2017
JSON: Cert_294927-306462_13TeV_UL2017_Collisions17_GoldenJSON /Charmonium/Run2017B-09Aug2019_UL2017-v1/AOD /Charmonium/Run2017C-09Aug2019_UL2017-v1/AOD /Charmonium/Run2017D-09Aug2019_UL2017-v1/AOD /Charmonium/Run2017E-09Aug2019_UL2017-v1/AOD /Charmonium/Run2017F-09Aug2019_UL2017-v1/AOD
Charmonium AOD 2018
JSON: Cert_314472-325175_13TeV_Legacy2018_Collisions18_JSON /Charmonium/Run2018A-12Nov2019_UL2018_rsb-v1/AOD /Charmonium/Run2018B-12Nov2019_UL2018-v1/AOD /Charmonium/Run2018C-12Nov2019_UL2018_rsb_v2-v2/AOD /Charmonium/Run2018D-12Nov2019_UL2018-v1/AOD

Legend: Run-2 Datasets used in this analysis. There are two different scenarios in 2016, the pre-VFP era and the pos-VFP era. The former refers to a period of data taking where CMS had an issue with high energy deposition in SiStrip sensors, causing saturation of the analog pipeline voltage mode (APV) front-end chip. The latter refers to a period when this problem was not present. Note that the pre-VFP era is also known as HIPM or APV.

Source: The author, 2023.

needed because the filter efficiency and the number of events considering one sample with dimuon p_T ranging from 9 to 100 GeV/c are enormous. Note that the AODSIM format is used as the primary dataset in the same way the AOD is used in the real data. Therefore, the conversion of AODSIM to NanoAODPlus is described in section (4.3) as well. All MC samples are shown in Appendix (D).

4.2.3 Monte Carlo Weighting

To properly compare data and MC corrections must be applied. All Monte Carlo samples must be normalized to the process cross-section so the correct number of events in the MC histograms are obtained. This weight is calculated as

$$weight = \frac{N_{events}^{data}}{N_{events}^{MC}}, \quad (25)$$

where N_{events}^{data} is the number of signal events in data determined by the fit and N_{events}^{MC} is the number of signal events in MC after all selection cuts.

Another important weight is the pile-up correction. Although in the DIGI2RAW²² step of the MC production the pile-up simulation is already considered, the number of vertices in the MC simulation is not the same number obtained with the real data. Therefore, a correction must be applied so that the MC can describe data correctly. The strategy for getting these weights is highlighted in Appendix E.

Finally, as muons are present in the final state, scale factors for identification and reconstruction are used to correct the muon distributions. Both scale factors are provided by the Muon Physics Object Group (POG) and are given in function of p_T and η (180, 181, 182).

4.2.4 Monte Carlo Matching

To guarantee that the reconstructed particles, *i.e.*, the particles that were generated and were submitted to the detector reconstruction, are compatible with the generated particle, a matching must be performed. This is done by comparing the kinematic variables of the final reconstructed particles and the generated particles. When a Monte Carlo generator is used to produce physics events, the generated particles produced are

²² DIGI2RAW is a data format where the digitized signals are converted into the RAW (the RAW contains full event information, *i.e.*, the detector information) format, which in turn is provided to the online system.

well known. However, after the simulation of the detector reconstruction, many other particles (due to pile-up, for instance) can appear, *i.e.*, as the detector is not 100% efficient, bad particle reconstruction can happen. Therefore, a criterion on the kinematic variables is imposed to guarantee the proper matching. This is known as Monte Carlo Truth Matching. In the case of the NanoAODPlus ntuple, this is performed with the use of Equations (26), (27), and (28).

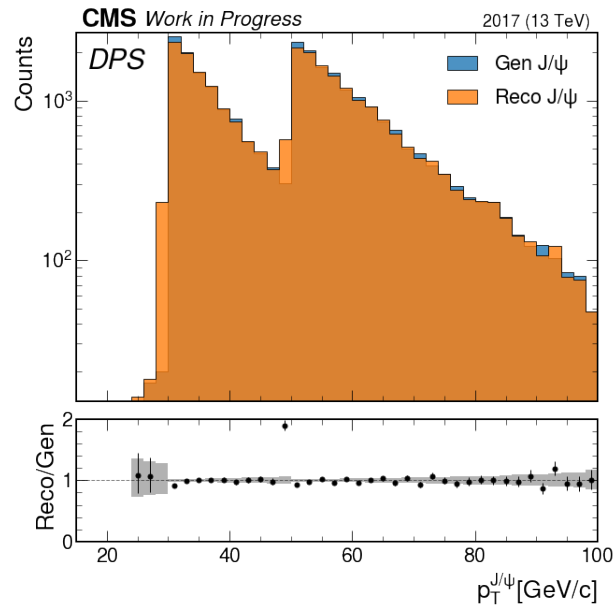
$$|A_{Reco}^{p_T} - A_{Gen}^{p_T}| < 0.1 \text{ GeV}/c \quad (26)$$

$$|A_{Reco}^{\eta} - A_{Gen}^{\eta}| < 0.1 \quad (27)$$

$$|A_{Reco}^{\phi} - A_{Gen}^{\phi}| < 0.1 \text{ rad} \quad (28)$$

where A is the particle in study. In the case of this analysis, it is important to analyze the matching of the oppositely charged muons in the J/ψ mass region ($2.95 \text{ GeV}/c^2 < M_{\mu^+\mu^-} < 3.25 \text{ GeV}/c^2$) and D^* . Figures (98), (99), and (100) show the p_T , η , and ϕ distributions of the generated and reconstructed dimuons using the DPS MC. In the case of D^* the same distributions are shown in Figures (101), (102), and (103). Figures (104), (105), (106), (107), (108), and (109) show the same set of plots in SPS case.

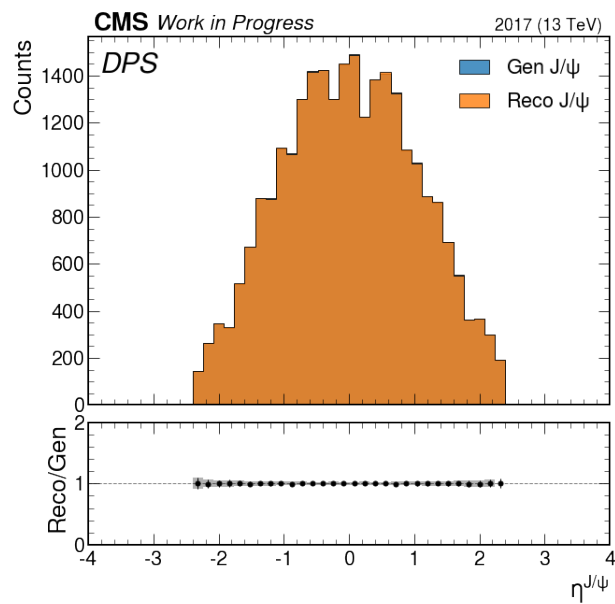
Figure 98 - Transverse momentum distribution of generated and reconstructed dimuons using DPS MC.



Legend: The distribution shows that the reconstructed particles are matched to the generated particles. However, at 30 GeV/c and 50 GeV/c, a large difference can be seen. This happens because of the smearing of the sample.

Source: The author, 2023.

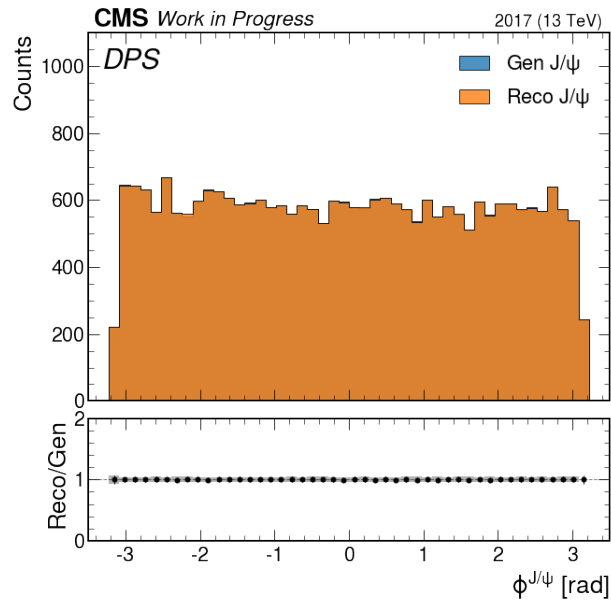
Figure 99 - Pseudorapidity distribution of generated and reconstructed dimuons using DPS MC.



Legend: The distribution shows that the reconstructed particles are matched to the generated particles.

Source: The author, 2023.

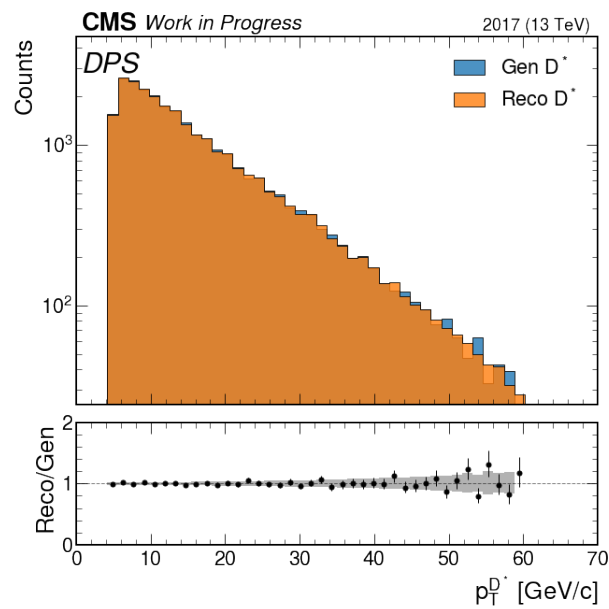
Figure 100 - Phi distribution of generated and reconstructed dimuons using DPS MC.



Legend: The distribution shows that the reconstructed particles are matched to the generated particles.

Source: The author, 2023.

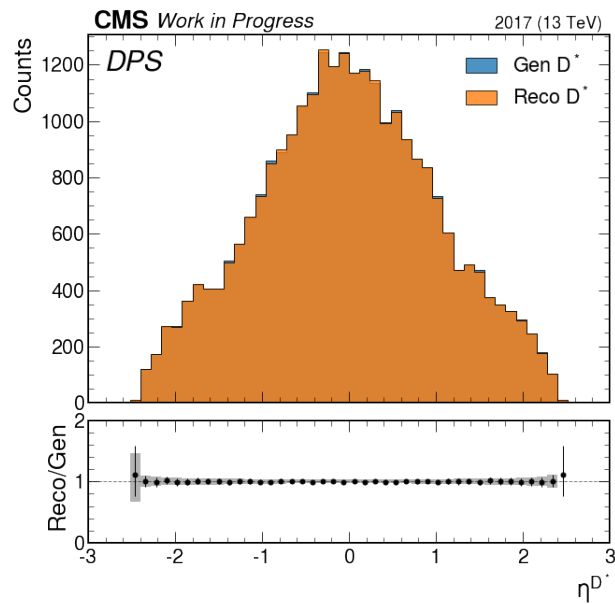
Figure 101 - Transverse momentum distribution of generated and reconstructed D^* using DPS MC.



Legend: The distribution shows that the reconstructed particles are matched to the generated particles.

Source: The author, 2023.

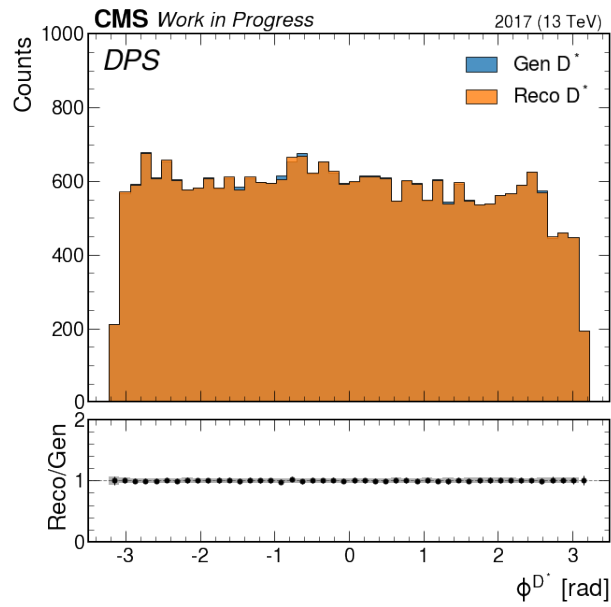
Figure 102 - Pseudorapidity distribution of generated and reconstructed D^* using DPS MC.



Legend: The distribution shows that the reconstructed particles are matched to the generated particles.

Source: The author, 2023.

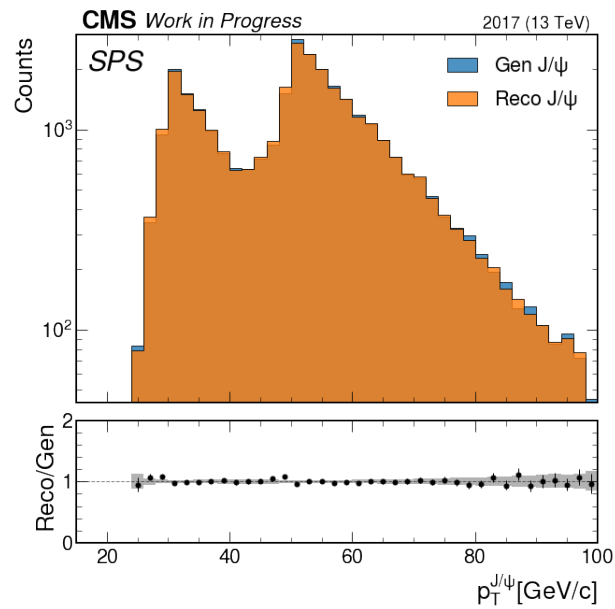
Figure 103 - Phi distribution of generated and reconstructed D^* using DPS MC.



Legend: The distribution shows that the reconstructed particles are matched to the generated particles.

Source: The author, 2023.

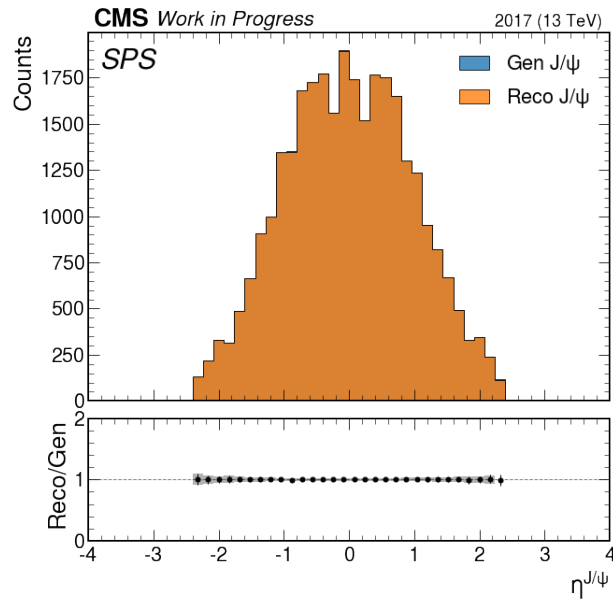
Figure 104 - Transverse momentum distribution of generated and reconstructed dimuons using SPS MC.



Legend: The distribution shows that the reconstructed particles are matched to the generated particles.

Source: The author, 2023.

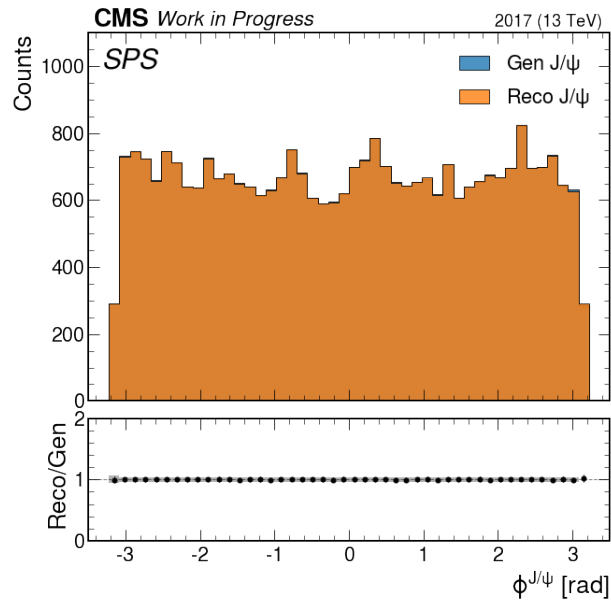
Figure 105 - Pseudorapidity distribution of generated and reconstructed dimuons using SPS MC.



Legend: The distribution shows that the reconstructed particles are matched to the generated particles.

Source: The author, 2023.

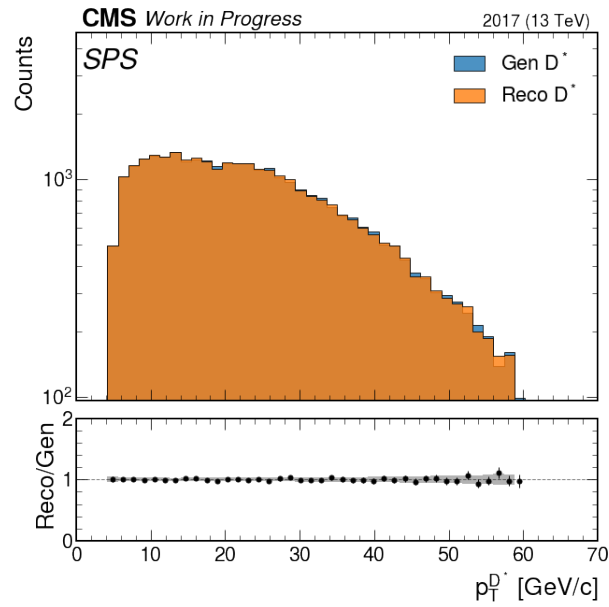
Figure 106 - Phi distribution of generated and reconstructed dimuons using SPS MC.



Legend: The distribution shows that the reconstructed particles are matched to the generated particles.

Source: The author, 2023.

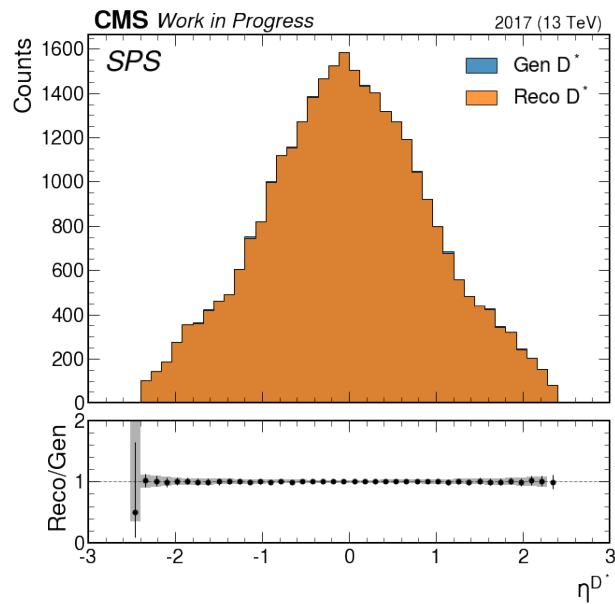
Figure 107 - Transverse momentum distribution of generated and reconstructed D^* using SPS MC.



Legend: The distribution shows that the reconstructed particles are matched to the generated particles.

Source: The author, 2023.

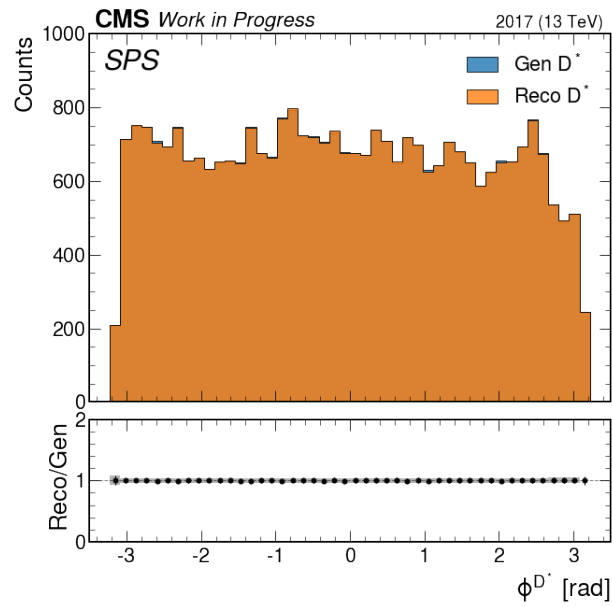
Figure 108 - Pseudorapidity distribution of generated and reconstructed D^* using SPS MC.



Legend: The distribution shows that the reconstructed particles are matched to the generated particles.

Source: The author, 2023.

Figure 109 - Phi distribution of generated and reconstructed D^* using SPS MC.



Legend: The distribution shows that the reconstructed particles are matched to the generated particles.

Source: The author, 2023.

Therefore, the reconstructed particles have a good match with the generated particles. This means that the Monte Carlo can be compared with the real data.

4.3 Selection Strategy

After selecting the primary dataset, a C++ code is used to convert the AOD data format to NanoAODplus. This data format is very similar to NanoAOD, *i.e.* it is a flat ntuple, meaning that it does not use the CMS Event Data Model (EDM), instead, all elements on this ntuple are readable with bare ROOT (183). It is worth mentioning that some EDM features are accessible in NanoAOD, where it contains a main TTree element containing several scalar branches. If the branches of a NanoAOD file are compared with a NanoAODplus file, it is possible to see that the latter contains information about D^0 and D^* mesons with very minor selection criteria. Besides, there is also a collection called *Dimu*, which contains two muons combined in the same object, with very minor selection criteria. These preselection cuts are discussed in the next subsection.

4.3.1 Preselection Cuts

When converting AOD format to NanoAODPlus, preselection cuts are already applied to identify dimuons and D mesons objects with a minimal quality. The *Dimu* collection comes with Soft and Global muons (this classification is commented in Section (4.3.3)) from the same vertex (not necessarily primary). In turn, D^* and D^0 comes with the following preselection cuts,

- Maximum relative track distance, separately in z and xy, for K and π from D^0 : **0.5 cm**.
- Maximum distance in z and xy for slow π track from D^0 vertex: **2 cm**.
- Maximum z distance of primary vertex from D^0 vertex to be considered for arbitration: **2 cm**.
- Maximum distance in z and xy for tracks from D^0 vertex for track sums: **0.5 cm**.

The other cuts used in the analysis level can be seen in Section (4.3.3).

4.3.2 High Level Trigger

In the NanoAODPlus ntuple, the trigger information is available, where each HLT path is saved in the TTree Events as a boolean. An event is considered to pass the trigger when the boolean of the HLT path is *True*. For all years the events are selected with a dimuon trigger, requiring opposite-sign muon pair. The path used in 2016 is HLT_Dimuon16_Jpsi while in 2017 and 2018 is HLT_Dimuon25_Jpsi, both designed for analysis with J/ψ mesons. For both triggers, the χ^2 probability of the fit of position and momenta for each muon to the common vertex is greater than 0.5%, the distance of closest approach between the two muons is smaller than 0.5 cm, the invariant mass of the dimuon pair is between 2.9 GeV/c² and 3.3 GeV/c² and maximum $|\eta|$ is 2.5. In 2016, the minimum p_T of the muon pair is 15.9 GeV/c while in 2017 and 2018 it is 24.9 GeV/c. The trigger efficiency is calculated in Section (4.6.3).

4.3.3 Selection Cuts

To improve the signal detection it is necessary to apply quality cuts in both objects, J/ψ and D^* . These quality cuts are based on previous analysis (184, 185) and, some of them, are subjected to a dedicated study with figures of merit to fine-tune their selection. This is explained in the next section.

Soft ID muons are required to reconstruct J/ψ . This muon ID²³ is optimized for quarkonia analysis, where low- p_T ²⁴ muons are well identified. Furthermore, muons reconstructed in this category are tracker muons that have a tracker track with high purity, using hits from at least six layers of the inner tracker, where at least one comes from the pixel detector. This reconstruction algorithm requires tight segment matching for the tracker muon, where it is loosely compatible with the primary vertex. The longitudinal impact parameter $|dz|$ is smaller than 20 cm and the transversal impact parameter $|dxy|$ is smaller than 0.3 cm (186).

In addition, muons with p_T greater than 3 GeV/c are required, as from this value the reconstruction efficiency of such muons is high enough to guarantee well reconstructed muons. Finally, a cut on the pseudorapidity is performed, $|\eta| < 2.4$, because this is the limit of the CMS detector. All J/ψ cuts are summarized in Table (12).

The D^* meson is reconstructed with three tracks, where one of them is recon-

²³ In CMS, muon selection is characterized by different IDs, where each ID is used for a specific purpose. For example, soft ID selects muons with low- p_T and are well-suited for B-physics and quarkonia analyses.

²⁴ According to the CMS Physics Object Group, a muon is classified as a low p_T muon when its p_T is between 3 GeV/c and 30 GeV/c.

Table 12 - Muons and J/ψ selection cuts.

Cut name	Value
Muon pair charge	0
Dimuon invariant mass	$2.95 < M_{\mu^+\mu^-} < 3.25 \text{ GeV}/c^2$
Muon soft ID	True
Muon p_T	$p_T > 3 \text{ GeV}/c$
Muon $ \eta $	$ \eta < 2.4$
Dimuon p_T	$16 < p_T < 100 \text{ GeV}/c$ (2016) $25 < p_T < 100 \text{ GeV}/c$ (2017/2018)
Dimuon rapidity	$ y < 2.4$

Legend: Selection cuts used to obtain the J/ψ candidates.

Source: The author, 2023.

structured with different cuts. After the selection of the primary vertex and the use of the pre-selection cuts the first selection criteria applied in D^* mesons is on a boolean value found in NanoAODplus, D^* *hasMuon* is selected as *False*. Furthermore, kinematic cuts listed in Table (13) are applied to D^* followed by cuts listed in Table (14), that are applied on the tracks, where tracks are π and K from D^0 from D^* . The track p_T cut is to assure high-efficiency selection, according to track POG studies (187). To assure that the selected tracks are originated from the primary interaction region the following cuts are used: cut in the $\chi^2/n.d.f$ of the track trajectory, cuts in the number of valid tracker and pixel hits, and cut in the impact parameter²⁵ (185, 189).

Table 13 - D^* selection cuts

Cut name	Value
D^* p_T	$4 < p_T < 60 \text{ GeV}/c$
D^* rapidity	$ y < 2.4$

Legend: Selection criteria applied in D^* . Note that only kinematic cuts are applied to this final state.

Source: The author, 2023.

Moreover, D^* also has a third track, known as π_{slow} (slow pion). It has this name because the main fraction of p_T of D^* goes to D^0 as it is much heavier than the mass of π_{slow} . Therefore, this track is known to have a lower p_T when compared with the tracks from D^0 . Because of that, the cuts listed in Table (15) are applied to this track.

Important cuts are also applied on the D^0 from D^* . Those cuts are very important

²⁵ In this case, the impact parameter is defined as the shortest distance between the track and the beam spot (188), which is the region where most of the pp collisions take place (189).

Table 14 - D* tracks selection cuts.

Cut name	Value
Track p_T	$p_T > 1.6 \text{ GeV}/c$
Track $\chi^2/n.d.f$	$\chi^2/n.d.f < 2.5$
Number of valid tracker hits	$> 4 \text{ hits}$
Number of valid pixel hits	$> 1 \text{ hit}$
Transversal impact parameter	$ d_{xy} < 0.5 \text{ cm}$
Longitudinal impact parameter	$ d_z < 0.5/\sin \theta \text{ cm}$

Legend: Selection criteria applied in the tracks from D* (π_{slow} is not considered here).

Source: The author, 2023.

Table 15 - Selection criteria applied in π_{slow} .

Cut name	Value
Track p_T	$p_T > 0.3 \text{ GeV}/c$
Track $\chi^2/n.d.f$	$\chi^2/n.d.f < 3$
Number of valid tracker hits	$> 2 \text{ hits}$

Legend: Selection criteria applied in π_{slow} . Note that the cut in p_T is smaller than that in the other tracks.

Source: The author, 2023.

to reduce the background level. The cut in the pointing angle ($\cos \phi$) assures that D^0 and D^* are well aligned; the cut $D_{PDGmass}^0 - 0.028 < M_{D^0} < D_{PDGmass}^0 + 0.028 \text{ GeV}/c^2$ is used to take the D^0 candidates at the mass peak, so the D^* signal is cleaner; the cut in $D^0 p_T$ is to assure high-efficiency selection, and the cut in D^0 decay length significance is to avoid the high number of vertices close to the primary vertex, which difficult the selection of good candidates. Table (16) shows the applied cuts.

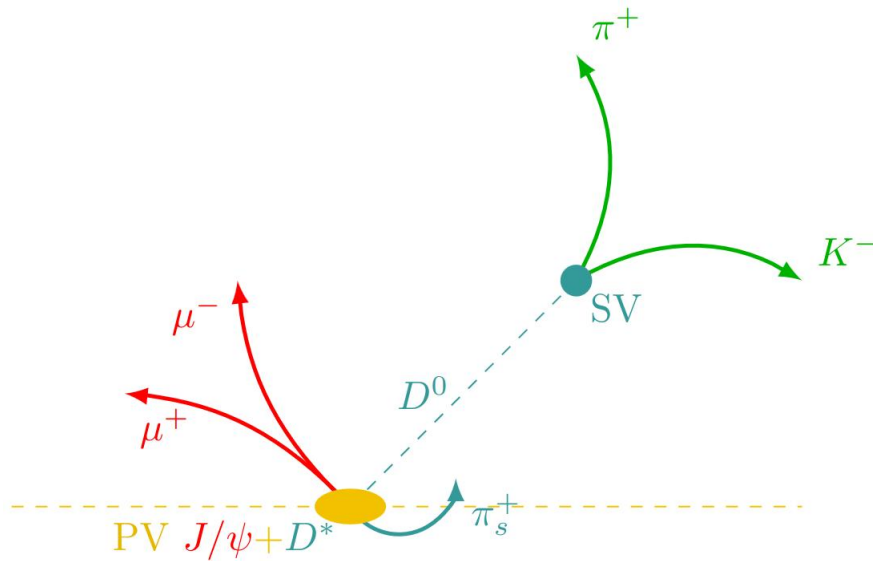
Table 16 - Selection criteria applied in D^0 .

Cut name	Value
D^0 (from D^*) $\cos \phi$ (pointing angle)	$\cos \phi > 0.99$
D^0 (from D^*) PDG mass difference	$D_{PDGmass}^0 - 0.028 < M_{D^0}$ $< D_{PDGmass}^0 + 0.028 \text{ GeV}/c^2$
D^0 (from D^*) p_T	$p_T > 4 \text{ GeV}/c^2$
D^0 (from D^*) decay length significance	$dl_{sig} > 2.5$

Legend: These cuts are very important for improving the signal/background ratio. In the next section, the optimization of the first, third, and fourth cuts is studied.

Source: The author, 2023.

To associate charmonium and open charm candidates a fit of the $\mu^+ \mu^- \pi_{slow}$ vertex is performed. With this strategy, it is possible to reduce the contribution b-hadron to both J/ψ and D^* candidates as well as to guarantee a good vertex association between both particles. Figure (110) shows the association vertex, as well as the secondary vertices with the other particle candidates. Table (17) shows the cut value.

Figure 110 - Association of J/ψ and D^* .

Legend: Note that the required event is at the primary vertex (PV), *i.e.* both particles are expected to be prompt.

Source: The author, 2023.

Table 17 - Vertex probability cut applied to the $\mu^+ \mu^- \pi_{slow}$ common vertex.

Cut name	Value
Vertex probability	associationProb > 0.05

Legend: Selection criteria applied in D*. Note that only kinematic cuts are applied to this final state.

Source: The author, 2023.

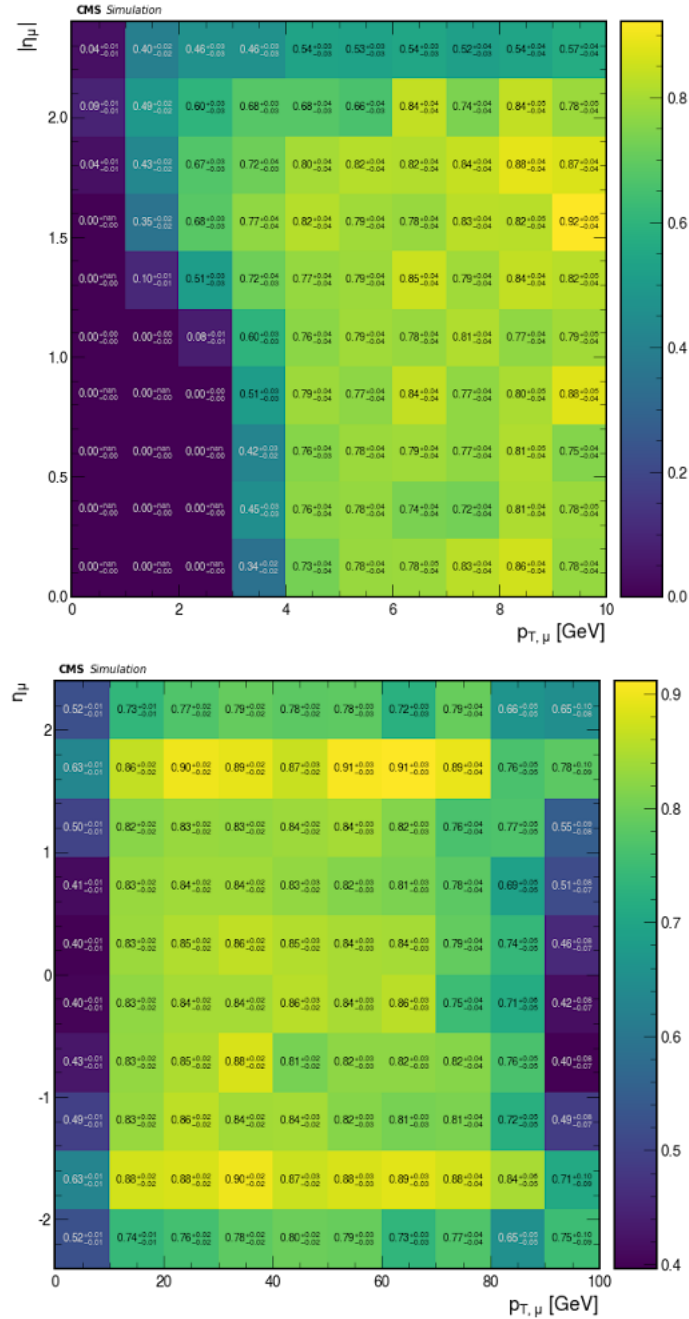
4.3.4 Acceptance studies to optimize Monte Carlo production

As the filter efficiency in the MC generation for the channel studied is low it is very important to optimize the kinematic region where the events are simulated. The optimization of the kinematic region was needed to increase the filter efficiency of the process and reduce the CPU usage during the Official Production of this MC in CMS. To do that, a particle gun MC is used to generate events flat in p_T and in η for both particles, J/ψ and D^* . The idea is to generate samples with loose cuts and from the acceptance values decide which region in p_T and η is suitable. The following conditions are used to produce the samples,

- Dimuons with different charges with invariant mass in the J/ψ mass region, $2.95 < M_{J/\psi} < 3.25 \text{ GeV}/c^2$.
- D^* with right charge (charge of kaon different of charge of pion),
- The ntuple parameter $D^* \text{ hasMuon}$ is selected as *False*,
- $D^* - D^0$ mass difference in the region $0.14 < M_{D^*} - M_{D^0} < 0.16 \text{ GeV}/c^2$,
- To get the 2D histograms the number of reconstructed particles is divided by the number of generated particles.

Figure (111) shows the muon acceptance for two different kinematic regions. From the figures, it is possible to see that for $|\eta| < 1.25$ the detector acceptance is zero for $p_T < 3 \text{ GeV}/c$. Thus, it is possible to conclude that in the endcap the muon reconstruction efficiency is better for low p_T . Between 10 and 100 GeV/c , most of the regions show good detector acceptance.

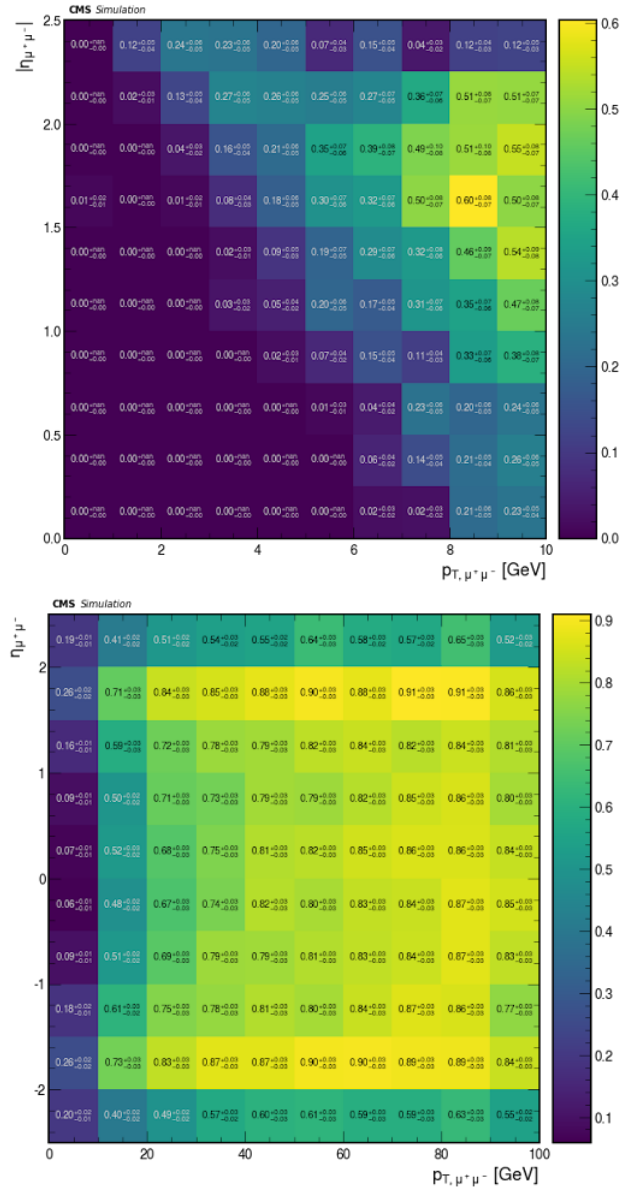
Figure 111 - Muon acceptance with particle gun sample.



Legend: The figure on the top shows muon acceptance in the region $0 < p_T < 10$ GeV/c and $|\eta| < 2.4$ and the figure on the bottom shows muon acceptance in the region $0 < p_T < 100$ GeV/c and $-2.4 < \eta < 2.4$.

Source: The author, 2023.

Figure (112) shows the J/ψ acceptance for two different kinematic regions. From the plots, it is possible to see that for $p_T < 10$ GeV/c the acceptance efficiency of the detector is practically zero. On the other hand, between 10 and 100 GeV/c most of the regions have good acceptance. Figure (113) shows the D^* acceptance for two different kinematic regions.

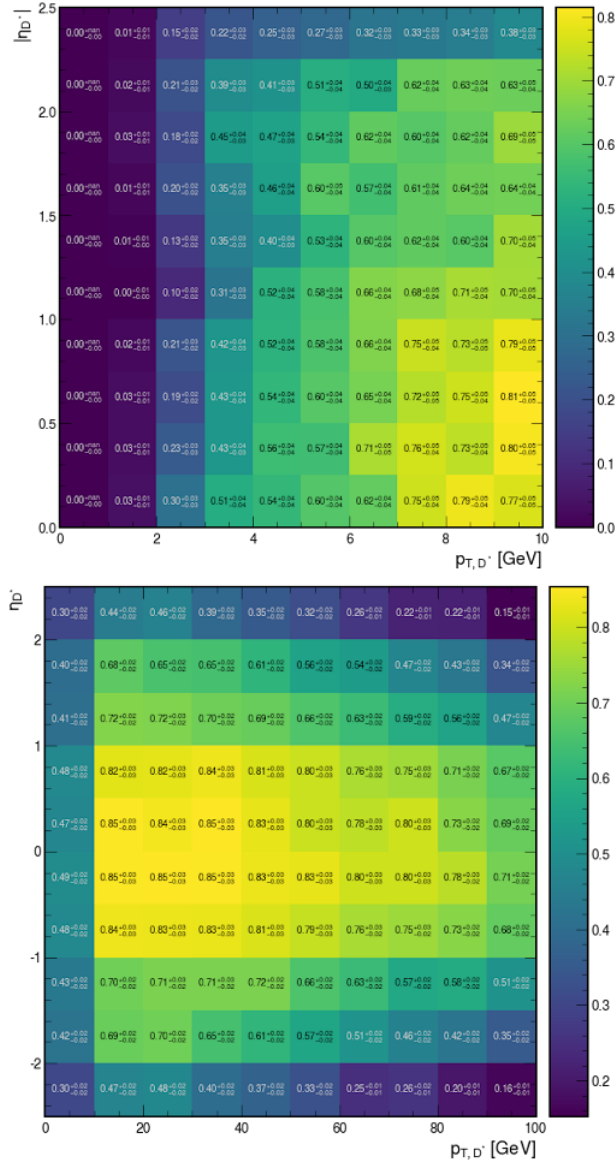
Figure 112 - J/ψ acceptance with particle gun sample.

Legend: The figure on the top shows J/ψ acceptance in the region $0 < p_T < 10$ GeV/c and $|\eta| < 2.5$ and the figure on the bottom J/ψ acceptance in the region $0 < p_T < 100$ GeV/c and $-2.5 < \eta < 2.5$.

Source: The author, 2023.

As there are no candidates in this sample with $p_T < 2$ GeV/c, all bins have zero acceptance. For $p_T > 5$ GeV/c it is already possible to have candidates with acceptance around 60 %. In Figure (113) it is possible to see that the region $-1.0 < \eta < 1.0$ has the best acceptance for the candidates.

Figure 113 - D^* acceptance with particle gun sample.



Legend: The figure on the top shows D^* acceptance in the region $0 < p_T < 10$ GeV/c and $|\eta| < 2.5$ and the figure on the bottom shows D^* acceptance in the region $0 < p_T < 100$ GeV/c and $-2.5 < \eta < 2.5$.

Source: The author, 2023.

4.3.5 Optimization of Selection Cuts

In this section, the optimization strategy for three important cuts is commented. These cuts are shown in the bullets below and the values studied are shown in Table (18).

- Cosine of pointing angle of D^0 from D^* . This is the angle between D^* p_T vector and the D^0 position vector (with reference at the secondary vertex).
- Transverse momentum of D^0 from D^* .
- Decay length significance of D^0 from D^* .

Table 18 - Cuts to be optimized.

Number	Cut name	Values
1	D^0 (from D^*) $\cos(\phi)$	0.999, 0.990 , 0.985, 0.975, 0.960, 0.850, 0.750, 0.500
2	D^0 (from D^*) p_T (GeV/c)	6.0, 5.0, 4.0 , 3.0, 2.0
3	D^0 (from D^*) decay length	3.0 , 2.9, 2.7, 2.5, 2.0, 1.5, 1.0, 0.5

Legend: The values in **bold** are the ones used before the optimization process.

Source: The author, 2023.

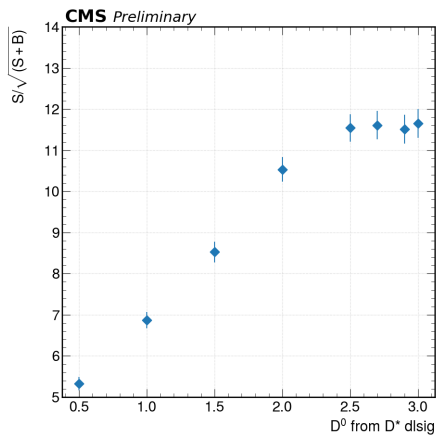
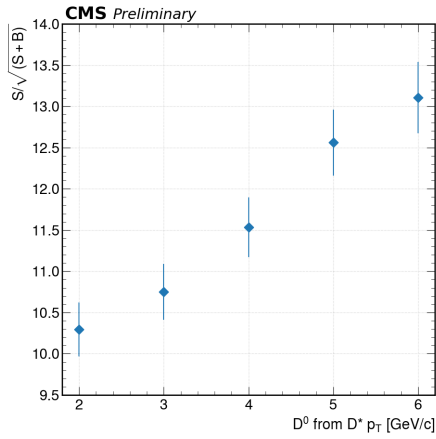
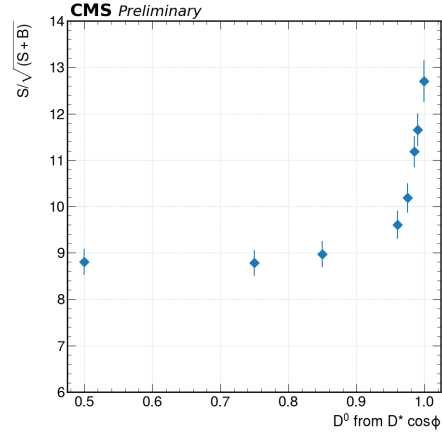
To study the effect of the cuts on the signal quality, sensitivity (pseudo-significance) is used, which is the estimated median significance. Instead of using the observed counts, the expected counts of the input model are used. In other words, the counts from the fitting functions should be used. If a signal is already known from past experiments, the signal (S) is compared with the statistical uncertainty of the signal plus background counts (S + B). This is calculated with Equation (29)

$$SEN = \frac{S}{\sqrt{S + B}}, \quad (29)$$

where S is the number of signal events and B is the number of background events. The use of Equation (29) is good in the sense that it does not diverge for small backgrounds. However, if the background counts are influenced by a systematic uncertainty, this equation can overestimate the proper significance. The goal here is to look for a cut value that maximizes the equation (29). Figure (114) shows plots for the mentioned cuts.

It is possible to see in Figure (114) that the pseudo-significance starts increasing after $\cos \phi = 0.9$. Note that the highest value for the pseudo-significance is achieved at $\cos \phi = 0.999$. However, to preserve the signal statistics the value of 0.990 is used. From Figure (114) the pseudo-significance is increasing more or less linearly with the p_T . The maximum value is at 6 GeV/c. However, as in the first case, the value of 4 GeV/c is used,

Figure 114 - Pseudo-significance versus applied cut.



Legend: Top: Pseudo-significance versus D^0 from $D^* \cos \phi$. Center:
Pseudo-significance versus D^0 from $D^* p_T$. Bottom:
Pseudo-significance versus D^0 from D^* decay length significance.

Source: The author, 2023.

to preserve statistics. Finally, from Figure (114), it is clear that the cuts between 2.5 and 3.0 can be used. Therefore, to preserve statistics and stay away from the values where the pseudo-significance starts to decrease the value of 2.5 is used. Table (19) shows the final value used.

Table 19 - Optimized cuts - final values.

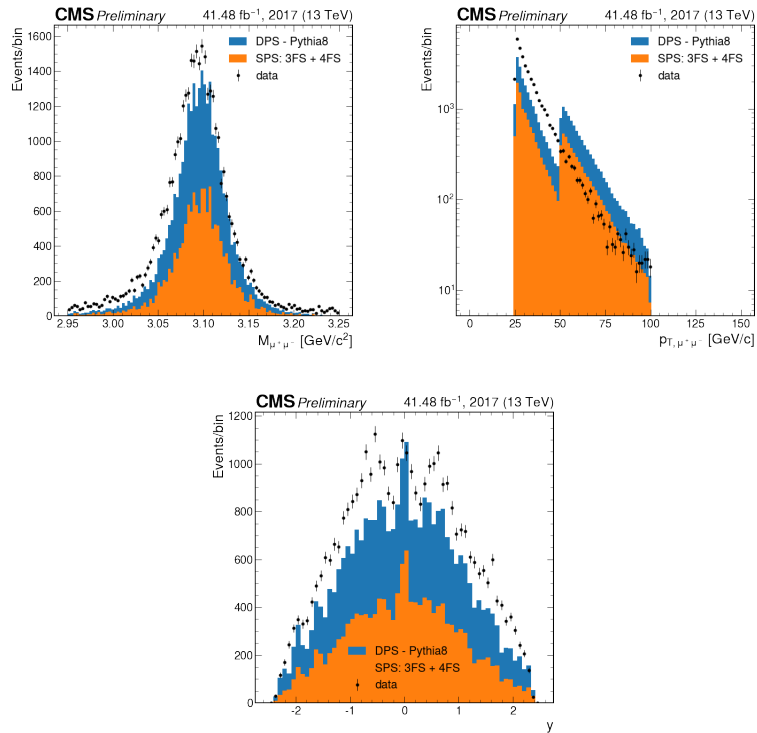
Number	Cut name	Values
1	D^0 (from D^*) $\cos(\phi)$	0.990
2	D^0 (from D^*) p_T (GeV/c)	4.0
3	D^0 (from D^*) decay length	2.5

Legend: The values in **bold** are the ones used before the optimization process.

Source: The author, 2023.

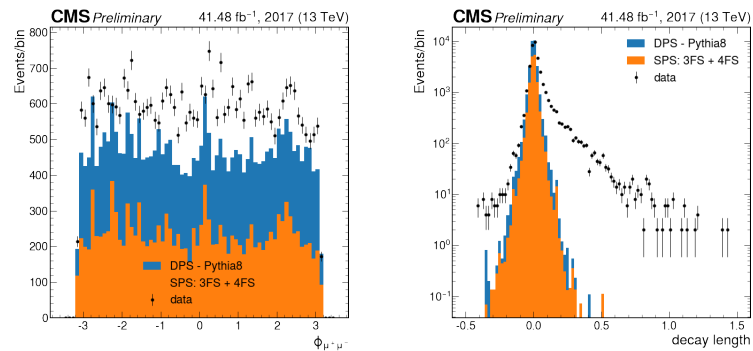
4.3.6 Control Plots

In this section, the main distributions of J/ψ , D^* , and $J/\psi D^*$ are shown. The real data and the SPS and DPS predictions are plotted on the same canvas. It is worth mentioning that the MC plots (DPS and SPS) are stacked. Figures (115), (116), (117), (118), and (119) show the control plots for 2017 data. The plots for other datasets are presented in Appendix (F).

Figure 115 - J/ψ control plots 1 - 2017 data.

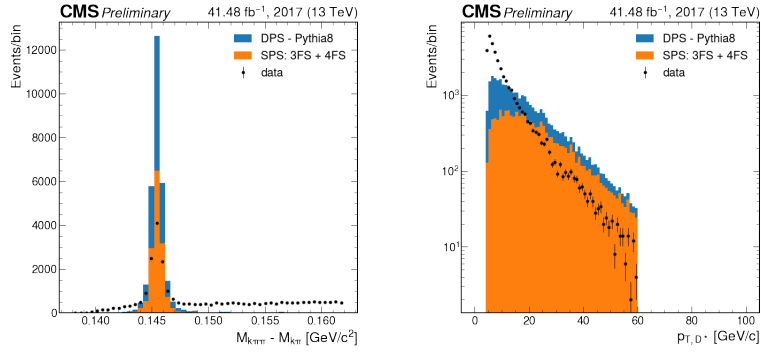
Legend: Top left: $\mu^+\mu^-$ invariant mass. Top right: J/ψ p_T . Bottom: J/ψ rapidity. It is observed that the contributions due to SPS and DPS are not enough to simulate the observed data. Therefore, other processes are needed to simulate it correctly. It is worth mentioning that the simulations for $p_T > 50$ GeV/c have an excess of events due to normalization.

Source: The author, 2023.

Figure 116 - J/ψ control plots 2 - 2017 data.

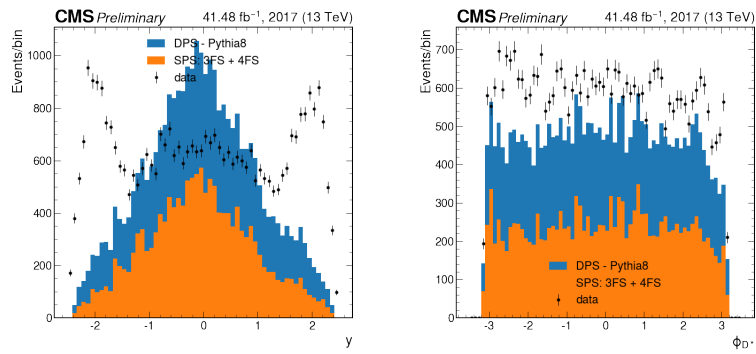
Legend: Left: J/ψ ϕ . Right: J/ψ decay length (mm). It is observed that both SPS and DPS contribute only to prompt J/ψ production.

Source: The author, 2023.

Figure 117 - D^* control plots 1 - 2017 data.

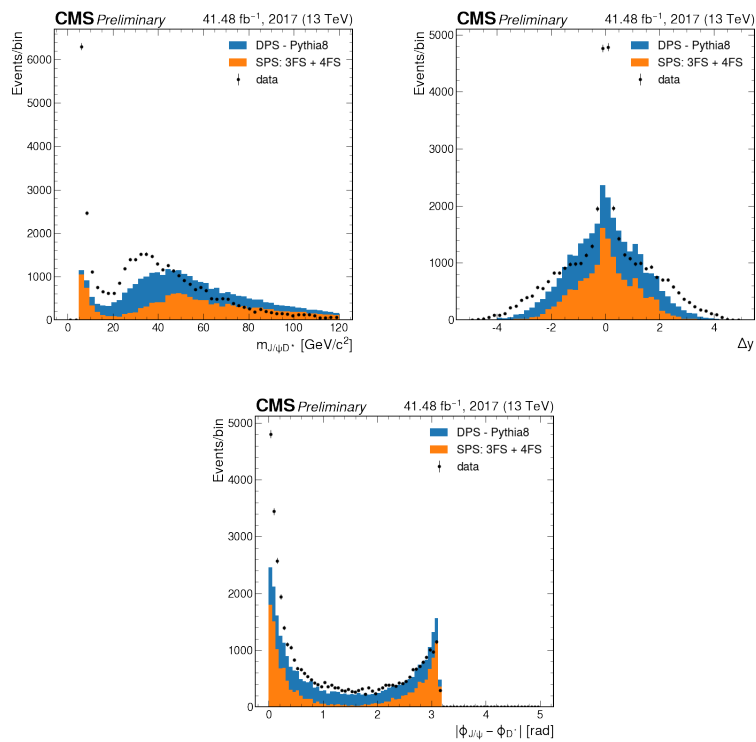
Legend: Left: $D^* - D^0$ mass difference. Right: $D^* p_T$.

Source: The author, 2023.

Figure 118 - D^* control plots 2 - 2017 data.

Legend: Left: D^* rapidity. Right: $D^* \phi$. It is observed that values around $y = \pm 2$ data and MC don't agree. Therefore, other contributions are needed to simulate the observed data

Source: The author, 2023.

Figure 119 - $J/\psi D^*$ control plots 1 - 2017 data.

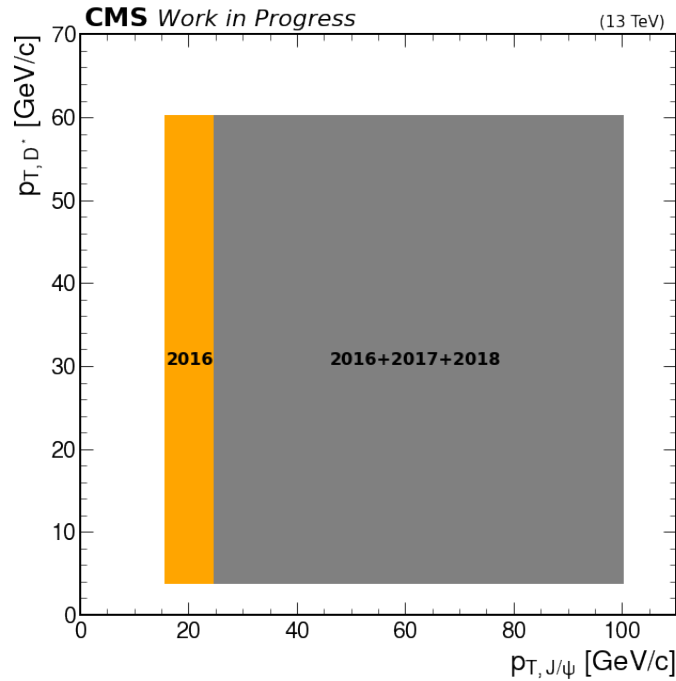
Legend: Top left: $J/\psi D^*$ invariant mass. Top right: $J/\psi D^*$ Δy . Bottom: $J/\psi D^*$ $\Delta\phi$. Note that the peak in the invariant mass region of 5-10 GeV/c² is not well simulated with SPS and DPS. It is possible to see similar peaks at $\Delta y = 0$ and $\Delta\phi = 0$.

Source: The author, 2023.

4.4 Signal Extraction

As commented in Section (4.3.3) the p_T threshold is different in 2016 compared to 2017 and 2018. The phase space is $16 < p_T^{J/\psi} < 100$ GeV/c (2016), $25 < p_T^{J/\psi} < 100$ GeV/c (2017 and 2018), $|y|^{J/\psi} < 2.4$, $4 < p_T^{D^*} < 60$ GeV/c, and $|y|^{D^*} < 2.4$. Figure (120) shows the difference in p_T for each year.

Figure 120 - Phase space as a function of p_T .



Legend: The only difference is in the p_T of J/ψ , where it starts in 16 GeV/c in 2016 and 25 GeV/c in 2017 and 2018.

Source: The author, 2023.

The unbinned non-extended composite model²⁶ is used with the ROOFIT package (190). The final model is composed of three different components:

- $\mu^+ \mu^-$ invariant mass in the J/ψ mass region $2.95 < M_{J/\psi} < 3.25$ GeV/ c^2 .
- Pseudo proper decay length of J/ψ $l^{J/\psi} = L_{xy} \cdot M_{J/\psi} / p_T^{27}$.
- $D^* - D^0$ mass difference given by the difference between the invariant mass of $K\pi\pi$ and $K\pi$ $0.14 < M_{D^*} < 0.16$ GeV/ c^2

²⁶ In the non-extended mode, the PDF coefficients are simply fractions. In addition, the number of coefficients is always less than the number of PDFs.

²⁷ L_{xy} is the most probable transverse decay length in the laboratory frame (191).

The $\mu^+ \mu^-$ invariant mass signal is modeled with the sum of Crystal Ball (CB) and Gaussian with a common mean. The CB guarantees the correct modeling of the initial state radiation, which contributes to events located left to the J/ψ average mass. For the combinatorial background, an exponential function is used. The parameters n and α of the CB have been obtained from the DPS Monte Carlo sample and the values were fixed in the data fit. The invariant mass fits are performed in the region $2.95 < M_{\mu^+\mu^-} < 3.25$ GeV/ c^2 . The functional form of the CB function is

$$CB(m) = \begin{cases} \frac{N}{\sqrt{2\pi}\sigma_{CB}} \exp\left[-\frac{(m-m_0)^2}{2\sigma_{CB}^2}\right], & \text{for } \frac{m-m_0}{\sigma_{CB}} > -\alpha; \\ \frac{N}{\sqrt{2\pi}\sigma_{CB}} \left(\frac{n}{|\alpha|}\right)^2 \exp\left(-\frac{|\alpha|^2}{2}\right) \left(\frac{n}{|\alpha|} - |\alpha| - \frac{m-m_0}{\sigma_{cb}}\right)^{-n}, & \text{for } \frac{m-m_0}{\sigma_{CB}} \leq -\alpha. \end{cases} \quad (30)$$

The J/ψ mesons are produced either in the primary vertex or as a decay from B mesons (B^+ , B^0 , B_s^0 , and B_c^+). The former is called prompt J/ψ and the latter is called non-prompt J/ψ . In this analysis, it is essential to discriminate between the two components. As the prompt DPS and SPS events are the interest it is important to guarantee that D^* is associated with only prompt J/ψ . To discriminate prompt and non-prompt J/ψ candidates the pseudo-proper decay length is used. In principle, non-prompt D^* candidates are expected to be negligible, as the vertex fit cut is used together with the pointing angle cut. This guarantees that the D^* is aligned to the primary vertex and reconstructed to the same vertex as the J/ψ .

To model prompt events a Gaussian resolution function is used to consider the detector resolution. The mean and the standard deviation of this function are estimated in the DPS MC and are fixed in the data, while the other parameters of this function are allowed to float in the data. Besides that, an additional Gaussian is used to take into account the possible errors in the primary vertex assignment. Its parameters are also free and calculated in the fit. To model the non-prompt events an exponential decay is convoluted with the resolution function used to model the prompt part.

In the case of a D^* signal ($D^* - D^0$ mass), Johnson's PDF (192) is used to model the signal peak, and the threshold function (TF) is used to model the background events. Johnson's PDF is well designed to fit a mass difference for charm decay, as is the case. Equation (31) is the functional form for this PDF

$$J = \frac{\delta}{\lambda\sqrt{2\pi}} \frac{1}{\sqrt{1 + \left(\frac{x-\mu}{\lambda}\right)^2}} \exp\left[-\frac{1}{2} \left(\gamma + \delta \arcsin\left(\frac{x-\mu}{\lambda}\right)\right)^2\right], \quad (31)$$

where x is the data parameter to be fitted, in this case, the D^* peak, μ is the mean value, λ is the standard deviation. All parameters are left free. The functional form of TF is

given by Equation (32)

$$TF = A \cdot (\Delta m - m_\pi)^B \cdot \exp [C \cdot (\Delta m - m_\pi)], \quad (32)$$

where Δm is the data parameter to be fitted, in this case, the $D^* - D^0$ mass difference, m_π is the π_s mass and A , B and C are free parameters. All PDFs and parameters are summarized below.

- $\mu^+\mu^-$ invariant mass
 - **Signal:** sum of a crystal ball and Gaussian with common mean.
 - **Background:** exponential function.
 - **Free parameters:** All, except α and n in the crystal ball which are taken from Monte Carlo fit.
- J/ψ decay length
 - **Prompt:** sum of resolution function and Gaussian function.
 - **Non-prompt:** convolution of exponential decay and another resolution function.
 - **Free parameters:** All parameters are free. Except for the mean and the standard deviation of the prompt model. They are first obtained in Monte Carlo fit and then provided to the main fit on data.
- $D^* - D^0$ mass difference
 - **Signal:** Johnson function.
 - **Background:** Threshold function
 - **Free parameters:** All parameters are free.

The likelihood function is composed of the combination of the three models described. This combination gives an equation with eight terms, one of which is the signal and the rest is background, according to Equation (33).

$$\begin{aligned}
 M_{J/\psi D^*}^{3D} = & S_{J/\psi}^{mass} \cdot P_{J/\psi} \cdot S_{D^*} + S_{J/\psi}^{mass} \cdot P_{J/\psi} \cdot B_{D^*} \\
 & + S_{J/\psi}^{mass} \cdot NP_{J/\psi} \cdot S_{D^*} + S_{J/\psi}^{mass} \cdot NP_{J/\psi} \cdot B_{D^*} \\
 & + B_{J/\psi}^{mass} \cdot P_{J/\psi} \cdot S_{D^*} + B_{J/\psi}^{mass} \cdot P_{J/\psi} \cdot B_{D^*} \\
 & + B_{J/\psi}^{mass} \cdot NP_{J/\psi} \cdot S_{D^*} + B_{J/\psi}^{mass} \cdot NP_{J/\psi} \cdot B_{D^*},
 \end{aligned} \quad (33)$$

where,

$S_{J/\psi}^{mass}$: J/ψ mass signal model;

$B_{J/\psi}^{mass}$: J/ψ mass background model;

$P_{J/\psi}$: J/ψ prompt model;

$NP_{J/\psi}$: J/ψ non-prompt model;

S_{D^*} : D^* - D^0 signal model;

B_{D^*} : D^* - D^0 background model;

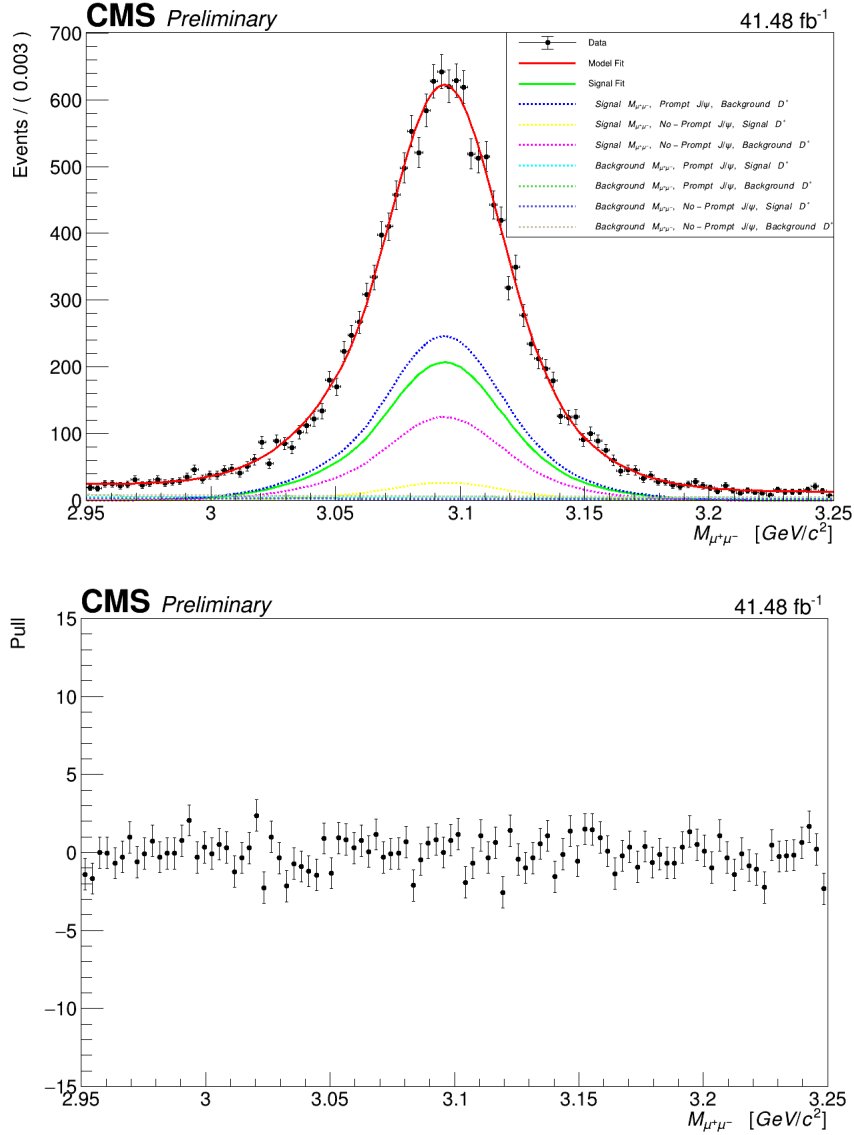
The signal component is given by the first term $S_{J/\psi}^{mass} \cdot P_{J/\psi} \cdot S_{D^*}$, which carries the components of J/ψ mass signal, J/ψ prompt and D^* - D^0 mass signal. The other components are either contaminated with J/ψ mass background, J/ψ non-prompt, or D^* background model. The third term $S_{J/\psi}^{mass} \cdot NP_{J/\psi} \cdot S_{D^*}$ is important in the sense that it contains the contamination of non-prompt J/ψ in the signal. The Appendix G shows the fitting strategy in detail. Figures (121), (122), and (123) show the 1D projections of the fits of $\mu^+\mu^-$ invariant mass, J/ψ decay length and D^* - D^0 mass, as well as their pull distributions²⁸, respectively. Only 2017 data is shown here, 2016-pre-VFP, 2016-pos-VFP, and 2018 fits are in Appendix G.

Tables (20), (21), (22), and (23) show the number of signal events for 2016-pre-VFP, 2016-pos-VFP, 2017 and, 2018 datasets, respectively. Note the similarity between 2017 and 2018, where the percentage of the signal is between 31 and 32%, approximately. However, in both 2016 datasets, this number is around 34-37 %. Therefore, it is worth mentioning here that this difference can be reduced if acceptance, efficiencies, and systematic uncertainties are taken into account. Besides that, it is noted that the number of non-prompt events contaminating the signal is very low. The use of the vertex probability cut applied to the $\mu^+\mu^-\pi_{slow}$ vertex is the main responsible for this reduction. This means that even with this cut, a small fraction of non-prompt J/ψ is still present.

4.5 Acceptance

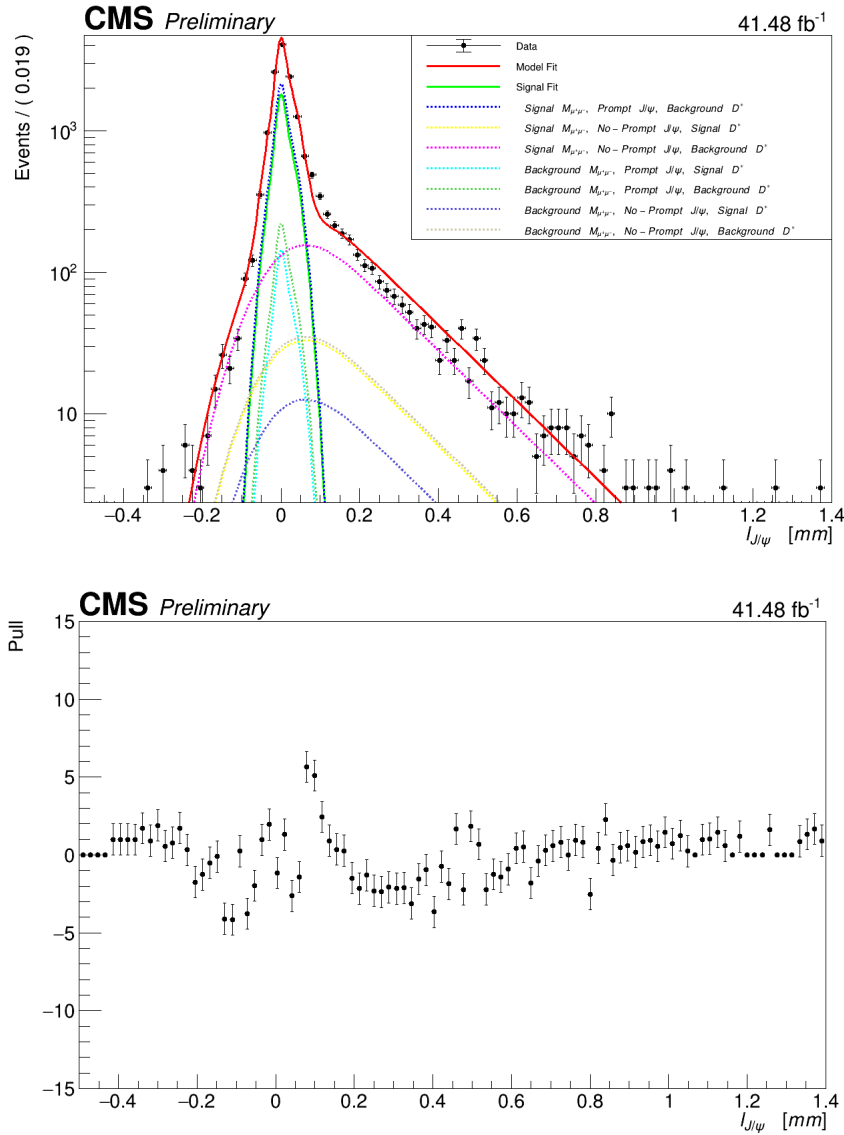
To obtain the correct number of events, acceptance and efficiency corrections must be applied. The latter is related to the instrumental effects of the detector, while the former is related to the geometrical and kinematic limits of the detector. As two different objects are involved, two acceptance corrections are applied, one for J/ψ , and one for D^* . It is worth mentioning that when AOD format is converted to NanoAODPlus, preliminary cuts are applied as explained in Section (4.3). Therefore they must be considered in the acceptance calculation. It is worth mentioning that the calculations performed in this section consider the fiducial region: $16 < p_T^{J/\psi} < 100$ GeV/c (2016), $25 < p_T^{J/\psi} < 100$ GeV/c (2017 and 2018), $|y|^{J/\psi} < 2.4$, $4 < p_T^{D^*} < 60$ GeV/c, and $|y|^{D^*} < 2.4$. In this

²⁸ The pull is defined as $\frac{N_{fit} - N_{data}}{\sigma_{data}}$

Figure 121 - The $\mu^+\mu^-$ invariant mass distribution

Legend: The figure on top shows the 1D projections of the fits of $\mu^+\mu^-$ invariant mass. The model fit (red) represents the fit of the $\mu^+\mu^-$ invariant mass distribution regardless of the other variables (J/ψ decay length and $D^* - D^0$ mass difference). The signal (green) is smaller when compared to the model fit distribution because it takes into account only the signal region of $\mu^+\mu^-$ invariant distribution, the prompt J/ψ , and the signal region of $D^* - D^0$ mass difference. The "Number of signal events" in Table (22) is obtained from this curve, and the "Number of non-prompt "signal" events" is obtained from the yellow curve. All other curves represent background contributions. The figure on the bottom shows the pull distribution.

Source: The author, 2023.

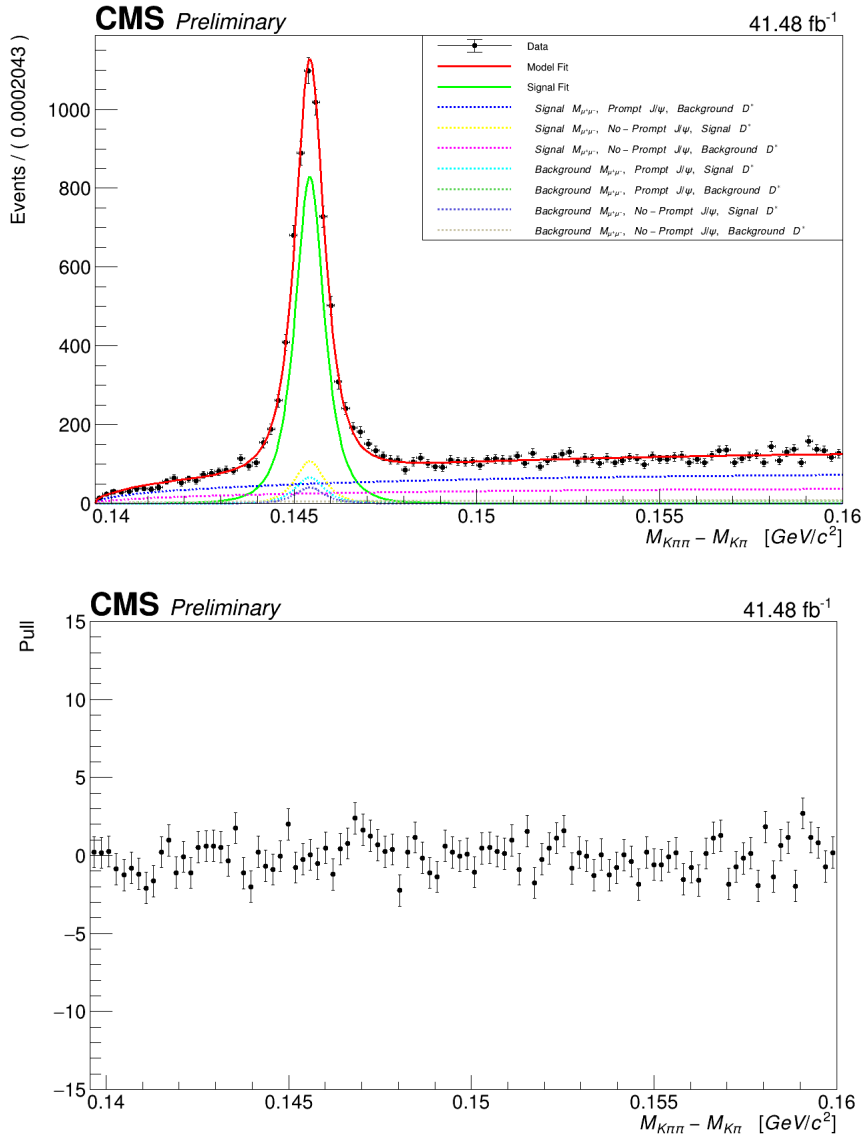
Figure 122 - J/ψ decay length

Legend: The figure on top shows the 1D projections of the fits of J/ψ decay length. The model fit (red) represents the fit of the J/ψ decay length distribution regardless of the other variables ($\mu^+\mu^-$ invariant mass and $D^* - D^0$ mass difference). Again, the signal (green) is smaller when compared to the model fit distribution. Note that the curve is not symmetric due to two different reasons, wrong assignments of the primary vertex (left part of the distribution) and the presence of non-prompt J/ψ (right part of the curve). The figure on the bottom shows the pull distribution.

Source: The author, 2023.

The main primary vertex is that with the largest sum of p_T^2 of tracks associated to it.

Figure 123 - $D^* - D^0$ mass difference distribution



Legend: The figure on top shows the 1D projections of the fits of $D^* - D^0$ mass difference. The model fit (red) represents the fit of the $D^* - D^0$ mass difference distribution regardless of the other variables ($\mu^+\mu^-$ invariant mass and J/ψ decay length). Again, the signal (green) is smaller when compared to the model fit distribution. The curve threshold is well fitted with the TF function (values around 0.14 GeV/c^2). The figure on the bottom shows the pull distribution.

Source: The author, 2023.

Table 20 - 2016-pre-VFP yields

Component	Value	Statistical Uncertainty	Comment
Number of events	6744	-	13.09 fb ⁻¹
Number of signal events	2321	48	≈ 34 % of total
Number of background events	4423	67	≈ 66 % of total
Number of non-prompt "signal" events	468	21	≈ 7 % of total

Legend: The number total of events in the fit is 6744. Out of this, 2321 events are classified as signal events, *i.e.*, events containing $J/\psi D^*$ at the J/ψ mass peak, J/ψ prompt region, and $D^* - D^0$ mass region. In turn, the number of background events is $6744 - 2321 = 4423$. Finally, the number of events containing non-prompt J/ψ that contaminate the signal is 468.

Source: The author, 2023.

Table 21 - 2016-pos-VFP yields

Component	Value	Statistical Uncertainty	Comment
Number of events	5349	-	13.26 fb ⁻¹
Number of signal events	1993	45	≈ 37 % of total
Number of background events	3356	58	≈ 63 % of total
Number of non-prompt "signal" events	280	16	≈ 6 % of total

Legend: The number total of events in the fit is 5349. Out of this, 1993 events are classified as signal events, *i.e.*, events containing $J/\psi D^*$ at the J/ψ mass peak, J/ψ prompt region, and $D^* - D^0$ mass region. In turn, the number of background events is $5349 - 1993 = 3356$. Finally, the number of events containing non-prompt J/ψ that contaminate the signal is 280.

Source: The author, 2023.

Table 22 - 2017 Yields.

Component	Value	Statistical Uncertainty	Comment
Number of events	15496	-	41.48 fb ⁻¹
Number of signal events	4950	70	≈ 32 % of total
Number of background events	10545	102	≈ 68 % of total
Number of non-prompt "signal" events	339	21	≈ 2 % of total

Legend: The number total of events in the fit is 15496. Out of this, 4950 events are classified as signal events, *i.e.*, events containing $J/\psi D^*$ at the J/ψ mass peak, J/ψ prompt region, and $D^* - D^0$ mass region. In turn, the number of background events is $15496 - 4950 = 10545$. Finally, the number of events containing non-prompt J/ψ that contaminate the signal is 339.

Source: The author, 2023.

Table 23 - 2018 yields

Component	Value	Statistical Uncertainty	Comment
Number of events	24349	-	59.76 fb ⁻¹
Number of signal events	7464	86	≈ 31 % of total
Number of background events	16855	145	≈ 69 % of total
Number of non-prompt "signal" events	456	28	≈ 2% of total

Legend: The number total of events in the fit is 24349. Out of this, 7464 events are classified as signal events, *i.e.*, events containing $J/\psi D^*$ at the J/ψ mass peak, J/ψ prompt region, and $D^* - D^0$ mass region. In turn, the number of background events is $24349 - 7464 = 16855$. Finally, the number of events containing non-prompt J/ψ that contaminate the signal is 456.

Source: The author, 2023.

section and in the next, acceptance and efficiency values are organized in tables, while the plots are shown in Appendix (H).

4.5.1 J/ψ Acceptance

This calculation is performed with DPS MC. In addition to the pre-selection cuts, the kinematic cuts listed in Table (24) are also considered.

Table 24 - Muon and J/ψ cuts considered in the acceptance calculation.

Cut	Value
Muon p_T	$p_T^\mu > 3 \text{ GeV}/c$
Muon η	$ \eta ^\mu < 2.4$
J/ψ p_T	$10 < p_T^{J/\psi} < 100 \text{ GeV}/c$
J/ψ rapidity	$ y ^{J/\psi} < 2.4$

Legend: The same cuts are applied to generated and reconstructed particles.

Note that the lowest value of p_T is 10 GeV/c, but it is limited to the trigger selection, which is 16 GeV/c in 2016 data, and 25 GeV/c in 2017 and 2018 data.

Source: The author, 2023.

Therefore, the J/ψ acceptance is calculated using Equation (34)

$$Acceptance^{J/\psi} \times \epsilon_{pre_cuts}^{J/\psi} = \frac{N_{reco\&pre-cuts}^{J/\psi}}{N_{gen}^{J/\psi}}, \quad (34)$$

where $N_{reco\&pre-cuts}^{J/\psi}$ is the number of reconstructed J/ψ that passed the pre-cuts and the cuts listed in Table (24) and are in the acceptance region; $N_{gen}^{J/\psi}$ is the number of generated J/ψ. The match between reconstructed and generated muons is performed here, to guarantee that this correction is applied to the correct reconstructed particles. To match the reconstructed object to the generated particle two criteria are required, as shown below.

- Generated and reconstructed muons have the same charge.
- $|\mu_{Reco}^{p_T} - \mu_{Gen}^{p_T}| < 0.1 \text{ GeV}/c$ and $|\mu_{Reco}^\eta - \mu_{Gen}^\eta| < 0.1$, and $|\mu_{Reco}^\phi - \mu_{Gen}^\phi| < 0.1 \text{ rad}$.

Table (25) shows J/ψ acceptance in the entire phase space considered in this study, $16 < p_T^{J/\psi} < 100 \text{ GeV}/c$ (2016), $25 < p_T^{J/\psi} < 100 \text{ GeV}/c$ (2017 and 2018), $|y|^{J/\psi} < 2.4$, $4 < p_T^{D^*} < 100 \text{ GeV}/c$, and $|y|^{D^*} < 2.4$.

Table 25 - J/ψ acceptance - entire phase space considered in the study.

Year	Value	Statistical Uncertainty
2016-pre-VFP	0.912	+0.000 -0.000
2016-pos-VFP	0.811	+0.000 -0.000
2017	0.833	+0.000 -0.000
2018	0.840	+0.001 -0.001

Legend: The values in 2016-pos-VFP, 2017, and 2018 are similar. On the other hand, the value in 2016-pre-VFP is around 9.5% lower relative to the others. The phase-space is $16 < p_T^{J/\psi} < 100$ GeV/c (2016), $25 < p_T^{J/\psi} < 100$ GeV/c (2017 and 2018), $|y|^{J/\psi} < 2.4$, $4 < p_T^{D^*} < 60$ GeV/c, and $|y|^{D^*} < 2.4$.

Source: The author, 2023.

Tables (26), (27), (28), (29) show the J/ψ acceptance in bins of p_T of 2016-pre-VFP, 2016-pos-VFP, 2017, and 2018 data taking periods, respectively.

4.5.2 D^* Acceptance

This acceptance is also calculated with the DPS MC. As in the J/ψ case, pre-cuts are also embedded. Furthermore, the kinematic cuts listed in Table (30) are used as well. It is worth mentioning that the match between reconstructed and generated D^* is performed.

Therefore, the D^* acceptance is calculated using Equation (35)

$$Acceptance^{D^*} \times \epsilon_{pre_cuts}^{D^*} = \frac{N_{reco\&pre-cuts}^{D^*}}{N_{gen}^{D^*}}, \quad (35)$$

where $N_{reco\&pre-cuts}^{D^*}$ is the number of reconstructed D^* that passed the pre-cuts and the cuts listed in Table (30), and match a generate D^* . $N_{gen}^{D^*}$ is the number of generated D^* . To have a match between reconstructed objects and generated particles the items below are required.

- $|D_{Reco}^{*pT} - D_{Gen}^{*pT}| < 0.1$ GeV/c.
- $|D_{Reco}^{*\eta} - D_{Gen}^{*\eta}| < 0.1$.
- $|D_{Reco}^{*\phi} - D_{Gen}^{*\phi}| < 0.1$ rad.

Table (31) shows D^* acceptance in the entire phase space where the measurement is performed.

Table 26 - J/ψ acceptance in bins of p_T in 2016-pre-VFP. The rapidity is $|y| < 2.4$.

p_T [GeV/c]	Acceptance	Statistical Uncertainty
16-20	0.903	+0.002 +0.002
20-25	0.917	+0.002 -0.002
25-30	0.908	+0.005 -0.005
30-40	0.903	+0.001 -0.001
40-50	0.898	+0.001 -0.001
50-60	0.873	+0.001 -0.001
60-70	0.895	+0.001 -0.001
70-80	0.889	+0.001 -0.001
80-90	0.875	+0.002 -0.002
90-100	0.836	+0.003 -0.003

Legend: In the regions where p_T is lower than 40 GeV/c the acceptance is higher than 90 %. After 60 GeV/c, a smooth drop is observed, where the lowest value (0.836) is in the range of 90-100 GeV. The kinematic parameters of D^* are $4 < p_T^{D^*} < 60$ GeV/c and $|y|^{D^*} < 2.4$.

Source: The author, 2023.

Table 27 - J/ψ acceptance in bins of p_T in 2016-pos-VFP. The rapidity is $|y| < 2.4$.

p_T [GeV/c]	Acceptance	Statistical Uncertainty
16-20	0.827	+0.002 +0.002
20-25	0.833	+0.003 -0.003
25-30	0.819	+0.005 -0.005
30-40	0.819	+0.001 -0.001
40-50	0.827	+0.002 -0.002
50-60	0.814	+0.001 -0.001
60-70	0.839	+0.001 -0.001
70-80	0.840	+0.002 -0.002
80-90	0.830	+0.003 -0.003
90-100	0.803	+0.004 -0.004

Legend: In this case, there is no clear trend as in the 2016-pre-VFP. It is noted that the difference between the highest (0.840) and the lowest value (0.803) is around 4%. The D^* kinematic parameters are $4 < p_T^{D^*} < 60$ GeV/c and $|y|^{D^*} < 2.4$.

Source: The author, 2023.

Table 28 - J/ψ acceptance in bins of p_T in 2017. The rapidity is $|y| < 2.4$.

p_T [GeV/c]	Acceptance	Statistical Uncertainty
25-30	0.813	+0.009 -0.009
30-40	0.827	+0.001 -0.001
40-50	0.845	+0.002 -0.002
50-60	0.828	+0.001 -0.001
60-70	0.854	+0.001 -0.001
70-80	0.861	+0.002 -0.002
80-90	0.855	+0.003 -0.003
90-100	0.825	+0.004 -0.004

Legend: The values increase from 0.813 at 25-30 GeV/c to 0.855 at 80-90 GeV/c (except at 50-60 GeV), decreasing to 0.825 at the last bin. All values are higher than 0.81. The D^* kinematic parameters are $4 < p_T^{D^*} < 60$ GeV/c and $|y|^{D^*} < 2.4$.

Source: The author, 2023.

Table 29 - J/ψ acceptance in bins of p_T in 2018. The rapidity is $|y| < 2.4$.

p_T [GeV/c]	Acceptance	Statistical Uncertainty
25-30	0.865	+0.010 -0.010
30-40	0.834	+0.001 -0.001
40-50	0.842	+0.002 -0.002
50-60	0.848	+0.001 -0.001
60-70	0.870	+0.001 -0.001
70-80	0.875	+0.002 -0.002
80-90	0.865	+0.003 -0.003
90-100	0.825	+0.005 -0.005

Legend: The higher values are in bins 60-70 (0.870) and 70-80 (0.875). All values are higher than 0.82. The D^* kinematic parameters are $4 < p_T^{D^*} < 60$ GeV/c and $|y|^{D^*} < 2.4$.

Source: The author, 2023.

Table 30 - D^* kinematic cuts considered in the acceptance calculation.

Cut	Value
p_T	$4 < p_T^{D^*} < 60 \text{ GeV}/c$
Rapidity	$ y ^{D^*} < 2.4$

Legend: The same kinematic cuts are applied to generated and reconstructed particles.

Source: The author, 2023.

Table 31 - D^* acceptance - entire phase space considered in the study.

Year	Value	Statistical Uncertainty
2016-pre-VFP	0.693	+0.001 -0.001
2016-pos-VFP	0.626	+0.000 -0.000
2017	0.711	+0.001 -0.001
2018	0.714	+0.001 -0.001

Legend: The values in the 2016 datasets are lower than the values in 2017 and 2018. The phase-space is $16 < p_T^{J/\psi} < 100 \text{ GeV}/c$ (2016), $25 < p_T^{J/\psi} < 100 \text{ GeV}/c$ (2017 and 2018), $|y|^{J/\psi} < 2.4$, $4 < p_T^{D^*} < 60 \text{ GeV}/c$, and $|y|^{D^*} < 2.4$.

Source: The author, 2023.

Tables (32), (33), (34), (35) show the D^* acceptance in bins of p_T in 2016-pre-VFP, 2016-pos-VFP, 2017, and 2018 data taking period, respectively.

Table 32 - D^* acceptance in bins of p_T in 2016-pre-VFP. The rapidity is $|y| < 2.4$.

p_T [GeV/c]	Acceptance	Statistical Uncertainty
4-10	0.677	+0.001 -0.001
10-20	0.683	+0.002 -0.002
20-30	0.661	+0.003 -0.003
30-60	0.647	+0.003 -0.003

Legend: The values are always higher in the first two bins, decreasing in the last two. The J/ψ kinematic parameters are $16 < p_T^{J/\psi} < 100$ GeV/c and $|y|^{J/\psi} < 2.4$.

Source: The author, 2023.

Table 33 - D^* acceptance in bins of p_T in 2016-pos-VFP. The rapidity is $|y| < 2.4$.

p_T [GeV/c]	Acceptance	Statistical Uncertainty
4-10	0.613	+0.001 -0.001
10-20	0.618	+0.001 -0.001
20-30	0.597	+0.002 -0.002
30-60	0.579	+0.002 -0.002

Legend: The same trend as in 2016-pre-VFP is found here. The J/ψ kinematic parameters are $16 < p_T^{J/\psi} < 100$ GeV/c and $|y|^{J/\psi} < 2.4$.

Source: The author, 2023.

4.6 Efficiencies

In addition to acceptance, four efficiencies are considered: D^* cuts efficiency, J/ψ cuts efficiency, trigger efficiency, and association efficiency. There is a subsection for each of them.

4.6.1 D^* cuts Efficiency

The numerator is given by the number of D^* that passes the pre-cuts and the cuts listed in Tables (14), (15), and (16). The denominator is given by the number of D^* that

Table 34 - D* acceptance in bins of p_T in 2017. The rapidity is $|y| < 2.4$.

p_T [GeV/c]	Acceptance	Statistical Uncertainty
4-10	0.712	+0.001 -0.001
10-20	0.677	+0.001 -0.001
20-30	0.654	+0.002 -0.002
30-60	0.634	+0.003 -0.003

Legend: In the first bin the value is higher than 0.7, decreasing to 0.634 in the last bin. The J/ψ kinematic parameters are $25 < p_T^{J/\psi} < 100$ GeV/c and $|y|^{J/\psi} < 2.4$.

Source: The author, 2023.

Table 35 - D* acceptance in bins of p_T in 2018. The rapidity is $|y| < 2.4$.

p_T [GeV/c]	Acceptance	Statistical Uncertainty
4-10	0.716	+0.001 -0.001
10-20	0.676	+0.001 -0.001
20-30	0.664	+0.003 -0.003
30-60	0.645	+0.003 -0.003

Legend: The same trend as in 2017 is found here. The J/ψ kinematic parameters are $25 < p_T^{J/\psi} < 100$ GeV/c and $|y|^{J/\psi} < 2.5$.

Source: The author, 2023.

passes only the pre-cuts and the cuts listed in Table (30). It is calculated as

$$\epsilon_{cuts}^{D^*} = \frac{N_{reco\&pass_cuts}^{D^*}}{N_{reco\&pre-cuts}^{D^*}}. \quad (36)$$

Table (36) shows D* cuts efficiency in 2016-pre-VFP, 2016-pos-VFP, 2017, and 2018. Again, it is calculated in the entire phase space where the measurement is performed.

Table 36 - D* cuts efficiency - entire phase space considered in the study.

Year	Value	Statistical Uncertainty
2016-pre-VFP	0.212	+0.001 -0.001
2016-pos-VFP	0.212	+0.001 -0.001
2017	0.253	+0.001 -0.001
2018	0.246	+0.001 -0.001

Legend: The values in 2016 are lower. The phase-space is $16 < p_T^{J/\psi} < 100$ GeV/c (2016), $25 < p_T^{J/\psi} < 100$ GeV/c (2017 and 2018), $|y|^{J/\psi} < 2.4$, $4 < p_T^{D^*} < 60$ GeV/c, and $|y|^{D^*} < 2.4$.

Source: The author, 2023.

Tables (37), (38), (39), (39) show the D* efficiency cuts in bins of p_T in 2016-pre-VFP, 2016-pos-VFP, 2017, and 2018 data taking periods, respectively.

Table 37 - D* cuts efficiency in bins of p_T in 2016-pre-VFP. The rapidity is $|y| < 2.4$.

p_T [GeV/c]	Efficiency	Statistical Uncertainty
4-10	0.125	+0.001 -0.001
10-20	0.318	+0.002 -0.002
20-30	0.383	+0.003 -0.003
30-60	0.410	+0.004 -0.003

Legend: The value at the first bin is very low but increases with the increase of p_T . The highest value is found in the last bin (0.410). The J/ ψ kinematic parameters are $16 < p_T^{J/\psi} < 100$ GeV/c and $|y|^{J/\psi} < 2.4$.

Source: The author, 2023.

4.6.2 J/ ψ Cuts Efficiency

The numerator is given by the number of J/ ψ that passes the pre-cuts and the cuts listed in Table (12). The denominator is given by the number of J/ ψ that passes

Table 38 - D* cuts efficiency in bins of p_T in 2016-pos-VFP. The rapidity is $|y| < 2.4$.

p_T [GeV/c]	Efficiency	Statistical Uncertainty
4-10	0.127	+0.001 -0.001
10-20	0.315	+0.001 -0.001
20-30	0.383	+0.002 -0.002
30-60	0.412	+0.003 -0.003

Legend: Similar behavior to 2016-pre-VFP is seen, with efficiencies slightly greater. The J/ψ kinematic parameters are $16 < p_T^{J/\psi} < 100$ GeV/c and $|y|^{J/\psi} < 2.4$.

Source: The author, 2023.

Table 39 - D* cuts efficiency in bins of p_T in 2017. The rapidity is $|y| < 2.4$.

p_T [GeV/c]	Efficiency	Statistical Uncertainty
4-10	0.161	+0.001 -0.001
10-20	0.342	+0.002 -0.002
20-30	0.405	+0.003 -0.003
30-60	0.420	+0.004 -0.004

Legend: Similar behavior to 2016 is seen, with values slightly higher. The J/ψ kinematic parameters are $25 < p_T^{J/\psi} < 100$ GeV/c and $|y|^{J/\psi} < 2.4$.

Source: The author, 2023.

Table 40 - D* cuts efficiency in bins of p_T in 2018. The rapidity is $|y| < 2.4$.

p_T [GeV/c]	Efficiency	Statistical Uncertainty
4-10	0.161	+0.001 -0.001
10-20	0.346	+0.002 -0.002
20-30	0.403	+0.003 -0.003
30-60	0.418	+0.004 -0.004

Legend: Similar behavior to 2016 is seen, with values slightly higher as well.

The J/ψ kinematic parameters are $25 < p_T^{J/\psi} < 100$ GeV/c and $|y|^{J/\psi} < 2.4$.

Source: The author, 2023.

only the pre-cuts and the cuts listed in Table (24).

$$\epsilon_{cuts}^{J/\psi} = \frac{N_{reco\&pass_cuts}^{J/\psi}}{N_{reco\&pre_cuts}^{J/\psi}} \quad (37)$$

Table (41) shows J/ψ cuts efficiency in 2016-pre-VFP, 2016-pos-VFP, 2017, and 2018. Again, it is calculated in the entire phase space where the measurement is performed.

Table 41 - J/ψ cuts efficiency - entire phase space considered in the study.

Year	Value	Statistical Uncertainty
2016-pre-VFP	0.971	+0.000 -0.000
2016-pos-VFP	0.979	+0.000 -0.000
2017	0.980	+0.000 -0.000
2018	0.980	+0.000 -0.000

Legend: In all periods the value is higher than 0.97. The D^* kinematic parameters are $4 < p_T^{D^*} < 60$ GeV/c and $|y|^{D^*} < 2.4$.

Source: The author, 2023.

Tables (42), (43), (44), (45) show the J/ψ efficiency cuts in bins of p_T in 2016-pre-VFP, 2016-pos-VFP, 2017, and 2018 data taking periods, respectively.

Table 42 - J/ψ cuts efficiency in bins of p_T in 2016-pre-VFP. The rapidity is $|y| < 2.4$.

p_T [GeV/c]	Efficiency	Statistical Uncertainty
16-20	0.968	+0.001 -0.001
20-25	0.971	+0.002 -0.003
25-30	0.969	+0.003 -0.003
30-40	0.971	+0.000 -0.000
40-50	0.972	+0.001 -0.001
50-60	0.972	+0.000 -0.000
60-70	0.971	+0.001 -0.001
70-80	0.971	+0.001 -0.001
80-90	0.968	+0.001 -0.001
90-100	0.971	+0.002 -0.002

Legend: All values are higher than 0.96. The D^* kinematic parameters are $4 < p_T^{D^*} < 60$ GeV/c and $|y|^{D^*} < 2.4$.

Source: The author, 2023.

Table 43 - J/ψ cuts efficiency in bins of p_T in 2016-pos-VFP. The rapidity is $|y| < 2.4$.

p_T [GeV/c]	Efficiency	Statistical Uncertainty
16-20	0.973	+0.001 -0.001
20-25	0.974	+0.001 -0.001
25-30	0.979	+0.002 -0.002
30-40	0.979	+0.000 -0.000
40-50	0.979	+0.001 -0.001
50-60	0.980	+0.000 -0.000
60-70	0.980	+0.001 -0.001
70-80	0.980	+0.001 -0.001
80-90	0.979	+0.001 -0.001
90-100	0.980	+0.002 -0.002

Legend: All values are higher than 0.97. It is noted that the values are higher than in 2016-pre-VFP. The D^* kinematic parameters are $4 < p_T^{D^*} < 60$ GeV/c and $|y|^{D^*} < 2.4$.

Source: The author, 2023.

Table 44 - J/ψ cuts efficiency in bins of p_T in 2017. The rapidity is $|y| < 2.4$.

p_T [GeV/c]	Efficiency	Statistical Uncertainty
25-30	0.981	+0.003 -0.004
30-40	0.979	+0.000 -0.000
40-50	0.981	+0.001 -0.001
50-60	0.981	+0.000 -0.000
60-70	0.981	+0.001 -0.001
70-80	0.981	+0.001 -0.001
80-90	0.980	+0.001 -0.001
90-100	0.980	+0.002 -0.002

Legend: All values are higher than 0.98. The D^* kinematic parameters are $4 < p_T^{D^*} < 60$ GeV/c and $|y|^{D^*} < 2.4$.

Source: The author, 2023.

Table 45 - J/ψ cuts efficiency in bins of p_T in 2018. The rapidity is $|y| < 2.4$.

p_T [GeV/c]	Efficiency	Statistical Uncertainty
25-30	0.977	+0.004 -0.005
30-40	0.979	+0.000 -0.000
40-50	0.980	+0.001 -0.001
50-60	0.981	+0.000 -0.000
60-70	0.979	+0.001 -0.001
70-80	0.981	+0.001 -0.001
80-90	0.985	+0.001 -0.001
90-100	0.981	+0.002 -0.002

Legend: All values are higher than 0.98 as well. The D^* kinematic parameters are $4 < p_T^{D^*} < 60$ GeV/c and $|y|^{D^*} < 2.4$.

Source: The author, 2023.

4.6.3 Trigger Efficiency

The numerator is given by the number of J/ψ that passes the pre-cuts, cuts, and the HLT cut ($HLT_Dimuon16_Jpsi$ in 2016 and $HLT_Dimuon25_Jpsi$ in 2017 and 2018). The denominator is given by the number of J/ψ that passes the pre-cuts and the cuts,

$$\epsilon_{HLT} = \frac{N_{reco\&pass_cuts\&trigger}^{J/\psi}}{N_{reco\&pass_cuts}^{J/\psi}}. \quad (38)$$

Table (46) shows HLT efficiency in 2016-pre-VFP, 2016-pos-VFP, 2017, and 2018. Again, it is calculated in the entire phase space where the measurement is performed.

Table 46 - High level trigger efficiency - entire phase space considered in the study.

Year	Value	Statistical Uncertainty
2016-pre-VFP	0.587	+0.001 -0.001
2016-pos-VFP	0.651	+0.000 -0.000
2017	0.610	+0.001 -0.001
2018	0.650	+0.001 -0.001

Legend: The value in 2016-pre-VFP is the lowest, while in the other years, they are greater than 0.6. The D^* kinematic parameters are $4 < p_T^{D^*} < 60$ GeV/c and $|y|^{D^*} < 2.4$.

Source: The author, 2023.

Tables (47), (48), (49), (50) show the HLT efficiency in bins of J/ψ p_T of 2016-pre-VFP, 2016-pos-VFP, 2017, and 2018 data taking period.

Table 47 - *HLT_Dimuon16_Jpsi* efficiency in bins of p_T in 2016-pre-VFP. The rapidity is $|y| < 2.4$.

p_T [GeV/c]	Efficiency	Statistical Uncertainty
16-20	0.562	+0.004 -0.004
20-25	0.620	+0.006 -0.006
25-30	0.640	+0.010 -0.010
30-40	0.626	+0.001 -0.001
40-50	0.603	+0.002 -0.002
50-60	0.572	+0.001 -0.001
60-70	0.547	+0.002 -0.002
70-80	0.527	+0.002 -0.002
80-90	0.504	+0.003 -0.003
90-100	0.481	+0.005 -0.005

Legend: Higher values are observed between 20 and 50 GeV/c, while lower values are observed in high p_T bins. The D^* kinematic parameters are $4 < p_T^{D^*} < 60$ GeV/c and $|y|^{D^*} < 2.4$.

Source: The author, 2023.

4.6.4 Association Efficiency

Finally, the association efficiency measures the efficiency of the vertex probability cut. The numerator is given by the number of $J/\psi D^*$ that passes all cuts from before (for both J/ψ and D^*) and the vertex probability cut. The denominator is given by the number of $J/\psi D^*$ that passes all cuts from before. It is calculated as

$$\epsilon_{\text{association}} = \frac{N_{\text{reco}\&\text{pass_cuts}\&\text{trigger}\&\text{association}}^{J/\psi D^*}}{N_{\text{reco}\&\text{pass_cuts}\&\text{trigger}}^{J/\psi D^*}}. \quad (39)$$

Table (51) shows the association efficiency in 2016-pre-VFP, 2016-pos-VFP, 2017, and 2018. Again, it is calculated in the entire phase space where the measurement is performed.

Tables (52), (53), (54), (55) show the association efficiency in bins of J/ψ p_T of 2016-pre-VFP, 2016-pos-VFP, 2017 and 2018 data taking period.

Table 48 - *HLL_Dimuon16_Jpsi* efficiency in bins of p_T in 2016-pos-VFP. The rapidity is $|y| < 2.4$.

p_T [GeV/c]	Efficiency	Statistical Uncertainty
16-20	0.608	+0.003 -0.003
20-25	0.682	+0.004 -0.004
25-30	0.678	+0.006 -0.006
30-40	0.685	+0.001 -0.001
40-50	0.670	+0.002 -0.002
50-60	0.644	+0.001 -0.001
60-70	0.619	+0.002 -0.002
70-80	0.601	+0.003 -0.003
80-90	0.579	+0.004 -0.004
90-100	0.562	+0.006 -0.006

Legend: Higher values are observed between 20 and 50 GeV/c, while lower values are observed in high p_T bins. It is noted that the values are higher than in 2016-pre-VFP. The D^* kinematic parameters are $4 < p_T^{D^*} < 60$ GeV/c and $|y|^{D^*} < 2.4$.

Source: The author, 2023.

Table 49 - *HLL_Dimuon25_Jpsi* efficiency in bins of p_T in 2017. The rapidity for J/ψ is $|y| < 2.4$.

p_T [GeV/c]	Efficiency	Statistical Uncertainty
25-30	0.629	+0.012 -0.013
30-40	0.641	+0.001 -0.001
40-50	0.640	+0.002 -0.002
50-60	0.628	+0.001 -0.001
60-70	0.603	+0.002 -0.002
70-80	0.580	+0.003 -0.003
80-90	0.575	+0.004 -0.004
90-100	0.565	+0.006 -0.006

Legend: Higher values are observed between 30 and 50 GeV/c, while lower values are observed in high p_T bins. The D^* kinematic parameters are $4 < p_T^{D^*} < 100$ GeV/c and $|y|^{D^*} < 2.5$.

Source: The author, 2023.

Table 50 - *HLLT_Dimuon25_Jpsi* efficiency in bins of p_T in 2018.
The rapidity is $|y| < 2.4$.

p_T [GeV/c]	Efficiency	Statistical Uncertainty
25-30	0.716	+0.014 -0.014
30-40	0.637	+0.001 -0.001
40-50	0.635	+0.002 -0.002
50-60	0.684	+0.002 -0.002
60-70	0.660	+0.002 -0.002
70-80	0.637	+0.003 -0.003
80-90	0.618	+0.005 -0.005
90-100	0.605	+0.007 -0.007

Legend: Higher values are observed between 25 and 50 GeV/c, while lower values are observed in high p_T bins. The D^* kinematic parameters are $4 < p_T^{D^*} < 60$ GeV/c and $|y|^{D^*} < 2.4$.

Source: The author, 2023.

Table 51 - Association efficiency - entire phase space considered in this study.

Year	Value	Statistical Uncertainty
2016-pre-VFP	0.831	+0.002 -0.002
2016-pos-VFP	0.879	+0.001 -0.001
2017	0.822	+0.002 -0.002
2018	0.832	+0.002 -0.002

Legend: The values in 2016 are higher than in 2017 and 2018. The J/ψ kinematic parameters are $16 < p_T^{J/\psi} < 100$ GeV/c in 2016 and $25 < p_T^{J/\psi} < 100$ GeV/c in 2017 and 2018, and $|y|^{J/\psi} < 2.4$.

Source: The author, 2023.

Table 52 - Association efficiency in bins of J/ψ p_T in 2016-pre-VFP.
The rapidity is $|y| < 2.4$.

p_T [GeV/c]	Efficiency	Statistical Uncertainty
16-20	0.885	+0.021 -0.024
20-25	0.904	+0.022 -0.027
25-30	0.871	+0.039 -0.050
30-40	0.884	+0.003 -0.003
40-50	0.877	+0.006 -0.007
50-60	0.875	+0.003 -0.003
60-70	0.876	+0.004 -0.005
70-80	0.874	+0.007 -0.007
80-90	0.841	+0.011 -0.011
90-100	0.897	+0.012 -0.013

Legend: The values are always higher than 0.8. The D^* kinematic parameters are $4 < p_T^{D^*} < 60$ GeV/c and $|y|^{D^*} < 2.4$.

Source: The author, 2023.

Table 53 - Association efficiency in bins of J/ψ p_T in 2016-pos-VFP.
The rapidity is $|y| < 2.4$.

p_T [GeV/c]	Efficiency	Statistical Uncertainty
16-20	0.865	+0.013 -0.014
20-25	0.865	+0.017 -0.019
25-30	0.896	+0.023 -0.028
30-40	0.873	+0.003 -0.003
40-50	0.875	+0.006 -0.006
50-60	0.866	+0.004 -0.004
60-70	0.871	+0.005 -0.005
70-80	0.867	+0.008 -0.008
80-90	0.875	+0.012 -0.013
90-100	0.868	+0.016 -0.018

Legend: The values are always higher than 0.8. The D^* kinematic parameters are $4 < p_T^{D^*} < 60$ GeV/c and $|y|^{D^*} < 2.4$.

Source: The author, 2023.

Table 54 - Association efficiency in bins of J/ψ p_T in 2017. The rapidity is $|y| < 2.4$.

p_T [GeV/c]	Efficiency	Statistical Uncertainty
25-30	0.818	+0.054 -0.067
30-40	0.827	+0.004 -0.004
40-50	0.841	+0.007 -0.007
50-60	0.832	+0.004 -0.004
60-70	0.819	+0.006 -0.006
70-80	0.802	+0.007 -0.007
80-90	0.812	+0.012 -0.012
90-100	0.800	+0.017 -0.018

Legend: The values are always higher than 0.8. The D^* kinematic parameters are $4 < p_T^{D^*} < 60$ GeV/c and $|y|^{D^*} < 2.4$.

Source: The author, 2023.

Table 55 - Association efficiency in bins of J/ψ p_T in 2018. The rapidity is $|y| < 2.4$.

p_T [GeV/c]	Efficiency	Statistical Uncertainty
25-30	0.647	+0.074 -0.081
30-40	0.830	+0.004 -0.004
40-50	0.840	+0.007 -0.007
50-60	0.834	+0.004 -0.004
60-70	0.844	+0.006 -0.006
70-80	0.833	+0.009 -0.009
80-90	0.814	+0.013 -0.014
90-100	0.792	+0.019 -0.021

Legend: The values are always higher than 0.8. The D^* kinematic parameters are $4 < p_T^{D^*} < 60$ GeV/c and $|y|^{D^*} < 2.4$.

Source: The author, 2023.

Tables (52), (53), (54), (55) shows the association efficiency in bins of D^* p_T of 2016-pre-VFP, 2016, 2017 and 2018 data taking period.

Table 56 - Association efficiency in bins of D^* p_T in 2016-pre-VFP.

The rapidity is $|y| < 2.4$.

p_T [GeV/c]	Efficiency	Statistical Uncertainty
4-10	0.854	+0.005 -0.005
10-20	0.886	+0.004 -0.004
20-30	0.881	+0.006 -0.006
30-60	0.886	+0.007 -0.007

Legend: The values are always higher than 0.8. The J/ψ kinematic parameters are $16 < p_T^{J/\psi} < 100$ GeV/c and $|y|^{J/\psi} < 2.4$.

Source: The author, 2023.

Table 57 - Association efficiency in bins of D^* p_T in 2016-pos-VFP.

The rapidity is $|y| < 2.4$.

p_T [GeV/c]	Efficiency	Statistical Uncertainty
4-10	0.836	+0.004 -0.004
10-20	0.887	+0.003 -0.003
20-30	0.876	+0.005 -0.005
30-60	0.890	+0.005 -0.006

Legend: The values are always higher than 0.8. The J/ψ kinematic parameters are $16 < p_T^{J/\psi} < 100$ GeV/c and $|y|^{J/\psi} < 2.4$.

Source: The author, 2023.

Table 58 - Association efficiency in bins of D^* p_T in 2017. The rapidity is $|y| < 2.4$.

p_T [GeV/c]	Efficiency	Statistical Uncertainty
4-10	0.781	+0.004 -0.004
10-20	0.843	+0.003 -0.003
20-30	0.845	+0.005 -0.005
30-60	0.850	+0.006 -0.006

Legend: Except in the first bin, all values are greater than 0.8. The J/ψ kinematic parameters are $25 < p_T^{J/\psi} < 100$ GeV/c and $|y|^{J/\psi} < 2.4$.

Source: The author, 2023.

Table 59 - Association efficiency in bins of D^* p_T in 2018. The rapidity is $|y| < 2.4$.

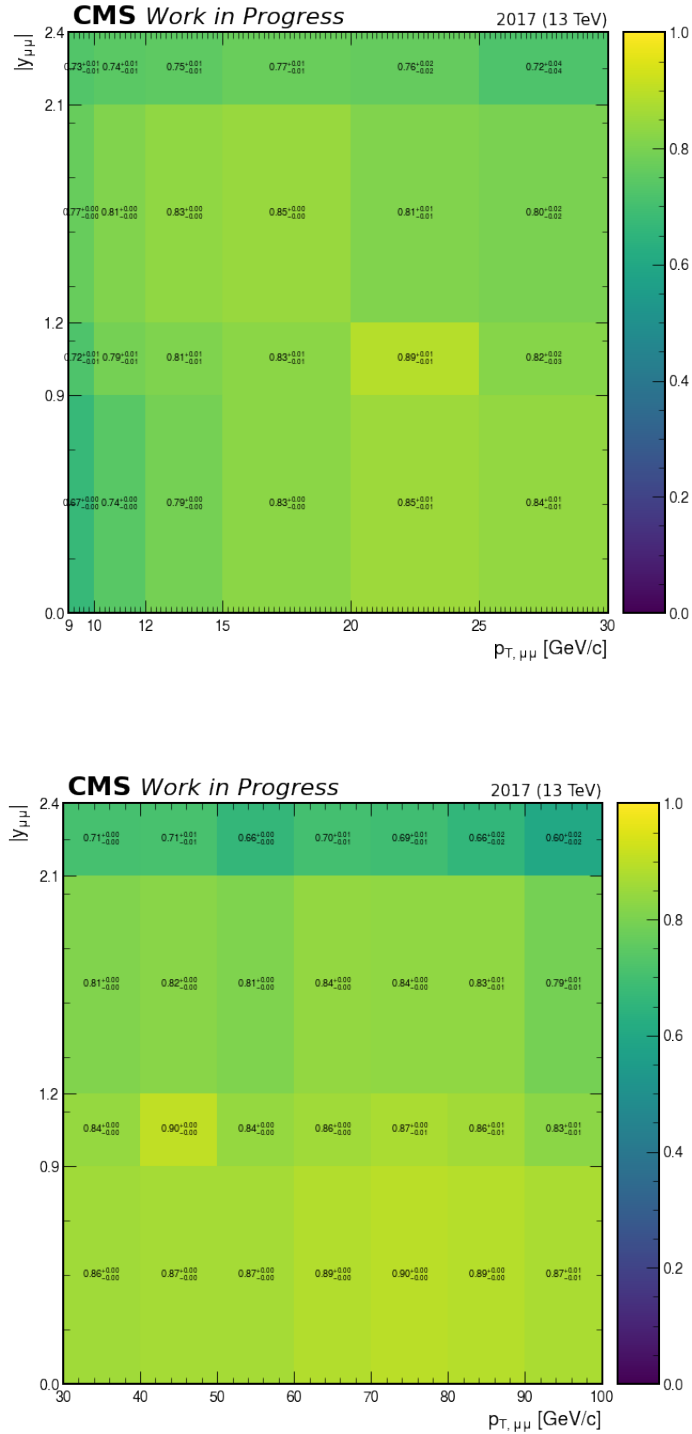
p_T [GeV/c]	Efficiency	Statistical Uncertainty
4-10	0.787	+0.004 -0.004
10-20	0.850	+0.003 -0.004
20-30	0.860	+0.005 -0.005
30-60	0.865	+0.006 -0.007

Legend: Except in the first bin, all values are greater than 0.8. The J/ψ kinematic parameters are $25 < p_T^{J/\psi} < 100$ GeV/c and $|y|^{J/\psi} < 2.4$.

Source: The author, 2023.

The plots of all acceptances and efficiencies in 2017 are shown in Figures (124), (125), (126), (127), (128), (129). The plots with 2016 and 2018 data are shown in Appendix (H).

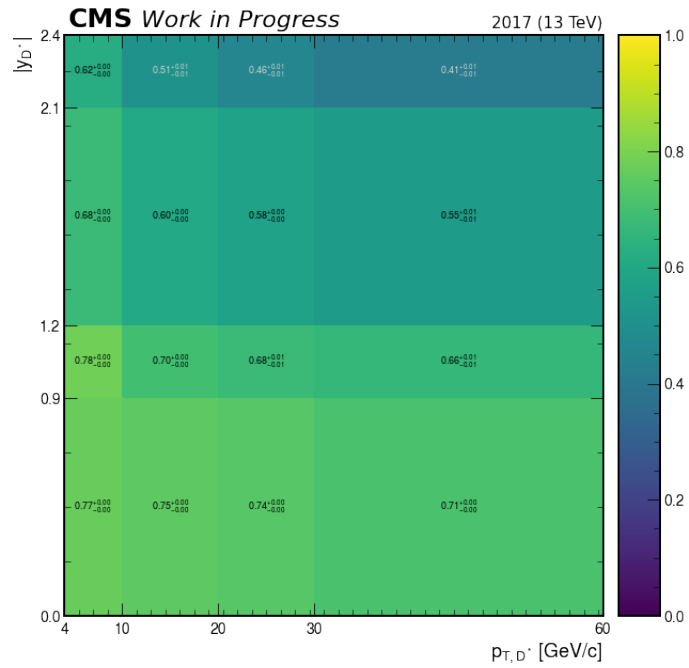
Figure 124 - J/ψ acceptance in bins of rapidity and p_T - 2017 data.



Legend: The figure on top shows the J/ψ acceptance in the region $|y| < 2.4$ and $9 < p_T < 30$ GeV/c and the figure on bottom shows it in the region $|y| < 2.4$ and $30 < p_T < 100$ GeV/c.

Source: The author, 2023.

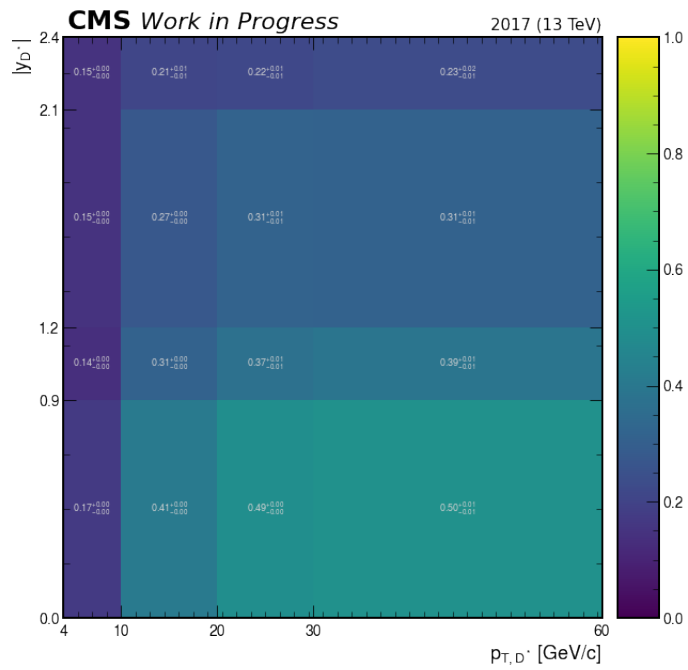
Figure 125 - D^* acceptance in bins of rapidity and p_T - 2017 data.



Legend: The figure shows the D^* acceptance in the region $|y| < 2.4$ and $4 < p_T < 60$ GeV/c .

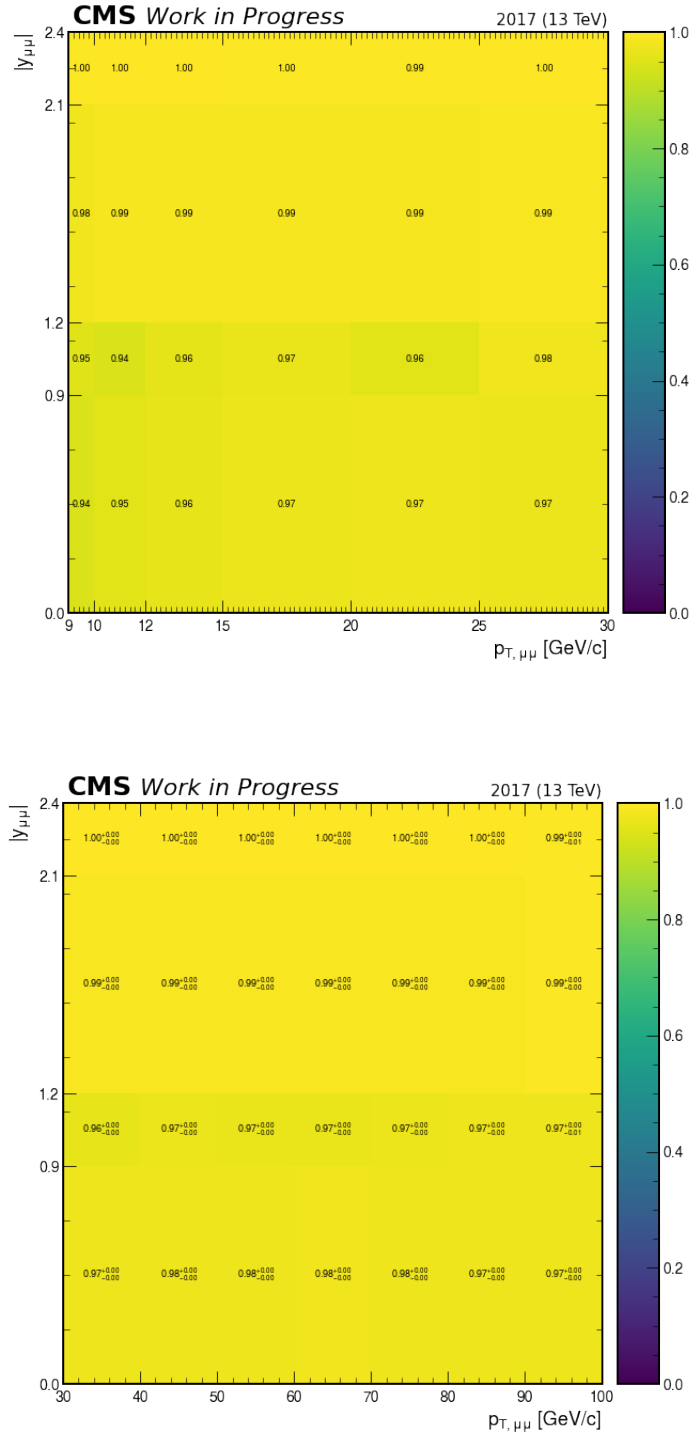
Source: The author, 2023.

Figure 126 - D^* cuts efficiency in bins of rapidity and p_T - 2017 data.



Legend: The figure shows the D^* cuts efficiency in the region $|y| < 2.4$ and $4 < p_T < 60$ GeV/c .

Source: The author, 2023.

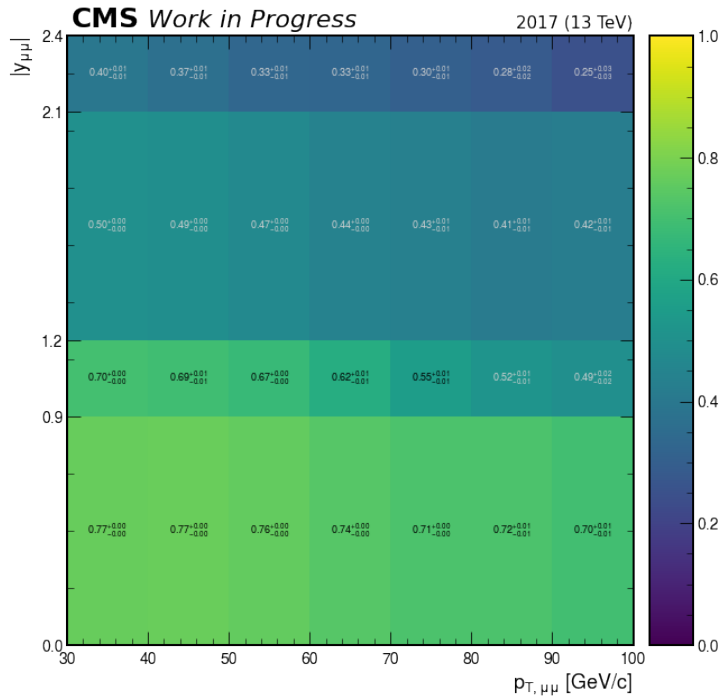
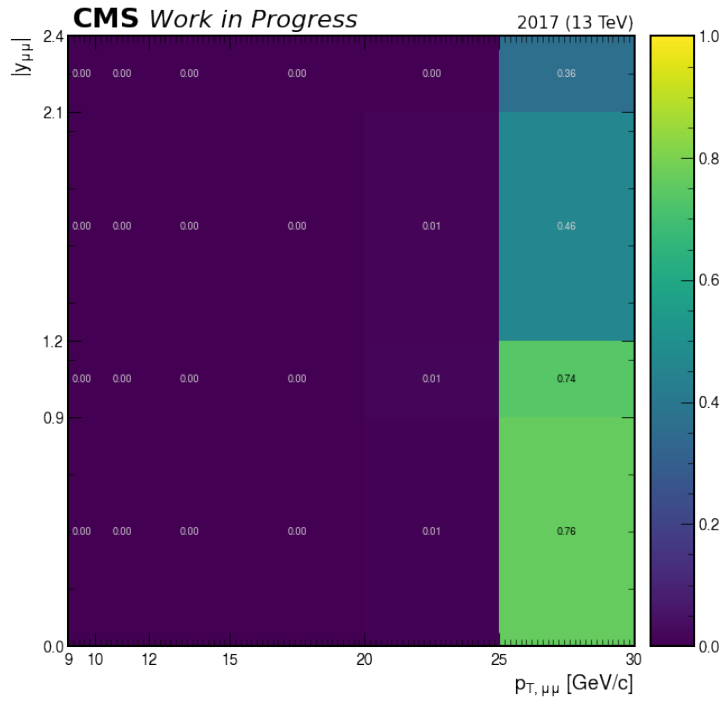
Figure 127 - J/ψ cuts efficiency in bins of rapidity and p_T - 2017 data.

Legend: The figure on top shows the J/ψ cuts efficiency in the region $|y| < 2.4$ and $9 < p_T < 30$ GeV/c and the figure on bottom shows it in the region $|y| < 2.4$ and $30 < p_T < 100$ GeV/c.

Top figure: uncertainties are purposely omitted for visualization purposes

Source: The author, 2023.

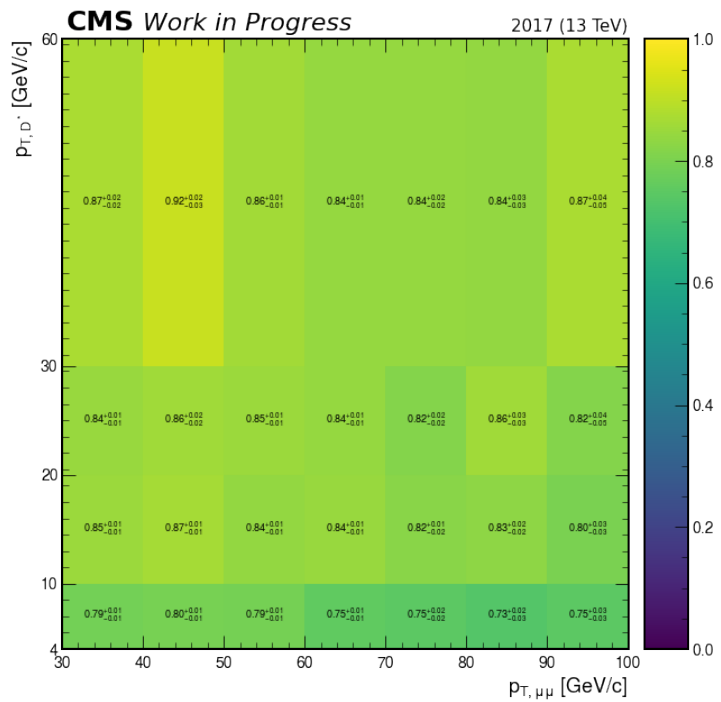
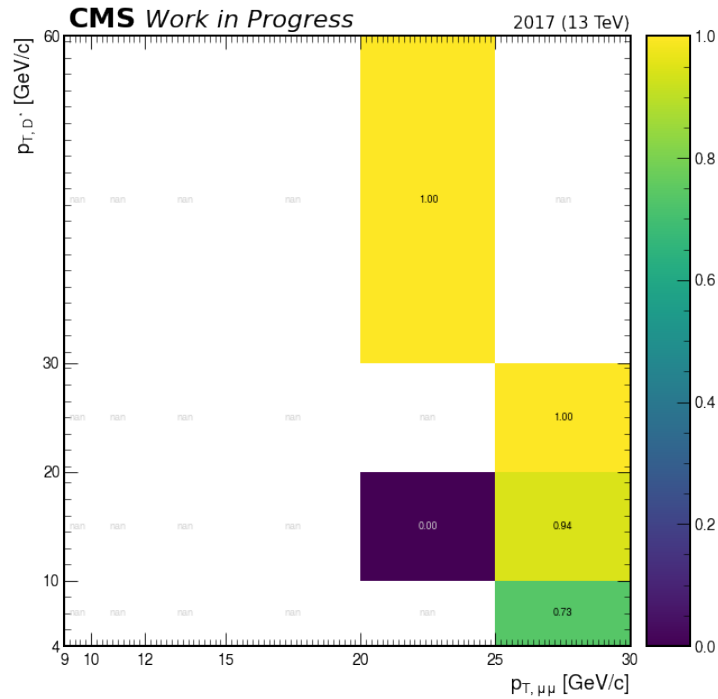
Figure 128 - HLT efficiency in bins of rapidity and p_T - 2017 data.



Legend: The figure on top shows the HLT efficiency in the region $|y| < 2.4$ and $9 < p_T < 30$ GeV/c and the figure on the bottom shows it in the region $|y| < 2.4$ and $30 < p_T < 100$ GeV/c. Top figure: uncertainties are purposely omitted for visualization purposes

Source: The author, 2023.

Figure 129 - Association efficiency in bins of D^* p_T and J/ψ p_T - 2017 data.



Legend: The figure on top shows the association efficiency in the region $4 < p_T^{D^*} < 60$ GeV/c and $9 < p_T^{D^*} < 30$ GeV/c and the figure on the bottom shows it in the region $4 < p_T^{D^*} < 60$ GeV/c and $30 < p_T^{D^*} < 100$ GeV/c. Top figure: uncertainties are purposely omitted for visualization purposes

Source: The author, 2023.

4.7 Systematic Uncertainties

Many factors can impact the systematic uncertainty of the cross-section measurement. They are summarized in the items below.

- Luminosity: the measurement of the integrated luminosity delivered to the CMS has a different uncertainty for each data taking period, 2016 (193), 2017 (194), and 2018 (195).
- Determination of signal yields: each probability function used to fit the distributions ($\mu^+\mu^-$ invariant mass, J/ψ decay length, and $D^* - D^0$ mass difference) is a source of systematic.
- J/ψ polarization.
- Residual misalignment in the tracker.
- Each track reconstructed in the final state has a systematic uncertainty.
- Monte Carlo sample statistics.
- Pile-up reweighting.
- Yield instability in 2016.
- Branching fraction
- Acceptance and efficiency.
- Systematic from the use of the theoretical formula

Not all sources are calculated in this thesis. The covered items are described in a dedicated subsection. Besides that, the possible correlations of the systematic uncertainties between the different years are not considered.

4.7.1 Luminosity

From (193), (194), and (195) the total systematic uncertainty (%) is extracted. Table (60) shows the values in % and in fb^{-1} .

Table 60 - Integrated luminosity - systematic uncertainty.

Year	Integrated Luminosity (fb ⁻¹)	Total Systematic Uncertainty (%)	Total Systematic Uncertainty (fb ⁻¹)
2016-pre-VFP	13.09	2.5	0.33
2016-pos-VFP	13.26	2.5	0.33
2017	41.48	2.3	0.95
2018	57.69	2.5	1.44

Legend: The uncertainty in 2016 and 2018 is 2.5%, while in 2017 it is 2.3%.

Note that the integrated luminosity in the second column refers to the amount of data collected with the triggers listed in Section (4.3.2).

Source: The author, 2023.

4.7.2 Branching Fraction

Each branching fraction used in the cross-section calculation has a systematic uncertainty assigned to it. Table (61) shows the nominal value and its related systematic uncertainty for each decay.

Table 61 - Branching fraction - systematic uncertainty.

Decay	Nominal value	Systematic uncertainty
$J/\psi \rightarrow \mu^+ \mu^-$	0.05961	± 0.00033
$D^* \rightarrow D^0 \pi_s$	0.677	± 0.005
$D^0 \rightarrow K^+ \pi^-$	0.03947	± 0.00030

Legend: Each measurement is taken from the particle data group (45).

Source: The author, 2023

4.7.3 Signal yields

Six different cases to obtain the number of signal and background events are considered. The first case is the nominal fit, *i.e.* the functions used are those defined in Section (4.4). The other five cases are based on the nominal fit, where one or more PDFs can be changed to fit the distributions. This method is known as fit variant (196). The six cases are shown in the bullets below,

- Case 1: nominal fit.
- Case 2: J/ψ signal: change crystal ball + gaussian to crystal ball only.

- Case 3: J/ψ background: change exponential function to linear function.
- Case 4: J/ψ prompt: change Resolution function to Gaussian.
- Case 5: D^* signal: change Johnson to double Gaussian.
- Case 6: D^* background: change the threshold function to the phenomenological threshold function³⁰.

To calculate the systematic uncertainty using this method, Equation (40) is used

$$\sigma_{sys} = \sqrt{\frac{\sum_{i=1}^N x_i^2 - N\bar{x}^2}{N-1}}. \quad (40)$$

Table (40) show the number of signal yields and systematic uncertainty in 2016-pre-APV, 2016-pos-APV, 2017, and 2018 data. All fits for all cases are shown in Appendix (I.1).

Table 62 - Signal yields - systematic uncertainty.

Case	2016-pre-VFP	2016-pos-VFP	2017	2018
(1)	2321	2077	4871	7310
(2)	2476	2016	4929	7324
(3)	2502	2086	5274	7303
(4)	2283	1721	5289	6538
(5)	2453	1968	5027	7436
(6)	2470	2061	4755	7233
Systematic	92	138	218	339
Ratio	4%	7%	4%	5%

Legend: The signal yield is calculated for each case highlighted in the bullets for the phase space considered in Section (4.3.3). The systematic is calculated with Equation (40) and the ratio is given by syst/nom.

Source: The author, 2023.

4.7.4 Tracking

Each reconstructed track in D^* is responsible for a systematic uncertainty. This comes from the tracking efficiency measurements calculated by the CMS tracking Physics

³⁰ The alternative phenomenological threshold function is given by $f = (1 - \exp(-(\frac{\Delta M - m_0}{p_0}))) \cdot (\frac{\Delta M}{m_0})^{p_1} + p_2(\frac{\Delta M}{m_0} - 1)$, where p_0 , p_1 , and p_2 are free parameters, ΔM is the parameter to be fitted, and m_0 is the pion mass.

Object Group (POG) (197). In the case of D^* , three tracks are considered, $K\pi\pi_s$. There is a difference in the uncertainty for each of these three tracks. Concerning K and π the value of the uncertainty is composed of a term coming from the PDG, it can not be used for both tracks, thus the uncertainty assigned to the first track is higher than the uncertainty assigned to the second track. Furthermore, as the π_s is reconstructed with a lower p_T , a different value is assigned to it. From (185) this value is 5.2%. Table (63) shows the uncertainty related to each track and the final value for D^* in each year. More details can be found in Appendix (I).

Table 63 - Tracking - systematic uncertainty.

Year	First track	Second track	Slow pion	D^*
2016	2.7%	2.4%	5.2%	10.3%
2017	2.2%	1.8%	5.2%	9.2%
2018	2.1%	1.6%	5.2%	8.8%

Legend: Each reconstructed track has a different efficiency value assigned to it.

Source: The author, 2023.

4.7.5 Cuts Efficiency

The following cuts are chosen to calculate the systematic uncertainties related to the efficiency of the cuts. They are shown in the bullets below,

- Muon ID: soft ID is changed to loose ID.
- D^0 (from D^*) $\cos\phi$ (Point angle): the nominal value of 0.990 is changed to a lower value of 0.985 and a superior value of 0.995.
- Association (Vertex probability): the nominal value of 0.05 is changed to a lower value of 0.01 and a superior value of 0.09.

The systematic uncertainty attributed to the second and third cuts is very important as it can be related to the amount of non-prompt D^* in the signal. Table (64) shows the systematic uncertainties in % for each data-taking period. The details of this calculation can be found in Appendix (I)

Table 64 - Acceptance and efficiency - systematic uncertainty.

Dataset	Systematic uncertainty
2016-pre-VFP	10%
2016-pos-VFP	23%
2017	10%
2018	18%

Legend: The values in 2016-pre-VFP and in 2017 are 10%. It is 18% in 2018 and 23% in 2016-pos-VFP.

Source: The author, 2023.

4.8 Cross-Section

The total cross-section can be expressed as the sum of the SPS and DPS cross-sections

$$\sigma_{J/\psi+D^*}^{TOTAL} = \sigma_{J/\psi+D^*}^{SPS} + \sigma_{J/\psi+D^*}^{DPS}, \quad (41)$$

where the first term comes from SPS contribution and the second comes from DPS contribution. In this section, the total cross-section is calculated in the entire phase-space considered in the study, *i.e.*, $16 < p_T^{J/\psi} < 100$ GeV/c (2016), $25 < p_T^{J/\psi} < 100$ GeV/c (2017 and 2018), $|y|^{J/\psi} < 2.4$, $4 < p_T^{D^*} < 60$ GeV/c, and $|y|^{D^*} < 2.4$. To calculate the total cross-section of $J/\psi + D^*$ Equation (42) is used

$$\sigma_{J/\psi+D^*}^{TOTAL} = \frac{N_{J/\psi+D^*}}{\mathcal{L} \cdot A \cdot \epsilon \cdot BR_{J/\psi \rightarrow \mu^+\mu^-} \cdot BR_{D^* \rightarrow D^0\pi_s} \cdot BR_{D^0 \rightarrow K\pi}}, \quad (42)$$

where $A \cdot \epsilon = (A \cdot \epsilon_{pre_cuts})^{J/\psi} \cdot (A \cdot \epsilon_{pre_cuts})^{D^*} \cdot \epsilon_{cuts}^{D^*} \epsilon_{cuts}^{J/\psi} \cdot \epsilon_{HLT} \cdot \epsilon_{association}$ and,

- $N_{J/\psi+D^*}$: number of events with $J/\psi D^*$. **(1)**
- \mathcal{L} : integrated luminosity of the dataset. **(2)**
- $(A \cdot \epsilon_{pre_cuts})^{J/\psi}$: J/ψ acceptance with pre-cuts efficiency. A match between reconstructed and generated muon is performed here. **(3)**
- $(A \cdot \epsilon_{pre_cuts})^{D^*}$: D^* acceptance with pre-cuts efficiency. A match between reconstructed and generated D^* is performed here. **(4)**
- $\epsilon_{cuts}^{D^*}$: D^* cuts efficiency. **(5)**
- $\epsilon_{cuts}^{J/\psi}$: J/ψ cuts efficiency. **(6)**

- ϵ_{HLT} : trigger efficiency. (7)
- $\epsilon_{association}$: association efficiency. (8)
- $BR_{J/\psi \rightarrow \mu^+ \mu^-}$: $J/\psi \rightarrow \mu^+ \mu^-$ branching ratio. (9)
- $BR_{D^* \rightarrow D^0 \pi_s}$: $D^* \rightarrow D^0 \pi_s$ branching ratio. (10)
- $BR_{D^0 \rightarrow K \pi}$: $D^0 \rightarrow K \pi$ branching ratio. (11)

All parameters (1-11) used to calculate the total cross-section have been obtained in the previous sections. Tables (65), (66), (67), and (68) show all parameters and the total cross-section in 2016-pre-VFP, 2016-pos-VFP, 2017, and 2018 data taking period, respectively.

Table 65 - Total cross-section - 2016-pre-VFP.

Parameter	Value	Statistical Uncertainty	Systematic Uncertainty
(1)	2321	48	92
(2)	13.09 fb ⁻¹	-	0.33 fb ⁻¹
(3)	0.912	± 0.000	-
(4)	0.693	± 0.001	-
(5)	0.212	± 0.001	± 0.070
(6)	0.971	± 0.000	± 0.030
(7)	0.587	± 0.001	-
(8)	0.879	± 0.002	± 0.070
(9)	0.05961	-	± 0.00033
(10)	0.677	-	± 0.005
(11)	0.03947	-	± 0.00030
$\sigma^{TOTAL}[pb]$	1658.25	± 35.42	± 249.97

Legend: Total cross-section in 2016-pre-VFP is restricted to the phase space: $4 < p_T^{D^*} < 60$ GeV/c, and $|y^{D^*}| < 2.4$ and $16 < p_T^{J/\psi} < 100$ GeV/c, and $|y^{J/\psi}| < 2.4$.

Source: The author, 2023.

Table (69) shows all cross-section results, highlighting the dataset used and the phase space considered. It is worth mentioning that 2016-pre-VFP and 2016-pos-VFP can not be directly compared with 2017 and 2018 results, as the phase space is different. If the compatibility of the results in the same phase space is analyzed, they are found to be compatible. In fact, the measurements in the 2016 datasets are compatible because $|\bar{x}_1 - \bar{x}_2| < 2 \cdot \sqrt{\sigma_{\bar{x}_1}^2 + \sigma_{\bar{x}_2}^2}$, where \bar{x}_1 is the total cross-section in 2016-pre-VFP, \bar{x}_2 is the total cross-section in 2016-pos-VFP, and $\sigma_{\bar{x}_1}$ and $\sigma_{\bar{x}_2}$ are their related uncertainties. Concerning the results in 2017 and 2018, it is noted that using the same criteria, they are compatible

Table 66 - Total cross-section - 2016-pos-VFP.

Parameter	Value	Statistical Uncertainty	Systematic Uncertainty
(1)	1993	46	138
(2)	13.26 fb ⁻¹	-	0.33 fb ⁻¹
(3)	0.811	± 0.000	-
(4)	0.626	± 0.000	-
(5)	0.212	± 0.001	± 0.120
(6)	0.979	± 0.000	± 0.140
(7)	0.651	± 0.001	-
(8)	0.868	± 0.001	± 0.140
(9)	0.05961	-	± 0.00033
(10)	0.677	-	± 0.005
(11)	0.03947	-	± 0.00030
$\sigma^{TOTAL}[pb]$	1584.80	± 36.93	± 431.61

Legend: Total cross-section in 2016-pos-VFP is restricted to the phase space: $4 < p_T^{D^*} < 60$ GeV/c, and $|y^{D^*}| < 2.4$ and $16 < p_T^{J/\psi} < 100$ GeV/c, and $|y^{J/\psi}| < 2.4$.

Source: The author, 2023.

Table 67 - Total cross-section - 2017.

Parameter	Value	Statistical Uncertainty	Systematic Uncertainty
(1)	4950	70	218
(2)	41.48 fb ⁻¹	-	0.96 fb ⁻¹
(3)	0.833	± 0.000	-
(4)	0.711	± 0.001	-
(5)	0.253	± 0.001	± 0.090
(6)	0.980	± 0.000	± 0.010
(7)	0.610	± 0.001	T.B.D
(8)	0.822	± 0.002	± 0.050
(9)	0.05961	-	± 0.00033
(10)	0.677	-	± 0.005
(11)	0.03947	-	± 0.00030
$\sigma^{TOTAL}[pb]$	1017.49	± 11.51	± 145.19

Legend: Total cross-section in 2017 is restricted to the phase space: $4 < p_T^{D^*} < 60$ GeV/c, and $|y^{D^*}| < 2.4$ and $25 < p_T^{J/\psi} < 100$ GeV/c, and $|y^{J/\psi}| < 2.4$.

Source: The author, 2023.

Table 68 - Total cross-section - 2018.

Parameter	Value	Statistical Uncertainty	Systematic Uncertainty
(1)	7464	86	339
(2)	57.69 fb ⁻¹	-	1.44 fb ⁻¹
(3)	0.840	± 0.001	-
(4)	0.714	± 0.001	-
(5)	0.246	± 0.001	0.130
(6)	0.980	± 0.000	0.050
(7)	0.650	± 0.001	-
(8)	0.832	± 0.002	0.100
(9)	0.05961	-	± 0.00033
(10)	0.677	-	± 0.005
(11)	0.03947	-	± 0.00030
$\sigma^{TOTAL}[pb]$	1038.77	± 12.86	± 211.43

Legend: Total cross-section in 2018 is restricted to the phase space: $4 < p_T^{D^*} < 60$ GeV/c, and $|y^{D^*}| < 2.4$ and $25 < p_T^{J/\psi} < 100$ GeV/c, and $|y^{J/\psi}| < 2.4$.

Source: The author, 2023.

as well. It is interesting to note that the cross-section in 2016 is higher than in the other years because the J/ψ p_T is lower, it starts at 16 GeV/c in 2016, while it starts at 25 GeV/c in 2017 and 2018. This difference is expected in theory and it was already measured in many experiments, *i.e.*, the lower the J/ψ p_T , the higher the cross-section (considering values higher than 2 GeV/c, as for values lower than this there is a turning point where the higher the p_T , the higher the cross-section). This can be checked in (198, 199) for results in pp collisions, (200) for results in p-Pb collisions, and (201) for theory predictions.

4.8.1 Effective Cross-Section Extraction

To calculate the effective cross-section, Equation (13) is used. In the case of $J/\psi + D^*$, the equation becomes

$$\sigma_{eff} = \frac{\sigma_{J/\psi} \cdot \sigma_{D^*}}{\sigma_{J/\psi+D^*}^{DPS}}, \quad (43)$$

where $\sigma_{J/\psi+D^*}^{DPS} = \sigma_{J/\psi+D^*}^{TOTAL} - \sigma_{J/\psi+D^*}^{SPS}$. The terms $\sigma_{J/\psi}$ and σ_{D^*} are the prompt inclusive production of J/ψ and D^* , that are obtained from (202) and (185), respectively. Considering the phase space $4 < p_T^{D^*} < 60$ GeV/c, $|y^{D^*}| < 2.1$, $25 < p_T^{J/\psi} < 100$ GeV/c, and $|y^{J/\psi}| < 1.2$, the cross-sections are shown in Table (70). Note that the phase space now

Table 69 - Total cross-section - all years

Dataset	Cross-section	Kinematic region
2016-pre-VFP	1658 ± 35 (stat) ± 250 (sys)	$4 < p_T^{D^*} < 60$ GeV/c $ y^{D^*} < 2.4$
		$16 < p_T^{J/\psi} < 100$ GeV/c $ y^{J/\psi} < 2.4$
2016-pos-VFP	1585 ± 37 (stat) ± 432 (sys)	$4 < p_T^{D^*} < 60$ GeV/c $ y^{D^*} < 2.4$
		$16 < p_T^{J/\psi} < 100$ GeV/c $ y^{J/\psi} < 2.4$
2017	1017 ± 12 (stat) ± 145 (sys)	$4 < p_T^{D^*} < 60$ GeV/c $ y^{D^*} < 2.4$
		$25 < p_T^{J/\psi} < 100$ GeV/c $ y^{J/\psi} < 2.4$
2018	1039 ± 13 (stat) ± 211 (sys)	$4 < p_T^{D^*} < 60$ GeV/c $ y^{D^*} < 2.4$
		$25 < p_T^{J/\psi} < 100$ GeV/c $ y^{J/\psi} < 2.4$

Legend: Note that the difference between the cross-sections in 2016 and 2017/2018 data is due to the different phase spaces. If the results in the same phase space are compared (2016-pre-VFP with 2016-pos-VFP and 2017 with 2018) they are found to be compatible. It is noted that the systematic uncertainties (15%, 26%, 15%, 21% in 2016-pre-VFP, 2016-pos-VFP, 2017, and 2018, respectively) have more impact on the result than the statistical uncertainties (2%, 2%, 1%, 1% in 2016-pre-VFP, 2016-pos-VFP, 2017, and 2018, respectively). This is not too different from other CMS analyses, where normally the systematic uncertainty is greater than the statistical uncertainty (198, 185).

Source: The author, 2023.

is different from that in Section (4.8).

Table 70 - Measurement of prompt inclusive J/ψ and D^* .

Parameter	Value	Source
$\sigma_{J/\psi}$	3.74 ± 0.02 (stat) ± 0.06 (sys) (nb)	(202)
σ_{D^*}	380.71 ± 9.90 (stat) ± 26.05 (sys) (μb)	(185)

Legend: The cross-section in both cases is calculated by summing the contribution of each p_T bin. Table A.1 of (202) is used to calculate the J/ψ cross-section and Table 5 of (185) is used to calculate the D^* cross-section.

Source: The author, 2023.

To obtain the total cross-section, the same strategy used in Section (4.8) is considered. The step-by-step calculation is the same and the only difference is in the phase space, evidenced by the difference in the rapidity of both particles, J/ψ and D^* .

Table 71 - Total cross-section for the σ_{eff} calculation.

Dataset	Total cross-section (pb)
2016-pre-VFP	579 ± 18 (stat) ± 88 (sys)
2016-pos-VFP	553 ± 21 (stat) ± 145 (sys)
2017	603 ± 10 (stat) ± 88 (sys)
2018	586 ± 9 (stat) ± 122 (sys)

Legend: The value of the cross-sections in this table are lower when compared with the results in Table (69). This is expected, as the phase space considered is smaller. Besides that, as all results are in the same phase space, they can be directly compared. Using the same assumptions as in Section (4.8), they are found to be compatible.

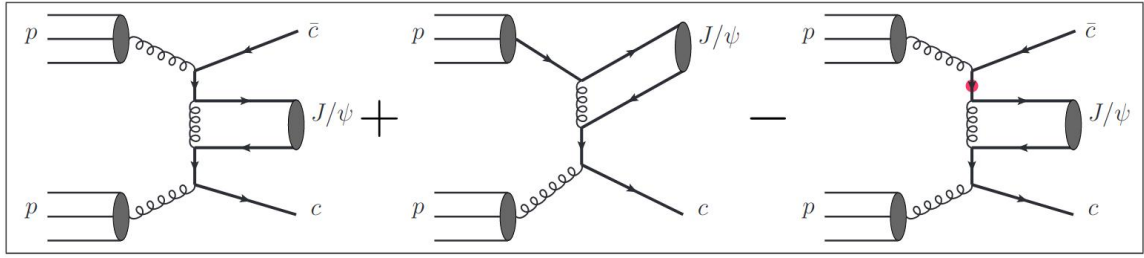
Source: The author, 2023.

To obtain $\sigma_{J/\psi+D^*}^{SPS}$ the Helac-Onia (178) generator is used, *i.e.*, the theoretical value is used to estimate this cross-section. The main contribution to the SPS production is given by the process $gg \rightarrow J/\psi + c\bar{c}$. However, it is important to consider the initial charm contributions in SPS production as well (178). These two processes are treated with three Feynman diagrams, where the first is for the process $gg \rightarrow J/\psi + c\bar{c}$, the second is for the initial charm contribution, and the third is used to subtract the overlap between the two contributions. Figure (130) shows the Feynman diagram for the SPS production.

Therefore, for the SPS VFNS predictions in color singlet mode, the phase space integrated cross-section is

$$\sigma_{J/\psi+D^*}^{SPS} \cdot BR_{D^* \rightarrow D^0 \pi_s} \cdot BR_{D^0 \rightarrow k\pi} \cdot BR_{J/\psi \rightarrow \mu^+ \mu^-} = 0.038_{-0.008-0.001}^{+0.016+0.001} pb, \quad (44)$$

Figure 130 - Feynman diagram for the SPS production.



Legend: The first diagram shows the $gg \rightarrow J/\psi + c\bar{c}$ contribution (ggF), the middle diagram shows the initial charm contribution (cgF), and the third diagram is used to perform the proper matching between the two first diagrams, where the matching scheme is used to subtract the overlap between them. This is referred to as the variable flavor number scheme (VFNS).

Source: SHAO, 2020, p. 3.

where the first uncertainties are from the factorization scale variations and the second uncertainties are from the PDF parameterization. Thus, taking both uncertainties in quadrature and dividing by the branching ratios,

$$\sigma_{J/\psi+D^*}^{SPS} = 24_{-5}^{+10} \text{ pb}. \quad (45)$$

This result was provided by the Helac-Onia developer and was produced with a private sample. It is worth mentioning that the phase space considered in this result is a little different from the one used to calculate the total cross-section of the associated production of $J/\psi D^*$, $4 < p_T^{D^*} < 100 \text{ GeV}/c$, $|y^{D^*}| < 2.4$, $25 < p_T^{J/\psi} < 100 \text{ GeV}/c$, and $|y^{J/\psi}| < 2.4$. Therefore, it is expected that the value given by Equation (45) is greater than the value in the phase space considered in this section. Still, the value should not be too different and this minor difference can be incorporated into the uncertainties. Therefore, using this result the DPS cross-section in each dataset is calculated as $\sigma_{J/\psi+D^*}^{DPS} = \sigma_{J/\psi+D^*}^{TOTAL} - \sigma_{J/\psi+D^*}^{SPS}$. Table (72) shows the DPS cross-section for each dataset.

Finally, to calculate the effective sigma, Equation (43) is used. Table (73) shows all values.

Table 72 - $J/\psi + D^*$ DPS cross-sections.

Dataset	DPS cross-section (pb)
2016-pre-VFP	$554.79^{+21.05}_{-19.17}$ (stat) $+88.23_{-87.80}$ (sys)
2016-pos-VFP	$528.80^{+22.89}_{-21.17}$ (stat) $+145.12_{-144.86}$ (sys)
2017	$579.25^{+14.43}_{-11.51}$ (stat) $+88.24_{-87.81}$ (sys)
2018	$562.54^{+13.30}_{-10.06}$ (stat) $+122.11_{-121.80}$ (sys)

Legend: Note again that in 2016-pos-VFP the values are higher. However, all values are compatible. Compared with the total cross-section, it is noted that the fraction of DPS is around 95%. It is worth mentioning that this number can be varied to 97-98% if the SPS cross-section ($23.86^{+10.07}_{-5.07}$ pb) is calculated in the correct phase space, this is discussed in Section (4.9).

Source: The author, 2023.

Table 73 - Effective sigma.

Dataset	σ_{eff} (mb)
2016-pre-VFP	$2.56^{+0.12}_{-0.11}$ (stat) $+0.42_{-0.44}$ (sys)
2016-pos-VFP	$2.69^{+0.14}_{-0.13}$ (stat) $+0.74_{-0.76}$ (sys)
2017	$2.46^{+0.09}_{-0.08}$ (stat) $+0.38_{-0.41}$ (sys)
2018	$2.53^{+0.09}_{-0.08}$ (stat) $+0.55_{-0.58}$ (sys)

Legend: All values are compatible. The discussion and comparison with other experiments are in Section (4.9)

Source: The author, 2023.

4.9 Discussion of Results and Conclusions

The total cross-section obtained in Section (4.8.1) is represented by symmetrical uncertainties. To combine the results shown in Table (71) in one measurement, Equation (46) is used

$$\bar{x} = \frac{\sum_{i=1}^4 w_i x_i}{\sum_{i=1}^4 w_i}, \quad \sigma_{\bar{x}} = \sqrt{\frac{1}{\sum_{i=1}^4 w_i}}, \quad (46)$$

where x_i is the nominal value, $w_i = 1/\sigma_i^2$, and σ_i is the uncertainty. It is worth mentioning that to calculate \bar{x} the σ_i are given by the quadrature sum of the statistical and systematic uncertainties. Therefore the combined value of the total cross-section shown in Table (71) is

$$\sigma_{J/\psi+D^*}^{TOTAL} = 585.32 \pm 5.99(stat) \pm 51.60(sys) \quad pb, \quad (47)$$

where the fiducial volume is defined as $4 < p_T^{D^*} < 60$ GeV/c, $|y^{D^*}| < 2.1$, $25 < p_T^{J/\psi} < 100$ GeV/c, and $|y^{J/\psi}| < 1.2$. It is worth mentioning that this is the first observation of the associated production of J/ ψ and D* mesons.

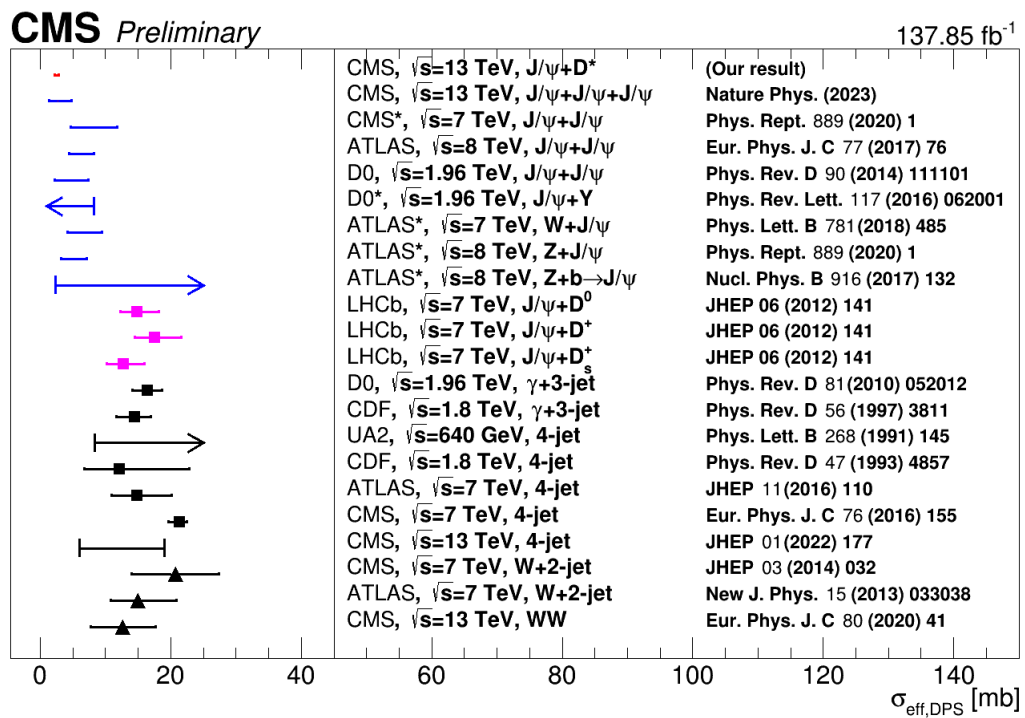
To estimate the fraction of SPS and DPS considering the correct phase space the total cross-section results in the phase space $4 < p_T^{D^*} < 60$ GeV/c, $|y^{D^*}| < 2.4$, $25 < p_T^{J/\psi} < 100$ GeV/c, and $|y^{J/\psi}| < 2.4$ are compared with the results in the phase space $4 < p_T^{D^*} < 60$ GeV/c, $|y^{D^*}| < 2.1$, $25 < p_T^{J/\psi} < 100$ GeV/c, and $|y^{J/\psi}| < 1.2$. If the results in 2017 and 2018 in Table (69) (997.75 ± 11.51 (stat) ± 145.19 (sys) pb and 1015.79 ± 12.86 (stat) ± 211.43 (sys) pb, respectively) are compared with the results in Table (71) (603.12 ± 10.34 (stat) ± 87.67 (sys) pb and 586.40 ± 8.69 (stat) ± 121.69 (sys) pb), they are around 1.7 higher. If this factor is considered in the SPS cross-section, *i.e.*, considering that the SPS cross-section varies in the same way as the total cross-section, the value of $23.86_{-5.07}^{+10.07}$ pb reduces to around 14 pb, which gives a fraction of DPS around 97.5% and a fraction of SPS around 2.5%. This is not too far from the theoretical value found in the studies discussed in Section (4.1.1), which is around 1% (203, 204).

Finally, using the combined result given by Equation (47), the effective sigma is

$$\sigma_{eff} = 2.53_{-0.08}^{+0.09}(stat)_{-0.29}^{+0.25}(sys) mb. \quad (48)$$

This result is compared with other experiments in Figure (131). The results in black refer to the final states with same-sign W bosons, W+jets, jets, and γ + jets; the results in magenta refer to final states with J/ ψ and D mesons; the results in blue refer to the final states with either quarkonia or quarkonia with other particles; and the result in red is that obtained in this thesis.

Figure 131 - Effective sigma measurements



Legend: The results in black refer to the final states with same-sign W bosons, W+jets, jets, and γ + jets; the results in magenta refer to final states with J/ψ and D mesons; the results in blue refer to the final states with either quarkonia or quarkonia with other particles; and the result in red is that obtained in this thesis.

Source: The author, 2023.

It is known from the literature that the σ_{eff} is expected to be higher for final states involving high- p_T jets and/or electroweak bosons (10-20 mb) when compared to final states involving pairs of quarkonia (3-10 mb). This difference occurs because in electroweak bosons more quarks contribute to the process, while in quarkonia more gluons contribute to the process (205). This difference can also be attributed to the poor discrimination of the SPS contribution, which can overestimate the DPS contribution, consequently reducing the value of the σ_{eff} (206). It is natural to compare the result of this work (2.53 mb) with the values measured by the LHCb (167) (12-17 mb), as the final states are similar. In fact, this is one of the motivations of this work. The low value measured in this work indicates that there is a very strong correlation between the interacting partons (207). Furthermore, as the phase space of the LHCb measurement is $3 < p_T^D < 12$ GeV/c, $2 < y^D < 4$, $p_T^{J/\psi} < 12$ GeV/c, and $2 < y^{J/\psi} < 4$, this gives a different parton profile in the proton, *i.e.* the $x = 2 \frac{m_p^T}{\sqrt{s}} \cdot \sinh(y)$ variable³¹ is different in the phase space considered in this thesis when compared with the phase space in the LHCb study. This variable gives information about the parton content in the proton (167, 207) and the difference in its value for different particle species ($x \approx 5 \times 10^{-4}$ in gluon-gluon for quarkonia production and $x \approx 10^{-2}$ in the production of electroweak bosons) and different phase space suggests that there is a dependence of the σ_{eff} on the x variable.

³¹ The x variable gives the fraction of momentum of proton carried by the parton, where m_p^T is the transverse mass of the parton.

CONCLUSION

In this work, two main subjects were discussed: the CMS-RPC upgrade project studies and the associated production of J/ψ and D^* in pp collisions at $\sqrt{s} = 13$ TeV with the full run 2 in CMS detector. Concerning the CMS-RPC upgrade project studies, two main works have been discussed. In the first, the performance of eco-friendly gas mixtures for RPC was analyzed. The performance studies performed at GIF++ comparing the standard gas mixture with two ecological gas mixtures were successfully performed. It is possible to compare the performance with cluster rates ranging from 0 to around 700 Hz/cm². The noise for all gases was found negligible, less than 1 Hz/cm². Both eco gases have currents higher than the ones found in standard gas, where for ecomix-2 it ranges between 79% and 315.90% and for ecomix-3 it ranges between 126.81% and 354.63%. The average difference in the first case is 158.70%, while in the second case is 190.32%. When comparing the WP at the efficiency knee with no radiation, for the ecomix-2 this value is around 1110 V greater than the one found in standard gas, while for the ecomix-3 this value is around 297 V. With cluster rates around 700 Hz/cm² the values are 1.2 kV and 0.4 kV. For low rates the drop in efficiency is higher for ecomix-3, followed by ecomix-2. After 600 Hz/cm² it is clear that ecomix-2 has lower efficiency when compared with the standard gas. Finally, when comparing the WP as a function of the gamma rate, the WP for the ecomix-2 when compared with standard gas is always greater than 1 kV, ranging from 1 kV to 1.2 kV. While for ecomix-3 this value ranges between 0.2 kV to 0.4 kV. The difference in the WP between ecomix-2 and ecomix-3 is between 0.8 kV and 0.9 kV. Therefore, with the studies performed here, it is possible to conclude that the performance of both ecogas mixtures used is slightly lower than the performance of the standard gas. Still, they can be classified as good candidates and more tests must be performed. It is very important to characterize these mixtures for higher rates. The ecogas collaboration is still working with these mixtures and the idea is to study the detector aging to compare its performance as a function of the accumulated charge. Besides that, more performance tests with test beams will be performed to study the same parameters and compare them with the previous studies.

The second work developed in the CMS-RPC upgrade project studies was the study of the aging of an iRPC prototype. The beam tests for an iRPC prototype and the monitoring of its ohmic and physics currents as a function of the accumulated charge were studied. The performance results during the beam tests are satisfactory. Using custom electronics with a threshold of 75 fC the drop in the efficiency between source off and the rate of 2.2 kHz/cm² is around 5.5%, while the increase in the WP is around 600 V. Moreover, using the threshold of 45 fC the drop in the WP is reduced to 380 V. These performance tests need to be validated in a new beam test with the current accumulated

charge. With the accumulated charge of 50 mC/cm², the level of currents in the top gap is acceptable. However, the ohmic current in the bottom gap is increasing and the cause of this increase is under study.

The associated production of J/ψ and D^* in pp collisions at $\sqrt{s} = 13$ TeV with the full Run 2 in CMS detector was studied. This is the first time that this associated production has been observed. The cross-section has been measured in the fiducial cross-section, $4 < p_T^{D^*} < 60$ GeV/c, $|y^{D^*}| < 2.1$, $25 < p_T^{J/\psi} < 100$ GeV/c, $|y^{J/\psi}| < 1.2$ as 585.32 ± 5.99 (stat) ± 51.60 (sys) pb, where the fraction due to the DPS contribution was estimated to be 97.5%. In this scenario, the effective cross-section was found to be $2.53_{-0.08}^{+0.09}$ (stat) $_{-0.29}^{+0.25}$ (sys) mb (It is worth mentioning that few systematic need to be calculated). This value is compatible with the values extracted in the triple J/ψ analysis (14), in the pair of quarkonia (10, 208) analysis, in W boson and J/ψ (209) analysis, and in Z boson and J/ψ analysis (209, 210). When the result is compared with those of the LHCb (167) it is observed that the different phase space leads to very different values for the effective sigma, suggesting that this parameter should have a dependence on the x variable.

Therefore, it is clear that the CMS detector is a good environment to measure the association of J/ψ and D^* . For the improvement of this work and for a future publication, it is suggested that the fraction of DPS be extracted in a data-driven way and the rest of the systematic uncertainties be calculated. Besides that, the differential cross-sections (in bins of the invariant mass, p_T of the associated object, for example.) can be calculated so the comparison with the theory can be easier. In the same direction, it is strongly suggested that the measurement of other states, such as J/ψ and D^0 (D^+ , D_s^+) be measured. Also, it is important that for the analysis in the LHC Run 3 a dedicated trigger be developed so that lower values of p_T be analyzed (such as values lower than 10 GeV/c). This will make the comparison with the LHCb results easier, as the p_T region will be similar. Finally, it is important to mention that the future circular collider (FCC) can be a very interesting environment to probe lower values of the variable x, providing a range of possibilities in different phase spaces and in different particle species.

REFERENCES

- 1 KHARE, A. The November (J/ψ) revolution: Twenty-five years later. *Current Science*, Temporary Publisher, [s. l.], v. 77, n. 9, p. 1210–1213, 1999. ISSN 00113891.
- 2 ZWEIG, G. *An SU_3 model for strong interaction symmetry and its breaking*; Version 1. Geneva : [s. n.], 1964.
- 3 GELL-MANN, M. A Schematic Model of Baryons and Mesons. *Phys. Lett.*, [s. l.], v. 8, p. 214–215, 1964.
- 4 GOLDHABER, G. et al. Observation in $e^+ e^-$ Annihilation of a Narrow State at $1865\text{-MeV}/c^2$ Decaying to $K \pi$ and $K \pi \pi \pi$. *Phys. Rev. Lett.*, [s. l.], v. 37, p. 255–259, 1976.
- 5 GOLDHABER, G.; WISS, J. E. Charmed Mesons Produced in $e^+ e^-$ Annihilation. *Ann. Rev. Nucl. Part. Sci.*, [s. l.], v. 30, p. 337–381, 1980.
- 6 LOBODZINSKA, E. M. Studies of double parton scattering in ATLAS. In: INTERNATIONAL WORKSHOP ON MULTIPLE PARTONIC INTERACTIONS AT THE LHC, 8., 2017, [s. l.]. [*Proceedings ...*]. [S. l.: s.n.], 2017.
- 7 KHACHATRYAN, V. et al. Measurement of Prompt J/ψ Pair Production in pp Collisions at $\sqrt{s} = 7$ TeV. *JHEP*, [S. l.], v. 09, p. 094, 2014.
- 8 AABOUD, M. et al. Measurement of the prompt J/ψ pair production cross-section in pp collisions at $\sqrt{s} = 8$ TeV with the ATLAS detector. *Eur. Phys. J. C*, [s. l.], v. 77, n. 2, p. 76, 2017.
- 9 AAIJ, R. et al. Measurement of the J/ψ pair production cross-section in pp collisions at $\sqrt{s} = 13$ TeV. *JHEP*, [s. l.], v. 06, p. 047, 2017. [Erratum: *JHEP* 10, 068 (2017)].
- 10 SHAO, H.-S.; ZHANG, Y.-J. Complete study of hadroproduction of a Y meson associated with a prompt J/ψ . *Phys. Rev. Lett.*, [s. l.], v. 117, n. 6, p. 062001, 2016.
- 11 AAIJ, R. et al. Observation of double charm production involving open charm in pp collisions at $\sqrt{s} = 7$ TeV. *JHEP*, [s. l.], v. 06, p. 141, 2012. [Addendum: *JHEP* 03, 108 (2014)].
- 12 AAIJ, R. et al. Production of associated Y and open charm hadrons in pp collisions at $\sqrt{s} = 7$ and 8 TeV via double parton scattering. *JHEP*, [s. l.]: v. 07, p. 052, 2016.
- 13 CMS COLLABORATION. Observation of same-sign WW production from double parton scattering in proton-proton collisions at $\sqrt{s} = 13$ TeV. [Geneva : CERN], 2022.

- 14 TUMASYAN, A. et al. Observation of triple J/ψ meson production in proton-proton collisions at $\sqrt{s} = 13$ TeV. *Nature Phys.*, [s. l.], 11 2021.
- 15 AAMODT, K. et al. The ALICE experiment at the CERN LHC. *JINST*, [s. l.], v. 3, p. S08002, 2008.
- 16 AAD, G. et al. The ATLAS Experiment at the CERN Large Hadron Collider. *JINST*, [s. l.], v. 3, p. S08003, 2008.
- 17 CHATRCHYAN, S. et al. The CMS experiment at the CERN LHC. *JINST*, [s. l.]: v. 3, p. S08004, 2008.
- 18 SZUMLAK, T. The LHCb experiment. *Acta Phys. Polon. B*, [s. l.], v. 41, p. 1661–1668, 2010.
- 19 OSTOJIC, R. LHC interaction region upgrade: Phase I. In: WORKSHOP ON ACCELERATOR MAGNET SUPERCONDUCTORS, DESIGN AND OPTIMIZATION, 2008, [s. l.]. [*Proceedings ...*]. [S.l.: s.n.], 2008. p. 1–7.
- 20 FERNANDEZ, I. Z. et al. *High-Luminosity Large Hadron Collider (HL-LHC):* Technical design report. [S. l.: s. n.], 2020. V. 10/2020.
- 21 ESTRADA, C. U. CMS improved resistive plate chamber studies in preparation for the High Luminosity phase of the LHC. *JINST*, [s. l.], v. 17, n. 09, p. C09029, 2022.
- 22 SAVIANO, G. et al. Properties of potential eco-friendly gas replacements for particle detectors in high-energy physics. *JINST*, [s. l.], v. 13, n. 03, p. P03012, 2018.
- 23 CARROLL, S. M. *Spacetime and geometry : An introduction to general relativity*. [S.l.: s.n.], 2004.
- 24 GAILLARD, M. K.; GRANNIS, P. D.; SCIULLI, F. J. The Standard model of particle physics. *Rev. Mod. Phys.*, [s. l.], v. 71, p. S96–S111, 1999.
- 25 BRIVIO, I.; TROTT, M. The standard model as an effective field theory. *Physics Reports*, Elsevier, [s. l.], v. 793, p. 1–98, 2019.
- 26 THOMSON, M. *Modern particle physics*. [S. l.]: Cambridge University Press, 2013.
- 27 CARROLL, S. M. *Spacetime and geometry*. [S. l.]: Cambridge University Press, 2019.
- 28 FERREIRA FILHO, M. B. *Efeitos da violação da simetria de Lorentz na polarização de ondas gravitacionais*, 2019. 93 f. Dissertação (Mestrado em Física) - Centro de Ciências, Universidade Federal do Ceará, Fortaleza, 2019.
- 29 PESKIN, M. *An introduction to quantum field theory*. [S.l.]: Westview Press, 1995.
- 30 HIGGS, P. W. Broken symmetries and the masses of gauge bosons. *Physical Review Letters*, APS, [s. l.], v. 13, n. 16, p. 508, 1964.

- 31 ENGLERT, F.; BROUT, R. Broken symmetry and the mass of gauge vector mesons. *Physical Review Letters*, APS, [s. l.], v. 13, n. 9, p. 321, 1964.
- 32 MCMAHON, D. *Quantum field theory demystified: a self-teaching guide*. New York: McGraw-Hill, 2009. SPIRES Entry.
- 33 GOLDSTONE, J. Field Theories with Superconductor Solutions. *Nuovo Cim.*, [s. l.]: v. 19, p. 154–164, 1961.
- 34 GURALNIK, G. S.; HAGEN, C. R.; KIBBLE, T. W. B. Global Conservation Laws and Massless Particles. *Phys. Rev. Lett.*, [s. l.]: v. 13, p. 585–587, 1964.
- 35 NAMBU, Y. Quasiparticles and Gauge Invariance in the Theory of Superconductivity. *Phys. Rev.*, [s. l.]: v. 117, p. 648–663, 1960.
- 36 CHATRCHYAN, S. et al. Observation of a New Boson at a Mass of 125 GeV with the CMS Experiment at the LHC. *Phys. Lett. B*, [s. l.], v. 716, p. 30–61, 2012.
- 37 BASS, S. D.; ROECK, A. D.; KADO, M. The Higgs boson implications and prospects for future discoveries. *Nature Reviews Physics*, Nature Publishing Group, [s. l.], v. 3, n. 9, p. 608–624, 2021.
- 38 GELL-MANN, M. Symmetries of baryons and mesons. *Phys. Rev.*, [s. l.]: v. 125, p. 1067–1084, 1962.
- 39 GREINER, W.; SCHRAMM, S.; STEIN, E. *Quantum chromodynamics*. [S. l.]: Springer, 2007.
- 40 ANSELMINO, M. et al. *Introdução à QCD perturbativa*. [S.l.]: Grupo Gen-LTC, 2000.
- 41 ELLIS, R. K.; STIRLING, W. J.; WEBBER, B. R. *QCD and collider physics*. [S.l.]: Cambridge University Press, 2003.
- 42 GRIFFITHS, D. *Introduction to elementary particles*. [S.l.]: Wiley, 2020.
- 43 ZHANG, H.-B. et al. Muon anomalous magnetic dipole moment in the μ vSSM *. *Chin. Phys. C*, [s. l.]: v. 46, n. 9, p. 093107, 2022.
- 44 RABBERTZ, K. Experimental Tests of QCD. In: RENCONTRES DU VIETNAM: WINDOWS ON THE UNIVERSE, 9., 2013, [s. l.]. [*Proceedings ...*]. . [S. l.: s.n.], 2013. P. 85–92.
- 45 GROUP, P. D. et al. Review of particle physics. *Progress of Theoretical and Experimental Physics*, [S. l.], v. 2020, n. 8, 2020.
- 46 PRICE, D. D. *Studies of quarkonium production and polarisation with early data at ATLAS*. 2008. Thesis (doctorate) - Faculty of Science and Technology, University of Lancaster, Lancaster, 2008.

- 47 ECKER, G. Chiral perturbation theory. *Progress in Particle and Nuclear Physics*. Elsevier, [S. l.], v. 35, p. 1–80, 1995.
- 48 USACHOV, A. *Study of charmonium production using decays to hadronic final states with the LHCb experiment*. 2008. Thesis (doctorate) - Laboratoire de l'accélérateur linéaire, l'Université Paris-Saclay, Paris, 2008.
- 49 LANSBERG, J.-P. New observables in inclusive production of quarkonia. *Physics Reports*, Elsevier, [s. l.], 2020.
- 50 APPELQUIST, T. et al. Spectroscopy of the new mesons. *Physical Review Letters*, APS, [s. l.], v. 34, n. 6, p. 365, 1975.
- 51 ALI, Y. et al. $\psi(2S)$ and J/ψ production in pp collisions at $\sqrt{s} = 7, 8$ and 13 TeV. *Turk. J. Phys.*, [s. l.]: v. 45, n. 2, p. 90–104, 2021.
- 52 SIRUNYAN, A. M. et al. Constraints on the χ_{c1} versus χ_{c2} Polarizations in Proton-Proton Collisions at $\sqrt{s} = 8$ TeV. *Phys. Rev. Lett.*, [s. l.]: v. 124, n. 16, p. 162002, 2020.
- 53 SZYMANOWSKI, L. *QCD collinear factorization, its extensions and the partonic distributions*. [S. l. : s. n.], 2012. ArXiv preprint arXiv:1208.5688.
- 54 BIALAS, A.; NAVELET, H.; PESCHANSKI, R. QCD dipole model and kT factorization. *Nuclear Physics B*, Elsevier, [s. l.], v. 593, n. 3, p. 438–450, 2001.
- 55 ANGELES-MARTINEZ, R. et al. *Transverse momentum dependent (tmd) parton distribution functions: status and prospects*. [S. l.: s. n.], 2015. ArXiv preprint arXiv:1507.05267.
- 56 AMUNDSON, J. et al. Colorless states in perturbative QCD: Charmonium and rapidity gaps. *Physics Letters B*, Elsevier, [s. l.], v. 372, n. 1-2, p. 127–132, 1996.
- 57 BRAMBILLA, N. et al. *Heavy Quarkonium Physics*. Geneva: CERN, 2005. 487 p. Published as CERN Yellow Report, CERN-2005-005.
- 58 AMUNDSON, J. et al. Quantitative tests of color evaporation: Charmonium production. *Physics Letters B*, Elsevier, [s. l.], v. 390, n. 1-4, p. 323–328, 1997.
- 59 CHISHOLM, A. *Measurements of the X_c and X_b Quarkonium States in pp Collisions with the ATLAS Experiment*. [S. l.]: Springer, 2015.
- 60 LANSBERG, J.-P. J/ψ production at and 7 TeV: colour-singlet model, NNLO and polarization. *Journal of Physics G: Nuclear and Particle Physics*, IOP Publishing, [s. l.], v. 38, n. 12, p. 124110, 2011.
- 61 BAIER, R.; RÜCKL, R. Hadronic collisions: a quarkonium factory. *Zeitschrift für Physik C Particles and Fields*, Springer, [s. l.]: v. 19, n. 3, p. 251–266, 1983.

- 62 ABE, F. et al. J/ψ and $\psi(2S)$ Production in pp Collisions at $\sqrt{s} = 1.8$ TeV. *Physical Review Letters*, APS, [s. l.]: v. 79, n. 4, p. 572, 1997.
- 63 ACOSTA, D. et al. Measurement of the J/ψ meson and b-hadron production cross sections in pp collisions at $\sqrt{s} = 1960$ GeV. *Physical Review D*, APS, [s. l.]: v. 71, n. 3, p. 032001, 2005.
- 64 ABAZOV, V. M. et al. Observation and studies of double J/ψ production at the Tevatron. *Physical Review D*, APS, [s. l.]: v. 90, n. 11, p. 111101, 2014.
- 65 BODWIN, G. T.; BRAATEN, E.; LEPAGE, G. P. Rigorous QCD analysis of inclusive annihilation and production of heavy quarkonium. *Physical Review D*, APS, [s. l.]: v. 51, n. 3, p. 1125, 1995.
- 66 BRAMBILLA, N. et al. Heavy quarkonium: progress, puzzles, and opportunities. *The European Physical Journal C*, Springer, [s. l.], v. 71, n. 2, p. 1–178, 2011.
- 67 ACHARYA, S. et al. Inclusive J/ψ production at mid-rapidity in pp collisions at $\sqrt{s} = 5.02$ TeV. *JHEP*, [s. l.]: v. 10, p. 084, 2019.
- 68 ABE, K. *B Physics with an Asymmetric Collider at KEK*. [S.l. : s. n.], 1990.
- 69 CLEO detector. Available in: https://www.classe.cornell.edu/public/lab-info/svx/cleo_det_proc.jpg. Access in 05 Jul. 2022.
- 70 BELLE II detector. Available in: [https://en.wikipedia.org/wiki/Belle_II_experiment/media/File:KEK_Belle_II_Detector_\(1\).jpg](https://en.wikipedia.org/wiki/Belle_II_experiment/media/File:KEK_Belle_II_Detector_(1).jpg). Access in 07 May 2022.
- 71 KIDONAKIS, N. Heavy-flavor production at accelerators. *Nuclear Physics A*, Elsevier, [s. l.], v. 827, n. 1-4, p. 448c–453c, 2009.
- 72 COELHO, E. *Analysis of central diffractive production of D^0 and D mesons in proton-proton collisions at 13 TeV with the CMS and TOTEM experiment*. 2019. Tese (doutorado) - Instituto de Física Armando Dias Tavares, Universidade do Estado do Rio de Janeiro, 2019.
- 73 BIEBEL, O. et al. Fragmentation Functions in e^+e^- Annihilation and Lepton-Nucleon DIS. *Journal of Physics G*, [s. l.], v. 33, p. 195, 2006
- 74 BJORKEN, J. Properties of hadron distributions in reactions containing very heavy quarks. *Physical Review D*, APS, [s. l.], v. 17, n. 1, p. 171, 1978.
- 75 SALAJEGHEH, M. et al. NNLO charmed-meson fragmentation functions and their uncertainties in the presence of meson mass corrections. *The European Physical Journal C*, Springer, [s. l.], v. 79, n. 12, p. 1–12, 2019.
- 76 ACKERSTAFF, K.; COLLABORATION, O. et al. Measurement of $f(c \rightarrow D^{*+} X)$, $f(b \rightarrow D^{*+} X)$ and $\Gamma_{cc} / \Gamma_{\text{had}}$ using $D^{*\pm}$ mesons. *The European Physical Journal C*, EDP Sciences, [S. l.], v. 1, n. 3/4, p. 439–459, 1998.

- 77 GLADILIN, L. Fragmentation fractions of cc and bc quarks into charmed hadrons at lep. *The European Physical Journal C*, Springer, [S. l.], v. 75, n. 1, p. 1–4, 2015.
- 78 ALICE COLLABORATION et al. Charm-quark fragmentation fractions and production cross section at midrapidity in pp collisions at the LHC. 2022.
- 79 BERGER, E. L. Investigations of Double Parton Scattering: Example of $pp \rightarrow b\bar{b} \text{jet jetX}$. In: RENCONTRES DE MORIOND ON QCD AND HIGH ENERGY INTERACTIONS, 46., [s. l.], 2011. [*Proceedings ...*]. [S. l.: s.n.], 2011. p. 227–232.
- 80 LEO, K. D. *Study of the double parton scattering in proton-proton collisions at the LHC and extraction of a new data-driven tune using multi-jet measurements*. 2019. Thesis (doctorate) - Dipartimento di Fisica, Università degli Studi di Trieste, INFN, Trieste, 2019.
- 81 GAUNT, J. R.; MACIUŁA, R.; SZCZUREK, A. Conventional versus single-ladder-splitting contributions to double parton scattering production of two quarkonia, two Higgs bosons, and $c\bar{c}c\bar{c}$. *Physical Review D*, APS, [s. l.], v. 90, n. 5, p. 054017, 2014.
- 82 MANOHAR, A. V.; WAALEWIJN, W. J. QCD analysis of double parton scattering: spin and color correlations, interference effects, and evolution. *Physical Review D*, APS, [s. l.], v. 85, n. 11, p. 114009, 2012.
- 84 AAIJ, R. et al. Observation of double charm production involving open charm in pp collisions at $s = 7$ TeV. *JHEP*, [s. l.], v. 06, p. 141, 2012. [Addendum: *JHEP* 03, 108, (2014)].
- 85 EVANS, L.; BRYANT, P. LHC machine. *Journal of Instrumentation*, IOP Publishing, [s. l.], v. 3, n. 08, p. S08001, 2008.
- 86 CERN. *The Large Hadron Collider*. Available in: <https://home.cern/science/accelerators/large-hadron-collider>. Accessed in: 30 Oct. 2021.
- 87 CERN. The CERN accelerator complex. Available in: <https://cds.cern.ch/record/2636343>. Accessed: 2021-10-30.
- 88 SEEZ, C. Compact Muon Solenoid, a general purpose detector for the LHC. *Nuclear Instruments and Methods in Physics Research Section A: Accelerators, Spectrometers, Detectors and Associated Equipment*, Elsevier, [s. l.], v. 344, n. 1, p. 1–10, 1994.
- 89 BUNKOWSKI, K. *Optimization, synchronization, calibration and diagnostic of the RPC pac muon trigger system for the cms detector*. 2009. Thesis (doctorate) - Institute of Experimental Physics, University of Warsaw, University of Warsaw, Warsaw, 2009.
- 90 CMS COLLABORATION. *The CMS track system*. Available in: <https://cms.cern/detector/identifying-tracks>. Accessed in: 02 Nov. 2021.
- 91 CHATRCHYAN, S. et al. Description and performance of track and primary-vertex reconstruction with the CMS tracker. *JINST*, [S.l.]: v. 9, n. 10, p. P10009, 2014.

- 92 ALY, R. *Search for Dark Matter Produced in Association With a Higgs Boson in the Four Leptons Final State Using Run II Data at $\sqrt{s} = 13$ TeV With the CMS Experiment*. 2021. Thesis (doctorate) - Dipartimento Interateneo di Fisica “M. Merlin”, Università Di Bari, Bari, 2021.
- 93 CERN. THE LHC EXPERIMENTS COMMITTEE. *Compact Muon Solenoid, Technical Design Report for the Pixel Detector Upgrade*. [Geneva : CERN], 2012.
- 94 ELMETENAWEE, W. CMS track reconstruction performance during Run 2 and developments for Run 3. *PoS*, [s. 1.], v. ICHEP2020, p. 733, 2021.
- 95 POG, C. *CMS Tracking POG Performance Plots For 2017 with Phase I pixel detector*. Available in: <https://twiki.cern.ch/twiki/bin/view/CMSPublicTrackingPOGPerformance2017MC>. Accessed: 2023-01-12.
- 96 CMS-COLLABORATION. *The CMS electromagnetic calorimeter project: Technical Design Report*. Geneva: CERN, 1997a. Technical Design Report CMS.
- 97 CMS-COLLABORATION. *The CMS hadron calorimeter project*. [Geneva: CERN], 1997b. Technical Design Report CERN-LHCC-97-31.
- 98 BARTOSIK, N. Performance of the CMS Electromagnetic Calorimeter in LHC Run2. *PoS*, [S.1]: v. LeptonPhoton2019, p. 126, 2019.
- 99 GUL, M. *Search for a heavy Higgs boson decaying into a pair of top quarks with the CMS 13 TeV dataset*. 2018, Thesis (doctorate) - Faculty of Sciences, Ghent University, 2018.
- 100 COOPER, S. I. Phase I Upgrade of the CMS Hadron Calorimeter. *Nucl. Part. Phys. Proc.*, [S. 1.], v. 273-275, p. 1002–1007, 2016.
- 101 ACQUISTAPACE, G.; CMS COLLABORATION et al. *CMS, the magnet project technical design report*. [Geneva : CERN], 1997. Technical Design Report CMS.
- 102 CMS-COLLABORATION. The CMS experiment at the CERN LHC. *JINST*, Citeseer, [s. 1.], v. 3, p. S08004, 2008.
- 103 CMS-COLLABORATION. *CMS MUON project Technical Design Report*. [Geneva: CERN], 1997d. P. 97–32. Preprint.
- 104 SIRUNYAN, A. M. et al. Performance of the CMS muon detector and muon reconstruction with proton-proton collisions at $\sqrt{s} = 13$ TeV. [S.1]: 2018.
- 105 CMS-COLLABORATION. Performance of the CMS cathode strip chambers with cosmic rays. *Journal of Instrumentation*, IOP Publishing, [s. 1.], v. 5, n. 03, p. T03018, 2010.

- 106 ACOSTA, D. et al. Efficiency of finding muon track trigger primitives in cms cathode strip chambers. *Nuclear Instruments and Methods in Physics Research Section A: Accelerators, Spectrometers, Detectors and Associated Equipment*, Elsevier, [S. l.], v. 592, n. 1-2, p. 26–37, 2008.
- 107 RESSEGOTTI, M. Overview of the CMS Detector Performance at LHC Run 2. *Universe*, [s. l.], v. 5, n. 1, p. 18, 2019.
- 108 GOH, J. et al. CMS RPC efficiency measurement using the tag-and-probe method. *JINST*, [s. l.], v. 14, n. 10, p. C10020, 2019.
- 109 PENG, J.-C.; QIU, J.-W. The Drell-Yan Process. *The Universe*, [s. l.]: v. 4, n. 3, p. 34–44, 2016.
- 110 BATTILANA, C. Performance of the CMS muon system in LHC Run-2. *Nucl. Instrum. Meth. A*, [S.l.]: v. 936, p. 472–473, 2019.
- 111 BAYATYAN, G. et al. *CMS: the TriDAS Project Technical Design Report*, v. 1 : the Trigger Systems. [Geneva: CERN], 2000.
- 112 TOSI, M. The CMS trigger in Run 2. *PoS*, [s. l.]: v. EPS-HEP2017, p. 523, 2017.
- 113 CMS-COLLABORATION. *Technical Proposal for the Phase-II Upgrade of the CMS Detector*. [Geneva: CERN], 2015.
- 114 CMS Phase-II Upgrades. Available in:
https://indico.ihep.ac.cn/event/14560/contributions/31570/attachments/15486/17653/20211128_CMSUpgrade_CLHCP2021.pdf. Access in 15 Jan. 2023.
- 115 CMS Physics Analysis Summary. Available in:
<https://cds.cern.ch/collection/CMS%20Physics%20Analysis%20Summaries>. Access in: 11 Apr. 2023.
- 116 KUMAR, P.; GOMBER, B. The CMS Level-1 Calorimeter Trigger for the HL-LHC. *Instruments*, [s. l.], v. 6, n. 4, p. 64, 2022.
- 117 COLALEO, A. et al. *CMS technical design report for the muon endcap GEM upgrade*. [Geneva: CERN], 2015.
- 118 ABBRESCIA, M.; PESKOV, V.; FONTE, P. *Resistive gaseous detectors: designs, performance, and perspectives*. [S. l.]: Wiley, 2018.
- 119 HILKE, H.; RIEGLER, W. Gaseous detectors. In: FABJAN, C. W.; SCHOPPER, H. (Eds.). *Particle Physics Reference Library, V. 2: Detectors for Particles and Radiation*. [S. l.]: Springer, 2020. P. 91–136.
- 120 SANTONICO, R.; CARDARELLI, R. Development of resistive plate counters. *Nuclear Instruments and Methods in physics research*, [s. l.], v. 187, n. 2-3, p. 377–380, 1981.

- 121 RPC design. Available in: <https://cms.cern/detector/detecting-muons/resistive-plate-chambers>. Access in 07 Jan. 2022.
- 122 ABBRESCIA, M. et al. Resistive plate chambers in avalanche mode: a comparison between model predictions and experimental results. *Nuclear Instruments and Methods in Physics Research Section A: Accelerators, Spectrometers, Detectors and Associated Equipment*. Elsevier, [S.l.], v. 409, n. 1-3, p. 1–5, 1998.
- 123 ANDERSON, D.; KWAN, S.; PESKOV, V. High counting rate resistive-plate chamber. *Nuclear Instruments and Methods in Physics Research Section A: Accelerators, Spectrometers, Detectors and Associated Equipment*, [s. l.], v. 348, n. 2-3, p. 324–328, 1994.
- 124 CARDARELLI, R.; MAKEEV, V.; SANTONICO, R. Avalanche and streamer mode operation of resistive plate chambers. *Nuclear Instruments and Methods in Physics Research Section A: Accelerators, Spectrometers, Detectors and Associated Equipment*, [s. l.], v. 382, n. 3, p. 470–474, 1996.
- 125 CMS COLLABORATION et al. The Phase-2 upgrade of the CMS Muon detectors. *Technical Design Report*, [s. l.]: 2017.
- 126 CABRERA-MORA, A. L. CMS resistive plate chambers performance at $s=13$ TeV. In: IEEE. *2016 IEEE Nuclear Science Symposium, Medical Imaging Conference and Room-Temperature Semiconductor Detector Workshop (NSS/MIC/RTSD)*. [S.l.], 2016. p. 1–3.
- 127 SIKDAR, A. K.; SADIQ, J.; BEHERA, P. K. Effect of variations in the gas mixture compositions on the timing and charge of glass RPC. *JINST*, [S. l.], v. 15, n. 01, p. C01003, 2020.
- 128 FARINHA, C. B.; BRITO, J.; VEIGA, M. D. R. *Eco-efficient rendering mortars: use of recycled materials*. [S. l.]: Woodhead Publishing, 2021.
- 129 CAPEANS, M.; GUIDA, R.; MANDELLI, B. Strategies for reducing the environmental impact of gaseous detector operation at the cern lhc experiments. *Nuclear Instruments and Methods in Physics Research Section A: Accelerators, Spectrometers, Detectors and Associated Equipment*, Elsevier, [S. l.], v. 845, p. 253–256, 2017.
- 130 EU HFC Phase Down. Available in: https://indico.cern.ch/event/999799/contributions/4204191/attachments/2236047/3789965/BMandelli_ECFA.pdf. Access in 07 Jan. 2022.
- 131 BERNARDINI, M.; FORAZ, K. Long shutdown 2 - LHC. *CERN Yellow Reports*, [s. l.], v. 2, p. 290–290, 2015.
- 132 FERREIRA FILHO, B. M.; CMS COLLABORATION et al. CMS RPC activities during LS2 and Commissioning. In: *The Ninth Annual Conference on Large Hadron Collider Physics*. [S.l.: s.n.], 2021. p. 338.

- 133 CORBETTA, M. Development of gas systems for gaseous detector operation at HL-LHC. Thesis (doctorate) - HYSIQUE ET ASTROPHYSIQUE DE LYON, Université de Lyon, Université de Lyon, 2021.
- 134 SAVIANO, G. et al. Properties of potential eco-friendly gas replacements for particle detectors in high-energy physics. *Journal of Instrumentation*, IOP Publishing, [s. l.], v. 13, n. 03, p. P03012, 2018.
- 135 ABBRESCIA, M. et al. Preliminary results of resistive plate chambers operated with eco-friendly gas mixtures for application in the cms experiment. *Journal of Instrumentation*, IOP Publishing, [s. l.], v. 11, n. 09, p. C09018, 2016.
- 136 RIGOLETTI, G. et al. Studies of RPC detector operation with eco-friendly gas mixtures under irradiation at the CERN Gamma Irradiation Facility. *PoS*, [s. l.]: v. EPS-HEP2019, p. 164, 2020.
- 137 JÄKEL, M. R. et al. CERN-GIF++ : a new irradiation facility to test large-area particle detectors for the High-Luminosity LHC program. *PoS*, [s. l.]: v. TIPP2014, p. 102, 2014.
- 138 GKOTSE, B. et al. Upgrades for the cern ep irradiation facilities (irrad, gif) and plans beyond the long shutdown 2. [S.l.]: 2021.
- 139 GRAFANA dashboard. Available in: <https://grafana.com/>. Access in: 16 Jan. 2023.
- 140 CFAGOT, A. *Consolidation and extension of the CMS Resistive Plate Chamber system in view of the High-Luminosity LHC upgrade*. 2020. Thesis (doctorate) - Faculty of Sciences, Ghent University, Ghent University, [Ghent], 2020.
- 141 PARK, S. et al. Development of RE1/1 RPCs for the CMS muon trigger system. *Nuclear Instruments and Methods in Physics Research Section A: Accelerators, Spectrometers, Detectors and Associated Equipment*, Elsevier, [s. l.]: v. 602, n. 3, p. 665–667, 2009.
- 142 CAEN - TOOLS FOR DISCOVERY. *V1190A TDC*. Available in: <https://www.caen.it/products/v1190a-2esst/>. Access in : 29 May 2022.
- 143 LEE, K. et al. Radiation tests of real-sized prototype RPCs for the Phase-2 Upgrade of the CMS Muon System. *Journal of Instrumentation*, IOP Publishing, [S.l.]:
- 144 CAEN - TOOLS FOR DISCOVERY. *A1526 N*. Available in: <https://www.caen.it/products/a1526/>. Access in : 11 Jun. 2022.
- 145 CAEN - TOOLS FOR DISCOVERY. *S1527*. Available in: <https://www.caen.it/products/a1526/>. Access in : 11 Jun. 2022.
- 146 VINCENZI, M. D. et al. Study of the performance of standard RPC chambers as a function of bakelite temperature. *Nuclear Instruments and Methods in Physics Research Section A: Accelerators, Spectrometers, Detectors and Associated Equipment*, Elsevier, [s. l.]: v. 508, n. 1-2, p. 94–97, 2003.

- 147 PAOLUCCI, P. et al. CMS Resistive Plate Chamber overview, from the present system to the upgrade phase I. *PoS*, [s. l.]: v. RPC2012, p. 004, 2012.
- 148 BENUSSI, L. et al. Performance of the gas gain monitoring system of the cms RPC muon detector. *Journal of Instrumentation*, IOP Publishing, [s. l.]: v. 10, n. 01, p. C01003, 2015.
- 149 EYSERMANS, J.; MORALES, M. I. P. Operation and performance of the CMS Resistive Plate Chambers during LHC run II. *J. Phys. Conf. Ser.*, [s. l.]: v. 912, n. 1, p. 012015, 2017.
- 150 CHATRCHYAN, S. et al. Performance Study of the CMS Barrel Resistive Plate Chambers with Cosmic Rays. *JINST*, [s. l.]: v. 5, p. T03017, 2010.
- 151 GUL, M. et al. Detector Control System and Efficiency Performance for CMS RPC at GIF++. *JINST*, [s. l.]: v. 11, p. C10013, 2016.
- 152 BAND, H. R. et al. Study of HF production in BaBar Resistive Plate Chambers. *Nucl. Instrum. Meth. A*, [s. l.]: v. 594, p. 33–38, 2008.
- 153 CARLINO, G. et al. Results on long-term performances and laboratory tests of the L3 RPC system at LEP. *Nucl. Instrum. Meth. A*, [s. l.]: v. 515, p. 328–334, 2003.
- 154 ABASHIAN, A. et al. The K(L) / mu detector subsystem for the BELLE experiment at the KEK B factory. *Nucl. Instrum. Meth. A*, [s. l.]: v. 449, p. 112–124, 2000.
- 155 ANULLI, F. et al. Performance of 2nd Generation BaBar Resistive Plate Chambers. *Nucl. Instrum. Meth. A*, [s. l.]: v. 552, p. 276–291, 2005.
- 156 BAND, H. R. et al. Performance and aging studies of BaBar resistive plate chambers. *Nucl. Phys. B Proc. Suppl.*, [s. l.]: v. 158, p. 139–142, 2006.
- 157 AIELLI, G. et al. Ageing test of ATLAS RPCs at CERN's Gamma Irradiation Facility. In: IEEE NUCLEAR SCIENCE SYMPOSIUM AND MEDICAL IMAGING CONFERENCE, 2004, [s. l.]. [*Proceedings ...*]. [S.l.: s.n.], 2004. p. 226–230.
- 158 PARK, S. et al. Systematic studies of aging effects in RPCs for the CMS/LHC experiment. *J. Korean Phys. Soc.*, [s. l.]: v. 47, p. 427–433, 2005.
- 159 ARNALDI, R. et al. Ageing test of RPC for the Muon Trigger System for the ALICE experiment. In: IEEE NUCLEAR SCIENCE SYMPOSIUM AND MEDICAL IMAGING CONFERENCE, 2004, [s. l.]. [*Proceedings ...*]. [S.l.: s.n.], 2004. P. 2072–2076.
- 160 BIZZETI, A. et al. First results from an aging test of a prototype RPC for the LHCb muon system. *Nucl. Instrum. Meth. A*, [s. l.]: v. 515, p. 348–353, 2003.

- 161 KUMARI, P.; BHATNAGAR, V.; SINGH, J. B. Aging Study for Resistive Plate Chambers (RPC) of the CMS Muon Detector for HL-LHC. *Springer Proc. Phys.*, [s. l.]: v. 261, p. 703–709, 2021.
- 162 IRPC installation. Available in: <https://cds.cern.ch/record/2792271>. Access in 11 Apr. 2023.
- 163 AMARILO, K. M. *RPC based tracking system at CERN GIF++ facility*. Geneva : [CERN], 2022.
- 164 AAIJ, R. et al. Prompt charm production in pp collisions at $\sqrt{s}=7$ TeV. *Nuclear Physics B*, Elsevier, [s. l.], v. 871, n. 1, p. 1–20, 2013.
- 165 KHACHATRYAN, V. et al. Prompt and Non-Prompt J/ψ Production in pp Collisions at $\sqrt{s}=7$ TeV. *Eur. Phys. J. C*, [s. l.]: v. 71, p. 1575, 2011.
- 166 BRODSKY, S. J.; LANSBERG, J.-P. Heavy-quarkonium production in high energy proton-proton collisions at RHIC. *Physical Review D*, APS, [s. l.], v. 81, n. 5, p. 051502, 2010.
- 167 AAIJ, R. et al. Observation of double charm production involving open charm in pp collisions at $\sqrt{s}=7$ TeV. *Journal of High Energy Physics*, Springer, [s. l.], v. 2012, n. 6, p. 1–36, 2012.
- 168 TUMASYAN, A. et al. Measurement of prompt open-charm production cross sections in proton-proton collisions at $\sqrt{s}=13$ TeV. *Journal of High Energy Physics*, Springer, [s. l.], v. 2021, n. 11, p. 1–48, 2021.
- 170 ALVES JR., A. A. et al. The LHCb Detector at the LHC. *JINST*, [s. l.]: v. 3, p. S08005, 2008.
- 171 CHATRCHYAN, S. et al. The CMS Experiment at the CERN LHC. *JINST*, [s. l.]: v. 3, p. S08004, 2008.
- 172 SZCZUREK, A. Double parton scattering at high energies. *Acta Phys. Polon. B*, [s. l.]: v. 46, n. 7, p. 1415–1437, 2015.
- 173 CMS Open data. Available in: <http://opendata.cern.ch/docs/about-cms>. Access in : 26 Nov. 2022.
- 174 FRANZONI, G. Dataset definition for CMS operations and physics analyses. *Nucl. Part. Phys. Proc.*, [s. l.]: v. 273-275, p. 929–933, 2016.
- 175 SJÖSTRAND, T. The Pythia event generator: Past, present and future. *Computer Physics Communications*, Elsevier, [s. l.], v. 246, p. 106910, 2020.
- 176 LANGE, D. J. The evtgen particle decay simulation package. Nuclear Instruments and Methods in Physics Research Section A: *Accelerators, Spectrometers, Detectors and Associated Equipment*, Elsevier, [s. l.], v. 462, n. 1-2, p. 152–155, 2001.

- 177 BOOS, E. et al. Generic User Process Interface for Event Generators. In: *2nd Les Houches Workshop on Physics at TeV Colliders*. [S. l.: s.n.], 2001.
- 178 SHAO, H.-S. J/ψ meson production in association with an open charm hadron at the LHC: A reappraisal. *Phys. Rev. D*, [s. l.]: v. 102, p. 034023, 2020.
- 179 NANO AOD PLUS code. Available in: <https://github.com/Mapse/NanoAOD>. Access in: 26 Nov. 2022.
- 180 MUON Scale Factor Corrections - 2016. Available in: <https://twiki.cern.ch/twiki/bin/viewauth/CMS/MuonUL2016>. Access in : 15 Feb. 2023.
- 181 MUON Scale Factor Corrections - 2017. Available in: <https://twiki.cern.ch/twiki/bin/viewauth/CMS/MuonUL2017>. Access in : 15 Feb. 2023.
- 182 MUON Scale Factor Corrections - 2018. Available in: <https://twiki.cern.ch/twiki/bin/viewauth/CMS/MuonUL2018>. Access in 15 Feb. 2023.
- 183 BRUN, R.; RADEMAKERS, F. ROOT: An object oriented data analysis framework. *Nucl. Instrum. Meth. A*, [s. l.]: v. 389, p. 81–86, 1997.
- 184 SIRUNYAN, A. M. et al. Measurement of quarkonium production cross sections in pp collisions at $\sqrt{s} = 13$ TeV. *Phys. Lett. B*, [s. l.]: v. 780, p. 251–272, 2018.
- 185 TUMASYAN, A. et al. Measurement of prompt open-charm production cross sections in proton-proton collisions at $\sqrt{s} = 13$ TeV. *Journal of High Energy Physics*, Springer, [s. l.], v. 2021, n. 11, p. 1–48, 2021.
- 186 CMS-COLLABORATION. Performance of the CMS muon detector and muon reconstruction with proton-proton collisions at $s = 13$ TeV. *JINST*, [s. l.], v. 13, n. 06, p. P06015, 2018.
- 187 CMS Tracking POG Performance Plots - 2017. Available in: <https://twiki.cern.ch/twiki/bin/view/CMSPublic/TrackingPOGPerformance2017MC>. Access in : 29 Mar. 2023.
- 188 VANLAER, P. *Contribution to the study of the central tracking system of the CMS detector, at the future proton collider LHC*. 1998. Thesis (doctorate) - Physics Department, Libre Bruxelles University, Brussels, 1998.
- 189 JOMHARI, N. Z. B. *Measurement of Total and Differential Charm Cross Sections at 7 TeV with the CMS Detector*. 2022. Thesis (doctorate) - Institute of Experimental Physics, Hamburg University, Hamburg, 2022.
- 190 VERKERKE, W.; KIRKBY, D. P. The RooFit toolkit for data modeling. *eConf*, [s. l.], v. C0303241, p. MOLT007, 2003.

- 191 BAINES, J. T. M. et al. *B-Physics Event Selection for the ATLAS High Level Trigger*. [S. 1 : s. n.], 2000.
- 192 JOHNSON, N.; KOTZ, S. Distributions in statistics: discrete distributions. boston, ma.: Houghton mifflin. *Johnson Distributions in Statistics: Discrete Distributions 1969*. [S. 1 : s. n.], 1969.
- 193 CMS COLLABORATION. *CMS Luminosity Measurements for the 2016 Data Taking Period*. Geneva: [CERN], 2017.
- 194 CMS COLLABORATION. *CMS luminosity measurement for the 2017 data-taking period at $\sqrt{s} = 13$ TeV*. Geneva: [CERN], 2018.
- 195 CMS COLLABORATION. *CMS luminosity measurement for the 2018 data-taking period at $\sqrt{s} = 13$ TeV*. Geneva: [CERN], 2019.
- 196 LINK, J. M. et al. Study of the Cabibbo Suppressed Decay Modes $D^0 \rightarrow \pi^- \pi^+$ and $D^0 \rightarrow K^- K^+$. *Phys. Lett. B*, [S. 1.], v. 555, p. 167–173, 2003.
- 197 CMS COLLABORATION. *Tracking performances for charged pions with Run 2 Legacy data*. Geneva: [CERN], 2022.
- 198 CMS COLLABORATION et al. *J/ψ prompt and non-prompt cross sections in pp collisions at $\sqrt{s} = 7$ TeV*. Geneva: [CERN], 2010.
- 199 ACHARYA, S. et al. Prompt and non-prompt J/ψ production cross sections at midrapidity in proton-proton collisions at $\sqrt{s} = 5.02$ and 13 TeV. *JHEP*, [s. 1.]: v. 03, p. 190, 2022.
- 200 ACHARYA, S. et al. Inclusive, prompt and non-prompt J/ψ production at midrapidity in p-Pb collisions at $\sqrt{s_{NN}} = 5.02$ TeV. *JHEP*, [s. 1.]: v. 06, p. 011, 2022.
- 201 BEREZHNOY, A. V. et al. Double cc production at LHCb. *Phys. Rev. D*, American Physical Society, [s. 1.]: v. 86, p. 034017, Aug 2012.
- 202 CMS COLLABORATION. *Quarkonium production cross sections in pp collisions at $\sqrt{s} = 13$ TeV*. Geneva: [CERN], 2016.
- 203 SCHÄFER, W.; SZCZUREK, A. Production of two $c\bar{c}$ pairs in gluon-gluon scattering in high energy proton-proton collisions. *Phys. Rev. D*, American Physical Society, [s. 1.], v. 85, p. 094029, May 2012.
- 204 LUSZCZAK, M.; MACIULA, R.; SZCZUREK, A. Production of two $c\bar{c}$ pairs in double-parton scattering. *Phys. Rev. D*, [s. 1.], v. 85, p. 094034, 2012.
- 205 BARTALINI, P.; GAUNT, J. R. *Multiple parton interactions at the LHC*. [S. 1.]: WSP, 2019. V. 29. ISBN 978-981-322-775-0, 978-981-322-777-4.

- 206 D'ENTERRIA, D.; SNIGIREV, A. Double, triple, and n-parton scatterings in high-energy proton and nuclear collisions. *Adv. Ser. Direct. High Energy Phys.*, [S. l.], v. 29, p. 159–187, 2018.
- 207 FLENSBURG, C. et al. Correlations in double parton distributions at small x. *Journal of High Energy Physics*, Springer, [s. l.], v. 2011, n. 6, p. 1–21, 2011.
- 208 ABAZOV, V. M. et al. Observation and Studies of Double J/ψ Production at the Tevatron. *Phys. Rev. D*, [s. l.], v. 90, n. 11, p. 111101, 2014.
- 209 LANSBERG, J.-P.; SHAO, H.-S.; YAMANAKA, N. Indication for double parton scatterings in W^+ prompt J/ψ production at the LHC. *Phys. Lett. B*, [s. l.], v. 781, p. 485–491, 2018.
- 210 LANSBERG, J.-P.; SHAO, H.-S. Phenomenological analysis of associated production of $Z^0 + b$ in the $b \rightarrow J/\psi X$ decay channel at the LHC. *Nucl. Phys. B*, [s. l.], v. 916, p. 132–142, 2017.
- 211 PARTICLE Gun Fragments. Available in: <https://codimd.web.cern.ch/rYLyq2hNTo-FIRZOLjzHMQ?bothParticle-gun>. Access in : 05 Jan. 2023.
- 212 PARTICLE Gun github. Available in: <https://github.com/Mapse/Particle-gun>. Access in : 05 Jan. 2023.
- 213 CODISPOTI, G. et al. Crab: A cms application for distributed analysis. In: IEEE NUCLEAR SCIENCE SYMPOSIUM CONFERENCE RECORD, 2008, [s. l.]. [*Proceedings ...*]. [S.l.: s.n.], 2008. P. 817–822.
- 214 CMSSW Application Framework - 2022. Available in: <https://twiki.cern.ch/twiki/bin/view/CMSPublic/WorkBookCMSSWFramework>. Access in : 03 Feb. 2022.
- 215 GEISER, A. *NanoAODPlus code - 2022*. Available in: <https://gitlab.cern.ch/cms-bph/nanoaodplus> harm. Access in : 03 Feb. 2022.
- 216 NANOAOPLUS: running the code. Available in: <https://codimd.web.cern.ch/rYLyq2hNTo-FIRZOLjzHMQ?bothRunning-NanoAODPlus>. Access in: 02 Mar. 2023.
- 217 HELAC-ONIA: Installation and compilation. Available in: <https://codimd.web.cern.ch/rYLyq2hNTo-FIRZOLjzHMQHelac-Onia>. Access in: 14 Dec. 2022.
- 218 PILE up weight. Available in: <https://codimd.web.cern.ch/rYLyq2hNTo-FIRZOLjzHMQ?viewPile-up>. Access in : 05 Jan. 2023.
- 219 SIGNAL extraction. Available in: <https://codimd.web.cern.ch/rYLyq2hNTo-FIRZOLjzHMQ?viewSignal-extraction>. Access in : 05 Jan. 2023.

220 FITTING codes. Available in: Available in:
https://github.com/Mapse/analysis_fit. Access in : 03 Feb. 202316.

APPENDIX A – Presentations and Awards

- **J/ ψ associated with D***

BPH Jamboree, December 15th, 2020: <https://indico.cern.ch/event/979184/contributions/4151704/attachments/2163077/3650176/Quarkonia_Open_Charm-Jamboree_15_Dec_2020.pdf>

P&P meeting, January 17th, 2022: <https://indico.cern.ch/event/1108863/contributions/4684974/attachments/2374068/4055158/Quarkonia_Open_Charm_PP_Meeting.pdf>

P&P meeting, August 9th, 2021: <https://indico.cern.ch/event/1065317/contributions/4479397/attachments/2292692/3898370/Charmonium_Open_Charm_Production%26Properties_09.Aug.2021.pdf>

P&P meeting, May 23th, 2022: <https://indico.cern.ch/event/1154900/contributions/4881765/attachments/2449358/4197423/May_23_2022_Charmonium_Open_Charm_PP_Meeting_-1.pdf>

P&P meeting, October 10th, 2022: <https://indico.cern.ch/event/1198393/contributions/5081709/attachments/2525440/4343434/October_10_2022_Charmonium_Open_Charm_PP_Meeting_.pdf>

- **Ecogas and aging**

Greenhouse gas mitigation: <https://indico.cern.ch/event/1205847/contributions/5085080/attachments/2530978/4354743/GHG_mitigation_CSC_RPC_Muon_winter_2022_October_19.pdf>

Greenhouse gas mitigation - Annual review: <https://indico.cern.ch/event/1180362/contributions/5081853/attachments/2537331/4370542/GHG_mitigation_CSC_RPC_Muon_Annual_Review_2022_Nov_03-1.pdf>

RPC longevity and ecogas: <https://indico.cern.ch/event/1165566/contributions/4918405/attachments/2467965/4232900/RPC_Ecogas_Muon_Week.pdf>

iRPC gaps aging: <https://indico.cern.ch/event/1076988/contributions/4531445/attachments/2312915/3936605/RPC_Upgrade_Workshop_1.4mm_gaps_ageing.pdf>

- **Awards**

CMS awards 2021: For crucial contributions to commissioning of RE4 super modules, consolidation studies of existing RPC, and ageing studies of iRPC.

Best poster - II Encontro de Primavera da Sociedade Brasileira de Física - II EPSBF 2022: Associated Production of J/ ψ and D* in pp Collisions at $\sqrt{s} = 13$ TeV in CMS detector.

APPENDIX B – Particle Gun Monte Carlo

The generator is the *Pythia8PtGun* that is specific to Pythia. Two fragments³² are used, one for J/ψ and muons and one for D^* . The fragments can be found on the online documentation (211) as well as on GitHub (212). On GitHub there are also instructions to generate the evens with CMS Remote Analysis Builder (CRAB)³³.

To simulate the events, a specific CMS software is used, CMSSW (214). The CMSSW versions used are,

- **CMSSW_10_6_20:** GEM-SIM, DIGI2RAW, AOD, NanoAODPlus
- **CMSSW_8_0_33_UL:** HLT (2016)
- **CMSSW_9_4_14_UL_patch1:** HLT (2017)
- **CMSSW_10_2_16_UL:** HLT (2018)

The generation steps are described below.

- **GEN-SIM Step:** this step generates the particles using the particle generators described in Section (4.2.2) and performs the detector simulation.

```
cmsDriver.py --filein file:GS.root --fileout file:DR.root --pileup NoPileUp
--mc --eventcontent PREMIXRAW --datatier GEN-SIM-RAW
--conditions 106X_mc2017_realistic_v7 --step DIGI,L1,DIGI2RAW --nThreads 1
--geometry DB:Extended --era Run2_2017 --python_filename
DR.py -n -1 --no_exec
```

- **DIGI2RAW Step:** this step performs the digitization and the production of raw data

```
cmsDriver.py --filein file:GS.root --fileout file:DR.root --pileup NoPileUp
--mc --eventcontent PREMIXRAW --datatier GEN-SIM-RAW
--conditions 106X_mc2017_realistic_v7 --step DIGI,L1,DIGI2RAW --nThreads 1
--geometry DB:Extended --era Run2_2017 --python_filename
DR.py -n -1 --no_exec
```

- **HLT Step:** this step performs the trigger simulation.

³² A fragment is a data card containing the conditions to be simulated. It is similar to a configuration file, where the user can write the conditions he wants in the simulation.

³³ CRAB is a specific CMS tool designed to handle distributed data using grid infrastructure (213)

```

cmsDriver.py --filein file:DR.root --fileout file:HLT.root --mc
--eventcontent RAWSIM --datatier GEN-SIM-RAW
--conditions 94X_mc2017_realistic_v15
--customise_commands 'process.source.bypassVersionCheck =
cms.untracked.bool(True)' --step HLT:2e34v40 --nThreads 1
--geometry DB:Extended --era Run2_2017
--python_filename HLT.py -n -1 --no_exec

```

- AOD Step: this step converts the raw data to AOD format.

```

cmsDriver.py --filein file:HLT.root --fileout file:AOD.root --mc
--eventcontent AODSIM --runUnscheduled --datatier AODSIM
--conditions 106X_mc2017_realistic_v7 --step RAW2DIGI,L1Reco,
RECO,RECO,RECO,RECO --nThreads 1 --geometry DB:Extended --era
Run2_2017 --python_filename AOD.py -n -1 --no_exec

```

- NanoAODPlus Step: this step converts the AOD format to the NanoAODPlus format

There is no specific command to run on CMSSW as in the previous steps. Instead, a private EDAnalyzer³⁴ code (215) is used to perform this step. The instructions for running this code are described on the online documentation (216).

³⁴ EDAnalyzer is a CMSSW module used to perform physics analysis with CMS data.

APPENDIX C – Single Parton Scattering Monte Carlo

To produce the LHE files, two different versions of Helac-Onia are used. Helac-Onia 2.7.1 is used to make the processes depicted in the left and middle Feynman diagrams that are shown in Figure (130). To produce the process depicted in the right Feynman diagram, HELAC-Onia-2.5.3-VFNS is used. The same fragments are used for both generators, they are found in the next sub-section. More details on the use of Helac-Onia can be found in the online documentation (217).

C.0.1 Fragments

Four different fragments are used. As in DPS production, SPS samples are divided into three, one for each dimuon p_T range: $9 < p_T^{\mu^+\mu^-} < 30$ GeV/c, $30 < p_T^{\mu^+\mu^-} < 50$ GeV/c, $50 < p_T^{\mu^+\mu^-} < 100$ GeV/c, . The only difference between them is the variable *minptconia*. In principle, it should be at least 10 GeV/c lower than the value of the first value of p_T in the range considered. In the first range, this value is 9 GeV/c, but, *minptconia* is set at 6 GeV. In the range, 30-50 GeV/c *minptconia* is set at 20 GeV/c, in the range 50-100 GeV/c, *minptconia* is set at 40 GeV/c, and in the range, 100-150 GeV/c, *minptconia* is set at 90 GeV.

C.0.1.1 Fragment 1: $9 < p_T^{\mu^+\mu^-} < 30$ GeV

```

set preunw = 100000
set nmc = 1000000
set nopt = 100000
set nopt_step = 100000
set noptlim = 1000000

set minptconia = 6d0

generate p p > cc~(3s11) c c~

define cc = c c~
generate g cc > cc~(3s11) cc
generate cc g > cc~(3s11) cc

```

```
decay jpsi > m+ m- @ 1d0
```

```
launch.
```

C.0.1.2 Fragment 1: $30 < p_T^{\mu^+\mu^-} < 50$ GeV

```
set preunw = 100000
```

```
set nmc = 1000000
```

```
set nopt = 100000
```

```
set nopt_step = 100000
```

```
set noptlim = 1000000
```

```
set minptconia = 20d0
```

```
generate p p > cc~(3s11) c c~
```

```
define cc = c c~
```

```
generate g cc > cc~(3s11) cc
```

```
generate cc g > cc~(3s11) cc
```

```
decay jpsi > m+ m- @ 1d0
```

```
launch.
```

C.0.1.3 Fragment 1: $50 < p_T^{\mu^+\mu^-} < 100$ GeV

```
set preunw = 100000
```

```
set nmc = 1000000
```

```
set nopt = 100000
```

```
set nopt_step = 100000
```

```
set noptlim = 1000000
```

```
set minptconia = 40d0
```

```
generate p p > cc~(3s11) c c~
```

```
define cc = c c~
```

```
generate g cc > cc~(3s11) cc  
generate cc g > cc~(3s11) cc
```

```
decay jpsi > m+ m- @ 1d0
```

```
launch.
```

APPENDIX D – Monte Carlo Samples

All MC samples (DPS and SPS) are shown in this section. Tables (74), (75), (76), (77) shows the DPS MC samples.

Table 74 - DPS Samples: 2016-pre-VFP.

Dimuon p_T range	Sample Name
9 to 30 GeV/c	/DPS_D0ToKPi_JPsiPt-9To30_JPsiFilter
	_TuneCP5_13TeV-pythia8-evtgen
	/RunIISummer20UL16RECOAPV-106X_mcRun2 _asymptotic_preVFP_v8-v2 /AODSIM
30 to 50 GeV/c	/DPS_D0ToKPi_JPsiPt-30To50_JPsiFilter
	_TuneCP5_13TeV-pythia8-evtgen
	/RunIISummer20UL16RECOAPV-106X_mcRun2 _asymptotic_preVFP_v8-v2 /AODSIM
50 to 100 GeV/c	/DPS_D0ToKPi_JPsiPt-50To100_JPsiFilter
	_TuneCP5_13TeV-pythia8-evtgen
	/RunIISummer20UL16RECOAPV-106X_mcRun2 _asymptotic_preVFP_v8-v2 /AODSIM

Legend: Three different samples are used. Each sample is characterized by the dimuon p_T range.

Source: The author, 2023.

Table 75 - DPS Samples: 2016-pos-VFP.

Dimuon p_T range	Sample Name
9 to 30 GeV/c	/DPS_D0ToKPi_JPsiPt-9To30_JPsiFilter
	_TuneCP5_13TeV-pythia8-evtgen
	/RunIISummer20UL16RECO-106X_mcRun2 _asymptotic_v13-v2 /AODSIM
30 to 50 GeV/c	/DPS_D0ToKPi_JPsiPt-30To50_JPsiFilter
	_TuneCP5_13TeV-pythia8-evtgen
	/RunIISummer20UL16RECO-106X_mcRun2 _asymptotic_v13-v2 /AODSIM
50 to 100 GeV/c	/DPS_D0ToKPi_JPsiPt-50To100_JPsiFilter
	_TuneCP5_13TeV-pythia8-evtgen
	/RunIISummer20UL16RECO-106X_mcRun2 _asymptotic_v13-v1 /AODSIM

Legend: Three different samples are used. Each sample is characterized by the dimuon p_T range.

Source: The author, 2023.

Table 76 - DPS Samples: 2017

Dimuon p_T range	Sample Name
9 to 30 GeV/c	/DPS_D0ToKPi_JPsiPt-9To30_JPsiFilter
	_TuneCP5_13TeV-pythia8-evtgen
	/RunIISummer20UL17RECO-106X_mc2017 _realistic_v6-v2 /AODSIM
30 to 50 GeV/c	/DPS_D0ToKPi_JPsiPt-30To50_JPsiFilter
	_TuneCP5_13TeV-pythia8-evtgen
	/RunIISummer20UL17RECO-106X_mc2017 _realistic_v6-v2 /AODSIM
50 to 100 GeV/c	/DPS_D0ToKPi_JPsiPt-50To100_JPsiFilter
	_TuneCP5_13TeV-pythia8-evtgen
	/RunIISummer20UL17RECO-106X_mc2017 _realistic_v6-v1 /AODSIM

Legend: Three different samples are used. Each sample is characterized by the dimuon p_T range.

Source: The author, 2023.

Table 77 - DPS Samples: 2018

Dimuon p_T range	Sample Name
9 to 30 GeV/c	/DPS_D0ToKPi_JPsiPt-9To30_JPsiFilter
	_TuneCP5_13TeV-pythia8-evtgen
	/RunIISummer20UL18RECO-106X_upgrade2018 _realistic_v11_L1v1-v2 /AODSIM
30 to 50 GeV/c	/DPS_D0ToKPi_JPsiPt-30To50_JPsiFilter
	_TuneCP5_13TeV-pythia8-evtgen
	/RunIISummer20UL18RECO-106X_upgrade2018 _realistic_v11_L1v1-v2 /AODSIM
50 to 100 GeV/c	/DPS_D0ToKPi_JPsiPt-50To100_JPsiFilter
	_TuneCP5_13TeV-pythia8-evtgen
	/RunIISummer20UL18RECO-106X_upgrade2018 _realistic_v11_L1v1-v2 /AODSIM

Legend: Three different samples are used. Each sample is characterized by the dimuon p_T range.

Source: The author, 2023.

The SPS LHE samples are produced with Helac-Onia generator. As is explained in Section (4.8.1) and in Appendix (C), SPS is described with three Feynman diagrams. The first two diagrams were centrally produced by CMS and are shown in Tables (78), (79), (80), (81), while the third diagram was produced privately. The instructions for producing the LHE files are highlighted in Appendix (C).

Table 78 - SPS Samples: 2016-pre-VFP.

Dimuon p_T range	Sample Name
9 to 30 GeV/c	/SPS_D0ToKPi_JPsiPt-9To30_TuneCP5_13TeV- helaconia-pythia8-evtgen
	/RunIISummer20UL16RECOAPV- 106X_mcRun2_symptotic_preVFP_v8-v2 /AODSIM
	/SPS_D0ToKPi_JPsiPt-30To50_TuneCP5_13TeV- helaconia-pythia8-evtgen
30 to 50 GeV/c	/RunIISummer20UL16RECOAPV- 106X_mcRun2_asymptotic_preVFP_v8_ext1-v2 /AODSIM
	/SPS_D0ToKPi_JPsiPt-50To100_TuneCP5_13TeV- helaconia-pythia8-evtgen
	/RunIISummer20UL16RECOAPV-106X_mcRun2 _asymptotic_preVFP_v8_ext4-v2 /AODSIM

Legend: Three different samples are used. Each sample is characterized by the dimuon p_T range.

Source: The author, 2023.

Table 79 - SPS Samples: 2016-pos-VFP.

Dimuon p_T range	Sample Name
9 to 30 GeV/c	/SPS_D0ToKPi_JPsiPt-9To30_TuneCP5_13TeV- helaconia-pythia8-evtgen
	/RunIISummer20UL16RECO- 106X_mcRun2_asymptotic_v13-v2 /AODSIM
	/SPS_D0ToKPi_JPsiPt-30To50_TuneCP5_13TeV- helaconia-pythia8-evtgen
30 to 50 GeV/c	/RunIISummer20UL16RECO- 106X_mcRun2_asymptotic_v13-v2 /AODSIM
	/SPS_D0ToKPi_JPsiPt-50To100_TuneCP5_13TeV- helaconia-pythia8-evtgen
	/RunIISummer20UL16RECO- ext6_106X_mcRun2_asymptotic_v13-v2 /AODSIM

Legend: Three different samples are used. Each sample is characterized by the dimuon p_T range.

Source: The author, 2023.

Table 80 - SPS Samples: 2017

Dimuon p_T range	Sample Name
9 to 30 GeV/c	/SPS_D0ToKPi_JPsiPt-9To30_TuneCP5_13TeV- helaconia-pythia8-evtgen
	/RunIISummer20UL17RECO- 106X_mc2017_realistic_v6_ext1-v2
	/AODSIM
30 to 50 GeV/c	/SPS_D0ToKPi_JPsiPt-30To50_TuneCP5_13TeV- helaconia-pythia8-evtgen
	/RunIISummer20UL17RECO- 106X_mc2017_realistic_v6-v2
	/AODSIM
50 to 100 GeV/c	/SPS_D0ToKPi_JPsiPt-50To100_TuneCP5_13TeV- helaconia-pythia8-evtgen
	/RunIISummer20UL17RECO- 106X_mc2017_realistic_v6_ext3-v2
	/AODSIM

Legend: Three different samples are used. Each sample is characterized by the dimuon p_T range.

Source: The author, 2023.

Table 81 - SPS Samples: 2018

Dimuon p_T range	Sample Name
9 to 30 GeV/c	/SPS_D0ToKPi_JPsiPt-9To30_TuneCP5_13TeV- helaconia-pythia8-evtgen
	/RunIISummer20UL18RECO- 106X_upgrade2018_realistic_v11_L1v1-v2
	/AODSIM
30 to 50 GeV/c	/SPS_D0ToKPi_JPsiPt-30To50_TuneCP5_13TeV- helaconia-pythia8-evtgen
	/RunIISummer20UL18RECO- 106X_upgrade2018_realistic_v11_L1v1_ext1-v2
	/AODSIM
50 to 100 GeV/c	/SPS_D0ToKPi_JPsiPt-50To100_TuneCP5_13TeV- helaconia-pythia8-evtgen
	/RunIISummer20UL18RECO- 106X_upgrade2018_realistic_v11_L1v1_ext4-v2
	/AODSIM

Legend: Three different samples are used. Each sample is characterized by the dimuon p_T range.

Source: The author, 2023.

APPENDIX E – Pile-up reweighting

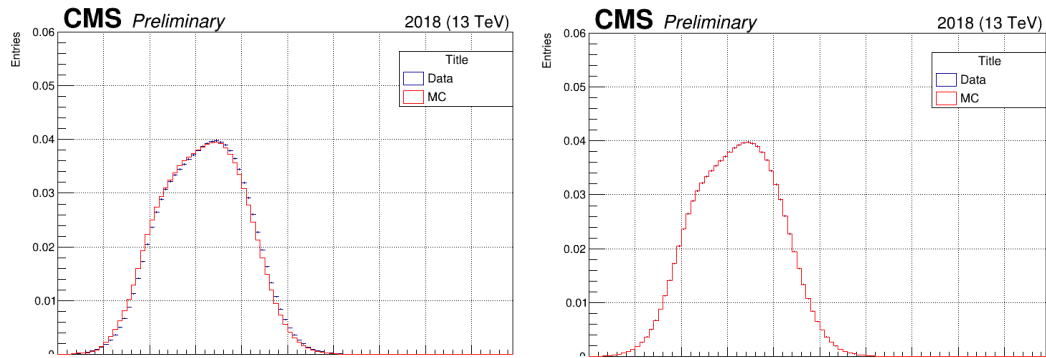
The pile-up is the total number of pp interactions per bunch crossing. It can be calculated with the use of the instantaneous luminosity

$$\mu = \frac{\mathcal{L}^i \sigma_{inel}}{f_{rev}}, \quad (49)$$

where σ_{inel} is the total pp inelastic cross-section and f_{rev} is the LHC orbit frequency.

The Luminosity POG provides a strategy to calculate the weights that are used in the Monte Carlo events. The idea is to get the histograms for the number of reconstructed vertices in both data in Monte Carlo. Due to the pile-up, these histograms do not match as pile-up is not properly simulated in Monte Carlo. Therefore, by dividing each bin of these histograms a weight is calculated for each bin. The strategy is highlighted in (218). Figure (132) shows the histogram with the number of reconstructed vertices before the weight correction and after the weight correction.

Figure 132 - Pile-up correction in Monte Carlo.



Legend: Both histograms show the number of reconstructed vertices normalized by area.

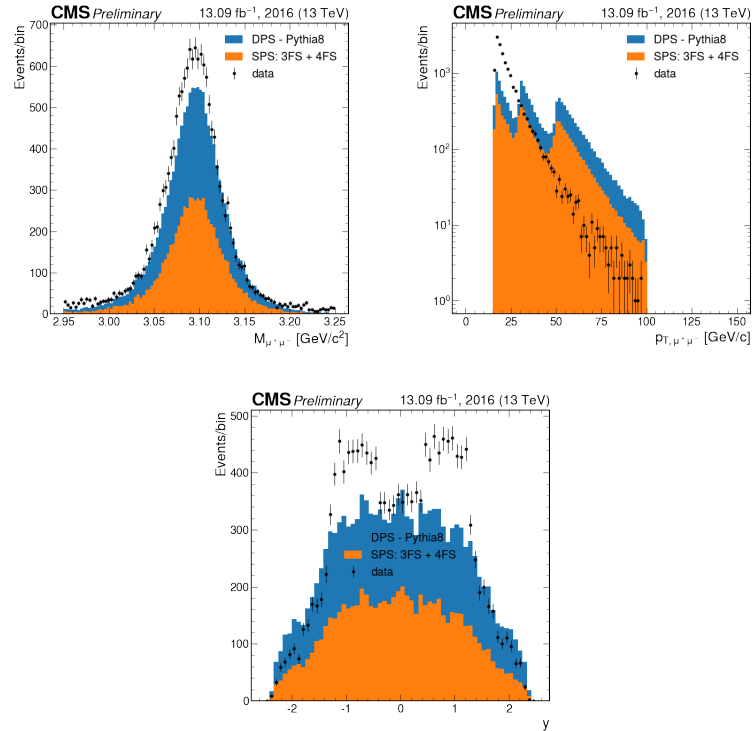
The figure on the left shows that before the pile-up correction, the histograms do not match. The figure on the right shows that after the correction, the histograms match.

Source: The author, 2023.

APPENDIX F – Control Plots

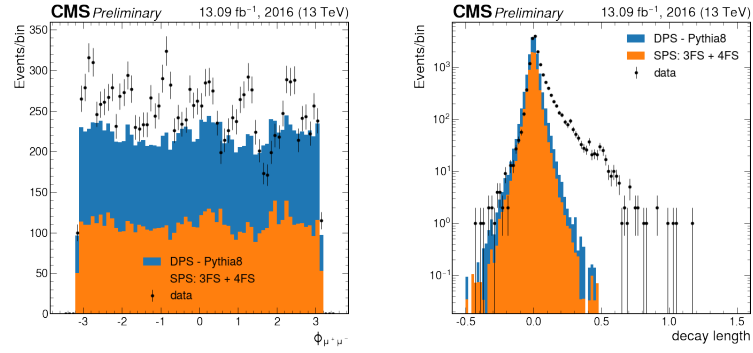
In this appendix, control plots of 2016-pre-VFP, 2016-pos-VFP, and 2018 are shown.

Figure 133 - J/ψ control plots 1 - 2016-pre-VFP data.



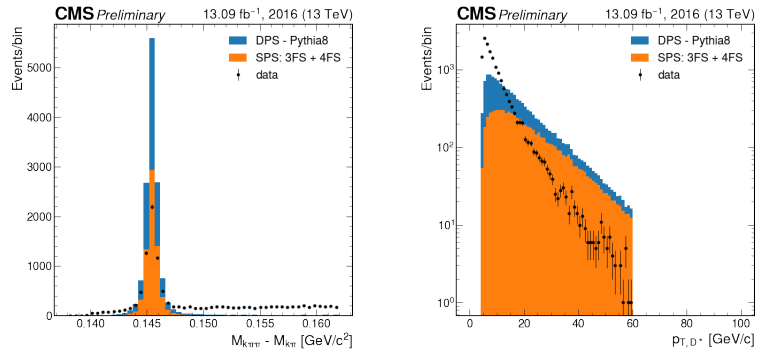
Legend: Top left: $\mu^+\mu^-$ invariant mass. Top right: J/ψ p_T . Bottom: J/ψ rapidity. It is observed that the contributions due to SPS and DPS are not enough to simulate the observed data. Therefore, other processes are needed to simulate it correctly. It is worth mentioning that the simulations for $p_T > 30$ GeV/c have an excess of events due to normalization.

Source: The author, 2023.

Figure 134 - J/ψ control plots 2 - 2016-pre-VFP data.

Legend: Left: J/ψ ϕ . Right: J/ψ decay length (mm). It is observed that both SPS and DPS contribute only to prompt J/ψ production.

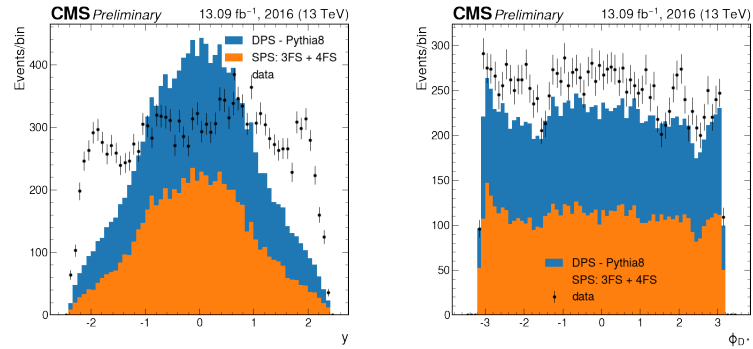
Source: The author, 2023.

Figure 135 - D^* control plots 1 - 2016-pre-VFP data.

Legend: Left: $D^* - D^0$ mass difference. Right: D^* p_T .

Source: The author, 2023.

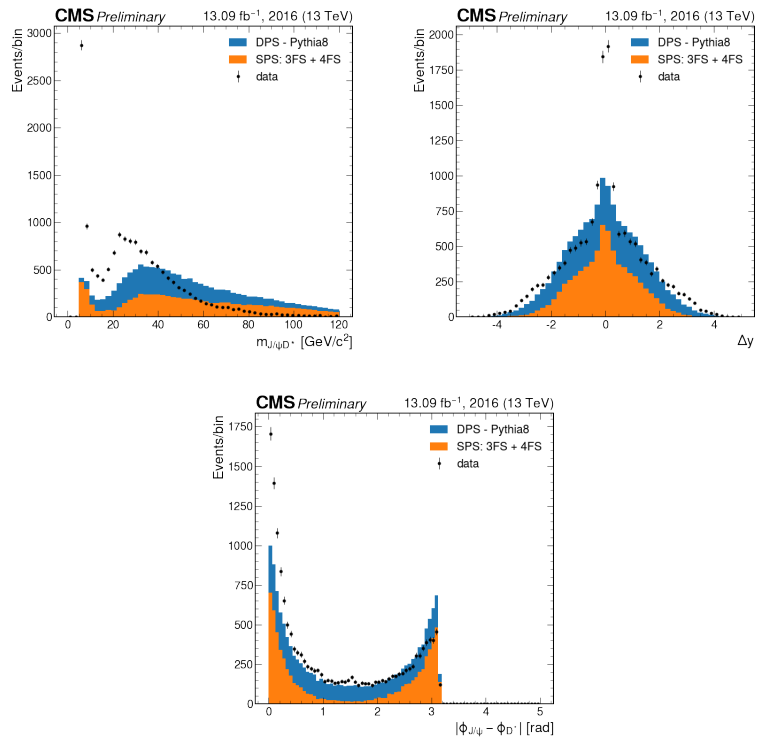
Figure 136 - D^* control plots 2 - 2016-pre-VFP data.



Legend: Left: D^* rapidity. Right: D^* ϕ . It is observed that values around $y = \pm 2$ data and MC don't agree. Therefore, other contributions are needed to simulate the observed data

Source: The author, 2023.

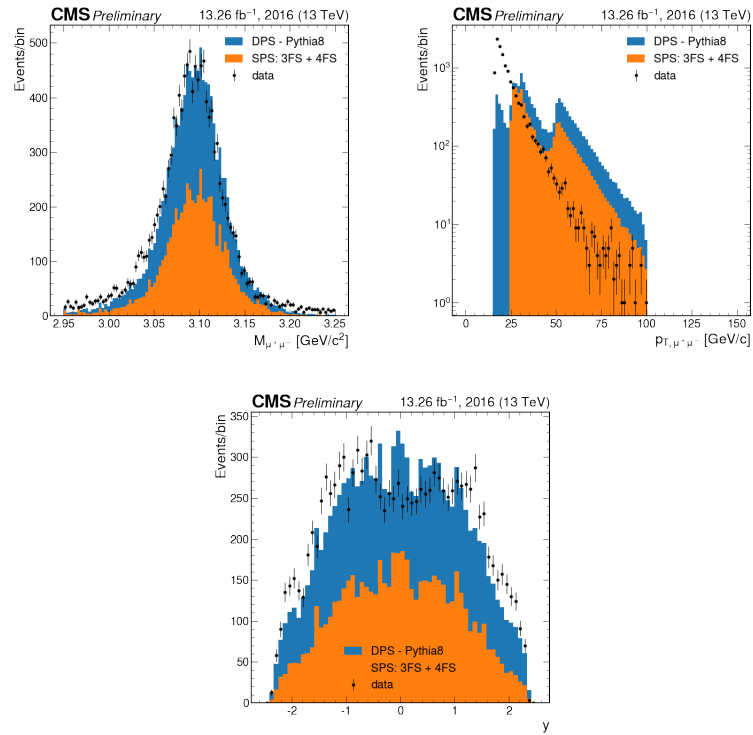
Figure 137 - $J/\psi D^*$ control plots 1 - 2016-pre-VFP data.



Legend: Top left: $J/\psi D^*$ invariant mass. Top right: $J/\psi D^*$ Δy . Bottom: $J/\psi D^*$ $\Delta\phi$. Note that the peak in the invariant mass region of 5-10 GeV/c^2 is not well simulated with SPS and DPS. It is possible to see similar peaks at $\Delta y = 0$ and $\Delta\phi = 0$.

Source: The author, 2023.

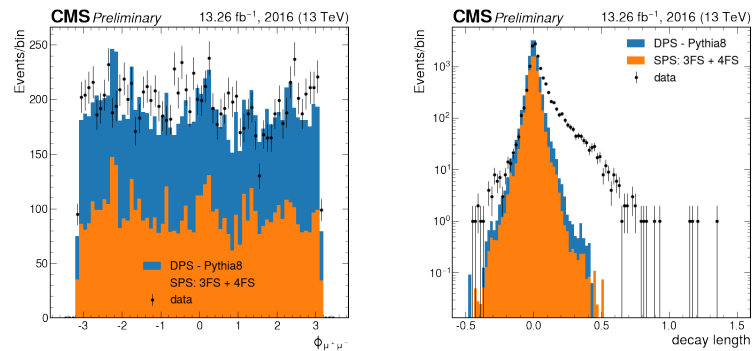
Figure 138 - J/ψ control plots 1 - 2016-pos-VFP data.



Legend: Top left: $\mu^+\mu^-$ invariant mass. Top right: J/ψ p_T . Bottom: J/ψ rapidity. It is observed that the contributions due to SPS and DPS seem to simulate well the observed data. However, this needs to be studied more carefully in the future. It is worth mentioning that the simulations for $p_T > 25$ GeV/c have an excess of events due to normalization.

Source: The author, 2023.

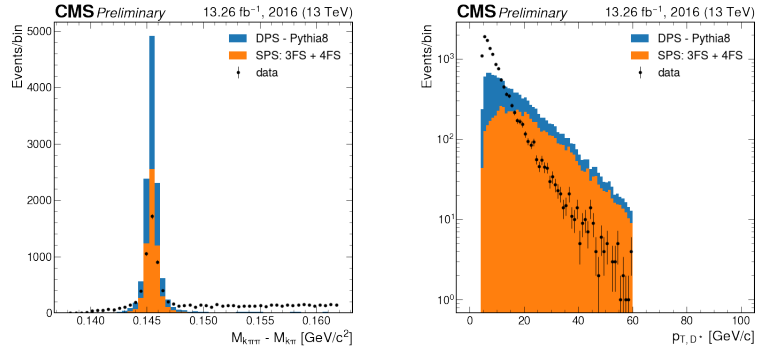
Figure 139 - J/ψ control plots 2 - 2016-pos-VFP data.



Legend: Left: J/ψ ϕ . Right: J/ψ decay length (mm). It is observed that both SPS and DPS contribute only to prompt J/ψ production.

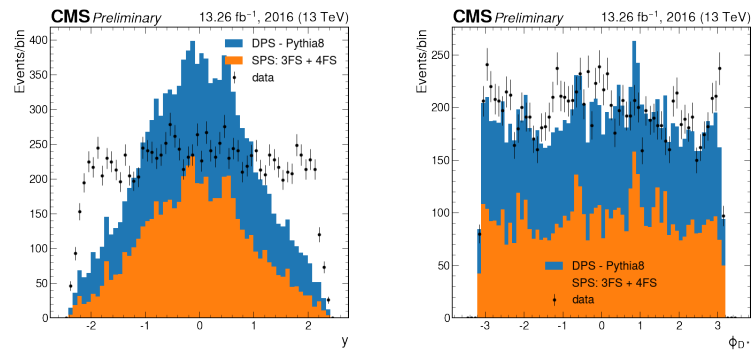
Source: The author, 2023.

Figure 140 - D^* control plots 1 - 2016-pos-VFP data.



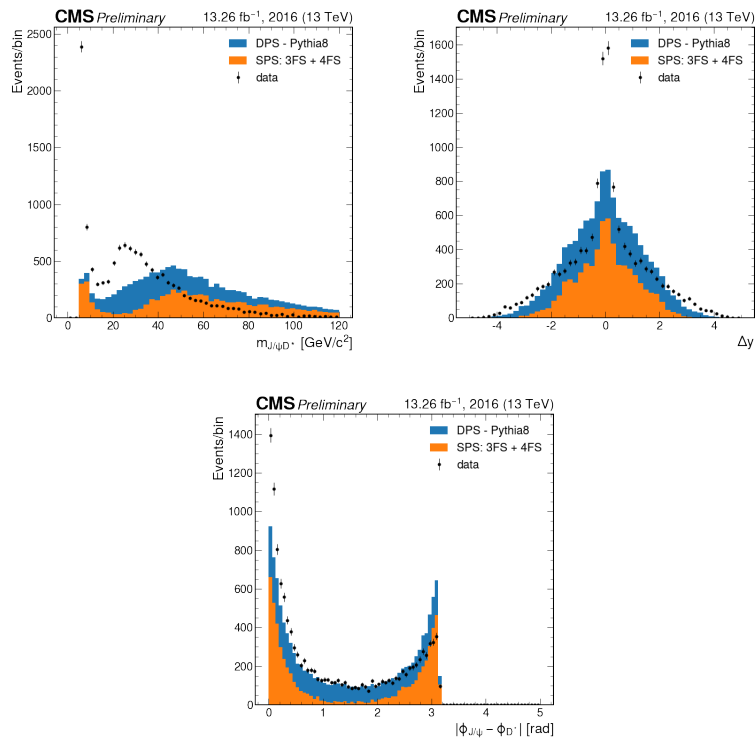
Legend: Left: $D^* - D^0$ mass difference. Right: $D^* p_T$.
Source: The author, 2023.

Figure 141 - D^* control plots 2 - 2016-pos-VFP data.



Legend: Left: D^* rapidity. Right: $D^* \phi$. It is observed that values around $y = \pm 2$ data and MC don't agree. Therefore, other contributions are needed to simulate the observed data

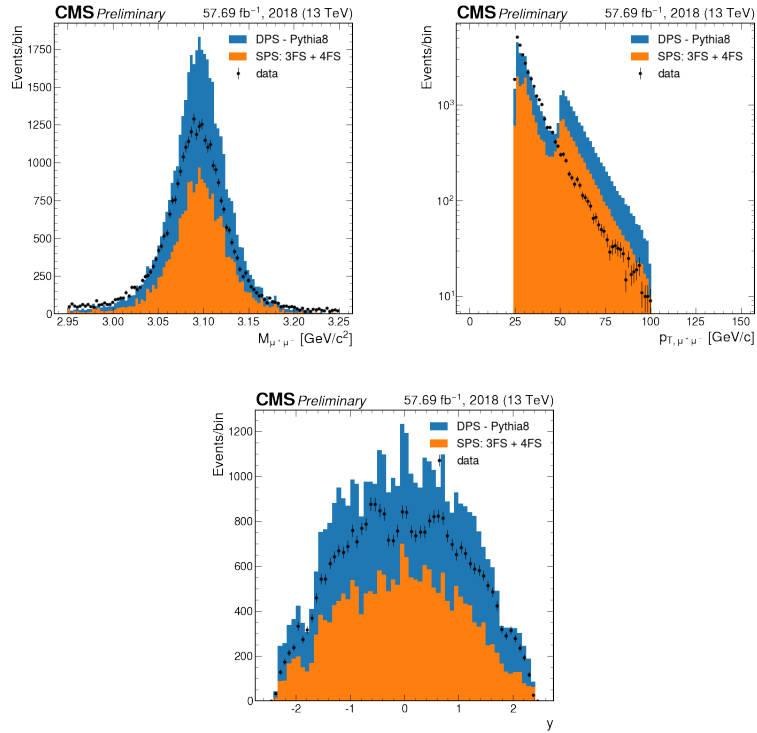
Source: The author, 2023.

Figure 142 - $J/\psi D^*$ control plots 1 - 2016-pos-VFP data.

Legend: Top left: $J/\psi D^*$ invariant mass. Top right: $J/\psi D^*$ Δy . Bottom: $J/\psi D^*$ $\Delta\phi$. Note that the peak in the invariant mass region of 5-10 GeV/c^2 is not well simulated with SPS and DPS. It is possible to see similar peaks at $\Delta y = 0$ and $\Delta\phi = 0$.

Source: The author, 2023.

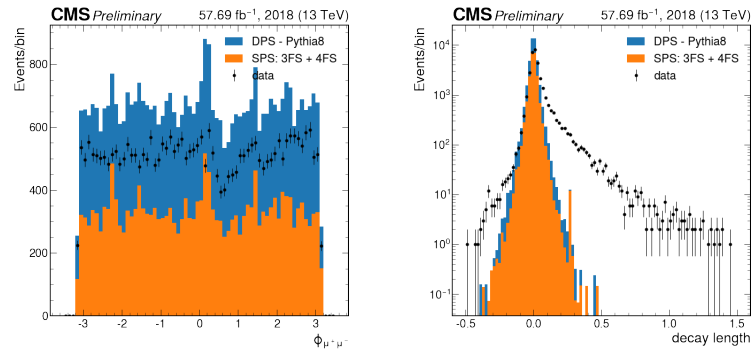
Figure 143 - J/ψ control plots 1 - 2018 data.



Legend: Top left: $\mu^+\mu^-$ invariant mass. Top right: J/ψ p_T . Bottom: J/ψ rapidity. In all 2018 data, an issue with normalization is observed. Therefore, that needs to be understood in the future before any conclusion.

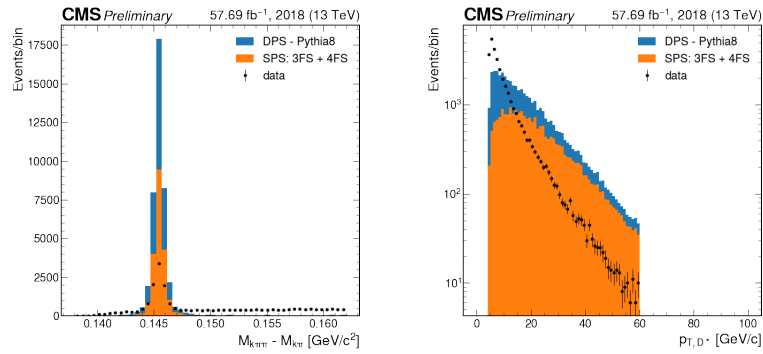
Source: The author, 2023.

Figure 144 - J/ψ control plots 2 - 2018 data.



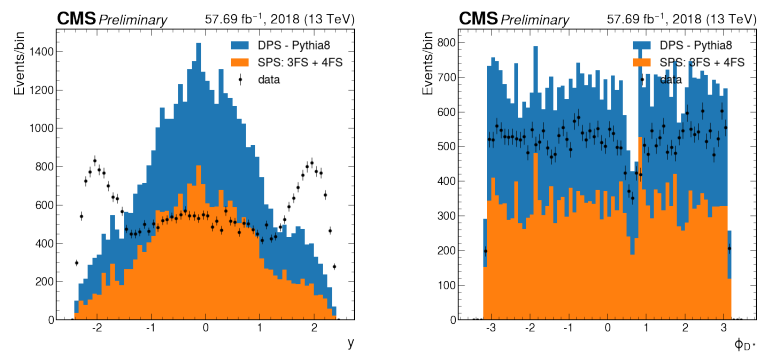
Legend: Left: J/ψ ϕ . Right: J/ψ decay length (mm). It is observed that both SPS and DPS contribute only to prompt J/ψ production.

Source: The author, 2023.

Figure 145 - D^* control plots 1 - 2018 data.

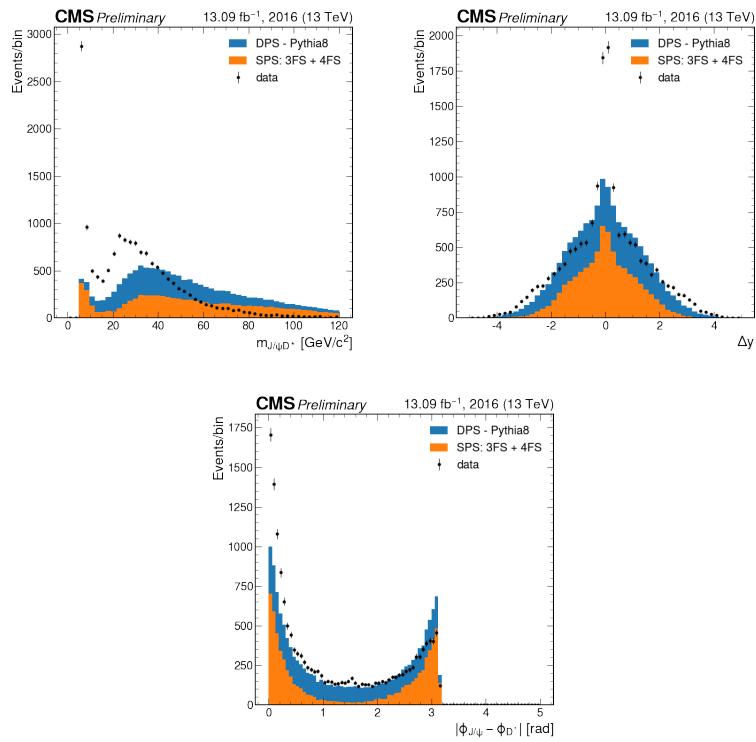
Legend: Left: $D^* - D^0$ mass difference. Right: $D^* p_T$.

Source: The author, 2023.

Figure 146 - D^* control plots 2 - 2018 data.

Legend: Left: D^* rapidity. Right: $D^* \phi$. It is observed that values around $y = \pm 2$ data and MC don't agree. Therefore, other contributions are needed to simulate the observed data

Source: The author, 2023.

Figure 147 - $J/\psi D^*$ control plots 1 - 2016-pre-VFP data.

Legend: Top left: $J/\psi D^*$ invariant mass. Top right: $J/\psi D^*$ Δy . Bottom: $J/\psi D^*$ $\Delta\phi$. Note that the peak in the invariant mass region of 5-10 GeV/c² is not well simulated with SPS and DPS. It is possible to see similar peaks at $\Delta y = 0$ and $\Delta\phi = 0$.

Source: The author, 2023.

APPENDIX G – Fitting Strategy

In this appendix, the fitting strategy for getting the yields is explained. As the data is described by multiple components ($\mu\mu^-$ invariant mass, J/ψ decay length, $D^* - D^0$ mass) a composite model is used (190). The fittings of the important distributions discussed in Chapter 4 are discussed in G.2, as well as the codes used to obtain them.

G.1 Fit model

A composite model is represented as

$$M(x) = \sum_{i=1}^{N-1} f_i F_i(x) + (1 - \sum_{i=1}^{N-1} f_i) F_N(x), \quad (50)$$

where N is the number of hypotheses, f_i is the fraction of events in the sample represented by the probability density function $F_i(x)$. This can be used recursively in the following way. For J/ψ fitting model f_G and $F_G(x)$ are the gaussian fraction and its PDF, f_{CB} and $F_{CB}(x)$ are the crystal ball fraction and its PDF and, f_{exp} and $F_{exp}(x)$ are the exponential background fraction and its PDF. The Equation (33) has eight terms. The first term is composed of the signal component and the rest are background. Therefore, using (50) is possible to see that if f_s is the fraction of signal (refers to $S_{J/\psi}^{mass} \cdot P_{J/\psi} \cdot S_{D^*}$) the fraction of background is simply $f_B = 1 - f_s$. So, if N_{evt} is the number of events that are fitted the number of signal and background events are

$$\begin{aligned} N_{signal} &= N_{evt} \cdot f_s, \\ N_{background} &= N_{evt} - N_{signal}. \end{aligned} \quad (51)$$

Moreover the term $S_{J/\psi}^{mass} \cdot NP_{J/\psi} \cdot S_{D^*}$ contains the number of non-prompt J/ψ that contaminates the signal. Still using (50) the number of events of this quantity is

$$N_{non-prompt} = N_{evt} \cdot (1 - f_s) \cdot (1 - f_{back1}) \cdot (1 - f_{back2}), \quad (52)$$

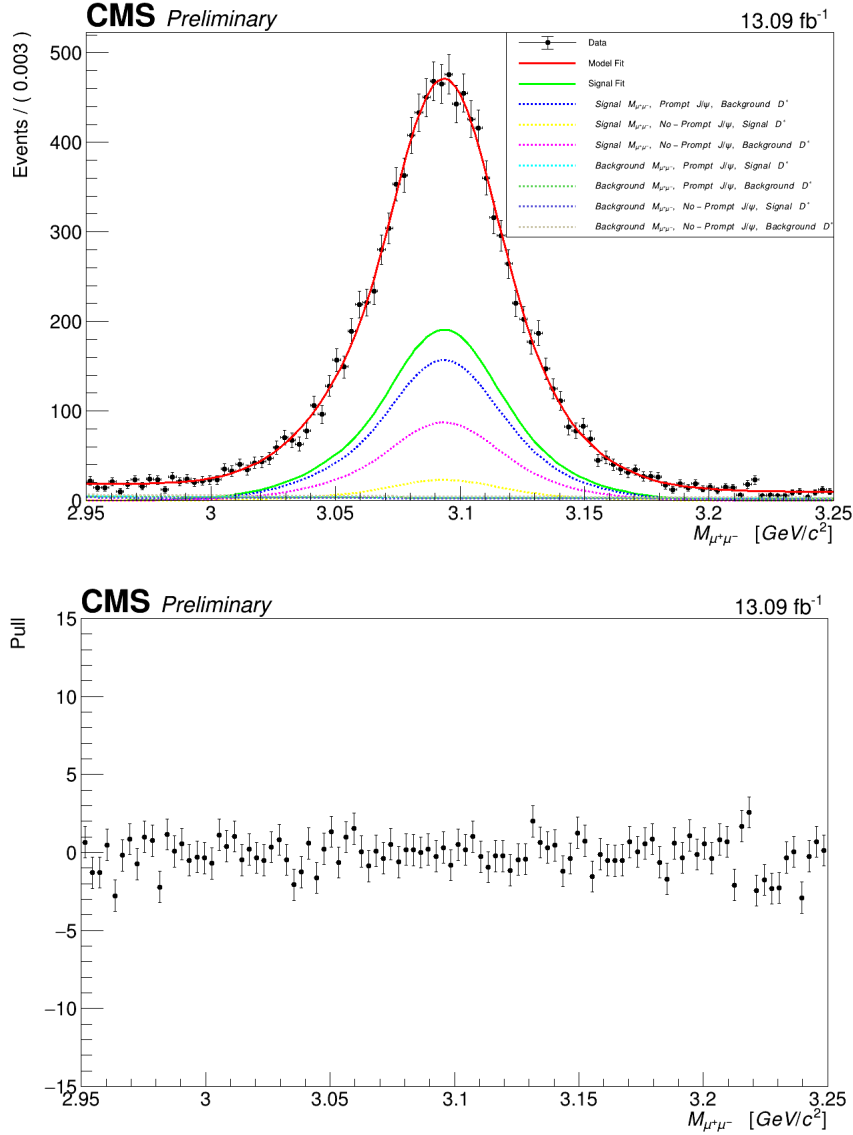
where f_{back1} is the fraction of events of component $S_{J/\psi}^{mass} \cdot P_{J/\psi} \cdot B_{D^*}$ and f_{back2} is the fraction of events of component $S_{J/\psi}^{mass} \cdot NP_{J/\psi} \cdot S_{D^*}$. The technicalities of this strategy are highlighted in (219).

G.2 Fitting distributions

The fitting of 2016 and 2018 data are shown in this subsection. It is worth mentioning that the fits for 2017 are in Section (4.4).

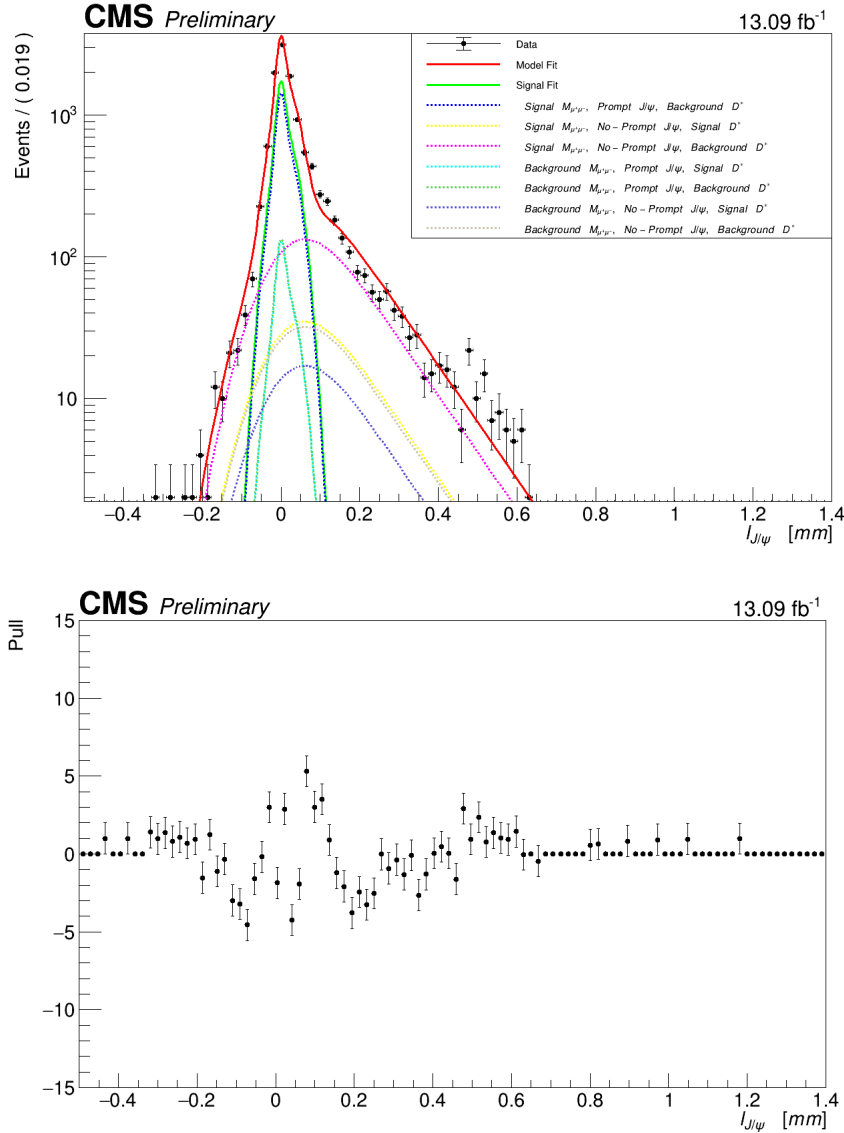
G.3 Producing plots

To get the fits, yields, and other information for the fit many different codes are used. The instructions can be found on GitHub (220).

Figure 148 - The $\mu^+\mu^-$ invariant mass distribution - 2016-pre-VFP data

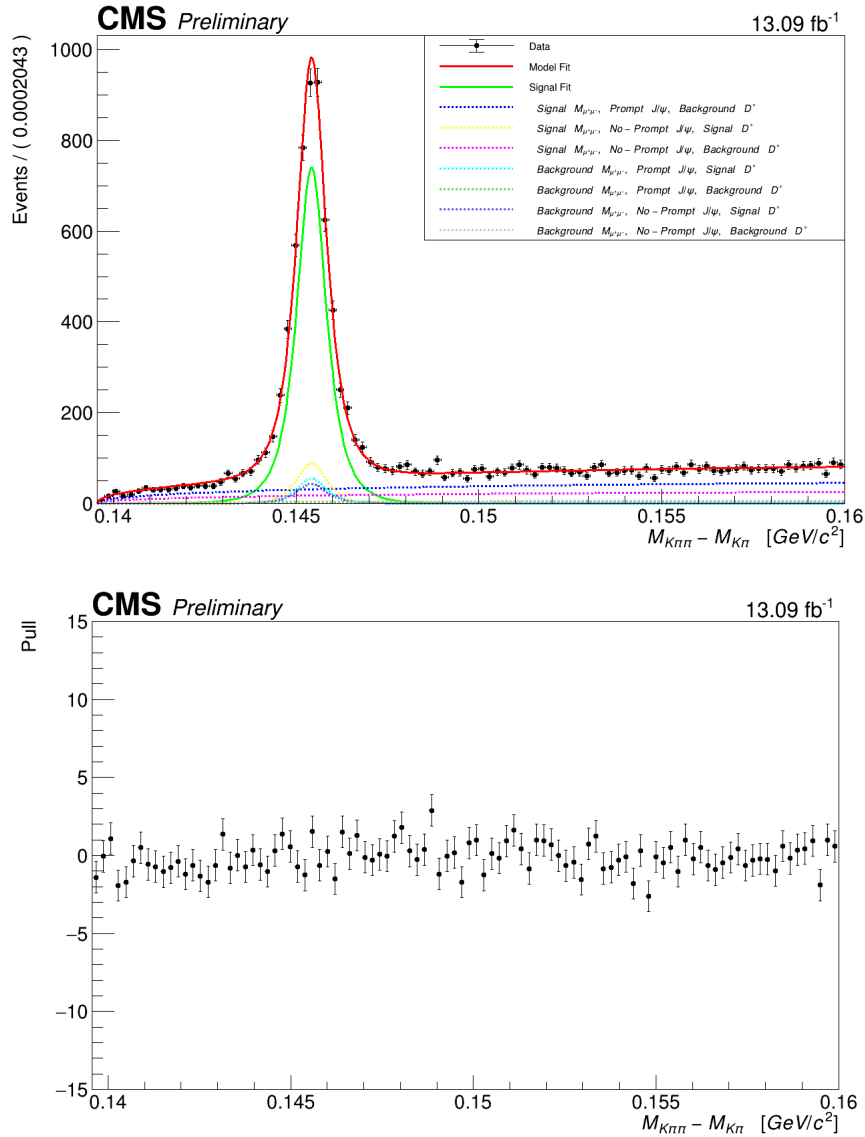
Legend: The figure on top shows the 1D projections of the fits of $\mu^+\mu^-$ invariant mass. The model fit (red) represents the fit of the $\mu^+\mu^-$ invariant mass distribution regardless of the other variables (J/ψ decay length and $D^* - D^0$ mass difference). The signal (green) is smaller when compared to the model fit distribution because it takes into account only the signal region of $\mu^+\mu^-$ invariant distribution, the prompt J/ψ , and the signal region of $D^* - D^0$ mass difference. The "Number of signal events" in Table (20) is obtained from this curve, and the "Number of non-prompt "signal" events" is obtained from the yellow curve. All other curves represent background contributions. The figure on the bottom shows the pull distribution.

Source: The author, 2023.

Figure 149 - J/ψ decay length - 2016-pre-VFP data

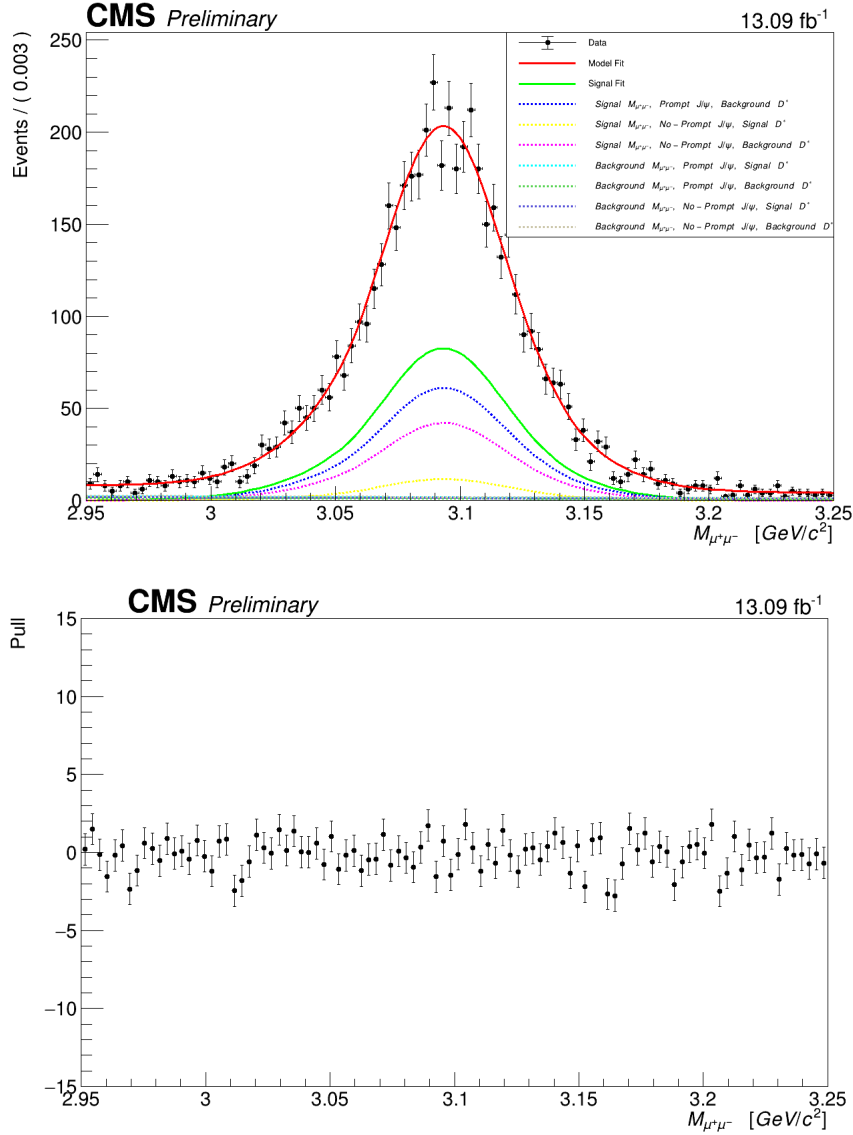
Legend: The figure on top shows the 1D projections of the fits of J/ψ decay length. The model fit (red) represents the fit of the J/ψ decay length distribution regardless of the other variables ($\mu^+\mu^-$ invariant mass and $D^* - D^0$ mass difference). Again, the signal (green) is smaller when compared to the model fit distribution. Note that the curve is not symmetric due to two different reasons, wrong assignments of the primary vertex (left part of the distribution) and the presence of non-prompt J/ψ (right part of the curve). The figure on the bottom shows the pull distribution.

Source: The author, 2023.

Figure 150 - $D^* - D^0$ mass difference distribution - 2016-pre-VFP data

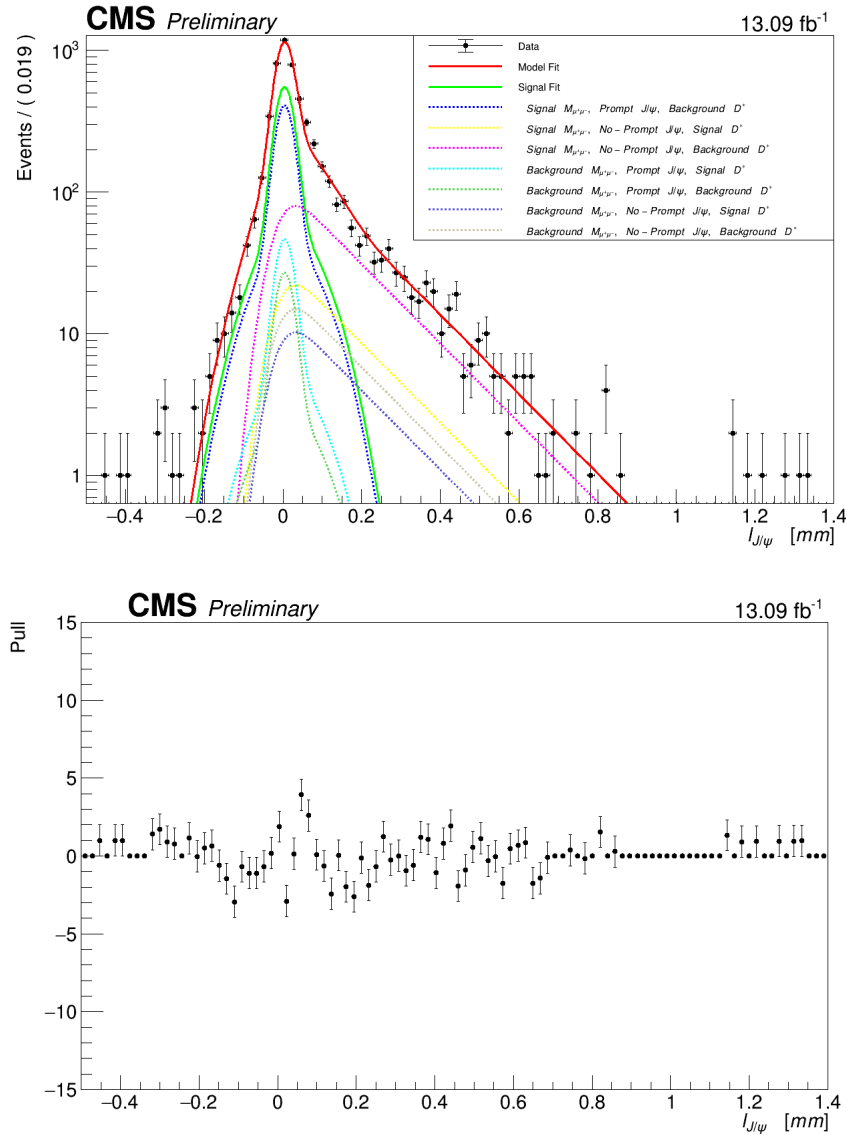
Legend: The figure on top shows the 1D projections of the fits of $D^* - D^0$ mass difference. The model fit (red) represents the fit of the $D^* - D^0$ mass difference distribution regardless of the other variables ($\mu^+\mu^-$ invariant mass and J/ψ decay length). Again, the signal (green) is smaller when compared to the model fit distribution. The curve threshold is well fitted with the TF function (values around 0.14 GeV/c^2). The figure on the bottom shows the pull distribution.

Source: The author, 2023.

Figure 151 - The $\mu^+\mu^-$ invariant mass distribution - 2016-pos-VFP data

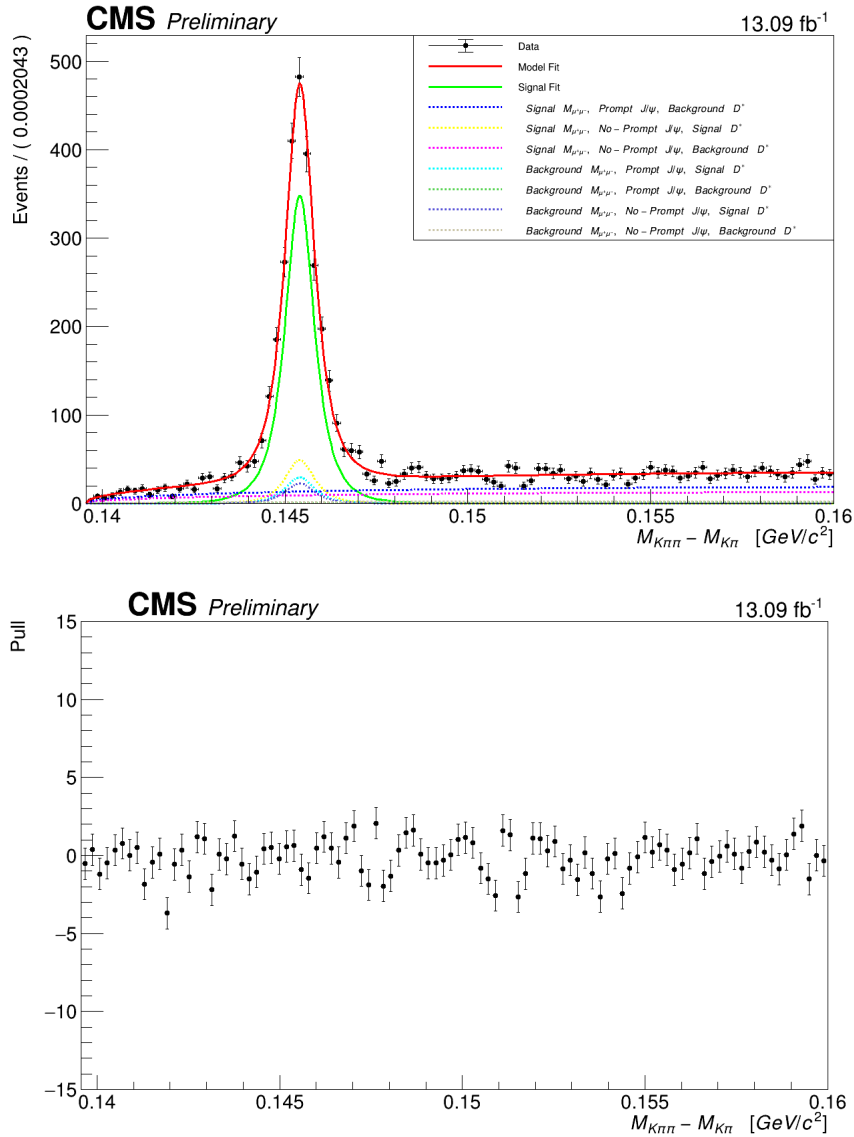
Legend: The figure on top shows the 1D projections of the fits of $\mu^+\mu^-$ invariant mass. The model fit (red) represents the fit of the $\mu^+\mu^-$ invariant mass distribution regardless of the other variables (J/ψ decay length and $D^* - D^0$ mass difference). The signal (green) is smaller when compared to the model fit distribution because it takes into account only the signal region of $\mu^+\mu^-$ invariant distribution, the prompt J/ψ , and the signal region of $D^* - D^0$ mass difference. The "Number of signal events" in Table (21) is obtained from this curve, and the "Number of non-prompt "signal" events" is obtained from the yellow curve. All other curves represent background contributions. The figure on the bottom shows the pull distribution.

Source: The author, 2023.

Figure 152 - J/ψ decay length - 2016-pos-VFP data

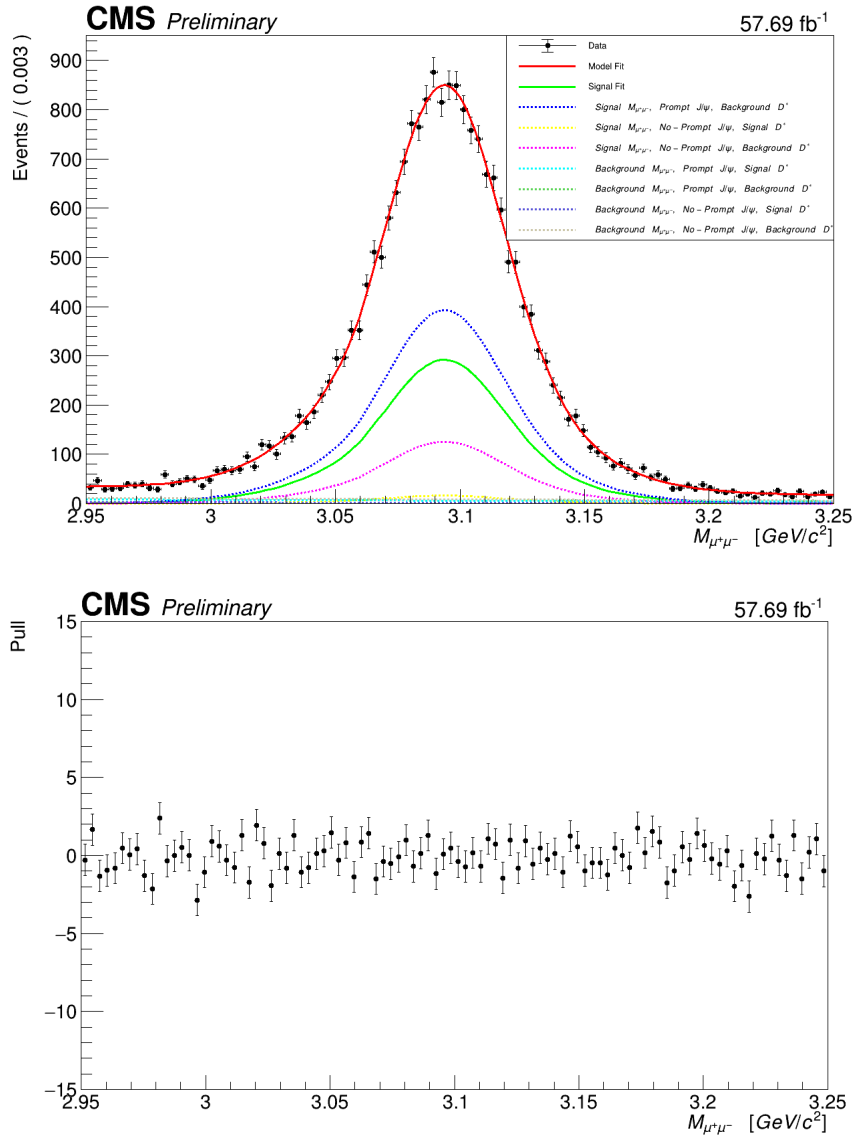
Legend: The figure on top shows the 1D projections of the fits of J/ψ decay length. The model fit (red) represents the fit of the J/ψ decay length distribution regardless of the other variables ($\mu^+\mu^-$ invariant mass and $D^* - D^0$ mass difference). Again, the signal (green) is smaller when compared to the model fit distribution. Note that the curve is not symmetric due to two different reasons, wrong assignments of the primary vertex (left part of the distribution) and the presence of non-prompt J/ψ (right part of the curve). The figure on the bottom shows the pull distribution.

Source: The author, 2023.

Figure 153 - $D^* - D^0$ mass difference distribution - 2016-pos-VFP data

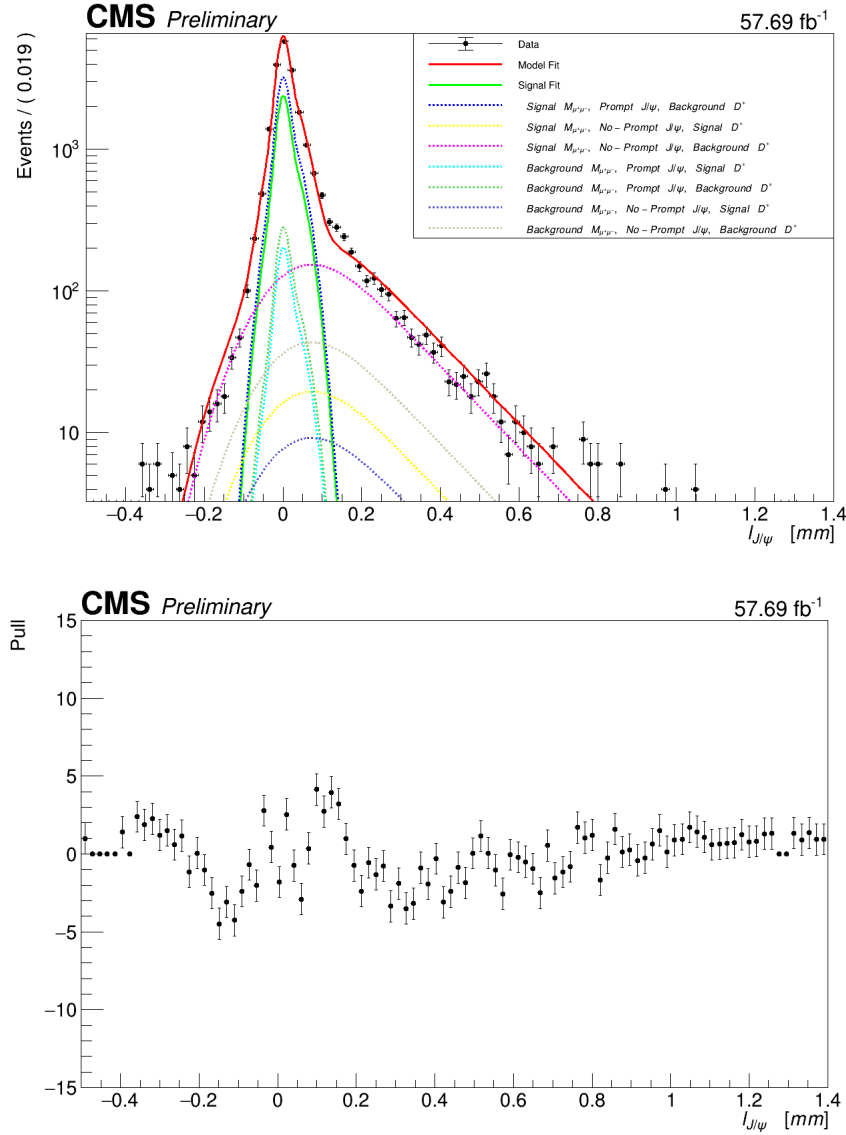
Legend: The figure on top shows the 1D projections of the fits of $D^* - D^0$ mass difference. The model fit (red) represents the fit of the $D^* - D^0$ mass difference distribution regardless of the other variables ($\mu^+\mu^-$ invariant mass and J/ψ decay length). Again, the signal (green) is smaller when compared to the model fit distribution. The curve threshold is well fitted with the TF function (values around 0.14 GeV/c²). The figure on the bottom shows the pull distribution.

Source: The author, 2023.

Figure 154 - The $\mu^+\mu^-$ invariant mass distribution - 2018 data

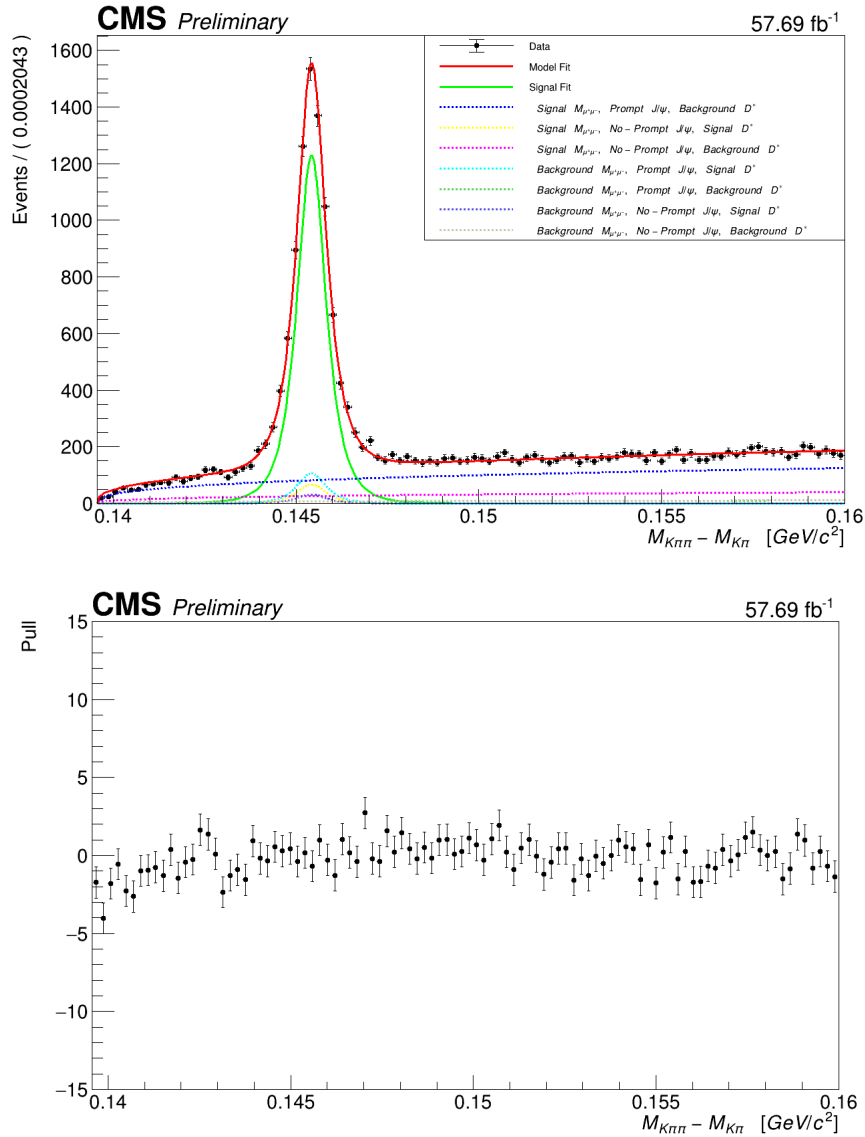
Legend: The figure on top shows the 1D projections of the fits of $\mu^+\mu^-$ invariant mass. The model fit (red) represents the fit of the $\mu^+\mu^-$ invariant mass distribution regardless of the other variables (J/ψ decay length and $D^* - D^0$ mass difference). The signal (green) is smaller when compared to the model fit distribution because it takes into account only the signal region of $\mu^+\mu^-$ invariant distribution, the prompt J/ψ , and the signal region of $D^* - D^0$ mass difference. The "Number of signal events" in Table (23) is obtained from this curve, and the "Number of non-prompt "signal" events" is obtained from the yellow curve. All other curves represent background contributions. The figure on the bottom shows the pull distribution.

Source: The author, 2023.

Figure 155 - J/ψ decay length - 2018 data

Legend: The figure on top shows the 1D projections of the fits of J/ψ decay length. The model fit (red) represents the fit of the J/ψ decay length distribution regardless of the other variables ($\mu^+\mu^-$ invariant mass and $D^* - D^0$ mass difference). Again, the signal (green) is smaller when compared to the model fit distribution. Note that the curve is not symmetric due to two different reasons, wrong assignments of the primary vertex (left part of the distribution) and the presence of non-prompt J/ψ (right part of the curve). The figure on the bottom shows the pull distribution.

Source: The author, 2023.

Figure 156 - $D^* - D^0$ mass difference distribution - 2018 data

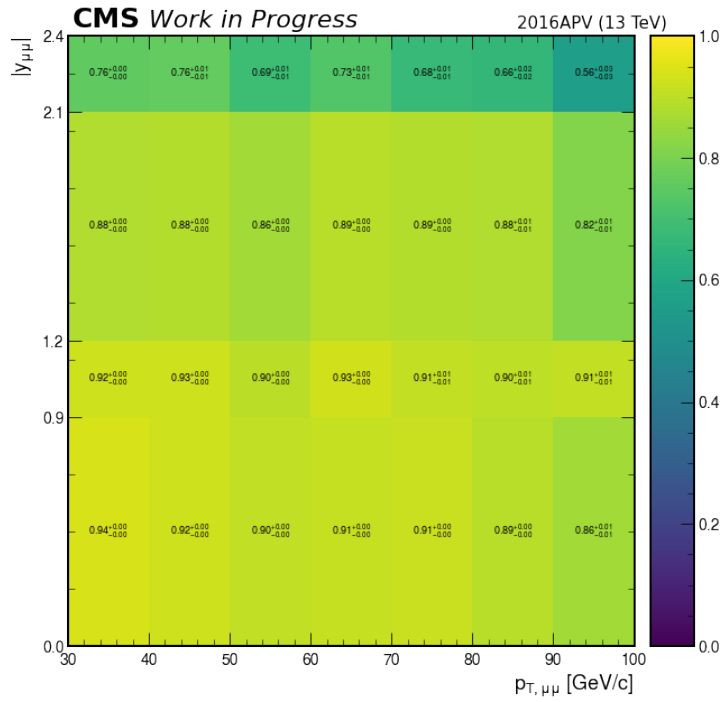
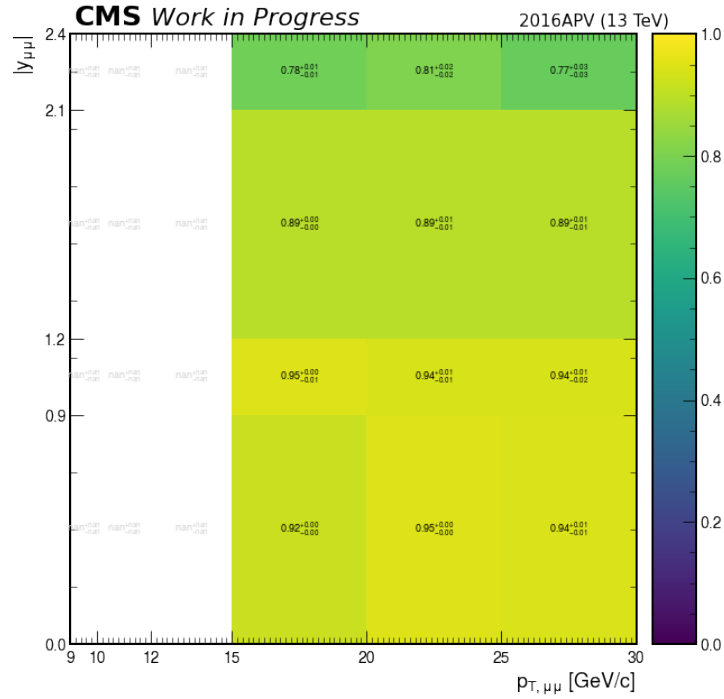
Legend: The figure on top shows the 1D projections of the fits of $D^* - D^0$ mass difference. The model fit (red) represents the fit of the $D^* - D^0$ mass difference distribution regardless of the other variables ($\mu^+\mu^-$ invariant mass and J/ψ decay length). Again, the signal (green) is smaller when compared to the model fit distribution. The curve threshold is well fitted with the TF function (values around 0.14 GeV/c²). The figure on the bottom shows the pull distribution.

Source: The author, 2023.

APPENDIX H – Acceptance and Efficiency - Plots

The plots of the efficiencies calculated in Sections (4.5) and (4.6.1) are shown in this appendix. The figures below show all situations discussed in the commented sections.

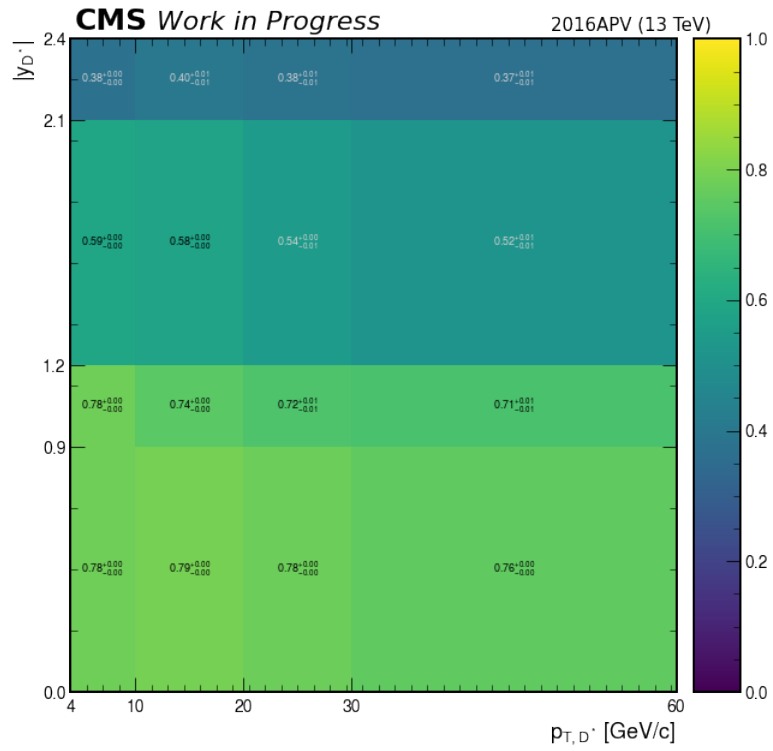
Figure 157 - J/ψ acceptance in bins of rapidity and p_T - 2016-pre-VFP data.



Legend: The figure on top shows the J/ψ acceptance in the region $|y| < 2.4$ and $9 < p_T < 30$ GeV/c and the figure on bottom shows it in the region $|y| < 2.4$ and $30 < p_T < 100$ GeV/c.

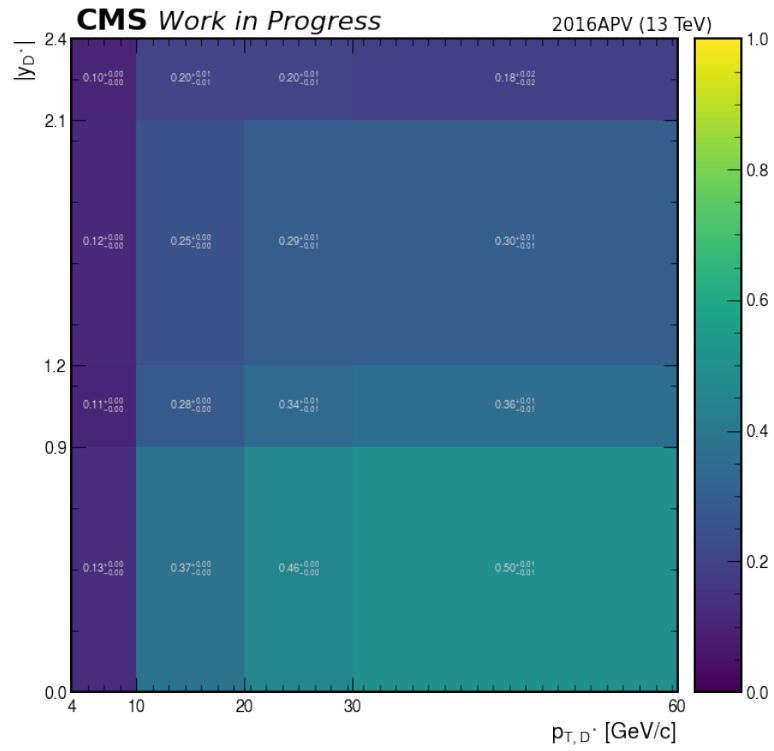
Source: The author, 2023.

Figure 158 - D^* acceptance in bins of rapidity and p_T - 2016-pre-VFP data.



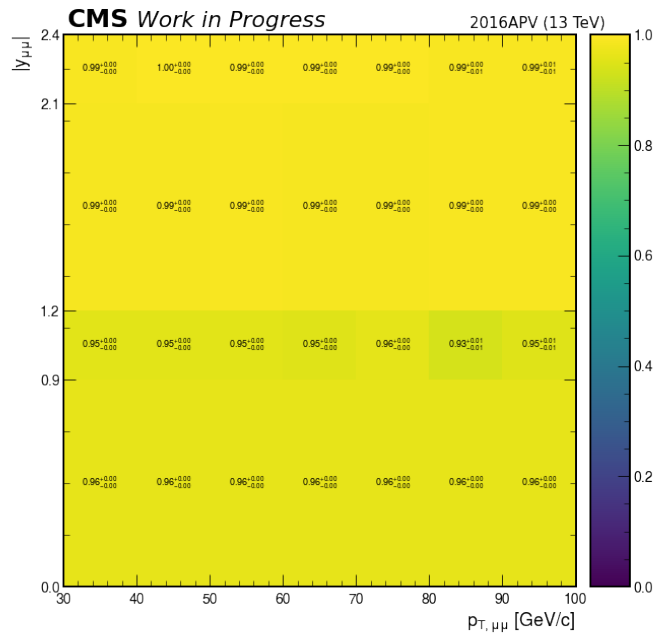
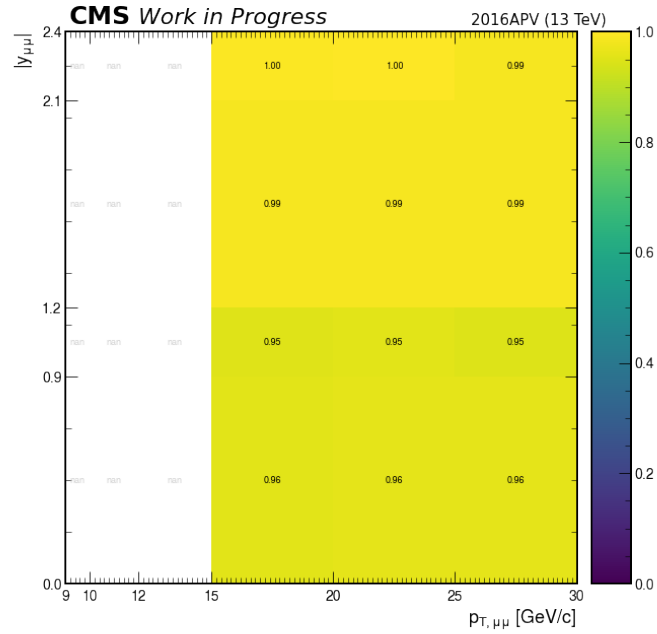
Legend: The figure shows the D^* acceptance in the region $|y| < 2.4$ and $4 < p_T < 60$ GeV/c .
 Source: The author, 2023.

Figure 159 - D^* cuts efficiency in bins of rapidity and p_T - 2016-pre-VFP data.



Legend: The figure shows the D^* cuts efficiency in the region $|y| < 2.4$ and $4 < p_T < 60$ GeV/c .
 Source: The author, 2023.

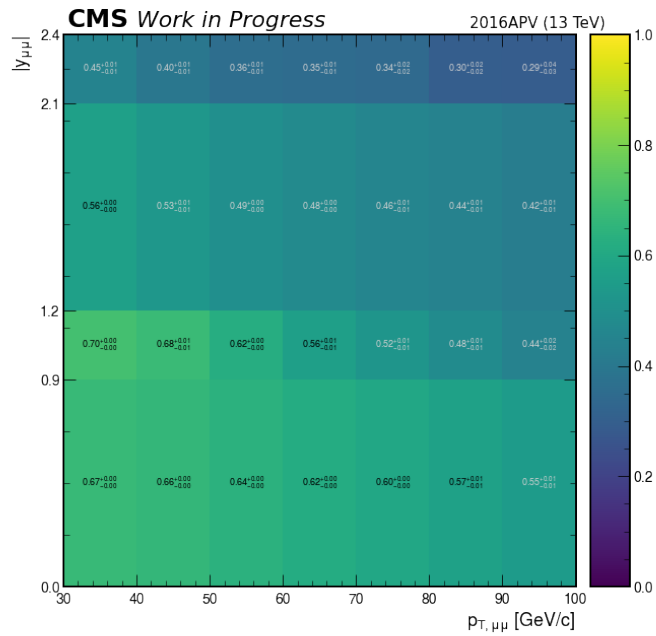
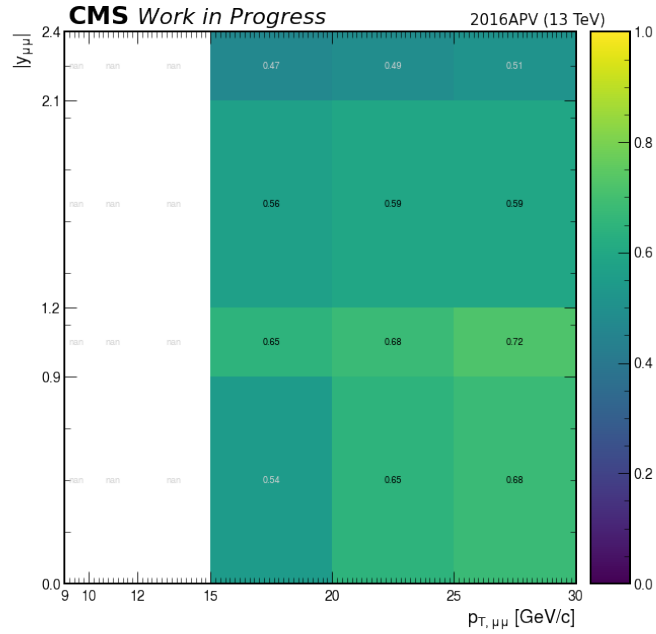
Figure 160 - J/ψ cuts efficiency in bins of rapidity and p_T - 2016-pre-VFP data.



Legend: The figure on top shows the J/ψ cuts efficiency in the region $|y| < 2.4$ and $9 < p_T < 30$ GeV/c and the figure on bottom shows it in the region $|y| < 2.4$ and $30 < p_T < 100$ GeV/c. Top figure: uncertainties are purposely omitted for visualization purposes.

Source: The author, 2023.

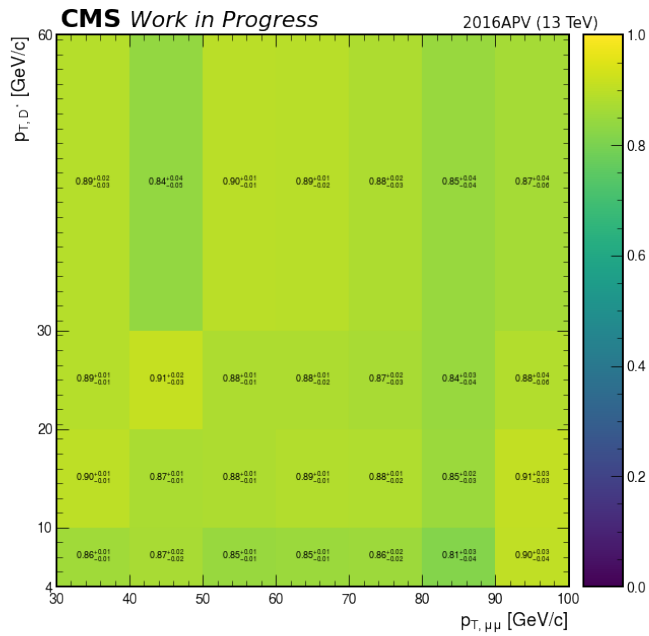
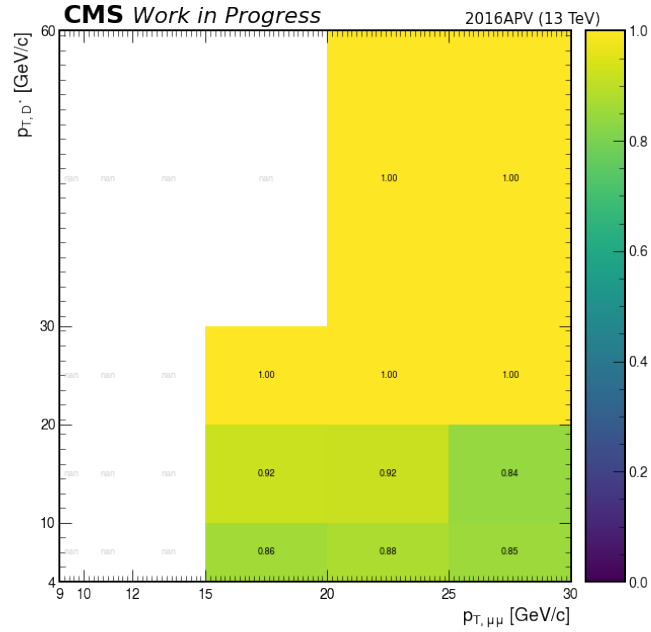
Figure 161 - HLT efficiency in bins of rapidity and p_T - 2016-pre-VFP data.



Legend: The figure on top shows the HLT efficiency in the region $|y| < 2.4$ and $9 < p_T < 30$ GeV/c and the figure on the bottom shows it in the region $|y| < 2.4$ and $30 < p_T < 100$ GeV/c. Top figure: uncertainties are purposely omitted for visualization purposes.

Source: The author, 2023.

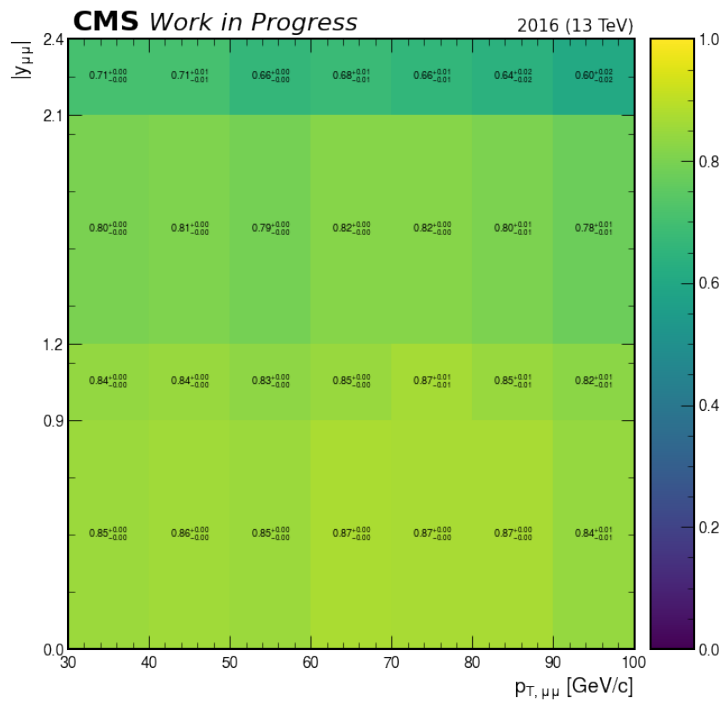
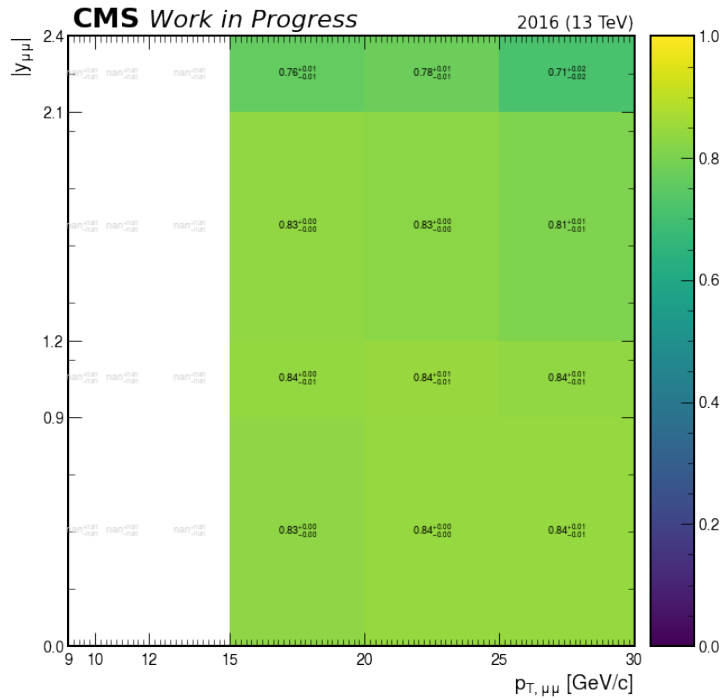
Figure 162 - Association efficiency in bins of D^* p_T and J/ψ p_T - 2016-pre-VFP data.



Legend: The figure on top shows the association efficiency in the region $4 < p_T^{D^*} < 60$ GeV/c and $9 < p_T^{D^*} < 30$ GeV/c and the figure on the bottom shows it in the region $4 < p_T^{D^*} < 60$ GeV/c and $30 < p_T^{D^*} < 100$ GeV/c. Top figure: uncertainties are purposely omitted for visualization purposes.

Source: The author, 2023.

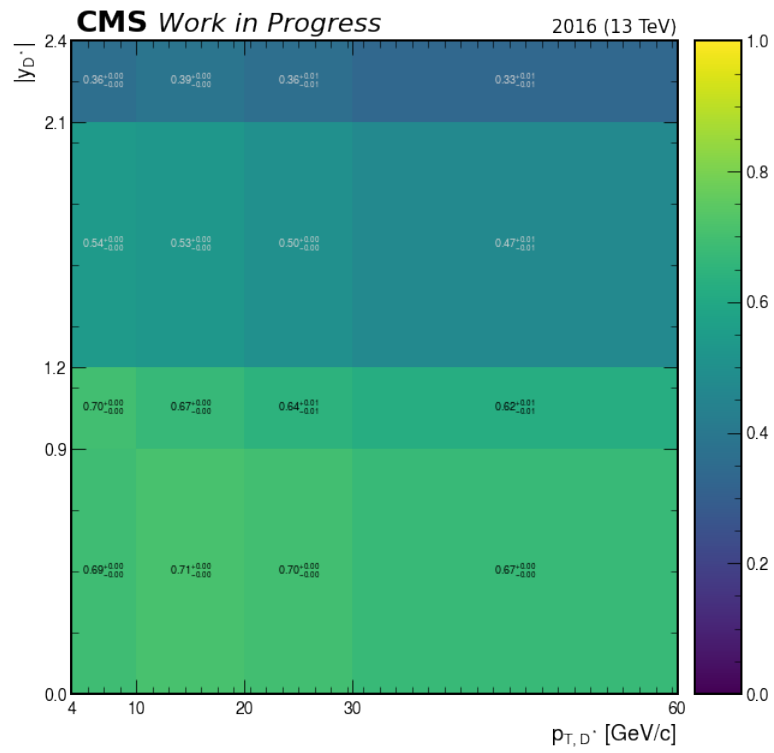
Figure 163 - J/ψ acceptance in bins of rapidity and p_T - 2016-pos-VFP data.



Legend: The figure on top shows the J/ψ acceptance in the region $|y| < 2.4$ and $9 < p_T < 30$ GeV/c and the figure on bottom shows it in the region $|y| < 2.4$ and $30 < p_T < 100$ GeV/c.

Source: The author, 2023.

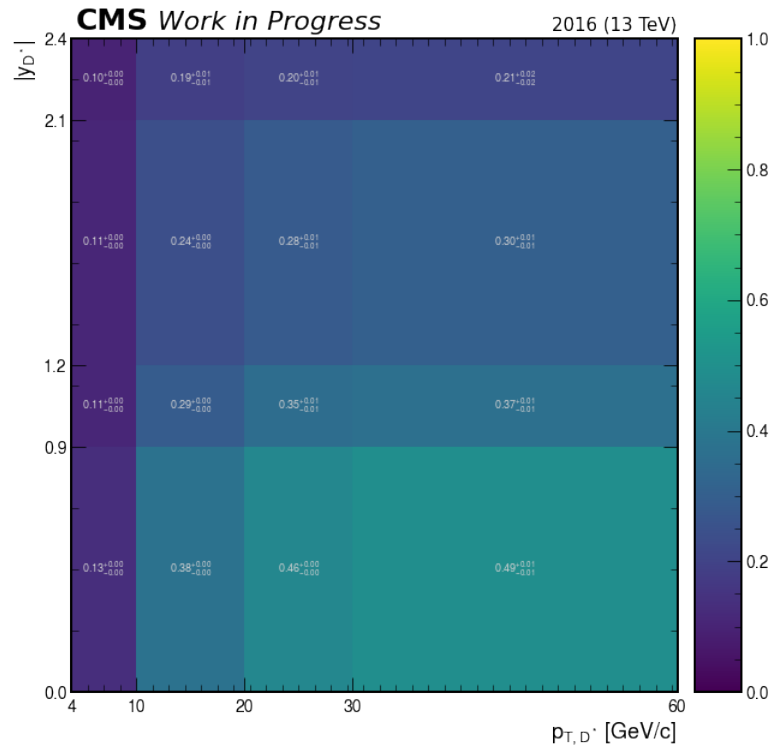
Figure 164 - D^* acceptance in bins of rapidity and p_T - 2016-pos-VFP data.



Legend: The figure shows the D^* acceptance in the region $|y| < 2.4$ and $4 < p_T < 60$ GeV/c .

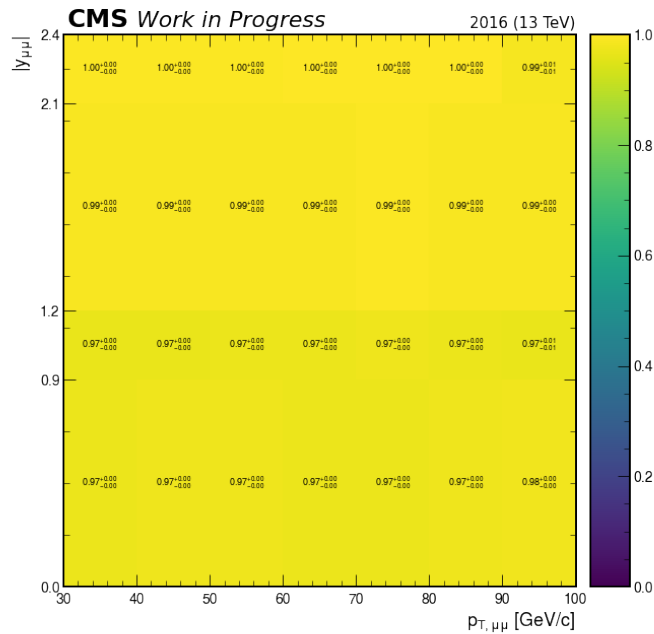
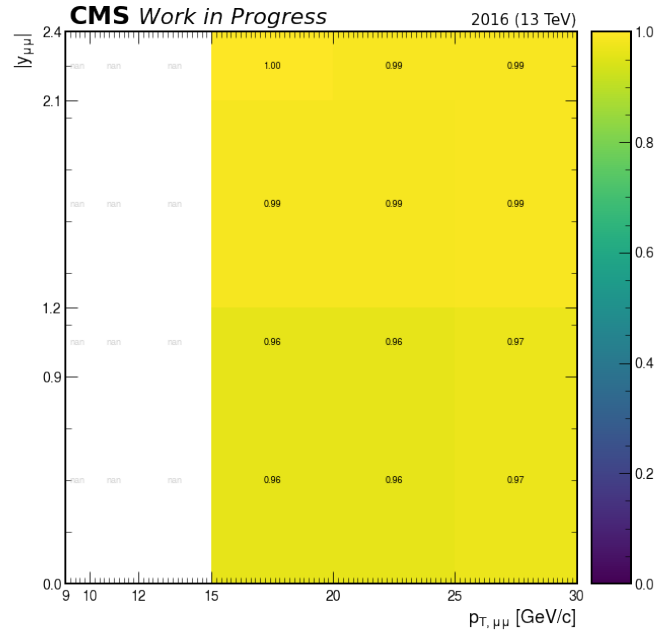
Source: The author, 2023.

Figure 165 - D^* cuts efficiency in bins of rapidity and p_T - 2016-pos-VFP data.



Legend: The figure shows the D^* cuts efficiency in the region $|y| < 2.4$ and $4 < p_T < 60$ GeV/c .
 Source: The author, 2023.

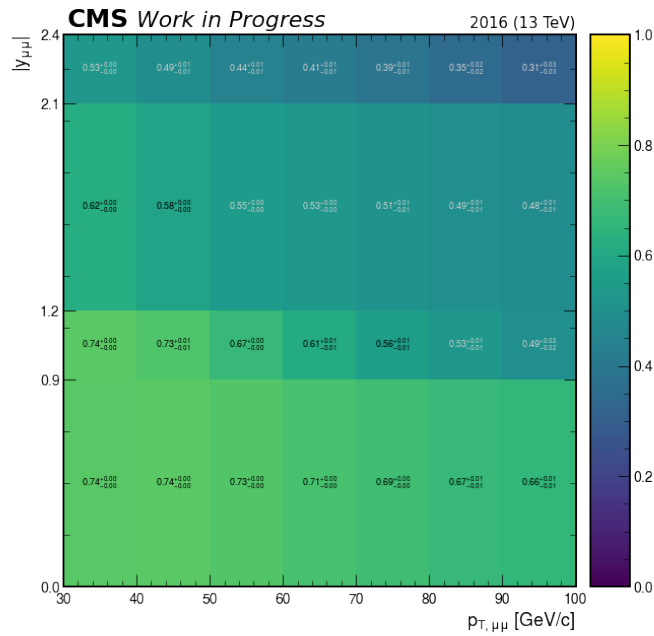
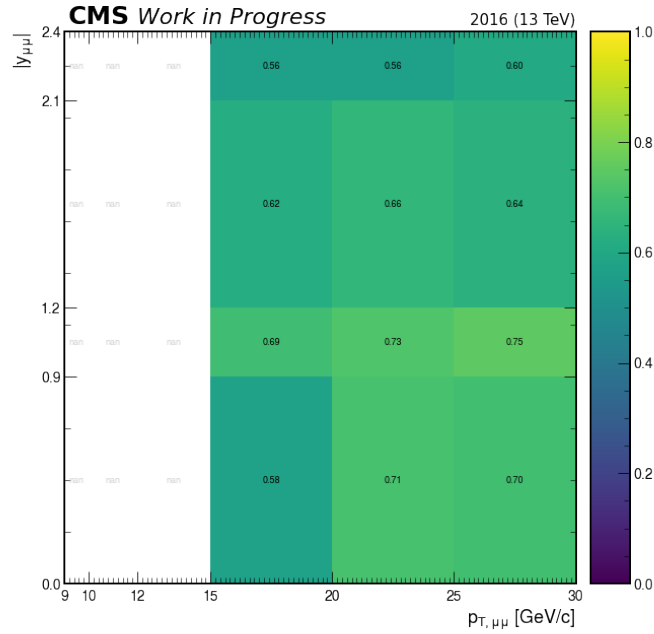
Figure 166 - J/ψ cuts efficiency in bins of rapidity and p_T - 2016-pos-VFP data.



Legend: The figure on top shows the J/ψ cuts efficiency in the region $|y| < 2.4$ and $9 < p_T < 30$ GeV/c and the figure on bottom shows it in the region $|y| < 2.4$ and $30 < p_T < 100$ GeV/c. Top figure: uncertainties are purposely omitted for visualization purposes.

Source: The author, 2023.

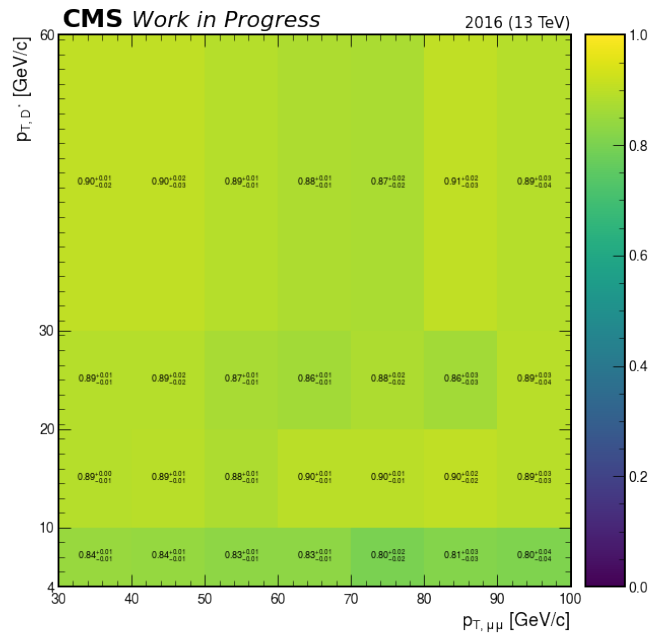
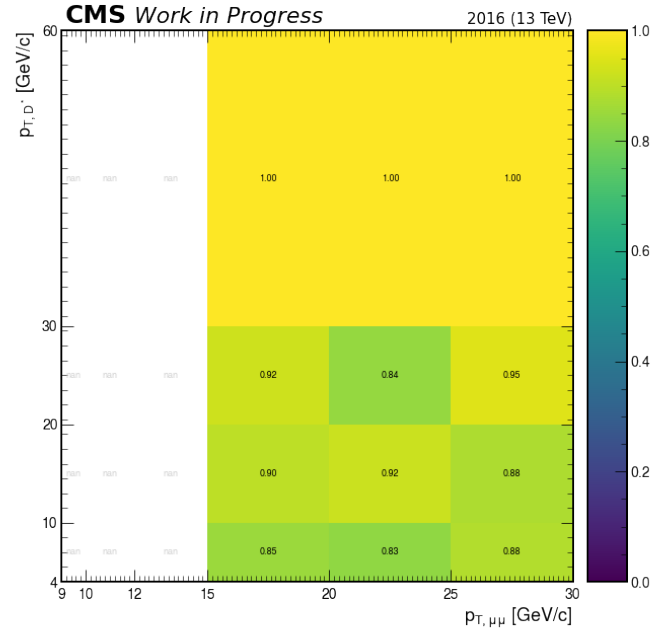
Figure 167 - HLT efficiency in bins of rapidity and p_T - 2016-pos-VFP data.



Legend: The figure on top shows the HLT efficiency in the region $|y| < 2.4$ and $9 < p_T < 30$ GeV/c and the figure on the bottom shows it in the region $|y| < 2.4$ and $30 < p_T < 100$ GeV/c. Top figure: uncertainties are purposely omitted for visualization purposes.

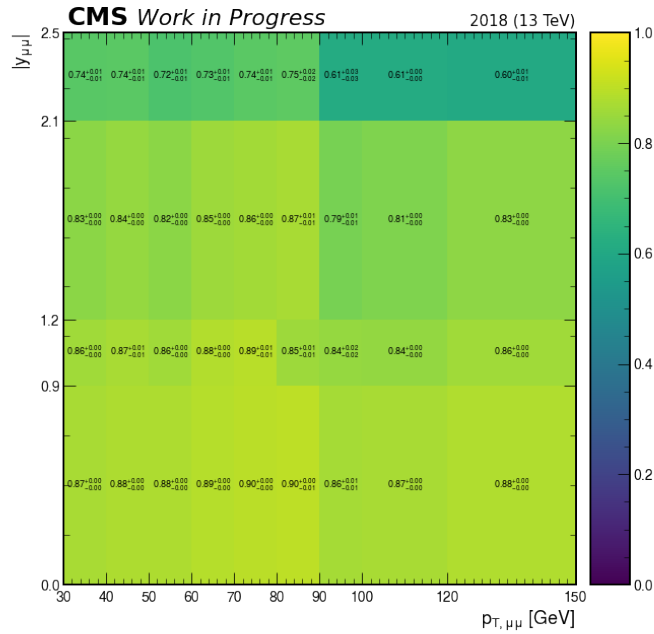
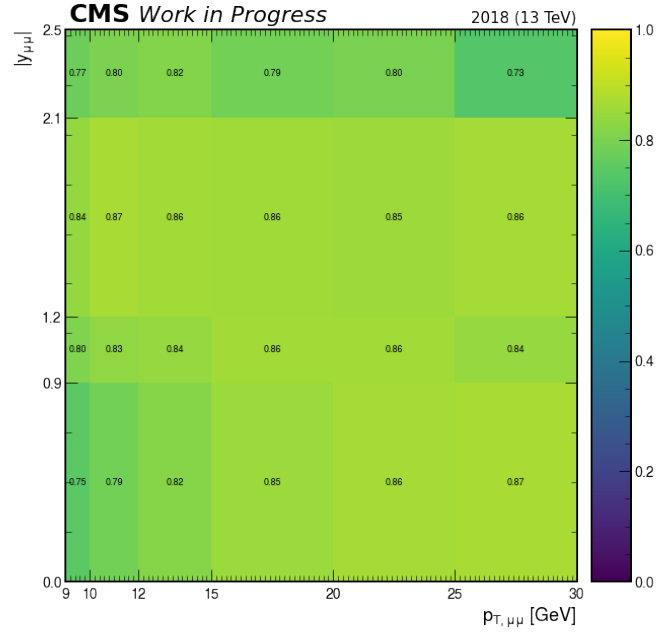
Source: The author, 2023.

Figure 168 - Association efficiency in bins of D^* p_T and J/ψ p_T - 2016-pos-VFP data.



Legend: The figure on top shows the association efficiency in the region $4 < p_T^{D^*} < 60$ GeV/c and $9 < p_T^{D^*} < 30$ GeV/c and the figure on the bottom shows it in the region $4 < p_T^{D^*} < 60$ GeV/c and $30 < p_T^{D^*} < 100$ GeV/c. Top figure: uncertainties are purposely omitted for visualization purposes.

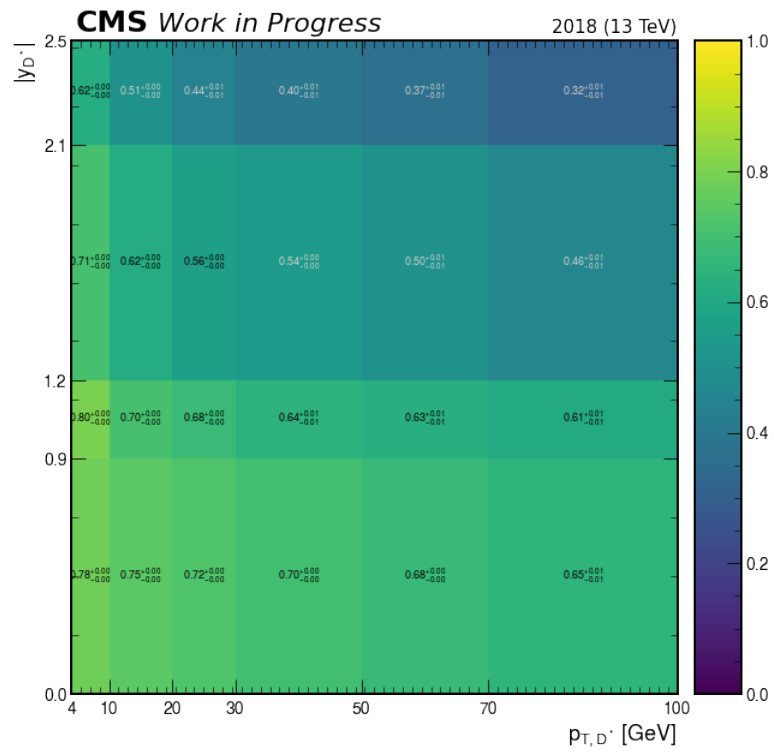
Source: The author, 2023.

Figure 169 - J/ψ acceptance in bins of rapidity and p_T - 2018 data.

Legend: The figure on top shows the J/ψ acceptance in the region $|y| < 2.4$ and $9 < p_T < 30$ GeV/c and the figure on bottom shows it in the region $|y| < 2.4$ and $30 < p_T < 100$ GeV/c. Top figure: uncertainties are purposely omitted for visualization purposes.

Source: The author, 2023.

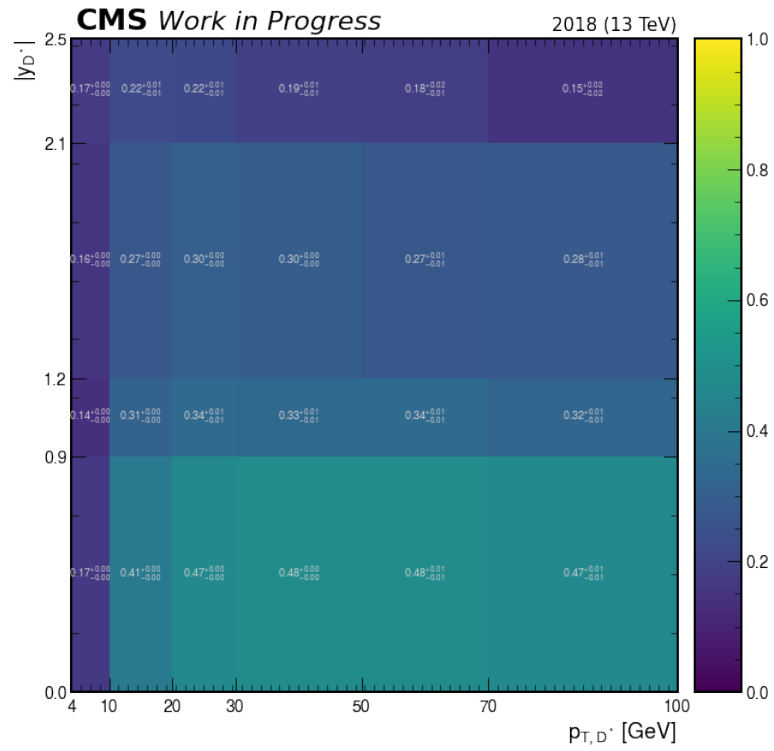
Figure 170 - D^* acceptance in bins of rapidity and p_T - 2018 data.



Legend: The figure shows the D^* acceptance in the region $|y| < 2.4$ and $4 < p_T < 60$ GeV/c .

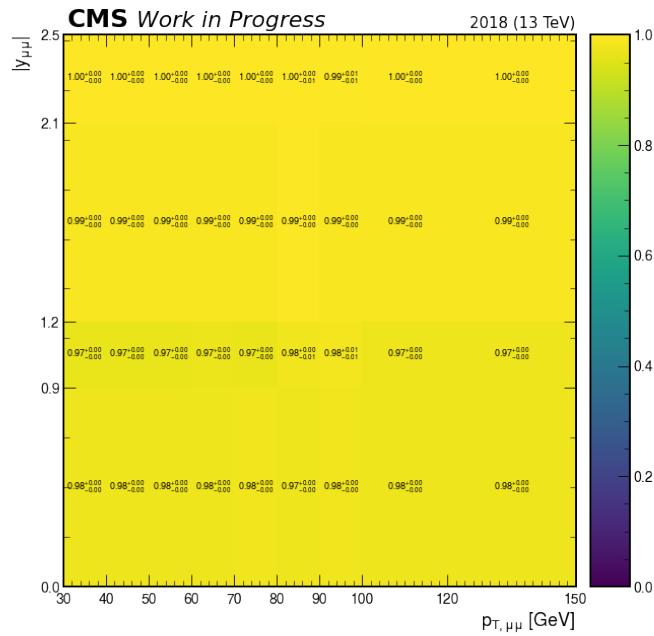
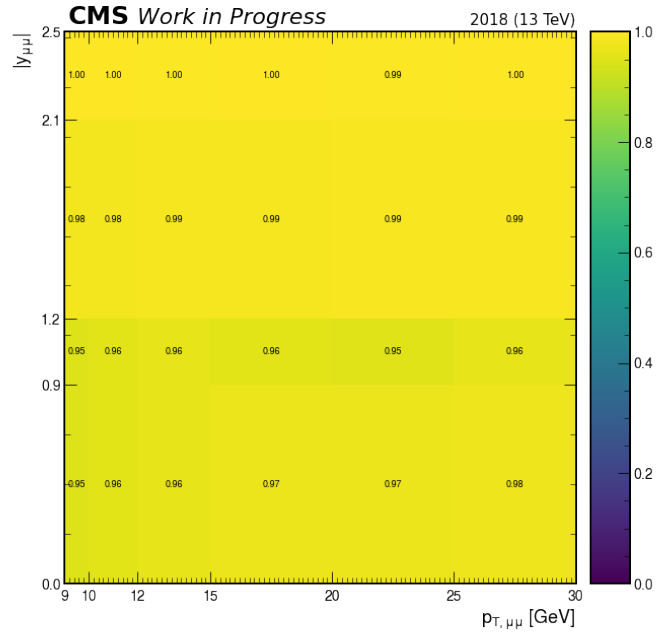
Source: The author, 2023.

Figure 171 - D^* cuts efficiency in bins of rapidity and p_T - 2018 data.



Legend: The figure shows the D^* cuts efficiency in the region $|y| < 2.4$ and $4 < p_T < 60$ GeV/c .
 Source: The author, 2023.

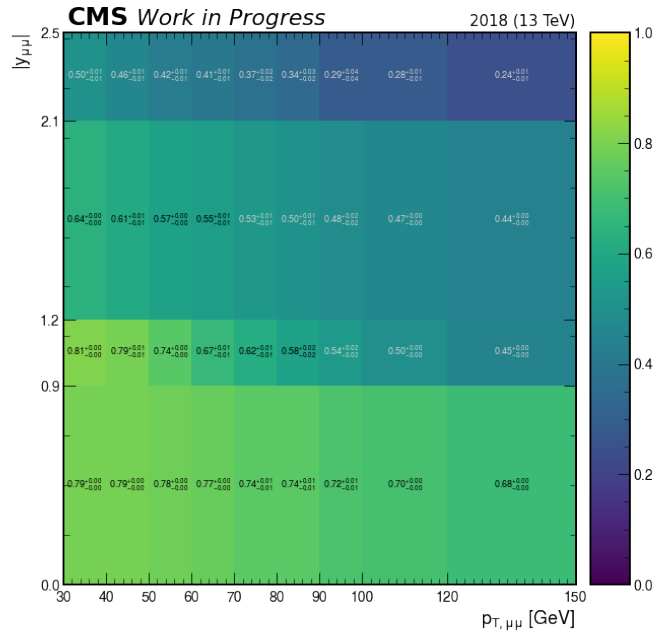
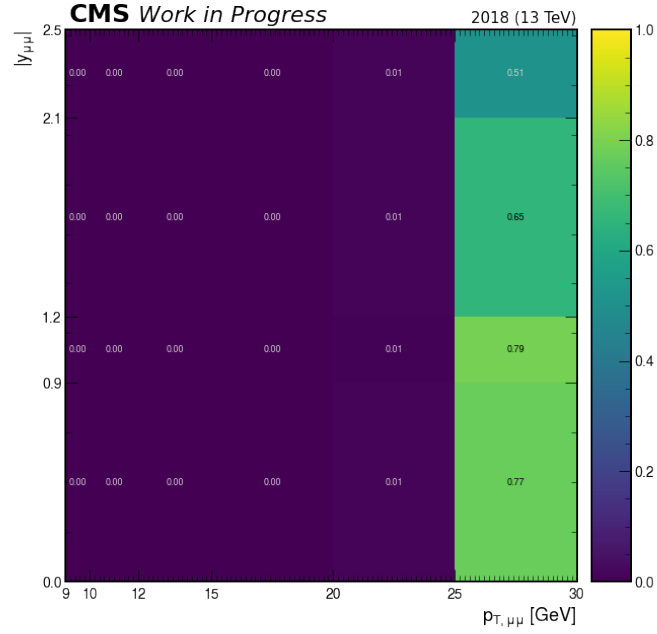
Figure 172 - J/ψ cuts efficiency in bins of rapidity and p_T - 2018 data.



Legend: The figure on top shows the J/ψ cuts efficiency in the region $|y| < 2.4$ and $9 < p_T < 30$ GeV/c and the figure on bottom shows it in the region $|y| < 2.4$ and $30 < p_T < 100$ GeV/c. Top figure: uncertainties are purposely omitted for visualization purposes.

Source: The author, 2023.

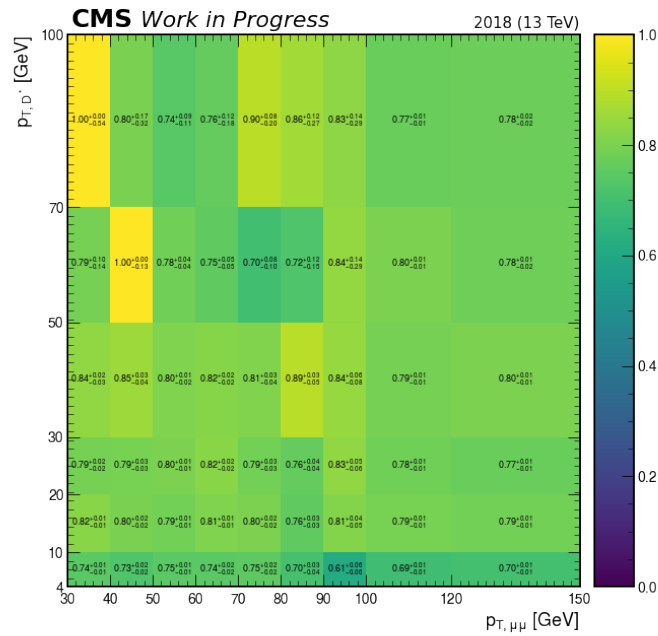
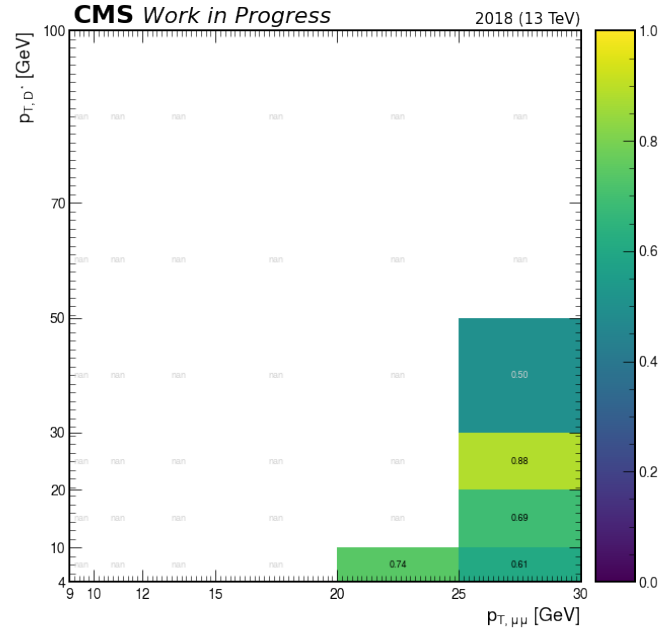
Figure 173 - HLT efficiency in bins of rapidity and p_T - 2018 data.



Legend: The figure on top shows the HLT efficiency in the region $|y| < 2.4$ and $9 < p_T < 30$ GeV/c and the figure on the bottom shows it in the region $|y| < 2.4$ and $30 < p_T < 100$ GeV/c. Top figure: uncertainties are purposely omitted for visualization purposes.

Source: The author, 2023.

Figure 174 - Association efficiency in bins of D^* p_T and J/ψ p_T - 2018 data.



Legend: The figure on top shows the association efficiency in the region $4 < p_T^{D^*} < 60$ GeV/c and $9 < p_T^{D^*} < 30$ GeV/c and the figure on the bottom shows it in the region $4 < p_T^{D^*} < 60$ GeV/c and $30 < p_T^{D^*} < 100$ GeV/c. Top figure: uncertainties are purposely omitted for visualization purposes.

Source: The author, 2023.

APPENDIX I – Systematic Uncertainties: strategies

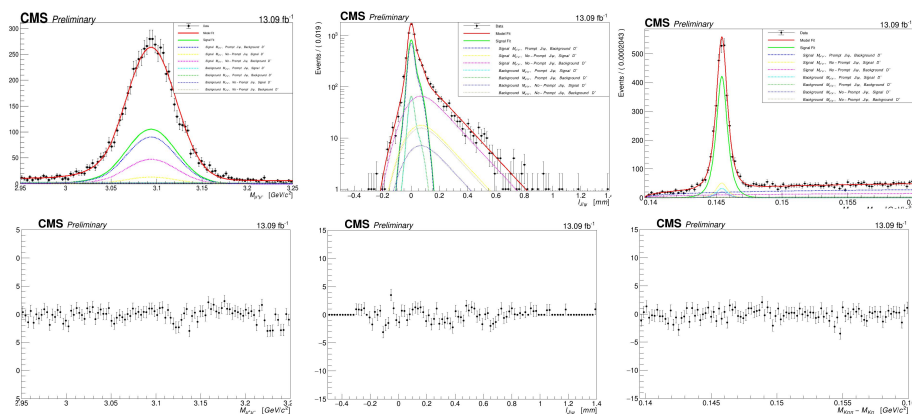
This section is dedicated to the details related to systematic uncertainties discussed in Section (4.7).

I.1 Signal yields

In this section, the fits of all cases mentioned in Section (4.7.3) are shown.

I.1.1 2016-pre-VFP

Figure 175 - 2016-pre-VFP data: case 2.



Legend: Left: 1D projections of the fits of $\mu^+\mu^-$ invariant mass (Top), pull distribution (bottom). Middle: 1D projections of the fits of J/ψ decay length (Top), pull distribution (bottom). Right: 1D projections of the fits of $D - D^0$ mass difference (Top), pull distribution (bottom).

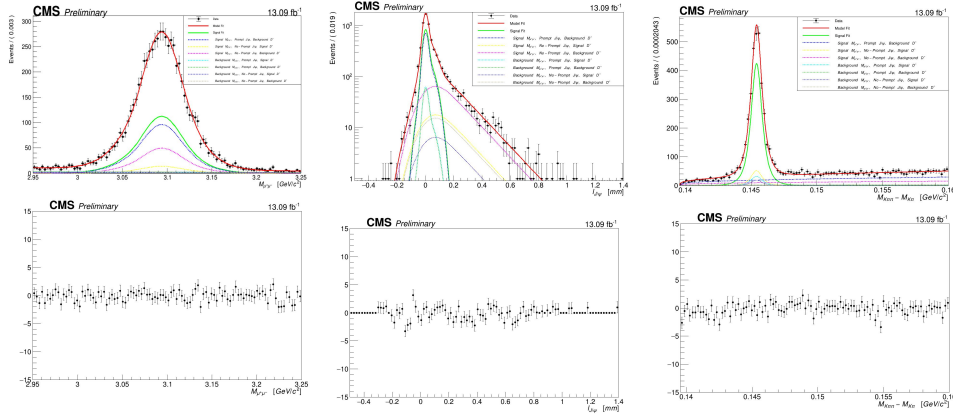
Source: The author, 2023.

I.1.2 2016-pos-VFP

I.1.3 2017

I.1.4 2018

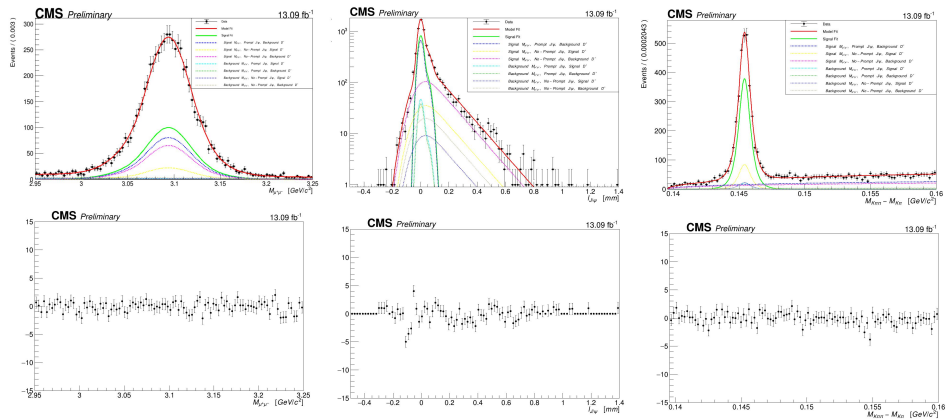
Figure 176 - 2016-pre-VFP data: case 3.



Legend: Left: 1D projections of the fits of $\mu^+\mu^-$ invariant mass (Top), pull distribution (bottom). Middle: 1D projections of the fits of J/ψ decay length (Top), pull distribution (bottom). Right: 1D projections of the fits of $D - D^0$ mass difference (Top), pull distribution (bottom).

Source: The author, 2023.

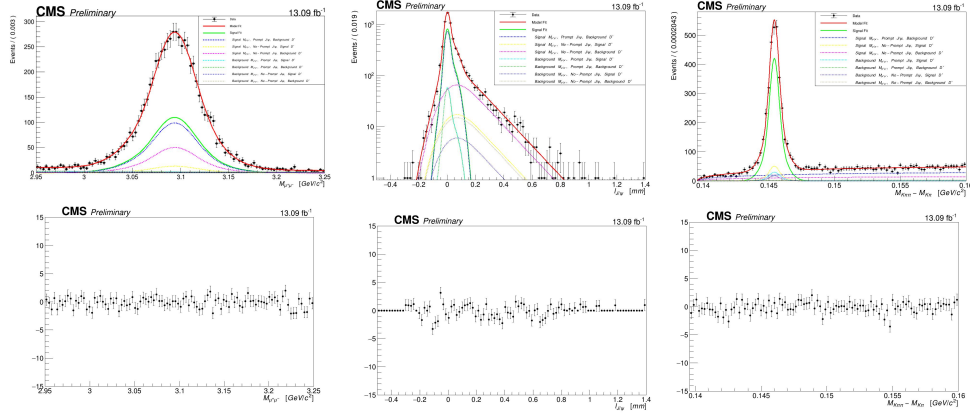
Figure 177 - 2016-pre-VFP data: case 4.



Legend: Left: 1D projections of the fits of $\mu^+\mu^-$ invariant mass (Top), pull distribution (bottom). Middle: 1D projections of the fits of J/ψ decay length (Top), pull distribution (bottom). Right: 1D projections of the fits of $D - D^0$ mass difference (Top), pull distribution (bottom).

Source: The author, 2023.

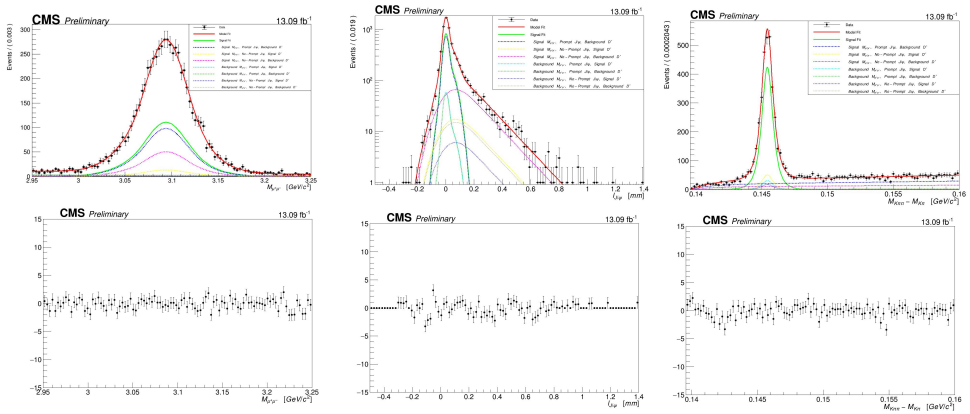
Figure 178 - 2016-pre-VFP data: case 5.



Legend: Left: 1D projections of the fits of $\mu^+\mu^-$ invariant mass (Top), pull distribution (bottom). Middle: 1D projections of the fits of J/ψ decay length (Top), pull distribution (bottom). Right: 1D projections of the fits of D - D⁰ mass difference (Top), pull distribution (bottom).

Source: The author, 2023.

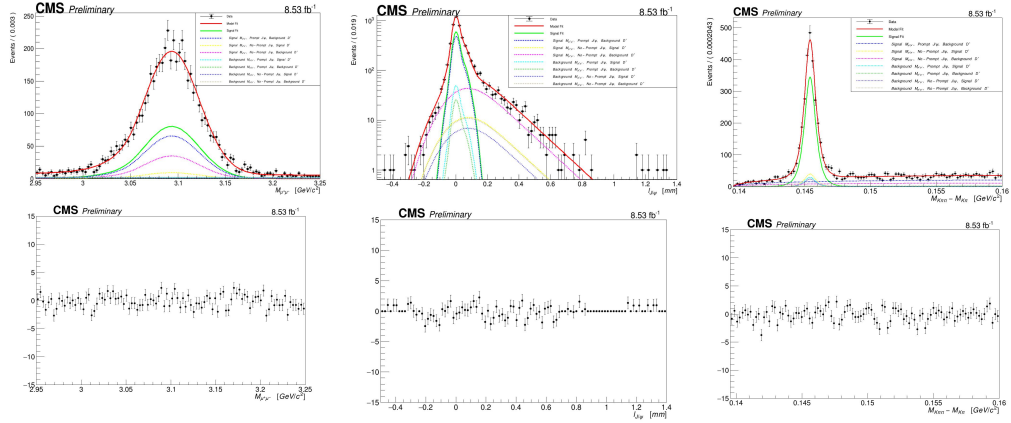
Figure 179 - 2016-pre-VFP data: case 6.



Legend: Left: 1D projections of the fits of $\mu^+\mu^-$ invariant mass (Top), pull distribution (bottom). Middle: 1D projections of the fits of J/ψ decay length (Top), pull distribution (bottom). Right: 1D projections of the fits of D - D⁰ mass difference (Top), pull distribution (bottom).

Source: The author, 2023.

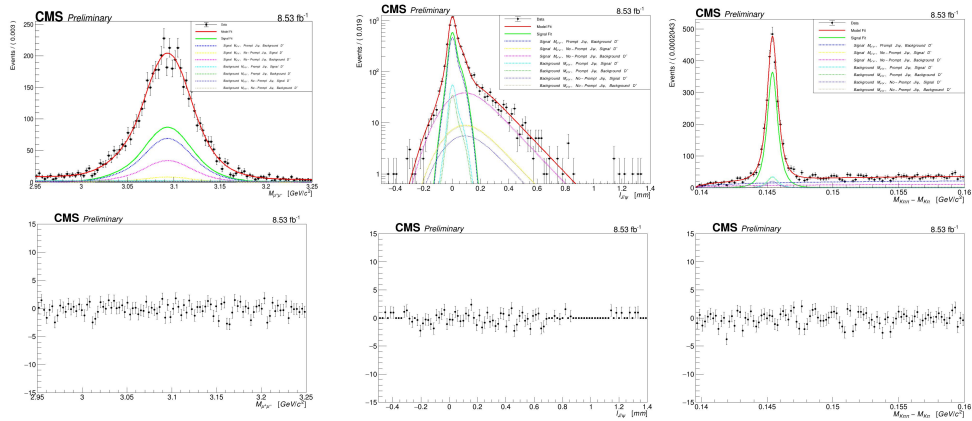
Figure 180 - 2016-pos-VFP data: case 2.



Legend: Left: 1D projections of the fits of $\mu^+\mu^-$ invariant mass (Top), pull distribution (bottom). Middle: 1D projections of the fits of J/ψ decay length (Top), pull distribution (bottom). Right: 1D projections of the fits of $D - D^0$ mass difference (Top), pull distribution (bottom).

Source: The author, 2023.

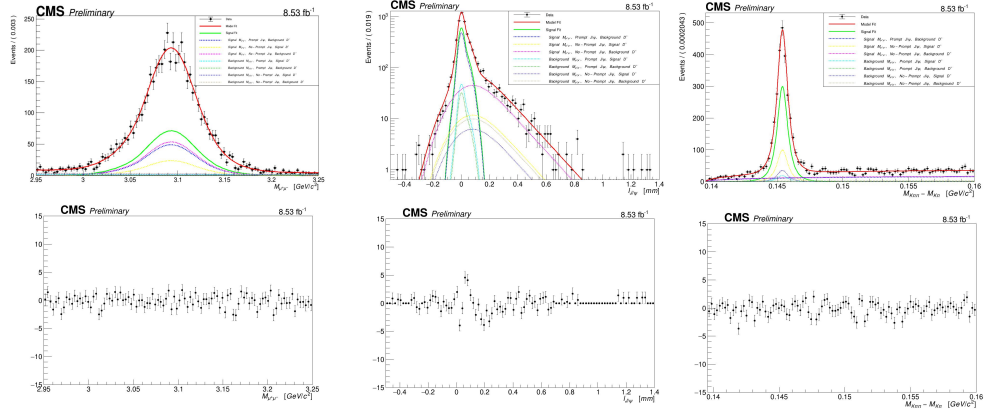
Figure 181 - 2016-pos-VFP data: case 3.



Legend: Left: 1D projections of the fits of $\mu^+\mu^-$ invariant mass (Top), pull distribution (bottom). Middle: 1D projections of the fits of J/ψ decay length (Top), pull distribution (bottom). Right: 1D projections of the fits of $D - D^0$ mass difference (Top), pull distribution (bottom).

Source: The author, 2023.

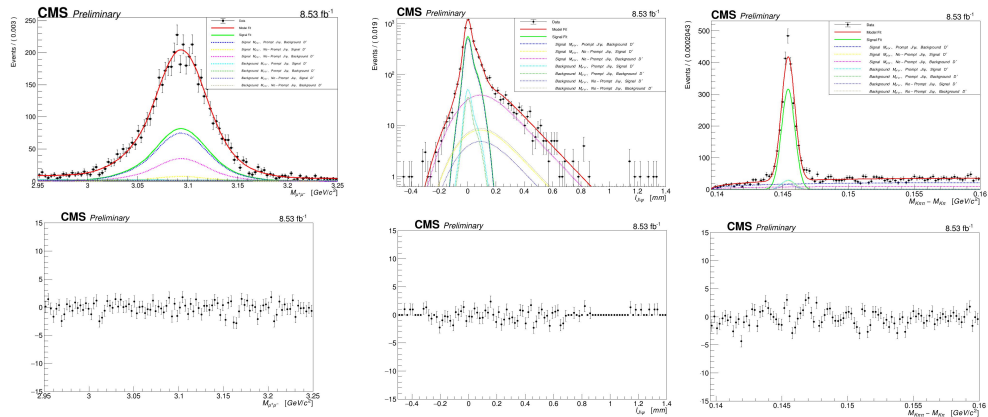
Figure 182 - 2016-pos-VFP data: case 4.



Legend: Left: 1D projections of the fits of $\mu^+\mu^-$ invariant mass (Top), pull distribution (bottom). Middle: 1D projections of the fits of J/ψ decay length (Top), pull distribution (bottom). Right: 1D projections of the fits of $D - D^0$ mass difference (Top), pull distribution (bottom).

Source: The author, 2023.

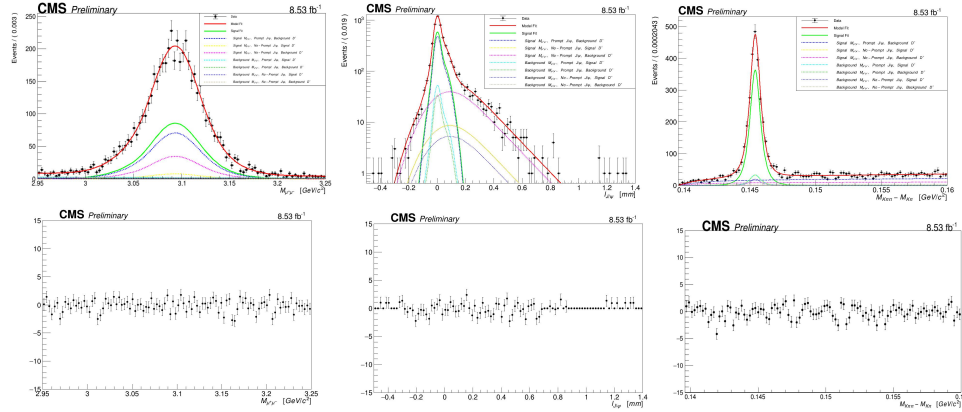
Figure 183 - 2016-pos-VFP data: case 5.



Legend: Left: 1D projections of the fits of $\mu^+\mu^-$ invariant mass (Top), pull distribution (bottom). Middle: 1D projections of the fits of J/ψ decay length (Top), pull distribution (bottom). Right: 1D projections of the fits of $D - D^0$ mass difference (Top), pull distribution (bottom).

Source: The author, 2023.

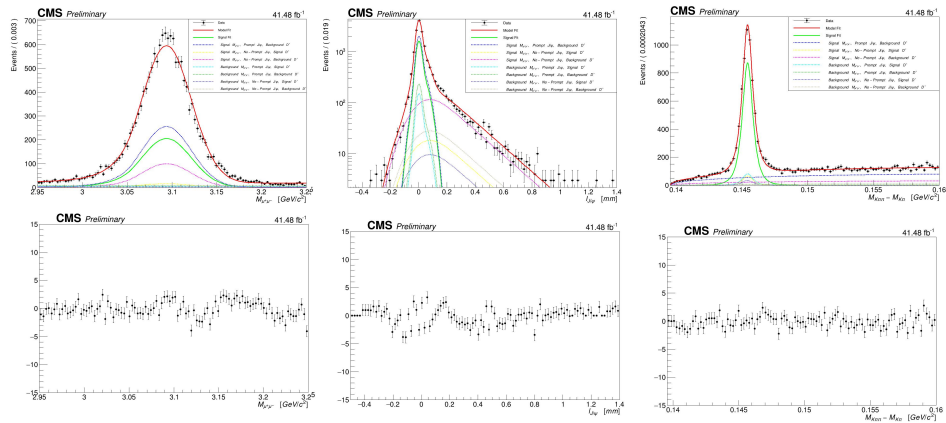
Figure 184 - 2016-pos-VFP data: case 6.



Legend: Left: 1D projections of the fits of $\mu^+\mu^-$ invariant mass (Top), pull distribution (bottom). Middle: 1D projections of the fits of J/ψ decay length (Top), pull distribution (bottom). Right: 1D projections of the fits of $D - D^0$ mass difference (Top), pull distribution (bottom).

Source: The author, 2023.

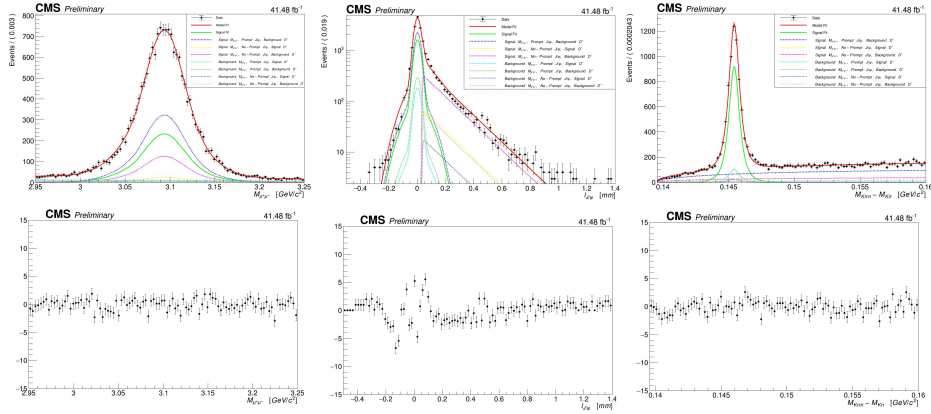
Figure 185 - 2017 data: case 2.



Legend: Left: 1D projections of the fits of $\mu^+\mu^-$ invariant mass (Top), pull distribution (bottom). Middle: 1D projections of the fits of J/ψ decay length (Top), pull distribution (bottom). Right: 1D projections of the fits of $D - D^0$ mass difference (Top), pull distribution (bottom).

Source: The author, 2023.

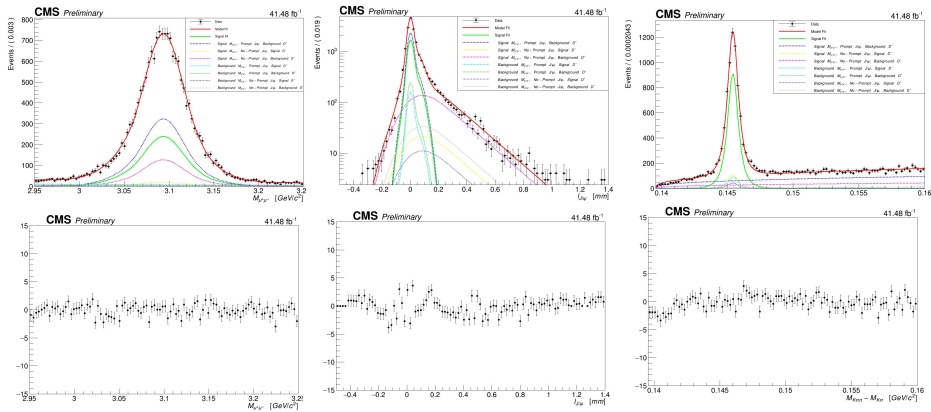
Figure 186 - 2017 data: case 3.



Legend: Left: 1D projections of the fits of $\mu^+\mu^-$ invariant mass (Top), pull distribution (bottom). Middle: 1D projections of the fits of J/ψ decay length (Top), pull distribution (bottom). Right: 1D projections of the fits of $D - D^0$ mass difference (Top), pull distribution (bottom).

Source: The author, 2023.

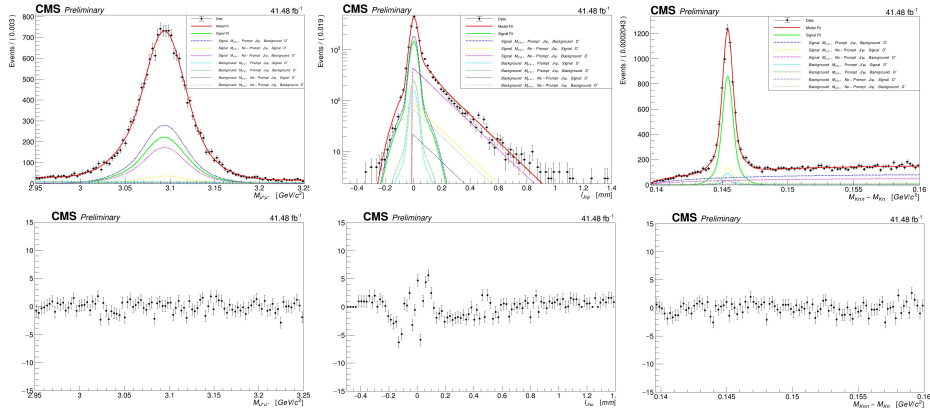
Figure 187 - 2017 data: case 4.



Legend: Left: 1D projections of the fits of $\mu^+\mu^-$ invariant mass (Top), pull distribution (bottom). Middle: 1D projections of the fits of J/ψ decay length (Top), pull distribution (bottom). Right: 1D projections of the fits of $D - D^0$ mass difference (Top), pull distribution (bottom).

Source: The author, 2023.

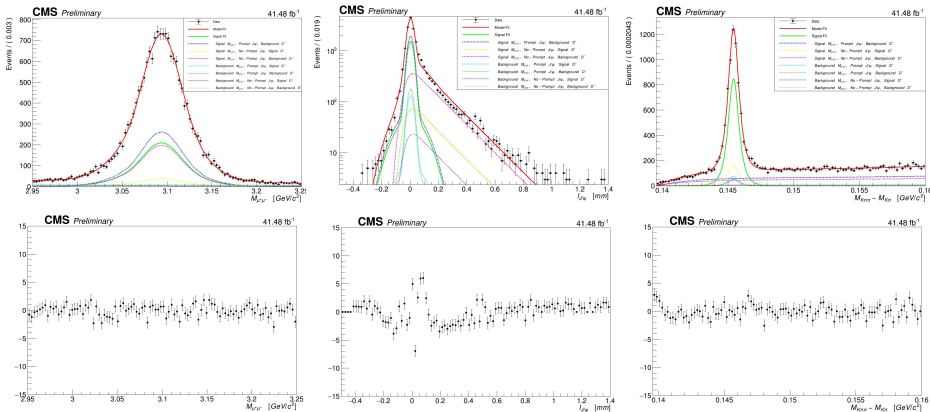
Figure 188 - 2017 data: case 5.



Legend: Left: 1D projections of the fits of $\mu^+\mu^-$ invariant mass (Top), pull distribution (bottom). Middle: 1D projections of the fits of J/ψ decay length (Top), pull distribution (bottom). Right: 1D projections of the fits of $D - D^0$ mass difference (Top), pull distribution (bottom).

Source: The author, 2023.

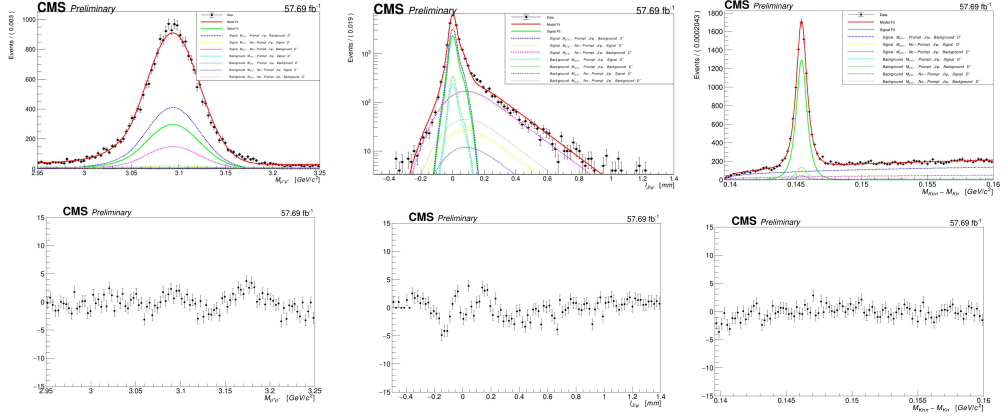
Figure 189 - 2017 data: case 6.



Legend: Left: 1D projections of the fits of $\mu^+\mu^-$ invariant mass (Top), pull distribution (bottom). Middle: 1D projections of the fits of J/ψ decay length (Top), pull distribution (bottom). Right: 1D projections of the fits of $D - D^0$ mass difference (Top), pull distribution (bottom).

Source: The author, 2023.

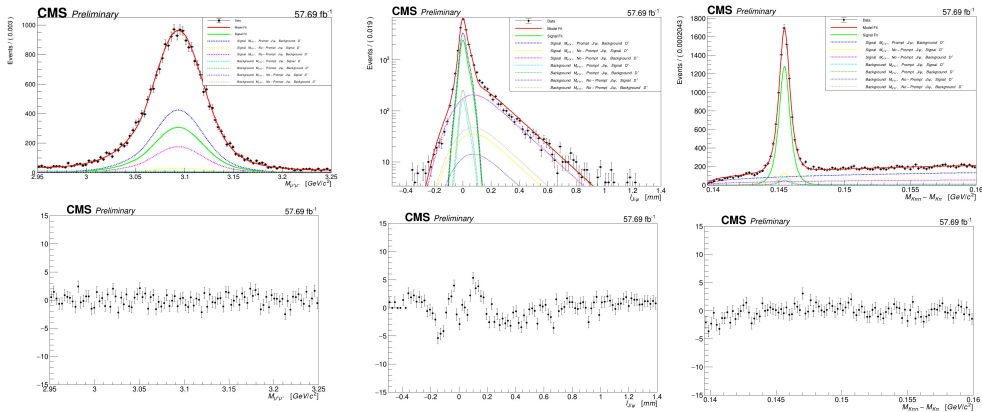
Figure 190 - 2018 data: case 2.



Legend: Left: 1D projections of the fits of $\mu^+\mu^-$ invariant mass (Top), pull distribution (bottom). Middle: 1D projections of the fits of J/ψ decay length (Top), pull distribution (bottom). Right: 1D projections of the fits of $D - D^0$ mass difference (Top), pull distribution (bottom).

Source: The author, 2023.

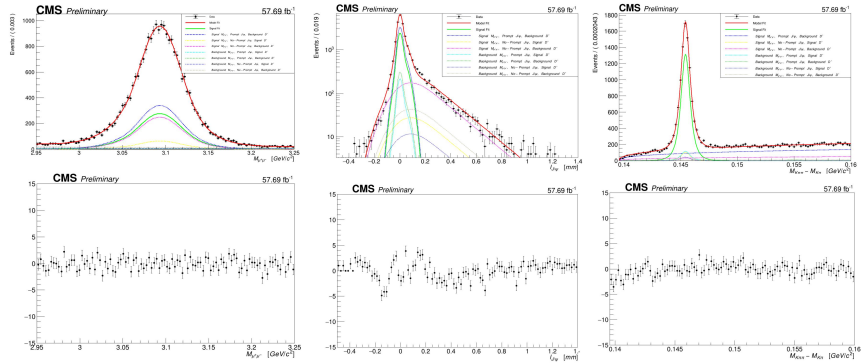
Figure 191 - 2018 data: case 3.



Legend: Left: 1D projections of the fits of $\mu^+\mu^-$ invariant mass (Top), pull distribution (bottom). Middle: 1D projections of the fits of J/ψ decay length (Top), pull distribution (bottom). Right: 1D projections of the fits of $D - D^0$ mass difference (Top), pull distribution (bottom).

Source: The author, 2023.

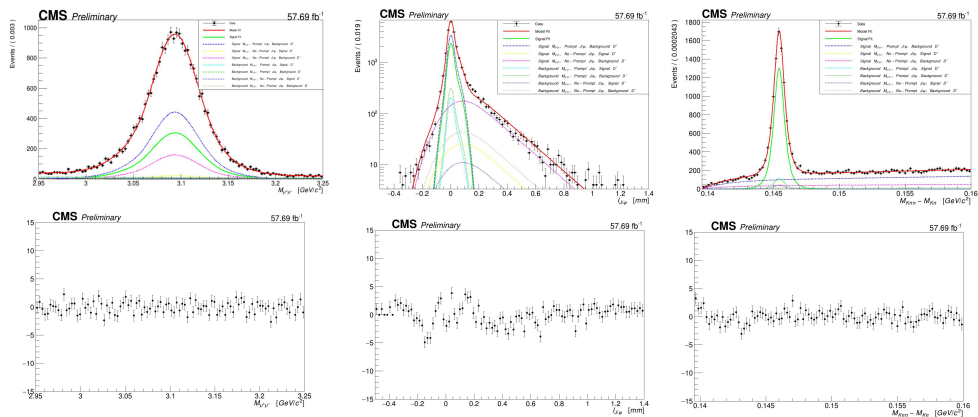
Figure 192 - 2018 data: case 4.



Legend: Left: 1D projections of the fits of $\mu^+\mu^-$ invariant mass (Top), pull distribution (bottom). Middle: 1D projections of the fits of J/ψ decay length (Top), pull distribution (bottom). Right: 1D projections of the fits of $D - D^0$ mass difference (Top), pull distribution (bottom).

Source: The author, 2023.

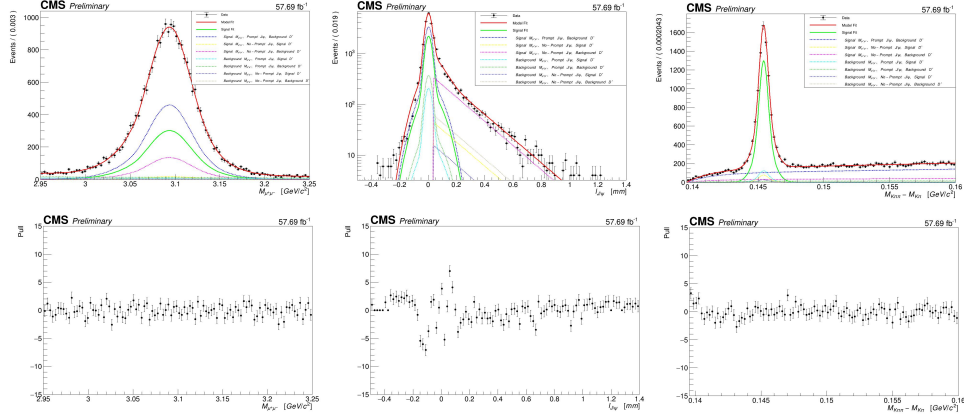
Figure 193 - 2018 data: case 5.



Legend: Left: 1D projections of the fits of $\mu^+\mu^-$ invariant mass (Top), pull distribution (bottom). Middle: 1D projections of the fits of J/ψ decay length (Top), pull distribution (bottom). Right: 1D projections of the fits of $D - D^0$ mass difference (Top), pull distribution (bottom).

Source: The author, 2023.

Figure 194 - 2018 data: case 6.



Legend: Left: 1D projections of the fits of $\mu^+\mu^-$ invariant mass (Top), pull distribution (bottom). Middle: 1D projections of the fits of J/ψ decay length (Top), pull distribution (bottom). Right: 1D projections of the fits of $D - D^0$ mass difference (Top), pull distribution (bottom).

Source: The author, 2023.

1.2 Tracking efficiency

The efficiencies are obtained from the tracking POG. Table (82) shows how the composition of the systematic uncertainty is.

Table 82 - Tracking - details of the systematic uncertainty.

Year	Tracking eff. (POG)	Stat. Uncert.	Syst. Uncert.	PDG Uncert.	Track 1	Track 2	Slow Pion	Total (%)
2016	1.016	0.021	0.012	0.012	0.027	0.024	0.052	10.3
2017	1.003	0.016	0.009	0.012	0.022	0.018	0.052	9.2
2018	0.0998	0.014	0.008	0.012	0.020	0.016	0.052	8.8

Legend: The values in the second, third, and fourth columns are calculated by the track POG (197).

Source: The author, 2023.

1.3 Cuts efficiency

The strategy for getting this systematic uncertainty is highlighted in Tables (83), (84), (85). The results shown here refer to the phase space $4 < p_T^{D^*} < 60$ GeV/c, $|y^{D^*}| < 2.1$, $25 < p_T^{J/\psi} < 100$ GeV/c, and $|y^{J/\psi}| < 1.2$. However, the strategy is the same regardless of the phase space used.

Table 83 - Muon ID - details of the systematic uncertainty.

Dataset	$\sigma_{nominal}$ (pb)	$\sigma_{variation}$ (pb)	Uncertainty (%)
2016-pre-VFP	615.08	595.29	3.2
2016-pos-VFP	552.67	473.41	12.1
2017	603.28	608.79	0.9
2018	586.4	616.27	5.1

Legend: The $\sigma_{variation}$ is obtained by changing the soft ID to loose ID. The uncertainty is taken as $(|\sigma_{nominal} - \sigma_{variation}|)/(\sigma_{nominal})$.
Source: The author, 2023.

Table 84 - Pointing angle - details of the systematic uncertainty.

Dataset	$\sigma_{nominal}$ (pb)	$\sigma_{variation}$ (pb)	Uncertainty (%)
2016-pre-VFP	615.08	657.28	6.86
2016-pos-VFP	552.67	485.89	12.08
2017	603.28	658.66	9.18
2018	586.4	666.31	13.63

Legend: Two different cuts were used to get the $\sigma_{variation}$, 0.985 and 0.995. The cut that provides the greatest difference between the $\sigma_{variation}$ and $\sigma_{nominal}$ is used. The uncertainty is taken as $(|\sigma_{nominal} - \sigma_{variation}|)/(\sigma_{nominal})$.
Source: The author, 2023.

Table 85 - Association - details of the systematic uncertainty.

Dataset	$\sigma_{nominal}$ (pb)	$\sigma_{variation}$ (pb)	Uncertainty (%)
2016-pre-VFP	615.08	573.77	6.72
2016-pos-VFP	552.67	477.4	13.62
2017	603.28	573.88	4.87
2018	586.4	649.3	10.73

Legend: Two different cuts were used to get the $\sigma_{variation}$, 0.01 and 0.09. The cut that provides the greatest difference between the $\sigma_{variation}$ and $\sigma_{nominal}$ is used. The uncertainty is taken as $(|\sigma_{nominal} - \sigma_{variation}|)/(\sigma_{nominal})$.
Source: The author, 2023.

To obtain the values shown in Table (64) the quadrature sum is performed

$$\sigma_{cuts} = \sqrt{\sigma_{muon ID}^2 + \sigma_{pointing angle}^2 + \sigma_{association}^2}. \quad (53)$$